UNIVERSITY OF SOUTHAMPTON

Faculty of Social and Human Sciences

Geography and Environment

Inter-comparison of multiple angle remotely sensed data across different spatial resolutions and sensors for determination of albedo

by

Hassan Khavarian Nehzak

Thesis for the degree of Doctor of Philosophy

March 2012

ABSTRACT

Surface albedo is one of the critical parameters required by studies of surface energy balance and climate models. Albedo is defined as the ratio of outgoing radiances to incoming irradiances over hemispherical view-illumination geometry. Remotely sensed albedo is usually based on multiple view angle observations and a Bidirectional Reflectance Distribution Function (BRDF) model. The accuracy of remotely sensed albedo depends on a variety of factors of which the main ones are the accuracy of atmospherically corrected observations, the reliability of observations, and the validity of the applied BRDF model. Fine spatial resolution airborne and satellite data are valuable for the validation of coarse spatial resolution satellite albedos as they may be validated using field measurements with higher reliability. In this study, a variety of remote sensing data and field measurements were used to estimate, validate and analyse albedo at different spatial resolutions. The main aim was to validate the MODIS albedo product under UK conditions using the methods of direct and indirect comparisons with other available data. The source of the fine spatial resolution data used was the NCAVEO Field Campaign 2006 that took place at the Chilbolton calibration test site in southern England. The CHRIS/PROBA albedo was used as a fine spatial resolution (34 m) albedo map to investigate the spatial variation of albedo. The results of this investigation provided valuable information about the possibility of the extension of the obtained albedo map from CHRIS/PROBA data. The MODIS albedo product with a coarser spatial resolution (500 m), relative to the NCAVEO datasets, was compared with the CHRIS/PROBA albedo map to examine the effect of spatial scale on the accuracy of albedo (direct comparison). The uncertainties in the obtained albedo maps, from both MODIS and CHRIS/PROBA, were mainly examined by testing the accuracy of the input reflectance data and the applied BRDF model (indirect comparison). The results showed the accuracy of the MODIS albedo product inferior to that claimed by the MODIS team.

Contents

List of figures

List of Tables

DECLARATION OF AUTHORSHIP

I, Hassan Khavarian Nehzak declare that the thesis entitled

Inter-comparison of multiple angle remotely sensed data across different spatial resolutions and sensors

and the work presented in the thesis are both my own, and have been generated by me as the result of my own original research. I confirm that:

- this work was done wholly or mainly while in candidature for a research degree at this University;
- where any part of this thesis has previously been submitted for a degree or any other qualification at this University or any other institution, this has been clearly stated;
- where I have consulted the published work of others, this is always clearly attributed;
- where I have quoted from the work of others, the source is always given. With the exception of such quotations, this thesis is entirely my own work;
- I have acknowledged all main sources of help;
- where the thesis is based on work done by myself jointly with others, I have made clear exactly what was done by others and what I have contributed myself;
- none of this work has been published before submission.

Signed: ……..

Date:……

Acknowledgements

I am sincerely thankful to my supervisors, Prof. Peter Atkinson and Prof. Ted Milton, whose supervision and valuable feedback from the preliminary to the concluding stages enabled me to develop an understanding of the subject. I am also heartily thankful to Dr. John Stewart whose encouragement and support from the early days of this PhD to the upgrade stage was always reassuring. His loss was a great sorrow for all of us who knew him, God bless him.

This research could not have taken place without the scholarship from the Erasmus Mundus program for Iran, Iraq and Yemen (EM7). Special thanks go to Prof. Peter Atkinson, and Mrs. Maggie Harriss whose efforts and guidance made this opportunity possible. I also thank Dr. Ali Abkar (ITC Coordinator of EM7 Program), and Dr. Samantha Cockings (UoS coordinator of EM7 Program) for their efforts.

Surely, the excellent datasets provided free of charge built up the framework of this study. I would like to sincerely thank the data providers such as the NERC Earth Observation Data Centre, the MODIS team, and the British Atmosphere Data Centre.

This research also received valuable advice from many people outside of the university. I greatly thank Prof. Crystal Schaaf and Dr. Zhousen Wang (from Boston University) for welcoming me for the time I was in Boston and for their advice and help about the MODIS albedo product. I am very grateful for the help I received from the ARSF Processing team for their technical help in processing of the CASI data. I also thank Dr. Luis Guanter for his help regarding the atmospheric correction of the CHRIS/PROBA data.

I also thank all the staff and my friends in the School of Geography for their support throughout my PhD. I especially thank Dr. Jegan Chockalingam and Dr. Francesco Vuolo, for their scientific help, and Mrs Julie Drewitt, for all the administrative help and advice. I thank my officemates in room 1019 (which is 1083 now) for the great time we had especially in lunch and coffee times. Speaking of coffee, I'd like to thank the Coffee Club managers and cake bakers in the last four years in my school, their coffee and cake kept me in the working mood.

My deepest gratitude goes to my family, especially my mother, for their support throughout my PhD; this research could not have been done without their help. Thanks to my father for his care and love throughout my life. His loss was a great sorrow and unbearable for me and if it wasn't the support of my family and relatives, it would have been very difficult for me to carry on my PhD.

Definitions and abbreviations

Each abbreviation and symbol is explained in the text when it is first introduced.

Symbol	Definition	Symbol	Definition
M	Amount of energy emitted by surface (Wm^{-2})	R_f	Reflectance factor (–)
σ	Stephan–Boltzmann constant, 5.67×10^{-8} ($Wm^{-2}K^{-4}$)	a, b, c, and d (in Equations 2–7 to 2–9)	Coefficients (–)
T	Surface temperature (K)	$F1$	Geometric parameter of Roujean and RTLSR BRDF models
λ_{max}	Wavelength at which the radiation of a surface will be greatest (μm)	$F2$	Volumetric parameter of Roujean and RTLSR BRDF models
b (in Equation 1–2)	2898 (μm K)	$\Delta(\theta_i, \theta_r, \varphi)$	Horizontal distance between the Sun and view angle directions (radian)
λ	Wavelength (μm)	φ	Relative azimuth angle ($\varphi_r - \varphi_r$) (°)
R_n	Net radiation flux (Wm^{-2})	ξ	Phase angle of scattering (°)
H	Sensible heat flux (Wm^{-2})	ξ_0	Characteristic angle (°)
LE	Latent heat flux (Wm^{-2})	f_{iso}	Isotropic parameter (–)
G	Soil heat flux (Wm^{-2})	f_{vol}	Volumetric parameter (–)
$R_s\downarrow$	Incoming solar radiation (Wm^{-2})	f_{geo}	Geometric–optical parameter (–)
α	Surface albedo (–)	K_{vol}	Volumetric kernel (–)

$L\downarrow$	Incoming long-wave radiation (Wm^{-2})	K_{geo}	Geometric-optical kernel (-)
$L\uparrow$	Outgoing long-wave radiation (Wm^{-2})	$O(\theta_i,\theta_r,\varphi)$	Overlap function of view and illumination shadows on ground (-)
ET_0	Water volume evaporated ($m^3s^{-1}m^2$)	b (in Equations 2-25, 2-28 and 2-29)	Vertical radius of crown (m)
Δ	Rate of change of saturation specific humidity with air temperature (Pa K^{-1})	r (in Equations 2-28 and 2-29)	Horizontal radius of crown (m)
c_p	Specific heat capacity of air (J kg^{-1} K^{-1})	h (in Equation 2-25)	Height to the centre of crown (m)
ρ_a	Dry air density (kg m^{-3})	ξ'	Phase angle between illumination and viewing direction (°)
δe	Vapor pressure deficit, or specific humidity (Pa)	θ_i'	Effective zenith angle of illumination direction, adjusted for spheroidal shape of crown (°)
g_a	Conductivity of air, atmospheric conductance (m s^{-1})	θ_r'	Effective zenith angle of view direction, adjusted for spheroidal shape of crown (°)
g_s	Conductivity of stoma, surface conductance (m s^{-1})	t	t-test statistic (-)
γ	Psychrometric constant ($\gamma \approx 66$) (Pa K^{-1})	X	Observations being examined
λ_v	Latent heat of vaporization (J g^{-1})	Y	Reference observations
α_{toa}	Albedo at the top of the	$\overline{X}$	Mean value of *X* dataset

	atmosphere (–)		
$\alpha_{path\_radiance}$	Albedo path radiance (–)	$\overline{Y}$	Mean value of *Y* dataset
τ_{sw}^2	Two-way atmosphere transmittance (–)	s_{X^2}	Variance value of *X* dataset
L_r	Reflected radiance (Wm^{-2})	s_{Y^2}	Variance value of *Y* dataset
L_i	Incoming irradiance (Wm^{-2})	n_{X-1}	Number of pixels in *X* dataset (–)
θ_r	View zenith angle (°)	n_{Y-1}	Number of pixels in *Y* dataset (–)
φ_r	View azimuth angle (°)	$t_{tabulated}$	t value from the t-test table (–)
θ_i	Illumination zenith angle (°)	$t_{calculated}$	Calculated t value (–)
φ_i	Illumination azimuth angle (°)	$P\ (\overline{X} > \overline{Y}\ )$	Probability of the significance difference in mean values (–)
A	Area of surface (m^2)	U	Mann-Whitney test statistic (–)
$\Delta\lambda$	Spectral band width (µm)	n_1	Size of the smaller group (–)
D	Fraction of direct irradiance (–)	n_2	Size of the larger group (–)
$\alpha(\Delta\lambda)$	Spectral albedo (–)	R_1	Sum of ranks in the smaller group (–)
$\rho(\theta_i,\varphi_i,2\pi;2\pi)$	Blue sky albedo (BHR or α) (–)	z	Standardized value (–)
$\rho(\ 2\pi;,2\pi)$	White sky albedo (a specific case of BHR) (–)	m_U	Mean of U value (–)
$\rho(\theta_i,\varphi_i,2\pi)$	Black sky albedo (DHR) (–)	σ_U	Standard deviation of U value (–)

$f_r(\theta_i,\varphi_i;\theta_r,\varphi_r;\Delta\lambda)$	BRDF (sr^{-1})		

Abbreviation	Definition	Abbreviation	Definition
6SV	Second Simulation of a Satellite Signal in the Solar Spectrum, Vector	LUT	Look-Up Table
ADEOS-II	Advanced Earth Observing Satellite-II	MAS	MODIS Airborne Simulator
AOT	Aerosol Optical Thickness	MERIS	Medium Resolution Imagine Spectrometer
ARSF	Airborne Research & Survey Facility	MFG	Meteosat First Generation
ASTER	Advanced Spaceborne Thermal Emission and Reflection Radiometer	MISR	Multi-angle Imaging SpectroRadiometer
ATCOR	Atmospheric and Topographic Correction for Satellite Imagery	MODIS	Moderate Resolution Imaging Spectroradiometer
AVHRR	Advanced Very High Resolution Radiometer	MODTRAN	MODerate resolution atmospheric TRANsmission
AVIRIS	Airborne Visible/Infrared Imaging Spectrometer	MSG	Meteosat Second Generation
BEAM	Basic ENVISAT toolbox for (A)ATSR and MERIS	MVA	Multi-View Angle
BHR	Bi-Hemispherical Reflectance	MVIRI	Meteosat Visible and Infrared Imager
BRDF	Bi-Directional Reflectance Distribution Function	MZA	Minimum Zenith Angle
CASI	Compact Airborne Spectrographic Imager	NASA	National Aeronautics and Space Administration
CCD	Charge-Coupled Device	NCAVEO	Network for Calibration and Validation of Earth Observation
CERES	Clouds & the Earth's Radiant Energy System	NEODC	NERC Earth Observation Data Centre
CFARR	Chilbolton Facility for Atmospheric and Radio Research	NERC	Natural Environment Research Council
CHRIS	Compact High Resolution Imaging Spectrometer	NIR	Near-InfraRed
CNES	Centre National d'Etudes Spatiales	NOAA	National Oceanic and Atmospheric Administration
DHR	Directional-Hemispherical Reflectance	NWP	Numerical Weather Prediction
DMC	Digital Mapping Camera	PARABOLA	Portable Apparatus or Rapid Acquisitions of Bi-directional Observations of Land and Atmosphere

EA	Environment Agency	POLDER	POLarization and Directionality of the Earth's Reflectances
EO	Earth Observation	PROBA	Project for On-Board Autonomy
ERBE	Earth Radiation Budget Experiment	RPV	Rahman-Pinty-Vestrate
ERBS	Earth Radiation Budget Satellite	RTLSR	Ross Thick Li Sparce Reciprocal
ET	EvapoTranspiration	SEB	Surface Energy Balance
ETM+	Enhanced Thematic Mapper Plus	SEBAL	Surface Energy Balance Algorithm for Land
FIFE	First International Satellite Land Surface Climatology Project (ISLSCP) Field Experiment	SEVIRI	Spinning Enhanced Visible and Infrared Imager
GCM	General Climate Model	SPOT	Système Pour l'Observation de la Terre
GCOS	Global Climate Observing System	TM	Thematic Mapper
GRE	Ground Resolution Element	TOA	Top Of Atmosphere
HRG	High Resolution Geometric	TRMM	Tropical Rainfall Measuring Mission
IFOV	Instantaneous Field-Of-View	TSI	Total solar irradiation
LAI	Leaf Area Index	UV	Ultra Violet

1 Introduction

Surface albedo is a major determinant of the loss of incoming solar energy from the Earth's surface and is thus of great interest to a wide variety of scientists. Astronomers have an interest in the albedo of the Earth and also that of other planets. Glaciologists study the heat balance of snow and ice which is affected by albedo. Agronomists are interested in the effect of albedo on the loss of water from plants. Hydrologists are familiar with albedo since it affects components of the hydrologic cycle such as evaporation and snowmelt runoff. Climatologists study the long-term changes of albedo as one of the key parameters that controls climate change. They also use albedo in climate models to study the different climates of the world. In general, surface albedo is a key parameter in the surface energy balance equation, which is applied in studies related to climate, climate change and hydrology.

1.1 Scientific necessity of surface albedo

1.1.1 Surface albedo and surface energy balance

To better understand the role of surface albedo in the Earth's energy balance system, the nature of incoming solar energy as a main driver of all environmental and biophysical processes on Earth is briefly explained.

The Sun constantly emits electromagnetic radiation in all directions and at all wavelengths. Only a small amount of this energy is intercepted by the Earth's surface; this energy heats the Earth's surface. Information about the amount of emitted energy and the related wavelengths can be quantified using mathematical models. While the Stefan-Boltzmann Law quantifies the amount of energy emitted by each surface (M, Wm^{-2}) as a function of surface temperature (T, Kelvin), Wien's Law determines the wavelength at which radiation of a surface will be greatest (λ_{max}, µm).

$$M = \sigma T^4 \qquad \textbf{Equation 1-1}$$

$$\lambda_{max} = \frac{b}{T} \qquad \textbf{Equation 1-2}$$

Where σ is the Stephan-Boltzmann constant, 5.67×10^{-8} $Wm^{-2}K^{-4}$, and b is a constant equal to 2898 µmK.

Given the Sun's and the Earth's surface temperatures of 6000 K and 300 K, respectively, and using Equations 1-1 and 1-2, we can calculate that the Sun radiates about 7.3×10^{11} Wm^{-2} of energy, only a small amount of which is received at the top of the Earth's atmosphere (1367 Wm^{-2} centred at wavelength 0.483 μm); meanwhile, the Earth emits about 1.7×10^{-5} Wm^{-2} centred at a wavelength of 9.66 μm.

The radiation spectrum can be divided into the ultraviolet ($\lambda < 0.4\ \mu m$), visible ($0.4 \leq \lambda \leq 0.7\ \mu m$), short-wave infrared ($0.7 < \lambda \leq 3\ \mu m$), thermal infrared ($3 < \lambda \leq 100\ \mu m$) and microwave ($\lambda > 100\ \mu m$) regions. About 9% of the incoming solar radiation is in the ultraviolet (UV), 40% in the visible, 50% in short-wave infrared and less than 1% in the longer wavelengths of the spectrum. Short-wave radiation is referred to as radiation in the UV, visible and short-wave infrared regions (Zhang et al., 2004). Different environmental applications define slightly different ranges of wavelengths as short-wave, but almost all of them fall in the range of 0.2-5 μm.

Short-wave solar radiation at the top of the atmosphere is scattered, absorbed and transmitted by the Earth's atmosphere and surface. The amounts of energy that are absorbed by the Earth's surface heat the surface and then provide energy to evaporate the Earth's water and conduct the air. The Surface Energy Balance (SEB) is the key driver of almost all biophysical processes in the Earth surface-atmosphere system. It considers the Earth as a physical system in which there is a balance between incoming and outgoing solar radiation and is mathematically defined as:

$$R_n - H - LE - G = 0 \qquad \textbf{Equation 1-3}$$

Where R_n is the net radiation, H is the sensible heat, LE is the latent heat of evaporation and G is the soil heat flux, all in Wm^{-2} (watt per metre squared) units.

Figure 1-1 shows the components of the surface energy balance model on vegetation. A numerical breakdown of the SEB illustrates how the incoming solar energy interacts with the atmosphere and surface (Figure 1-2).

Figure 1-1 Surface energy balance components (www.iac.ethz.ch/education/bachelor/climate.../Surface-Energy-Balance.pdf).

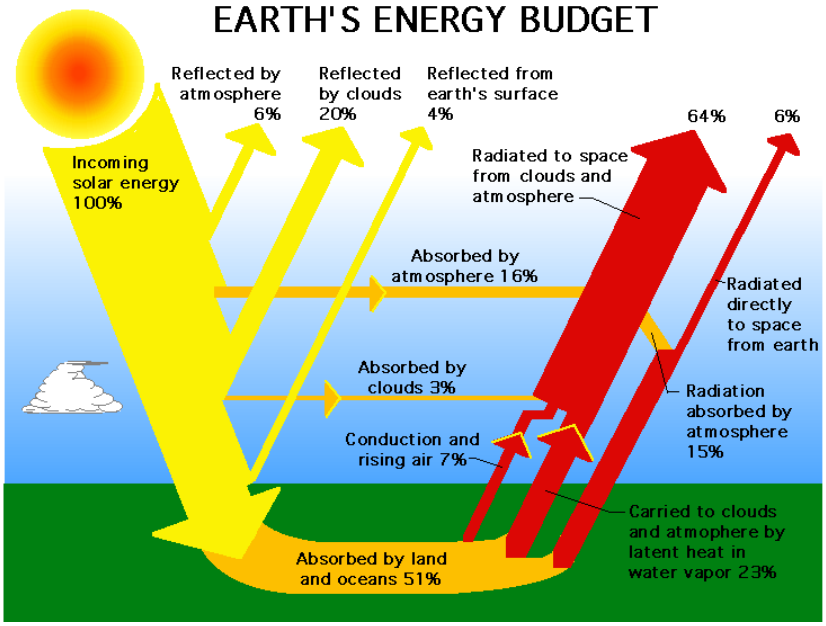

Figure 1-2 Breakdown of the incoming solar energy (http://www.windows2universe.org/earth/Atmosphere/earth_atmosph_radiation_budget.html)

Surface net radiation (R_n) describes the amount of absorbed shortwave solar energy at the Earth's surface which is then returned to space as other heat fluxes (*H, LE* and *G*) and is thus the fundamental part of Equation 1-3. It is defined as a function of incoming solar radiation ($R_s\downarrow$) and surface albedo (α):

$$R_n = R_s\downarrow (1-\alpha) + L_\downarrow - L\uparrow \qquad \textbf{Equation 1-4}$$

Here, $L\downarrow$ and $L\uparrow$ are the incoming and outgoing long-wave radiation, respectively.

Incoming solar radiation varies with the angle of the Sun above the horizon. In the tropics at mid-latitudes it is at a maximum when the Sun radiates vertically and has an angle of close to 90°. At the poles, where the angle of the Sun reaches 0°, the intensity of radiation is reduced. The Sun's angle at a particular location, then, depends on the latitude of the location, the time of day and the time of year (Strahler and Strahler, 2002). The atmosphere has a significant effect on the solar radiation through the scattering and absorption of energy. Surface albedo is the percentage of reflected short-wave energy which then determines the amount of absorbed energy at the Earth's surface. To see how an error in surface albedo can affect net radiation we use the following example based on work presented by Raschke (2005): If we assume the incoming solar radiation at surface to be 189 Wm^{-2}, surface albedo to be 0.13 and net long-wave radiation at the surface to be -50 Wm^{-2}, using Equation 1-4 the amount of net radiation at the top of the atmosphere will equal 115 Wm^{-2}. Now, if we change the albedo by 50% (i.e. 0.13±0.065) the change in the calculated net radiation will become ±12 Wm^{-2}. Some current efforts in producing a high accuracy net radiation product have shown there is still an uncertainty of about 30 Wm^{-2} (Shahi et al., 2011). This indicates that an increase in the accuracy of albedo may significantly increase the accuracy of estimated net radiation.

1.1.2 Surface albedo and climate change

Climate change has been one of the most crucial environmental issues in recent decades. Determination and prediction of climate responses to changes in land surface and meteorological parameters such as greenhouse gases, temperature and surface albedo requires an accurate climate simulation which is still a primary issue in climate change modelling (Dickinson, 1995). The essential terrestrial variables, including albedo, are required to characterize the global climate system and its variability, monitor the forcing of the climate system, including both natural and anthropogenic contributions, support the attribution of the causes of climate change and the prediction of global climate change, project global climate change information down to regional and national scales,

characterize extreme events important in impact assessment and adaptation, and assess risk and vulnerability (Global Climate Observing System (GCOS), 2003).

Surface albedo controlling the amount of absorbed insolation has an important impact on climate. A decrease in the extent of snow and ice due to an increase in temperature exposes low-albedo surfaces such as land and water, having a warming effect on the climate. Conventional climate models use an average amount of albedo for each land cover which is based on values from the literature. However, climate models require an accuracy of 0.02-0.05 of surface albedo at the desired spatial and temporal resolution (Henderson-Sellers and Wilson, 1983).

Albedo depends greatly on land cover, and anthropogenic changes to land cover influence surface albedo. Different agricultural systems with changing land covers have important impacts on climate. However, this impact varies according to the geographical position. In North America and Europe deforestation has a cooling effect while in India it has a warming effect (Kvalevåg et al., 2010).

Remotely-sensed albedo products have been provided since 2000 from different sensors such as MODIS; these can be applied directly in climate models. Prior to 2000, especially over the last 25 years or so since Earth observation satellites started operating, surface albedo can be generated, but with limited accuracy due to problems such as sensor calibration (Schaaf et al., 2008).

1.1.3 Surface albedo and hydrology

As the population grows, the demand for fresh water is increased. To manage this life resource, knowledge of the components of the hydrological cycle is essential. Evaporation and snowmelt runoff are the most difficult elements of the hydrological cycle to measure or estimate. Surface albedo determines the amount of available energy for evaporation from plants, water and reservoirs and can also provide useful information for snowmelt models.

1.1.3.1 Surface albedo and evapotranspiration

Evapotranspiration (ET) is the sum of the evaporation from open water and moist soil surfaces and transpiration from living plants. It is of great importance for hydrologists since it is required for runoff prediction, reservoir losses and water balance calculations. One of the conventional methods of ET calculation is to use the physically-based Penman-Monteith equation (Monteith, 1965):

$$ET_0 = \frac{\Delta R_n + \rho_a C_p (\delta_e) g_a}{\left(\Delta + \gamma\left(1 + \frac{g_a}{g_s}\right)\right)\lambda_v}$$ **Equation 1-5**

Where ET_0 is the water volume evaporated ($m^3 s^{-1} m^2$),

Δ is the rate of change of saturation specific humidity with air temperature (Pa K-1),

R_n is net radiation (W m^{-2}),

c_p is the specific heat capacity of air (J kg^{-1} K^{-1}),

ρ_a is the dry air density (kg m^{-3}),

δe is vapor pressure deficit, or specific humidity (Pa),

g_a is the conductivity of air, atmospheric conductance (m s^{-1}),

g_s is the conductivity of stoma, surface conductance (m s^{-1}),

γ is the Psychrometric constant ($\gamma \approx 66$ Pa K^{-1}), and

λ_v is the latent heat of vaporization, energy required per unit mass of water vaporized, (J/g).

R_n is a key term and describes the amount of available energy. Albedo is then the determinant of the amount of absorbed energy and is a crucial factor in ET calculations. Non-remote sensing methods usually use albedo values from the literature which are typically for a limited range of land covers. Errors in the estimation of albedo can then introduce a large error in the calculation of the available energy for evapotranspiration. ET can be more accurately mapped using remote sensing data. Remote sensing of ET is mainly based on a surface energy balance algorithm. Short-wave albedo is then a key factor in the net radiation calculation and has a great effect on ET. Some remote sensing algorithms such as SEBAL (Surface Energy Balance Algorithm for Land) (Bastiaanssen et al., 1998) use surface albedo to calculate other components of the energy balance model. Albedo is calculated as follows (Chen and Ohring, 1985, Koepke et al., 1985):

$$\alpha = \frac{\alpha_{toa} - \alpha_{path\_radiance}}{\tau_{sw}^2}$$ **Equation 1-6**

Where α_{toa} is the albedo at the top of the atmosphere, which is calculated by assigning weighted coefficients to each spectral reflectance value at the top of the atmosphere, $\alpha_{path\_radiance}$ is the albedo path radiance and a value in the range of 0.025 to 0.04 is normally used, and τ_{sw}^2 is the two-way atmosphere transmittance and is calculated as a function of elevation above sea level.

Albedo as estimated above assumes a homogenous atmosphere for the entire globe and across different time periods. The uncertainties resulting from such a weak assumption

could introduce large errors in the estimated albedo and the resulting ET. On the other hand, validation of the estimated albedo is usually based on values from the literature. Albedo values reported in the literature, as a single value or a range of values, are usually for a broad range of land covers. For example, albedo is reported for crops as a single land cover whereas albedo may vary significantly among different crops even if all other climate and surface conditions remain unchanged (for further information refer to section 2.3.5.3). Thus, a validation based on the literature values is a weak validation which may not be able to measure the errors in the estimated albedo.

1.1.3.2 Surface albedo and snow

Snow, which produces runoff, and groundwater recharge have important roles in the hydrological cycle. Water managers have a great interest in snow cover maps, snow depth, snow-water equivalent and snowmelt runoff.

The importance of the snow cover map for hydrologists is in using developed empirical relationships for specific basins to estimate snowmelt runoff. The snow cover map can be produced from satellite sensor data using spectral information in the visible and near-infrared regions of the spectrum. Fresh snow will have an albedo of 90% or more whereas the albedo of older snow can be less than 40% due to the accumulation of litter and dust (Foster et al., 1987, as cited by Engman and Gurney, 1991). As snow ages, its reflectance will decrease more in the infrared, rather than visible, regions. Melting and refreezing will result in an increase in the grain size of the snow which will cause a larger decrease in the infrared region. Aerosols, dust and pollen can be the main reasons for the decrease of the reflectance in the visible-region of snow. However, snow has a higher contrast than non-snow areas in the visible, rather than infrared, regions of the spectrum (Engman and Gurney, 1991). Broadband visible albedo can then be used in snow cover mapping.

Snow depth has a major role in snowmelt runoff. McGinnis et al. (1975), as cited by Engman and Gurney (1991), developed an empirical relationship between differences in albedo and snow depth using NOAA-AVHRR satellite sensor data for shallow snowpacks.

The presence of liquid water in the snow is important in snowmelt and is of great importance for hydrologists. The presence of liquid water in snow does not change the spectral reflectance of snow; but it has an effect on the albedo through the melting and refreezing process which increases the snow grain size. Dozier et al. (1981), as cited by

Engman and Gurney (1991), showed how black-sky albedo in the infrared regions decreases as snow grain size increases.

The reflectivity and, therefore, albedo depends upon snow properties such as the grain size and shape, water content, surface roughness, depth, and presence of impurities. The albedo of snow, then, varies greatly in space and time. It produces useful information regarding snowmelt modelling and snow cover mapping. Mapping the changes in snow albedo is also of great importance in climate change studies.

1.2 Remote sensing albedo

'Remote sensing is the practice of deriving information about the Earth's land and water surfaces using images acquired from an overhead perspective, using electromagnetic radiation in one or more regions of the electromagnetic spectrum, reflected or emitted from the Earth's surface' (Campbell, 2002, page 6). As albedo is a physical property of the surface that is defined by its interaction with electromagnetic radiation, remote sensing offers a way to measure this over large areas. However, there are several pitfalls in using remote sensing to measure albedo:

(i) Spectral limitations

Albedo is defined over a continuous range of wavelengths from 0.4 to 4 μm (Liang et al., 2005). In contrast, remote sensing systems are limited to relatively few spectral bands or, in the case of hyperspectral systems, to a limited range of wavelengths. In principle, a remote sensor should be able to measure the reflected or emitted energy in the entire electromagnetic region; however, mostly due to technological restrictions and atmospheric effects, certain wavelengths are commonly excluded.

(ii) Sensor location

The measurement of albedo involves integration of the incident and reflected flux over the complete hemisphere, and this presents a problem for remote sensing systems, especially those on satellite platforms. First, although it is possible to measure total solar irradiation (TSI) from space (Mishchenko et al., 2010), this does not relate directly to TSI at the ground as it omits the diffuse (sky) component, which can contribute up to 40% of the total for clear blue skies (Badescu, 2008). Diffuse irradiation originates from the atmosphere, below the level at which satellites operate. Aircraft sensors are not the complete answer, as they fly within the atmosphere and therefore it is still necessary to

estimate the contribution of the atmosphere below the aircraft to the diffuse flux reaching the surface.

(iii) Sampling geometry

Most remote sensing systems operating in optical wavelengths are designed to create images by acquiring samples of the reflected flux from adjacent small areas of the Earth's surface. They have an instantaneous field-of-view (IFOV) which is associated with an effective ground resolution element (GRE), the geometry of which is defined by surface topography and sensor properties, principally view angle and point spread function. Subsequent resampling then converts this data stream into a rectangular image of picture elements (pixels). For most purposes, the fact that each pixel contains multispectral data from the Earth's surface is more important than the ambiguity introduced by each sample having slightly different view geometry and the limited range of reflected flux directions sampled. However, for the measurement of albedo it is essential that the reflected flux is sampled over as many angles as possible, ideally over the whole hemisphere. The only way to do this with current remote sensing systems is to combine the sparse angular set of observations with a numerical BRDF model. In practice, there are two multi-view angle (MVA) sampling geometries used: along-track and across-track. Across-track sensors, such as Terra-MODIS, scan the Earth surface using a rotating mirror and detectors for each spectral band across the track of the satellite or aircraft (De Jong and Van der Meer, 2004). The resulting image from these sensors is created line by line as the platform moves. Along-tack sensors, such as the Compact High Resolution Imaging Spectrometer (CHRIS) on board PROBA, scan the Earth's surface using a set of charge-coupled devices (CCD). One entire image line is recorded at a time as the platform moves forward. They each have strengths and weaknesses in albedo studies (Table 1-1).

Table 1-1 The characteristics of along-track and across-track sensors in albedo retrieval

Characteristics	Along track sensors	Across track sensors
Are the observations simultaneous?	Yes	No (from multiple dates)
Capturing the changes in view geometry	Yes	Yes
Capturing the changes in	No	Yes

Sun geometry		
Swath width	Small	Large
Signal to noise ratio	Large (longer dwell time)	Small (shorter dwell time)

In addition to these factors which must be considered when using a remote sensing system to measure albedo, there are a number of technical issues that must be considered as part of the whole information system, for example, the appropriate spatial resolution for the specific application, and whether the radiometric resolution of the proposed sensor is adequate for the task. Radiometric resolution is especially important in albedo studies because we are often interested in small changes in a variable which has a very wide range, from almost 1.0 (e.g. fresh snow) to <0.03 (e.g. organic-rich soil).

1.3 Aims

The main aim of this study was to establish whether it is possible to validate the MODIS albedo product under UK conditions by the method of direct comparison with other remotely sensed estimates of albedo of the same area of ground. Validation, here, is defined as testing the absolute accuracy of remote sensing products using independent datasets and methods (Milton et al., 2004). As reported below, the MODIS albedo product has already been validated under optimal conditions (clear skies, large uniform surfaces etc.), so the aim was not to assess the quality of the product or the validity of the approach and algorithms used, although comments on these matters will be made where appropriate. Instead, this study considers for the first time whether independent estimates of albedo acquired under the same sub-optimal conditions have a role to play in validating the MODIS product. One of the first principles of instrument calibration is that the measurements should be made under conditions as close as possible to those encountered in operational use, and this principle can be extended to the validation of EO data products. Users will have more confidence in EO products if they have been validated under similar conditions to those prevailing in the region where they apply the data.

A further principle of good validation is that independent methods, algorithms and sensors should be used where possible. Consequently, this study is based on data acquired with alternative sensing systems (SPOT-HRG, CHRIS/PROBA, airborne imaging spectrometry) and with algorithms that differ from those used by NASA for MODIS (e.g. MODTRAN rather than 6S for atmospheric correction).

One of the principal requirements of a validation study based on direct comparison with independent measurements is to have near-simultaneous measurements of the same area of ground made with a range of different remote sensing systems. This would normally be exceptionally difficult to arrange within the constraints of time and resources of a three-year postgraduate project, but the existence of the NCAVEO Field Campaign data set (Milton et al., 2011) meant that suitable data were available. Once this was established, it became feasible to undertake for the first time an independent validation of the MODIS product under conditions of UK. The overall aim of the research and the approach adopted is challenging, but such studies are vital if EO data products are to become established as trusted sources of scientific data.

There are some other studies that validated the MODIS albedo product using fine resolution remote sensing data and field measurements; however, there are some main differences between this study and previous studies. The main difference was the difference in the climate and surface conditions over the validation sites used by other studies with UK conditions. Clear sky and large homogeneous surfaces are the main assumptions on which the MODIS albedo product was based. Most of the validation studies, especially those from the early days of production of this product, were based on these optimal conditions such as the work by Schaaf et al. (2002) and Jin et al. (2003). Other studies were carried out under heterogeneous surfaces but cloud-free sky such as the work by Liang et al. (2002). Some studies were carried out under cloudy sky but homogeneous surfaces such as that by Klein and Stroeve (2002). However, there was a lack of information about the accuracy of the MODIS albedo for areas that are both cloudy throughout most of the year and heterogeneous in the MODIS pixel size (500 m). Disney et al. (2004) validated the MODIS albedo product under UK conditions. The main issue in their work, however, was that the reference data used were not simultaneous with the MODIS albedo products. This study, however, for the first time challenged the validation of the MODIS albedo product in suboptimal conditions (cloudy and heterogeneous surfaces) of the UK using simultaneous field and fine resolution remote sensing measurements. This was a concise study which provided unique information about the accuracy of the MODIS albedo product and also presented a challenging methodology for the validation of the MODIS product in the UK. To achieve this aim, the following objectives needed to be fulfilled.

1.4 Research objectives

1. Investigate how the MODIS reflectance and albedo products are derived, and clarify the assumptions of the algorithms used, with particular reference to the data collected

during the period of the NCAVEO Field Campaign (June 2006). This part of the study was conducted during a visit to the research group at the University of Boston responsible for producing the MODIS albedo product (Chapters 2, 3, and 4).

2. Compare the nadir spectral reflectance measured by MODIS with that measured near-simultaneously by an airborne imaging spectrometer (Itres CASI) and two satellite sensors (SPOT-HRG and CHRIS/PROBA). The MODIS albedo product is derived in part from the MODIS reflectance product, so this comparison is an important step towards validating the albedo product. It also enables error arising from the mismatch of sensor properties and differences in atmospheric correction methods to be separated from error introduced during the creation of the MODIS albedo product (Chapters 3 and 6).

3. Compare the MODIS albedo product with an albedo map created by using a land cover map to scale-up near-simultaneous MVA data from CHRIS/PROBA to MODIS spatial resolution. MODIS and CHRIS/PROBA both provide MVA data, but they differ in the way they acquire the input data for the albedo model. MODIS builds up the sampled reflectance hemisphere over several days, whereas CHRIS/PROBA acquires near-instantaneous 'strings' of data. By studying each of these approaches in a real-world application it was expected that insights would be gained into the strengths and weaknesses of each method, as well as validation of the MODIS albedo product (Chapters 5 and 6).

Although these were the three main research objectives, there were several intermediate objectives that also had to be met in order to complete the study:

It was necessary to compare two different implementations of the MODTRAN atmospheric model for correction of the CHRIS/PROBA data (ATCOR2 and BEAM). The results of this investigation are presented in Appendix 1. These results provided valuable information about the accuracy of the CHRIS/PROBA atmospheric correction.

The area covered by each of the CHRIS/PROBA datasets was larger than that covered by the CHRIS/PROBA albedo map. The possibility of the extension of the CHRIS/PROBA albedo map was then investigated using each of the CHRIS/PROBA reflectance datasets. The results of this investigation are presented in Appendix 2. This relationship was also investigated in different land covers within the study site and the results are presented in Appendix 3.

A further investigation of the possibility of the extension of the albedo map using a land cover map was also carried out. For this purpose, the spatial variability of albedo was presented over all pixels in each land cover in Appendix 4.

2 Remote sensing of albedo

2.1 Nature and definition of albedo

2.1.1 Definition

Surface albedo is defined as the ratio of the outgoing to incoming solar energy from a unit surface area over the entire hemisphere and across all solar wavelengths. It is also called bihemispherical reflectance (BHR) and is mathematically defined as follows (Schaepman-Strub et al., 2006):

$$\alpha = \frac{dA\int_0^{2\pi}\int_0^{\pi/2} dL_r(\theta_i,\varphi_i;2\pi;\theta_r,\varphi_r)\sin\theta_r\cos\theta_r d\theta_r d\varphi_r}{dA\int_0^{2\pi}\int_0^{\pi/2} dL_i(\theta_i,\varphi_i)\sin\theta_i\cos\theta_i d\theta_i d\varphi_i}$$ **Equation 2-1**

Where L_r is reflected radiance at the view zenith angle θ_r and view azimuth angle φ_r and L_i is incoming irradiance at the illumination zenith angle θ_i and illumination azimuth angle φ_i and *A* is the area.

Albedo is a unitless physical parameter which characterises the reflectivity of the Earth's surface and has values between 0 (no reflectance) and 1 (no absorption). There are several terms for describing albedo, and the differences between them are described here.

2.1.2 Spectral and Broadband albedo

Spectral albedo is the ratio of spectral outgoing radiance to spectral incoming irradiance over the hemisphere. As it is very difficult to measure surface albedo at each wavelength, the measurements are made over a range of wavelengths. Remote sensing measurements of albedo are either acquired in discrete narrow spectral bands (multispectral sensors) such as Landsat-TM data, or in contiguous narrow bands (hyperspectral sensors) such as Airborne Visible/Infrared Imaging Spectrometer (AVIRIS) sensor. It is mathematically defined as follows (Schaepman-Strub et al., 2006):

$$\alpha(\Delta\lambda) = \frac{dA\int_0^{2\pi}\int_0^{\frac{\pi}{2}}\int_{\lambda_1}^{\lambda_2} dL_r(\theta_r,\varphi_r,\Delta\lambda)\sin\theta_r\cos\theta_r d\theta_r d\varphi_r}{dA\int_0^{2\pi}\int_0^{\frac{\pi}{2}}\int_{\lambda_1}^{\lambda_2} dL_i(\theta_i,\varphi_i,\Delta\lambda)\sin\theta_i\cos\theta_i d\theta_i d\varphi_i}$$ **Equation 2-2**

Where $\Delta\lambda = \lambda_2 - \lambda_1$ is the spectral band width.

Spectral albedo is therefore could be described as the amount of albedo in a narrow band of the shortwave region. The spectral albedo is found to vary with wavelength. This variation can then be used for the classification of land cover. This classification has a stronger physical basis than classification based on broad-band albedo.

Broadband albedo or broadband shortwave albedo (Equation 2-1) is the calculated or measured albedo over the entire range of shortwave wavelengths. A similar expression is also assigned to the albedo in visible or near-infrared wavelengths; these are specified with the names 'broadband visible albedo' and 'broadband near-infrared (NIR) albedo'. The surface albedo applied in climate and surface energy balance models is broadband shortwave albedo. Broadband visible and NIR albedo are also used, since the differences between these two albedos usually vary for different land covers.

2.1.3 Black-, White- and Blue-sky albedo

Black-sky albedo is also called Directional-Hemispherical reflectance (DHR). It is the hemispherical reflectance of a surface which has been illuminated with a parallel beam of light from a single direction and is mathematically defined as follows (Schaepman-Strub et al., 2006):

$$DHR = \rho(\theta_i,\varphi_i,2\pi) = \frac{dA\int_0^{2\pi}\int_0^{\frac{\pi}{2}} dL_r(\theta_i,\varphi_i;\theta_r,\varphi_r)\cos\theta_r \sin\theta_r d\theta_r d\varphi}{d\varphi_i(\theta_i,\varphi_i)}$$ **Equation 2-3**

Black-sky albedo is a function of solar zenith angle and produced by the MODIS team at the local solar zenith angle.

White-sky albedo is the special case of bihemispherical reflectance (BHR) with pure diffuse isotropic incident radiation and is mathematically defined as follows (Schaepman-Strub et al., 2006):

$$BHR = \rho(2\pi;,2\pi) = \frac{1}{\pi}\int_0^{2\pi}\int_0^{\frac{\pi}{2}} DHR(\theta_i,\varphi_i,2\pi)\cos\theta_i \sin\theta_i d\theta_i d\varphi_i$$ **Equation 2-4**

White-sky albedo may be the case for an area if there is a thick cloud or aerosol layer (Lucht and Lewis, 2000).

Directional–hemispherical

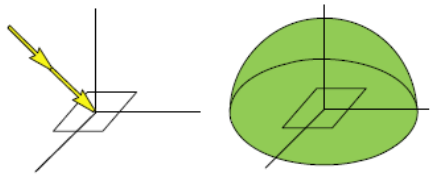

Figure 2-1 Visual graphics of black-sky albedo (on the left) and white-sky albedo (on the right) (Schaepman-Strub et al., 2006).

Actual albedo is called blue-sky albedo (BHR or α) and is function of black-sky albedo, white-sky albedo and the fraction of diffuse or direct radiation and is mathematically defined as follows (Schaepman-Strub et al., 2006):

$$BHR = \rho(\theta_i,\varphi_i,2\pi;2\pi) = \rho(\theta_i,\varphi_i,2\pi)D + \rho(2\pi;2\pi)(1-D)$$ **Equation 2-5**

Where *D* is the fraction of direct irradiance.

Blue-sky albedo is therefore a value between black-sky and white-sky albedo and can be either spectral or broadband albedo.

2.1.4 Spatial variation

Albedo is highly variable: land covers such as fresh snow and thick clouds reflect most of the solar radiation and have an albedo as high as 0.9 (90%) (Chylek et al., 1984) while deep clear water absorbs most of the energy and has an albedo as low as 0.05 (5%) (Cogley, 1979). The southern hemisphere is expected to have a lower albedo than the northern hemisphere because of the dominance of water, but the existence of a higher ratio of clouds makes the albedo nearly the same in both hemispheres. More specifically, albedo varies greatly in space as the physical and chemical structure of the Earth's surface changes and then it may not be a constant value, even for each land cover.

2.1.5 Temporal variation

Albedo also varies greatly in time due to its dependence on the direction of the incoming solar radiation. In the daytime, albedo has the highest values at dawn and at sunset when the solar zenith angle is at its maximum (the Sun radiates horizontally). Seasonally, albedo follows the change in the tilt of the Earth's axis and is at a minimum in the summers of the northern hemisphere when the Sun's angle is at its minimum (the Sun radiates vertically). This is mainly due to the proportion of the diffuse

radiation which is at a minimum when the Sun is nearly perpendicular to the Earth's surface.

Surface albedo, then, varies greatly in space and time and can explain the changes in climate and surface hydrology.

2.2 Remote sensing of albedo

Surface albedo is a hemispherical integration of surface reflectance and can be measured using field instruments or remote sensors. Whereas field measurements can directly measure albedo, remote sensing of albedo is based on the directional observation of surface reflectance which is then modelled across the hemisphere. BRDF is a term for specifying the directionality of reflectance under specific illumination and its hemispherical variation then needs to be modelled correctly.

2.2.1 Bidirectional Reflectance Distribution Function (BRDF)

Remotely-sensed surface reflectance can change greatly due to the variation either in the viewing angle of one single image, such as NOAA-AVHRR data with wide field-of-view angle, or in the solar geometry of multi-temporal data, such as Meteosat data. Since the resulting errors associated with these effects can have considerable impacts on both time series and single imagery, a model of correction of BRDF effects is necessary for different applications of remote sensing (Roujean et al., 1992). The following results have been obtained from many studies:

- Reflectance increases with an increase in the view zenith angle in all azimuth angles,
- An increase in the solar zenith angle causes an increase in reflectance,
- The maximum reflectance occurs in the solar principal plane due to the back-scattering effect.

The Bidirectional Reflectance Distribution Function (BRDF) is then a derivative, a distribution function, relating the irradiance incident from one given direction to its contribution to the reflectance in another direction (Nicodemus et al., 1977).

$$BRDF = f_r(\theta_i,\varphi_i;\theta_r,\varphi_r;\Delta\lambda) = \frac{dL_r(\theta_i,\varphi_i;\theta_r,\varphi_r;L_i;\Delta\lambda)}{dL_i(\theta_i,\varphi_i;\Delta\lambda)} \quad [sr^{-1}] \qquad \textbf{Equation 2-6}$$

Considering and correcting the BRDF effect is necessary in studies such as those that make use of vegetation indices, such as the prediction of LAI, atmospheric correction, land cover mapping and prediction of surface albedo. Since remote sensing data are

generally recorded at a few view angles, a BRDF model is required to estimate reflectance at other directions.

2.2.2 BRDF-based albedo models

To demonstrate the anisotropy of a surface, instantaneous hyper-directional observations under a given illumination geometry are required. Although this is possible using appropriate instruments in the field which provide sufficient observations, the result is a point measurement which is not appropriate for regional studies. On the other hand, remote sensing instruments observe the targets with one or a few view angles, which are insufficient for albedo calculation. To be able to estimate surface albedo, an appropriate BRDF model is required that captures the anisotropy of the surface given only a few observations. Maginan et al. (2004) classify BRDF models into:

- Ray-tracing simulations (Gascon et al., 2001, Gemmell and McDonald, 2000)
- Complex models that fully analyse the radiative transfer within the canopy (Chen and Leblanc, 1997, Kuusk, 1995)
- Analytical models based on various approximations of the radiative transfer process (Rahman et al., 1993, Roujean et al., 1992), and
- Empirical models (Walthall et al., 1985).

The empirical models are statistically-based and easier to use but are mostly site-specific, while the physical models are more complicated, but can be applied globally based on physical laws. Semi-empirical models are more robust than empirical models due to the application of certain physical assumptions and are easier to run than physical models.

2.2.2.1 Empirical models

Empirical models can be applied to the observed data to estimate the best fit between the desired parameters (unknowns) and the existing data (given). They are usually site-specific, but can be applied for larger areas in similar situations. They have largely been and are being used due to their simplicity, but can only model the situations that the observed data present. One empirical model that is still being used is the Walthall model. Walthall et al. (1985) developed a simple empirical three-parameter linear model for several canopy and bare-soil surfaces that describe the distribution of reflectance as a function of the zenith and azimuth view angles and the solar azimuth angle.

$$R_f = a\theta_r^2 + b\theta_r \cos(\varphi_r - \varphi_i) + c \qquad \textbf{Equation 2-7}$$

Where R_f is the reflectance factor, and *a, b* and c are the coefficients of the equation.

The hemispherical reflectance (BHR) is computed with the following equation which is derived from integrating the reflectance over the hemisphere.

$$BHR = \frac{2.305a}{\pi} + c$$ **Equation 2-8**

On a negative note, it does not characterize the hot-spot effect and did not fit for all situations present in the experiments, such as furrow structure and smooth surface of bare soil. Nilson and Kuusk (1989) proposed a four-parameter version of the Walthall model which considered the Sun zenith angle variable (θ_s).

$$R_f = a(\theta_i^2 + \theta_r^2) + b(\theta_i^2\theta_r^2) + c(\theta_i\theta_r \cos(\varphi_r - \varphi_i)) + d$$ **Equation 2-9**

2.2.2.2 Semi-empirical models

Semi-empirical BRDF models use some physical assumptions, which mean that the models may perform a better interpolation or extrapolation of observed BRDF over the hemisphere than empirical models. They are also called semi-empirical kernel-driven models since they use a set of kernels to describe BRDF shape. Typically, semi-empirical kernel-driven models consist of three terms: an isotropic term, which is reflectance from a Lambertian surface; a volumetric term, which models the scattering of light in a horizontally homogenous plant canopy based on radiative transfer models; and a geometric-optical term, which models the light scattering in forest-like canopies of distinct crown shapes. Wanner et al. (1995) divide semi-empirical models into three categories: First, models which use only geometric terms (no physical terms) such as Ross kernel (Ross, 1981) and Roujean geometric-optical kernel (Roujean et al., 1992); second, models which apply one or a few physical terms such as geometric-optical Li kernel (Li and Strahler, 1992); and, finally, non-linear models such as the three-parameter model by Rahman et al. (1993).

Roujean et al. (1992) presented a simple linear model which applies simple physical considerations of the dependence of reflectance on the view and sun angle directions. The semi-empirical three-parameter linear Roujean model (Roujean, 1992) is also called the Ross thick model (Wanner et al., 1995a). The model consists of a physical parameter (*F2*) which considers the radiative transfer within a vegetation canopy (Ross, 1981) assuming large optical thickness and an empirical parameter (*F1*) which considers the directional dependence of the view/illumination geometry.

$$F1 = \frac{1}{2\pi}\left[(\pi - \varphi)\cos\varphi + \sin\varphi\right]\tan\theta_i \tan\theta_r - \frac{1}{\pi}\left[\tan\theta_i + \tan\theta_r + \Delta\left(\theta_i, \theta_r, \varphi\right)\right]$$ **Equation 2-10**

$$F2 = \frac{4}{3\pi}\frac{1}{\cos\theta_i + \cos\theta_r}\left[\left(\frac{\pi}{2} - \xi\right)\cos\xi + \sin\zeta\right] - \frac{1}{3}$$ **Equation 2-11**

Where φ is the relative azimuth angle ($\varphi_r - \varphi_r$), ξ is the phase angle and Δ is the horizontal distance between the Sun and the view angle directions in units of radian:

$$\cos\xi = \cos\theta_i \cos\theta_r + \sin\theta_i \sin\theta_r \cos\varphi$$ **Equation 2-12**

$$\Delta(\theta_i, \theta_r, \varphi) = \sqrt{\tan^2\theta_i + \tan^2\theta_r - 2\tan\theta_i \tan\theta_r \cos\varphi}$$ **Equation 2-13**

The three-parameter linear Ross Thick Li Sparse reciprocal combination (Ross-Li) model is a physical model considering the radiative transfer within the canopy (*F2* in Roujean model) and mutual shadowing of protrusions (*F1*) and is employed in the BRDF/Albedo product of MODIS (Lucht and Lewis, 2000).

$$F1 = \frac{m}{\pi}(t - \sin t \cos t - \pi) + \frac{1 + \cos\xi}{2\cos\theta_i \cos\theta_r}$$ **Equation 2-14**

$$\cos t = \frac{2}{m}\sqrt{\Delta^2 + (\tan\theta_i \tan\theta_r \sin\varphi)^2}$$ **Equation 2-15**

$$m = \frac{1}{\cos\theta_i} + \frac{1}{\cos\theta_r}$$ **Equation 2-16**

Considering the radiative transfer within the canopy, without adding a free parameter, in the linear Ross-Li model increases the accuracy of the BRDF model, but does not significantly change the estimated surface albedo (Maignan et al., 2004). The hot spot term, $(1 + \frac{1}{1 + \xi / \xi_0})$, (Bréon et al., 2002) is added to the second component of the Roujean and Ross-Li models.

$$F2 = \frac{4}{3\pi}\frac{1}{\cos\theta_i + \cos\theta_r}\left[\left(\frac{\pi}{2} - \xi\right)\cos\xi + \sin\zeta\right] * (1 + \frac{1}{1 + \xi / \xi_0}) - \frac{1}{3}$$ **Equation 2-17**

where ξ_0 is a characteristic angle that can be related to the ratio of the scattering element size to the canopy vertical density.

Rahman et al. (1993) developed a three-parameter non-linear semi-empirical model called the Rahman-Pinty-Vestrate (RPV) model (Rahman et al., 1993). The model consists of an empirical parameter considering the view/Sun zenith angle (Minnaert, 1941), a Henyey-Greenstein function P(ξ) considering the phase function of scattering elements, and a hot spot parameter:

$$F1 = \frac{m}{\pi}(t - \sin t \cos t - \pi) + \frac{1 + \cos \xi}{2 \cos \theta_i \cos \theta_r}$$ **Equation 2-18**

$$\cos t = \frac{2}{m}\sqrt{\Delta^2 + (\tan \theta_i \tan \theta_r \sin \varphi)^2}$$ **Equation 2-19**

$$m = \frac{1}{\cos \theta_i} + \frac{1}{\cos \theta_r}$$ **Equation 2-20**

One of the main differences between different semiempirical models is the physical assumptions used. Roujean et al. (1992) use one physical term which considers volume scattering inside homogenous vegetation whereas RTLSR uses two physical terms adding the mutual shadowing effect. The non-linear RPV model, on the other hand, is a modified empirical model adding a physical term. Therefore, the Roujean and RTLSR models are more reliable than the non-linear RPV model for the surfaces which match the physical assumptions used such as dense homogenous vegetation and/or sparse forest. However, for surfaces which deviate from the assumptions used such as snow, the RPV model could provide more accurate results (Maignan et al., 2004). Wanner et al. (1995) mentioned some advantages of linear kernel-driven models such as Roujean (1992) and RTLSR. They can be solved avoiding numerical inversion problems, they are faster to run, and they account for mixed pixels and allow for upscaling. The non-linear BRDF models such as RPV, on the other hand, are time-consuming to invert which restricts their use at the global scale (Maignan et al., 2004). Therefore, for operational products the Roujean and RTLSR models perform better than the RPV model. The linear RTLSR model, thus, having more physical terms seems to be a better choice for the operational remote sensing products as its validity was shown by several studies (Wanner et al., 1995b, Wanner et al., 1997, Privette et al., 1997, Lucht et al., 2000). However, one should bear in mind that the climate and surface conditions of the area being studied may affect the accuracy of the resulting albedo.

2.3 Albedo measurements

Lambertian surfaces reflect incoming light equally in all directions and do not depend on the view angle. The Earth's surface is generally not Lambertian but anisotropic, making reflectance directionally dependent. To measure surface albedo, the anisotropy of the surface needs to be taken into account.

2.3.1 Problems with field measurements of albedo

Field equipment for measuring albedo can be based on either multi-view angle sensors, such as a Goniometer, or hemispherical-view angle sensors such as a Pyranometer. The former captures the reflectance anisotropy and reflectance is then aggregated, while the latter is more accurate since it measures both irradiance and radiance hemispherically, and the errors resulting from narrow-to-broadband conversion and BRDF models are eliminated.

Since surface albedo varies greatly in space and time, extensive ground measurements are required, and measurement can be extremely difficult and expensive, especially in large heterogeneous areas. Milton et al. (2009) described some outstanding issues in field spectroscopy:

- Issues regarding the multidimensional nature of measurements
- The instability of instruments and uncertainty of the standards used to calibrate these instruments
- Unavailability of the used methodologies to minimize the errors of measurements and instruments
- Uncertainty about the stability of integrating spheres used to transfer radiance calibrations to spectroradiometers
- The size and weight of some instruments may limit their portability
- The price of advanced instruments may limit their widespread use.

In contrast to point field measurements, optical spaceborne and airborne sensors cover large areas, recording the returned solar radiation from the entire scanned area at different spatial scales, from less than one metre to more than one kilometre, and at different time scales, for example, hourly to bi-weekly. Satellite sensor data then offer large-area synoptic information and seem an appropriate means to obtain this physical variable. Uncertainties such as geometric and atmospheric correction and sensor calibration need to be taken into account while using satellite sensor data.

2.3.2 Measurement of albedo using remote sensing

Albedo is now routinely obtained from remote sensing data at a variety of spatial and temporal resolutions. Sensors aboard polar orbiting satellites, such as Terra/Aqua-MODIS, Multi-angle Imaging SpectroRadiometer (MISR) on board Terra, Clouds & the Earth's Radiant Energy System (CERES) on board Terra and Aqua, Polarization and Directionality of the Earth's Reflectances (POLDER) on board ADEOS-II and Medium Resolution Imagine Spectrometer (MERIS) on board ENVISAT, and on-board geostationary satellites, such as Meteosat Visible and Infrared Imager (MVIRI) on board Meteosat and Spinning Enhanced Visible and Infrared Imager (SEVIRI) on board MSG,

have specific processing capabilities for albedo estimation. The remote sensing measurements of albedo require cloud-free multiple-view observations, an accurate atmospheric correction method such as radiative transfer models, an appropriate BRDF model that produces an accurate BRDF magnitude and shape using sparse satellite data, and a correct relationship to broadband short-wave albedo.

Multiple-view observations required by BRDF models are collected by satellites either in a single pass or during multiple passes. A single-pass observation of albedo can be achieved either by a satellite with a sensor which looks at a particular area on the Earth at different view angles as the satellite moves forward, such as CHRIS/PROBA, or by satellites with multiple-view angle sensors which simultaneously observe a target, such as Terra-MISR. Most satellites, such as Terra-MODIS for example, observe the Earth with one view angle sensor and cannot collect enough view angle observations from a target in a single pass. Multiple-view angle observations of a target are therefore collected from multiple orbits or acquisition times which may be from 16-day observations, such as MODIS, to 35-day collections such as MERIS. Geostationary satellites collect the MVA data in a different way., They continuously observe an area of the Earth with one view angle and from one position relative to Earth and the MVA data are then collected at multiple sun angles.

With regard to collected data from multiple orbits or acquisition times, issues such as temporal variations in atmosphere and surface need to be considered. There are several steps in deriving surface albedo from remote sensing data:

- An accurate atmospheric correction of calibrated, geo-located radiance data as observed from a satellite
- Providing multiple-view angle observations from a single sensor such as CHRIS/PROBA or combination of sensors such as MODIS/MISR combination observations
- Using an appropriate BRDF model
- Spectral to Broadband albedo conversion.

2.3.2.1 Atmospheric correction

Atmospheric correction is the critical step in computing surface albedo. Solar energy can be mostly reflected or absorbed before reaching the Earth's surface. Atmospheric correction methods may be divided into empirical and physical models.

Empirical models normally use two objects on Earth with high contrast; usually, one is water or dense vegetation which absorbs most of the energy and another is bright bare soil which appears bright from the sensor. There are limitations to the empirical

models: firstly, there is a need to take field measurements at the time of overpass of the satellite; secondly, there is a difference in spatial scale which makes such measurements less reliable; and, thirdly, they assume a linear relationship between surface reflectance and at-sensor radiance over the entire image, which may not be true.

Physical models, radiative transfer models, simulate the variation of atmospheric parameters for the whole area based on variables such as the location of each pixel, height of the sensor and sun, and view geometry. They seem to do a better atmospheric correction but may be affected by the assumptions applied in the models, such as the condition of presence of dense vegetation. Radiative transfer models need to be validated for the area and the necessary corrections should then be applied.

2.3.2.2 Multiple-view angle data

Remote sensing BRDF-based models require multiple-view angle data which are provided as either nearly simultaneous observations (such as POLDER and CHRIS/PROBA) or multiple-day data from the same area (such as MODIS and NOAA). Simultaneous multiple-view angle data are more appropriate for BRDF modeling due to having the same weather and surface conditions as well as the same sun geometry, while multiple-day data have uncertainties such as changes in surface moisture due to rainfall or irrigation (surface gets wetter) or wind speed (surface gets drier), changes in the physical structure of the vegetation, especially in the transition stage, the probability of existence of thin clouds, and changes in the accuracy of the atmospheric correction on different days.

2.3.2.3 An appropriate BRDF model

Regarding surface albedo, the single- or multiple-view angle remote sensors cannot measure the hemispherical radiance. To be able to measure albedo, a BRDF model is required. In comparison with empirical and physical models, semi-empirical linear kernel-based models are more appropriate for most of the current satellites. Using three-parameter BRDF models, at least four view angles are required to invert the model. As the number of view angles increases, the model can adapt itself better to the actual observations. The distribution of angles is also important and they should be evenly distributed over hemispherical space.

Most of the satellites, however, don't have a large number of view angles and/or the distribution of angles may be poor. Thus, the model which can produce reasonable results under such an observation is crucial in the remote sensing of BRDF. Most of the

semi-empirical linear kernel-based models, such as the Roujean model, seem to produce similar results and, if one model doesn't produce a good output, others may not either (Schaaf et al., 2002). On the other hand, the conditions of the areas at which these models were developed may not be the same as the area being studied, so as mentioned before (2.2.2.2 section), choosing an appropriate BRDF model should be based on the climate and surface characteristics of the area being studied.

2.3.2.4 Spectral-to-Broadband albedo conversion

Multispectral and hyperspectral sensors on satellites and aircraft acquire data in a number of spectral bands which can produce a spectral albedo for the same bands as the used data. On the other hand, climate- and surface energy-balance studies mostly require total albedo or albedo in the visible and near-infrared regions of the spectrum. While total short-wave and near-infrared albedo is less sensitive to atmospheric conditions and the solar zenith angle (except for solar zenith angles greater than 70° or very low atmospheric visibility) and broadband visible albedo is insensitive to both the solar zenith angle and atmosphere aerosols, the diffuse and direct components of near-IR albedo are more sensitive to visibility and high solar zenith angles (Liang et al., 1999b). This shows that calculating the instantaneous broadband albedo in visible, near-IR and total short-wave can indicate the daily mean value of broadband albedo even if the atmospheric conditions are highly variable over time, provided that the surface state, such as soil moisture and the LAI of vegetation, doesn't change over time.

Spectral albedo, then, needs to be converted to broadband albedo (α) using weighting coefficients obtained from the spectral distribution of incoming solar radiation, which are dependent on the solar zenith angle. Since the spectral bands may not cover the entire short-wave region (0.3-5 μm), the missing spectral regions need to be estimated using interpolation and extrapolation methods. Each sensor also has a spectral function, usually a Gaussian function, which explains the distribution of received radiance in each spectral band. The amount of spectral solar irradiance then needs to be calculated based on these functions. We can summarize the required steps for the conversion of spectral to broadband albedo:

- Calculating the solar irradiance for each spectral band of the satellite imagery using the spectral distribution function of sensor
- Interpolating and extrapolating of spectral solar irradiance to fill the spectral gap; this may not be necessary if the spectral bands continuously cover the entire short-wave region (0.3-5 micron) or only one of the interpolations or extrapolations may be needed.

- Calculating the weighting coefficients using the spectral irradiance and total short-wave irradiance.

The conversion coefficients can be calculated by using either ground measurements or Top of the Atmosphere (TOA) measurements. Ground measurements can be made by measuring both the spectral irradiance and reflectance in different view-sun geometry and then assigning appropriate weighting coefficients based on the spectral distribution of solar radiation and validation of the obtained coefficients using measured broadband albedo, using a Pyranometer (Irons et al., 1988). These measurements are valid just for that area, since the spectral distribution of the downward solar flux varies under different atmospheric conditions (Liang, 2003).

Inherent narrowband albedo acquired by remote sensing data needs to consider the solar zenith angle and atmosphere state to obtain broadband albedo. The conversion coefficient developed under different climates and using different methods, such as ground measurements (Russell et al., 1997) and radiative transfer models (Valiente et al., 1995), are usually study- and area-specific. For Landsat spectral bands, the spectral to visible, near-infrared and middle-infrared conversion coefficients were calculated assuming a Lambertian reflectance (Brest and Goward, 1987), while another study obtained the conversion coefficients by considering the anisotropy of the surface (Irons et al., 1988).

2.3.3 The MODIS albedo product

The albedo product of MODIS has been available since July 2000. At first, it was designed to obtain albedo from observations from Terra-MODIS, Aqua-MODIS and Terra-MISRinstruments but, later on, it used only the observations from MODIS instruments. The algorithm of obtaining albedo is similar in both cases, so we here describe the MODIS-MISR albedo product.

2.3.3.1 MODIS Specifications

Terra and Aqua satellites, launched in December 1999 and May 2002 respectively, carry MODIS,MISR and other instruments. As Terra passes from north to south and monitors an area in the morning (10:30 am local time), Aqua passes from south to north and monitors the same area in the afternoon at 1:30 pm; this has given MODIS the capability of providing information twice a day from any area, which allows consideration of the changes over a day, such as the creation or disintegration of clouds and changes in sea or land surface temperature. Having 36 spectral bands (ranging from 0.4 to 14.5 μm), a spatial resolution from 250m to 1000m, wide coverage (viewing a swath 2,330 km wide) and low-cost data has made MODIS a

unique sensor that has attracted the attention of a wide range of researchers studying the Earth and its atmosphere.

The other advantage of using MODIS data is its products, which provide various types of information extracted from the initial data, each or any combination of which can be directly used by researchers; this has obviated the necessity of having a detailed knowledge of initial data and processing methods. MODIS has calibration, atmosphere, land, cryosphere and ocean products at different levels of processing: Level 0 (L0) are raw data; Level 1A (L1A) are the Digital Number (DN) and ancillary data in HDF format; Level 1B (L1B) are calibrated and geo-located radiance; Level 2 (L2) are the geo-located data that have not been re-projected; Level 3 (L3) are the re-projected data.

2.3.3.2 MISR Specifications

MISR is a pushbroom multi-angle instrument with nine cameras covering a wide variety of view angles. It has four cameras to the aft, four cameras to the fore and one nadir-view camera; the fore and aft cameras have view angles of 26.1, 45.6, 60.0, and 70.5 degrees. Each camera has four bands, centred at 446, 558, 672, and 867 nanometres respectively. It provides information for the entire globe every 9 days in four bands (blue, green, red, and near-infrared). The cross-track swath width is 360 km, which is the common overlap of all 9 cameras.

2.3.3.3 MODIS/MISR combination albedo product

Multi-date multispectral surface reflectance data from both MODIS and MISR are used to create the BRDF/Albedo product of MODIS every 16 days at spatial resolutions of 500 m, 1000 m and 5600 m. Seven bands of MODIS, centred at 645, 858.5, 469, 555, 1240, 1640, 2125 nanometres respectively, and four bands of MISR in visible and near-infrared are used to produce spectral albedo in seven bands of MODIS.
Using spectral-to-broadband albedo conversion coefficients (Liang et al., 1999a), spectral albedo in bands 1 to 7 of MODIS is then integrated to create the visible (0.3 - 0.7 μm), near-infrared (0.7 - 5 μm), and total short-wave (0.3 - 5 μm) albedo which are desirable for climate and agriculture models.
The product is available as black-sky and white-sky albedo from semi-empirical and empirical methods, BRDF/Albedo model parameters, and nadir BRDF-adjusted reflectance and quality assurance information. When there are insufficient view-angle states, such as cloudy times, a back-up algorithm is used, which constrains the BRDF shape using prior information and adjusts it to the current observations.

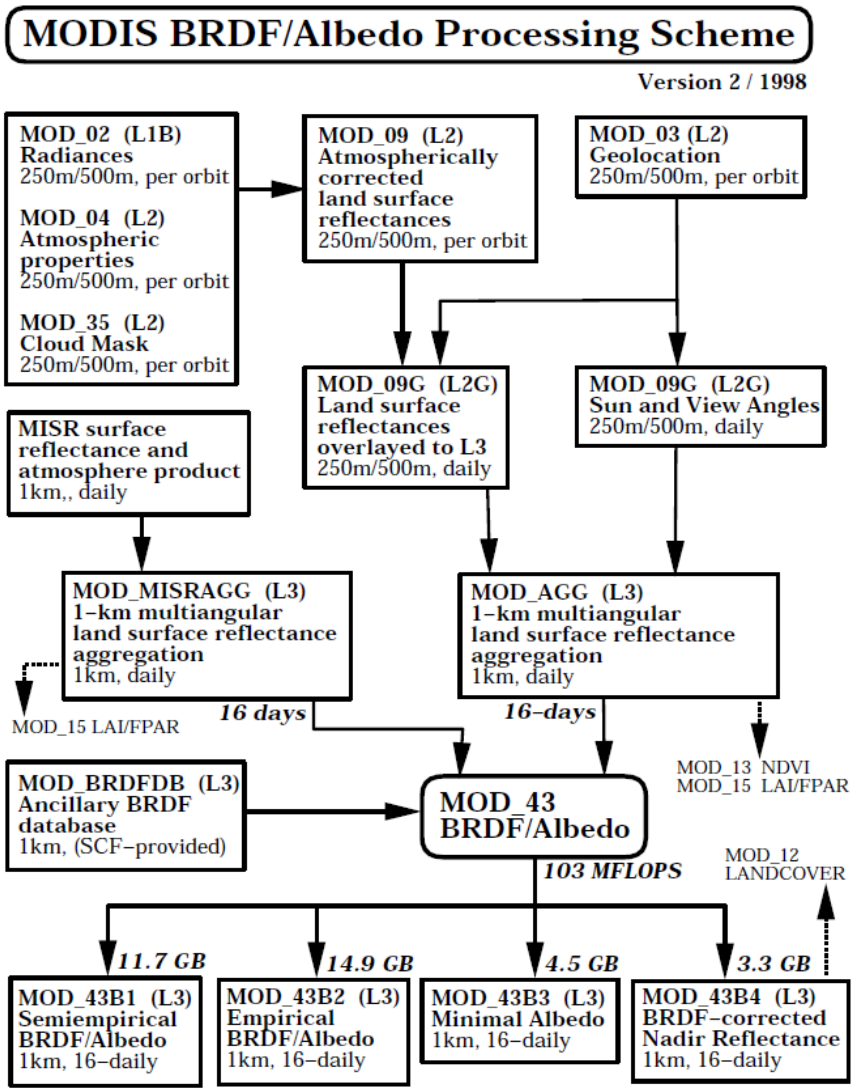

Figure 2-2 Flowchart of the procedure of producing the BRDF/Albedo product where MOD_xx stands for MODIS and process codes (Strahler et al., 1999).

As mentioned above, although the albedo product of MODIS was supposed to use MISR data, in addition to MODIS data, some problems such as the registration issues of the two MODIS and MISR sensors caused the albedo product of MODIS to use only MODIS data, from Terra and Aqua. The described procedure of producing the MODIS albedo product (Figure 2-2) is for the full inversion operational model as it is being used for this study. When there are not enough clear sky observations, the full inversion of the RTLSR model is not possible and then the BRDF parameters from the previous clear sky observations and the MODIS land cover map are used to obtain albedo values (Friedl et al., 2010).

The spectral and broadband black-sky albedo are computed for the local noon zenith angle for each location (Schaaf et al., 2002) and, for other sun geometry, it needs to be calculated using BRDF model parameters which also have good accuracy (Liu et al., 2009). The BRDF/Albedo product of MODIS uses a linear kernel-based semi-empirical model, 'RossThick-LiSparse-R' which was tested over different land covers (Privette et al., 1997) and comprises three components: isotropic, volumetric and geometric-optical (Roujean, 1992, Strahler et al., 1999, Wanner et al., 1995a).

$$f_r(\theta_i,\varphi_i;\theta_r,\varphi_r) = f_{iso} + f_{vol}K_{vol}(\theta_i,\varphi_i;\theta_r,\varphi_r) + f_{geo}K_{geo}(\theta_i,\varphi_i;\theta_r,\varphi_r) \quad \textbf{Equation 2-21}$$

Where f_{iso}, f_{vol}, f_{geo} are isotropic, volumetric and geometric-optical parameters, respectively, and K_{vol} and K_{geo} are volumetric and geometric-optical kernels, respectively.

The volumetric component, the 'RossThick' kernel (Ross, 1981), applies a single-scattering radiative transfer model for a uniform dense leaf canopy with a Lambertian background.

$$K_{vol} = K_{RT} = \frac{(\pi/2 - \xi)\cos\xi + \sin\xi}{\cos\theta_i + \cos\theta_r} - \frac{\pi}{4} \quad \textbf{Equation 2-22}$$

The geometric-optical component, the 'LiSparse-R' kernel (Li and Strahler, 1992), considers the shadow-casting effect on reflectance, based on the height and the shape of objects, for a sparse canopy with a Lambertian background.

$$K_{geo} = K_{LSR} = O(\theta_i,\theta_r,\varphi) - \sec\theta_i' - \sec\theta_r' + \frac{1}{2}(1+\cos\xi')\sec\theta_i'\sec\theta_r' \quad \textbf{Equation 2-23}$$

$$O(\theta_i,\theta_r,\varphi) = \frac{1}{\pi}(t - \sin t\cos t)(\sec\theta_i' + \sec\theta_r'), \quad \textbf{Equation 2-24}$$

$$\cos t = \frac{h}{b}\frac{\sqrt{D'^2 + (\tan\theta_i'\tan\theta_r'\sin\varphi)^2}}{\sec\theta_i' + \sec\theta_r'} \quad \textbf{Equation 2-25}$$

$$D' = \sqrt{\tan^2\theta_i' + \tan^2\theta_r' - 2\tan\theta_i'\tan\theta_r'\cos\varphi} \quad \textbf{Equation 2-26}$$

$$\cos\xi' = \cos\theta_i'\cos\theta_r' + \sin\theta_i'\sin\theta_r'\cos\varphi \quad \textbf{Equation 2-27}$$

$$\theta_i' = \tan^{-1}(\frac{b}{r}\tan\theta_i) \quad \textbf{Equation 2-28}$$

$$\theta_r' = \tan^{-1}(\frac{b}{r}\tan\theta_r) \quad \textbf{Equation 2-29}$$

Where *O* is the overlap function of view and illumination shadows on the ground, θ_i' (and θ_r') are the effective zenith angle of illumination (and view) direction, adjusted for spheroidal shape of the crown, ξ' is the phase angle between the illumination and viewing directions, θ_i' (and θ_r') is the effective zenith angle of illumination (and view) direction, adjusted for spheroidal shape of the crown, *h* is the height to the centre of crown, and *b* and *r* are the vertical and horizontal radius of the crown, respectively.

For the dense cropland where shadowing effect is at a minimum, the optical-geometric component is close to zero while, for the sparse woodland, the Li kernel is large.
The MODIS observations can be combined with other multiple angular data, such as MERIS, to fill the gap due to low temporal resolution of those sensors (Muller et al., 2007).

2.3.3.4 Assumptions and limitations

The assumptions applied in producing the albedo product of MODIS are:

- Invariability of the surface reflectance during the 16-day period
- Lambertian scattering of background bare soil applied in the volumetric and geometric kernels of the BRDF model
- Single-scattering radiative transfer model applied in the volumetric kernel of the BRDF model
- Back-up algorithm assumes that the shape of BRDF has a linear relationship with overall reflectance of the scene.

The assumption applied in the RTLSR BRDF model may not be representative of the real situation although its validity has been shown by some studies under optimal conditions. The uncertainty arises from not including many types of land cover which are dominant in other areas of the globe. Also, the same land cover may show different reflectance and absorption behaviour in different climates and geographical locations. Clouds and shadows could greatly affect the atmospherically-corrected surface reflectance which may limit its validity in cloudy areas.

2.3.4 Other Albedo products

The directional radiance of the Earth's surface required for BRDF and albedo computations is provided by satellites in different ways:

- Sequential time series, such as MODIS, AVHRR
- Simultaneous multiple-view angle observations such as MISR, POLDER, CHRIS/PROBA

- Geostationary platforms such as Meteosat: These kinds of sensors provide sequential observations during the daytime at different sun geometries at the same view angle.

Since the time-consuming and complicated albedo computations may not be desirable for many scientists, several albedo products from different satellites have been released. The appropriate sensors for producing albedo can also be categorized into those without albedo products, such as historical AVHRR data, and those with the products, such as MODIS.
The albedo product of MODIS gains an on-board sensor calibration, accurate atmospheric and geometric correction, and high spatial and spectral resolution.

Table 2-1 Comparison between different satellite albedo products

Platforms	Sensors	Temporal resolution	Spatial resolution	Bands used in albedo calculations	Data source
Polar orbiting satellites	Terra/Aqua MODIS (Gao and Lucht, 2005, Schaaf et al., 2002	16 days	500 m, 0.05°	7 bands at 459-479 (3) , 545-565 (4), 620-670 (1), 841-876 (2), 1230-1250 (5), 1628-1652 (6), and 2105-2155 (7)	Multi-date reflectance
	Terra-MISR (Diner et al., 2008b)	9 days at equator and 2 days at poles	1100 m	4 bands at 425-467, 543-572, 661-683, 847-886	Simultaneous multi-angle data (at view zenith angles 0,±26.1,±45.6,±60

					and ±70.5 degrees)
	Terra-CERES (Rutan, 2006)	Monthly	1°	1 band at 200-4000	
	MERIS (Muller, 2006)	16 days, monthly	0.05°	4 bands at 490±5(3), 560±5 (5), 665±5 (7) and 865±10 (13)	Multi-date data and MODIS BRDF parameter
	POLDER (Bacour and Bréon, 2005, Hautec et al., 1998, Leroy et al., 1997, Maignan et al., 2004)	30 days	6 km	5 bands at 443±10, 565±10, 670±10 , 765 865±20 nm	Multi-date, simultaneous multi-angle data (14 view angles which ranged in ±50° across-track, ±61° along-track)
Geostationary satellites	MVIRI-Meteosat (Govaerts et al., 2006, Pinty et al., 2000)	10 days (Europe, Africa)	2.5 km (at equator) 4 km (at mid-latitude)	1 band 0.4-1.1µm	Multiple daytime Reflectance (30 min intervals)
	MSG-SEVIRI (Geiger et al., 2003, van Leeuwen and Roujean, 2002)	Daily and 30-days composite	3 km	3 bands at 0.6, 0.8 and 1.6µm	Multiple daytime Reflectance (15 min intervals)

2.3.5 Validation of remotely-sensed albedo

Validation or accuracy assessment of remote sensing data is necessary so that the sources of errors can be identified and corrected, which will then increase the quality of the data and the resulting information. The validation process needs reference data whose accuracy is high or acceptable for the kind of study undertaken. The quantity and distribution of reference data are functions of the map information distribution

and the assumptions applied in the produced map. The validation of remotely-sensed data in general and albedo in particular can be categorized based on the type of reference data into the following:

2.3.5.1 Validation using simultaneous field measurements

Field measurements of land surface variables, such as reflectance and albedo, have become more organized and meaningful since the advent of satellite data and the need for validation. One of these field campaigns was the FIFE (First International Satellite Land Surface Climatology Project (ISLSCP) Field Experiment) project which was undertaken in Kansas, US in the late 1980s. Simultaneous measurements of meteorological and surface parameters were gathered by a large number of scientists and a variety of field instruments, as the existing satellites such as Landsat were monitoring the Earth underneath. The problems discovered during the FIFE campaign led to improvements in field measurement techniques and were a good basis for further field studies (Asrar, 1989).

Although field measurements can be a good source of valid information, the conditions under which the experiment is conducted should be taken into account when the measurements are compared with satellite data. Issues such as mismatch of variables measured, imperfect calibration of instruments and disturbance of the site can sometimes cause large errors which, if not corrected, may make such data invalid. Also, practical issues limit those measurements to small areas, much smaller than even one pixel of data from MODIS.

BRDF, which is its hemispherical integration produces albedo, can never be measured directly due to the insufficiency of measurable radiance in such a small solid angle (Nicodemus et al., 1977), and field radiometers actually measure the reflectance factor which is the integration of BRDF over finite solid angles (Robinson and Biehl, 1979). The measured reflectance factor is affected by uncertainties in the measured irradiance and instrument characteristics (Asrar, 1989). Changes in irradiance, due to factors such as thin clouds, while making the separate measurements of radiance and irradiance can cause large errors of up to 100%, which can be minimised by making simultaneous measurements of irradiance and radiance (Duggin and Cunia, 1983). Since a radiometer measures the radiance, it should be numerically converted to a reflectance factor using a reference surface. This requires a perfect lossless Lambertian surface as a reference surface, which is in contrast to the state of artificial and actual surfaces, and non-ideal surfaces can cause errors of up to 27 % for large solar zenith angles (Asrar, 1989). Another concern regarding the use of field instruments is the difference in the responses of similar instruments, which determines the calibration

accuracy of the instruments; this uncertainty may cause errors of up to 10% (Asrar, 1989, Guenther, 1987).

In spite of the mentioned uncertainties, the field measurements are the only possible way of measuring reflectance at a large number of angles, since the current remote sensors usually do not have large-view angles and are limited in the number of observations from different angles. The measurements, once corrected for errors, can then be used in the validation of BRDF and albedo measurements; also, the BRDF model can be used with remote sensing data.

2.3.5.2 Validation using literature values

There have been a number of BRDF and albedo field measurements, some of which were designed for validation of the BRDF models and satellite data while others were taken for other studies. As surface reflectance varies greatly with view and sun geometry, the measurements taken at specific view and sun angles cannot be used for the validation of the data with different view-sun geometries. Considering the atmosphere and surface dependence of reflectance, the albedo measurements of a specific land cover in the dry climates of the southern US can differ greatly from those taken under the cloudy, humid atmosphere of the UK for the same land cover and sun-view geometry. If no other data are available, literature values can be used provided that the conditions of the measurements of the obtained values are taken into account.

2.3.5.3 Validation using simultaneous other remote sensing data

Using data from different satellites is likely to result in the estimation of albedo based on multiple-view angle observations in which the number and distribution of the angles may differ between different sensors. Also, there are differences in the spatial, spectral, radiometric and temporal resolutions of the data, which cause differences in the estimated albedo. Sensors such as MODIS, which produce a routine albedo product, then need to be validated. Ground measurements of albedo are usually point measurements, which may not be representative of an area of 25 ha (the finest resolution of MODIS albedo product) or more. The situation might be worse if we want to compare the point field values with an area of 3 by 3 pixels, which is preferable to choosing a single pixel due to the uncertainty in the geometric correction accuracy and adjacency effects of neighbouring pixels. The distribution of point measurements depends on the number of land covers which, in an optimal way, can be measurements for each land cover class. This will result in the need for tens to hundreds of point measurements, which is quite expensive and difficult to achieve. High spatial resolution data, as long as they have appropriate spectral and angular information,

provide continuous information which is more valid for comparison with point ground measurements. The validated high spatial resolution can then be used to validate the coarser resolution data such as MODIS by providing a large number of continuous pixels which are at least representative of several pixels and land covers. They can also be very useful in increasing the spatial resolution and accuracy of the albedo map.

2.3.6 Validation of the albedo product of MODIS

The albedo product of MODIS is used either as a direct input to climate and hydrology models or as ancillary data for other applications of remote sensing and other products of MODIS. This product has many positive points such as having high spatial and temporal resolution, an accurate geometric correction, and use of concurrent atmosphere parameters obtained from the related spectral bands of MODIS in the atmospheric correction, onboard calibration and high validation efforts. On the other hand, there are other albedo products that are comparable with the MODIS albedo products. MERIS has a similar temporal resolution but the lower number of bands in the shortwave region and its reliability on the MODIS BRDF parameters has caused it not to be able to use its finer spatial resolution. The simultaneous POLDER observations from different view angles as well as a better distribution across the hemisphere could provide valuable information about BRDF and albedo but has coarser spatial, spectral and temporal resolutions. The main reason for which the MODIS albedo product is widely used is its availability in comparison to other albedo products. Having other coarser spatial and temporal resolution albedo products which may be desirable in climate models has made the MODIS albedo product more useful for a large variety of climatologists, hydrologists and environmentalists etc., who may not wish to be involved in the processing of remote sensing data, which is time-consuming and requires a detailed knowledge of remote sensing and the atmosphere. Validation of this product (and other products) is important so any errors can be identified and corrected or taken into account while using the product in other models. Since point ground measurements cannot be representative of the large pixel size of MODIS, high spatial resolution data such as Landsat, which can be validated using ground data, are used for the validation process (Liang et al., 2002). Since the validation process starts before the launch of the sensor and continues after the launch, validation of the albedo product of MODIS can be categorized into the measurements taken before launch and those taken after launch.

2.3.6.1 Pre-flight Validation

The pre-flight validation was mostly focused on the validation of the models used. The accuracy of the atmospheric correction method of MODIS depends on sensor calibration, inputs, utilizations of LUTs, inverse solving and BRDF correction (Vermote

and Vermeulen, 1999). Pre-launch validation activities are based on using sun-photometer and existing sensors such as TM, MODIS Airborne Simulator (MAS) and AVHRR. The results of early validation efforts show the high level of agreement of the MODIS reflectance product with high spatial resolution data validated by ground measurements as well as the aerosol product (Figure 2-3). The errors in atmospheric correction of MODIS data were shown to increase in cases of high aerosol and sparse vegetation (Vermote et al., 1997a).

Figure 2-3 On the left: results of atmospheric correction using TM data over Hong Island (Vermote and Vermulen, 1999); and on the right: retrieval of AOT using MAS data (Roger et al. as cited in Vermote and Vermulen, 1999)

Global remote sensing BRDF models need to be able to correctly show reflectance anisotropy using a few view-angle observations with different distributions and under a variety of land covers and sun geometries from pole to pole (Strahler et al., 1999). Several studies have presented the ROSSThick-LiSparse-R BRDF model as having greater accuracy than other BRDF models for the global estimation of albedo (Lucht et al., 2000, Privette et al., 1997, Wanner et al., 1995a, Wanner et al., 1997). The BRDF model of MODIS was validated using PARABOLA field radiometer data for different land covers such as crops, bare soil, forest, desert and snow. The field measurements are mostly representative of hemispherical BRDF at several solar zenith angles and showed a RMSE of about 20 percent of the modelled white-sky albedo (Strahler et al., 1999). The validation results show the good performance of the BRDF model over a wide variety of land covers (Privette et al., 1997, NCAVEO, 2006), with noisy data (Lucht and Lewis, 2000) and sparse observations (Lucht, 1998).

The conversion coefficients of the MODIS narrowbands to shortwave broadband albedo (Liang et al., 1999a) were validated using the spectra of several land covers from the ASTER spectral library (Strahler et al., 1999). The reference shortwave, visible and NIR

albedos were then computed from the used ASTER spectra. The spectral MODIS albedo was converted to shortwave, visible and NIR albedo using the conversion coefficients. The results showed a mean relative error of 6 percent for the shortwave albedo, 4 percent for visible albedo and 3 percent for NIR albedo. This showed the errors resulting from the conversion of spectral-to-broadband albedo were 0.02 of the absolute albedo values for green vegetation which was desirable for climatologists.

2.3.6.2 After-flight Validation

One of the early validation efforts after the launch of MODIS instruments in space is the work by Liang et al. (2002). Their work was based on the ground measurements and ETM+ Landsat data at one of the EOS Land Core Validation Sites. The methodology used was scaling up the point field measurements to the MODIS resolution to validate the MODIS reflectance and albedo products. Their validation work was carried out over vegetated surfaces, assumed to be Lambertian, on the MODIS and ETM data in clear days with nadir view geometry. The comparison of broadband albedos of MODIS and ETM (Figure 2-4) showed that the largest difference was in the visible band, which could be due to inaccurate aerosol correction of the MODIS data, while there was a good match in the NIR band. The overall accuracy of the MODIS reflectance and albedo products was found to be reasonably good with less than 5% absolute error. They related the observed errors to the uncertainties in the input atmospheric parameters, mainly aerosol optical depth, the Lambertian assumption of surface, and using the values from the 16-day albedo product.

Figure 2-4 Validating the black sky MODIS albedo product (Liang et al., 2002).

Jin et al. (2003) evaluated the MODIS albedo product using ground measurements and some satellite measurements, CERES, AVHRR and ERBE. The results showed a good level of accuracy in the MODIS albedo, a RMSE of 0.018 during the growing seasons April September 2001, and larger errors in winter when spatial heterogeneity was higher. MODIS albedo showed a high level of agreement with the satellite measurements, with bias ranging from 0.016 to 0.034, despite the differences in instruments and retrieval algorithms.

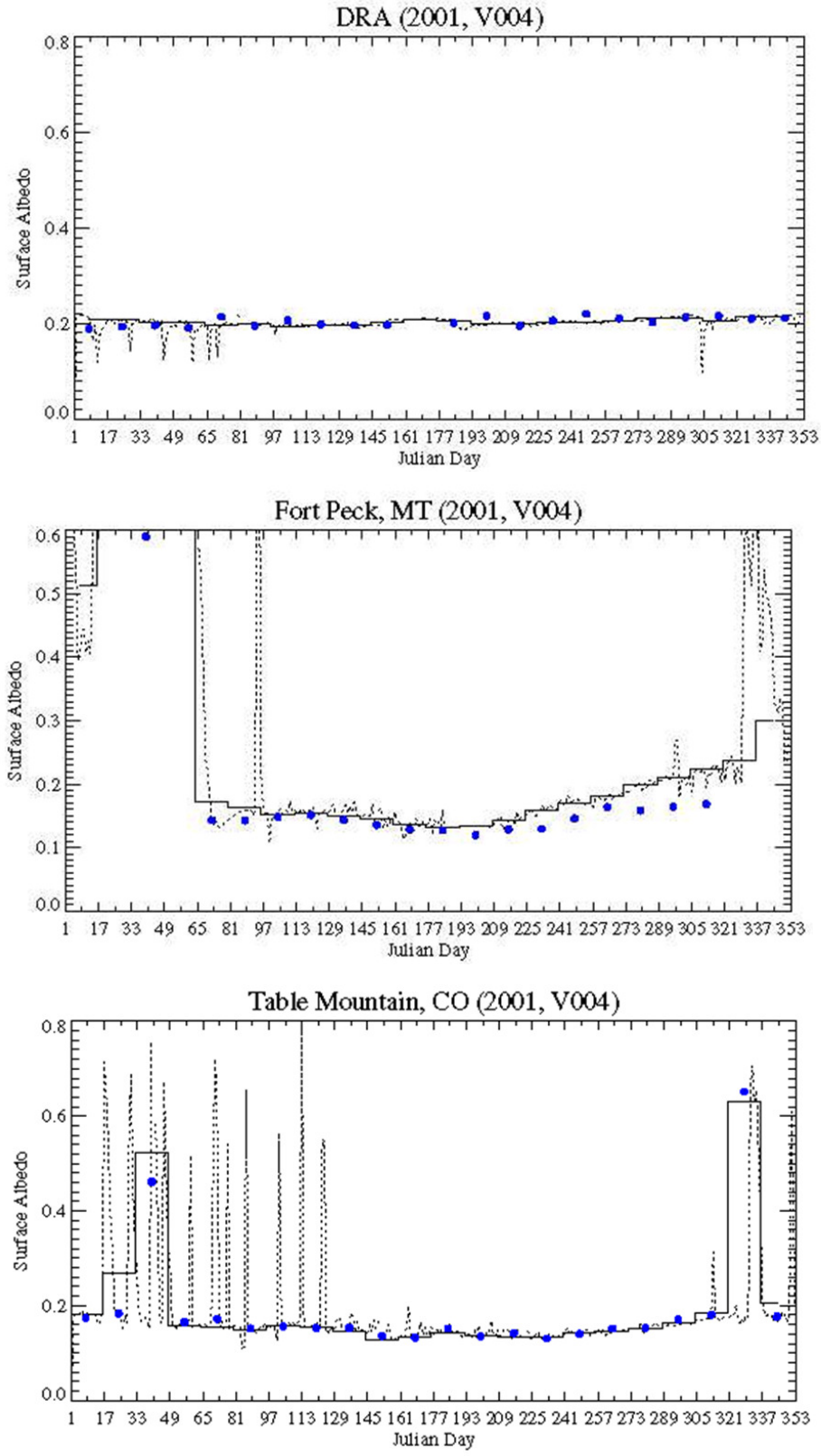

Figure 2-5 The validation results of the MODIS albedo product (Jin et al. as cited in http://landval.gsfc.nasa.gov/Results.php?TitleID=mod43_valsup1)

Disney et al. (2004) examined the accuracy of the MODIS albedo product over a MODIS validation site in the UK. They used a variety of field, airborne and satellite measurements. The field measurements of albedo were upscaled to the MODIS spatial resolution of 1 km using the intermediate high spatial resolution remote data. The MODIS albedo product was obtained from the MODIS albedo backup algorithm due to insufficiency of cloud-free observations. The authors found a high level of agreement between the MODIS albedo and field measurements with an error of only a few percent, despite problems such as the effect of cloud cover on the MODIS albedo product and differences in the timing of measurements.

Figure 2-6 Validation of the broadband MODIS albedo (top image) and the spectral MODIS albedo (bottom image) (Disney et al., 2004)

2.4 Conclusion

Most of the validation efforts after the launch of the MODIS instruments have been carried out in the US and focused mainly on validation of the total shortwave albedo. This gives rise to a need for validation studies in other parts of the world, especially those with different climate and surface states than the ones which have already been used. Although some studies investigated the accuracy of the MODIS albedo in cloudy conditions, there are uncertainties in the method and data used. For example, Disney et al. (2004) had to use the albedo obtained from the MODIS backup algorithm, and not the current MODIS operational product, due to the insufficiency of cloud-free observations. In addition, the number and distribution of these efforts are still limited. There is also a need to carry out validation of the remotely sensed spectral albedo which requires reference measurements by specific field instruments such as the Goniometer. As the MODIS albedo uses black sky albedo and white sky albedo to calculate actual blue sky albedo, there is also a need to develop methods of validation of black sky and white sky albedo. As reflectance changes with time, there is a need to test the assumption of invariability of reflectance during the 16-day period which is being used in producing the MODIS albedo product. MODIS albedo uses 16 day observations and a BRDF model to calculate albedo. As validation of the final albedo values is important, the source of errors may not be identified in the case of unacceptable albedo errors. Validation efforts are then required to test the accuracy of

atmospherically corrected data input to the BRDF model as well as the accuracy of the BRDF model itself.

3 Study site and data

3.1 Introduction

With the purpose of the Calibration and Validation (Cal/Val) of remotely sensed data, a knowledge exchange network called NCAVEO (Network for Calibration and Validation in Earth Observation) was established by the UK Natural Environment Research Council (NERC). The main aims of NCAVEO were providing data through a website, holding meetings and workshops and identifying the necessary research related to validation and calibration (http://www.ncaveo.ac.uk). The NCAVEO 2006 field campaign (NFC06) in southern England took place from June 13 to June 23 with the co-operation of researchers and organisations from inside and outside of the UK. A variety of ground measurements and remote sensing data, imaging spectrometers, LiDARs and digital cameras, were gathered during NFC06. The important characteristics of the gathered data were (i) being nearly simultaneous making them valuable for Cal/Val and (ii) being standardised to international levels to make the data useful for long term use. The main aims of NFC06 were to gain experience in the collection and use of ground measurements in the Cal/Val of reflectance and LAI and also to archive a variety of remote sensing data which can be used as valuable data in Cal/Val studies (Milton and NCAVEO Partnership, 2008). After the event, Prof. Ted Milton, the NCAVEO co-ordinator, commented that "56 people, 4 aircraft, 5 satellites and 6 international visitors were involved over 10 days to conduct the NCAVEO 2006 Field Experiment at Chilbolton, Hampshire. Early indications suggest that we have a complete set of ground, airborne and satellite data from the 'Golden Day', Saturday 17th June, and many other partial data sets with which to tackle specific research questions" (http://www.ncaveo.ac.uk). A full description of the study site and datasets can be found in Milton et al. (2008) and http://www.ncaveo.ac.uk.

3.2 Study site

Chilbolton was the base for the NCAVEO Field Campaign 2006 (NCF06). It is located in the south of England, latitude 51° 8' 41.57" N, longitude 1° 26' 18.00" W, and altitude 88 m, approximately 45 km north of Southampton. The location of the Chilbolton Facility for Atmospheric and Radio Research (CFARR), which is surrounded by agricultural lands, was the main reason for choosing it as the test area.

Figure 3-1 Chilbolton site (http://www.ncaveo.ac.uk). This shows the position of the site relative to the main surrounding cities (the image on the left) and CFARR inside the site (the image on the right).

The area around the research station was mainly agricultural fields which, in June 2006, were planted with barley, wheat, oats and oilseed rape or left fallow. The detailed area studied also included Harewood Forest, which has compartments of conifers and areas of semi-natural broadleaf woodland, and the floodplain of the River Test, parts of which were formerly managed as water meadows. Two areas of semi-natural wet grassland were also included: Chilbolton Cow Common and Bransbury Common, the latter having protected status as a site of special scientific interest (SSSI).

3.3 Ground measurements

Ground measurements consist of the measurements of leaf area index (LAI), land cover, river habitat, ground spectra, and atmospheric properties. The land cover survey and some atmospheric measurements were used in this study.

3.3.1 Land cover survey

The Chilbolton area was part of a larger region which was selected for land cover survey on 12th May 2006. The Centre for Ecology and Hydrology Land Cover 2007 Pilot Project was undertaken in a large area (60 km × 60 km) on 12th May 2006. The map coordinates of the surveyed area in National Grid Reference was X = 400000 to 460000, Y = 095000 to 155000 which included the Chilbolton test site. The output of the measurements which were recorded using a tablet device in the area was produced either as a GIS shape file or as a GIS polygon file for a smaller area (9 km × 6 km) for

which a field-by-field survey was carried out. The scheme used to collect the sample points was based on the land cover map (LCM) 2007 scheme (Morton et al., 2011). The purpose of LCM 2007 was to identify the broad habitats in the UK for biodiversity studies. The surveyed data then covered a wider range of land covers in comparison with the other land cover schemes such as that from the MODIS data (Friedl et al., 2010). This provided more detailed information about land covers such as subcategories of acid, improved and neutral grasslands land cover. However, due to the purpose of the survey this lacks the other useful information for albedo studies such as the phenology and structure of different kinds of vegetation.

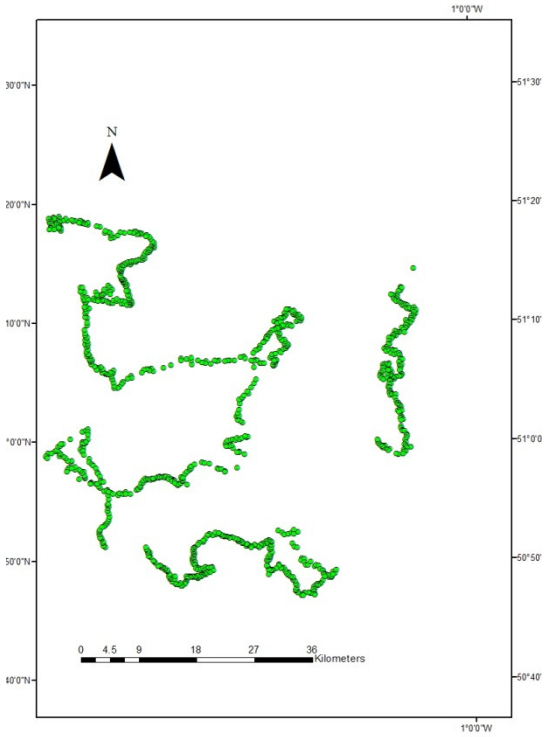

Figure 3-2 The surveyed land cover points and polygons on 12th May 2006.

3.3.2 Atmospheric measurements

The CFARR facility in Chilbolton provided valuable information on atmospheric conditions at the time of the ground and satellite sensor measurements. The installed instruments measure rainfall amount, air and ground temperatures, air pressure, dew point, wind speed and direction, aerosol optical thickness (AOT), total water vapour, cloud thickness and more. Although some of the instruments were not active at the time of the field campaign, the atmospheric variables needed for the atmospheric correction of remote sensing data were collected extensively. Sunphotometers measured atmospheric parameters every 15 minutes when the sky was clear.

The metadata of the Chilbolton NEODC website showed that some of the sunphotometers were used in different locations of the study site during the airborne data acquisition to measure the spatial variability in AOT and water vapour amount across the site every five minutes between 09:30 and 11:30 GMT (Figure 3-3, Figure 3-4, and Figure 3-5). Some photographs of the sky, as seen hemispherically in an upward direction showed the sky conditions at the time of the main measurements. Measurements of spectral irradiance of the sky were also made at many times and for different parts of the sky. The total and diffuse sky irradiance were measured every minute from 10:30 to 13:00 hours on the 17th June 2006, a total of 150 readings. The direct energy of the Sun on the instrument is calculated from the difference between the total energy and diffuse component recorded simultaneously. The angular distribution of spectral sky radiance (400-1000 nm) was measured at frequent intervals on the 17th June.

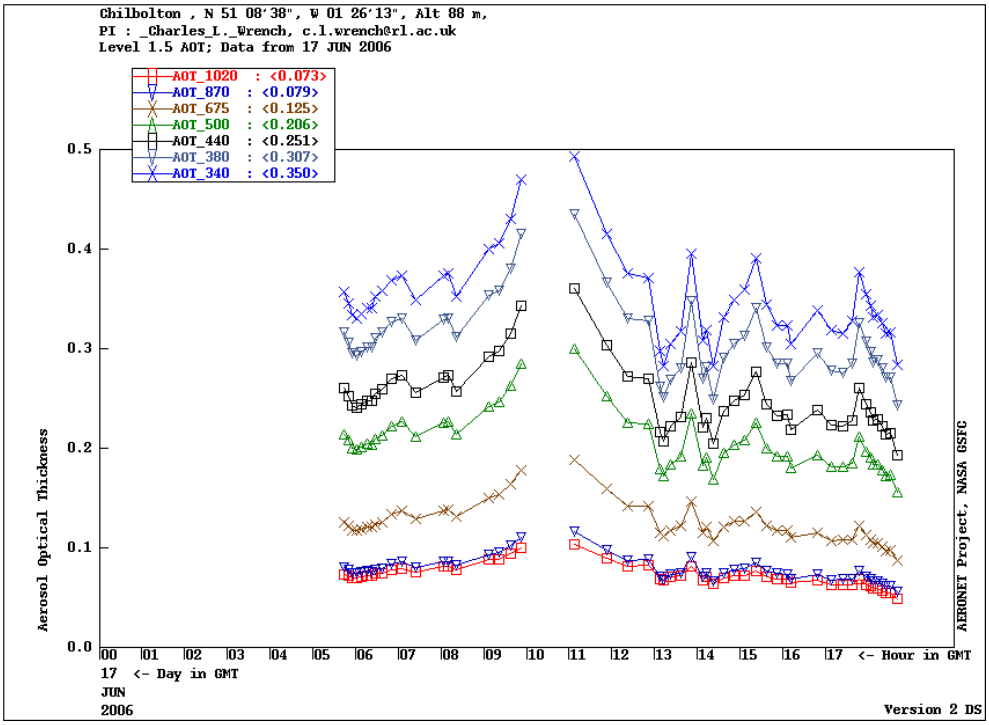

Figure 3-3 Aerosol Optical thickness data collected on 17th June 2006 (http://www.neodc.rl.ac.uk/)

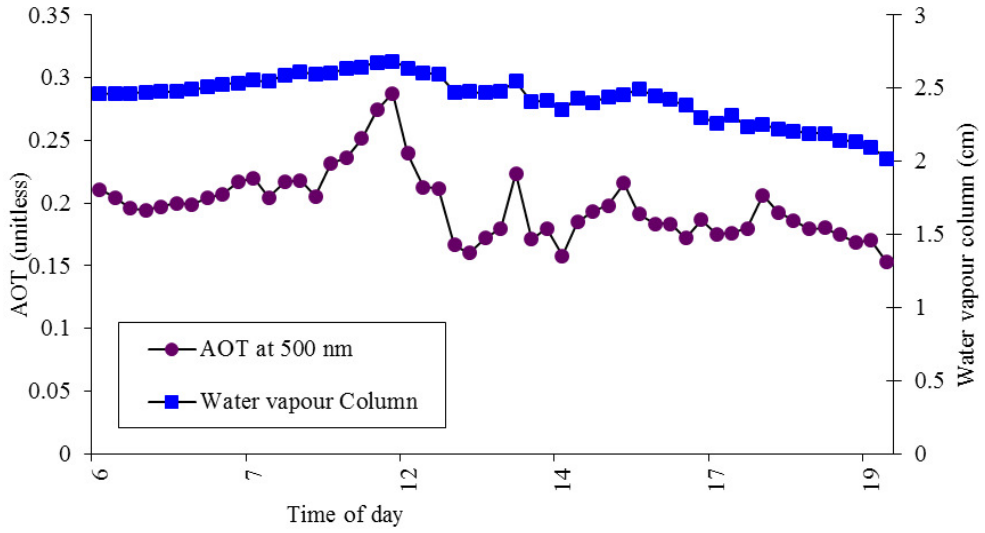

Figure 3-4 Temporal variation of AOT and water vapour over the Chilbolton Observatory Site on 17th June 2006.

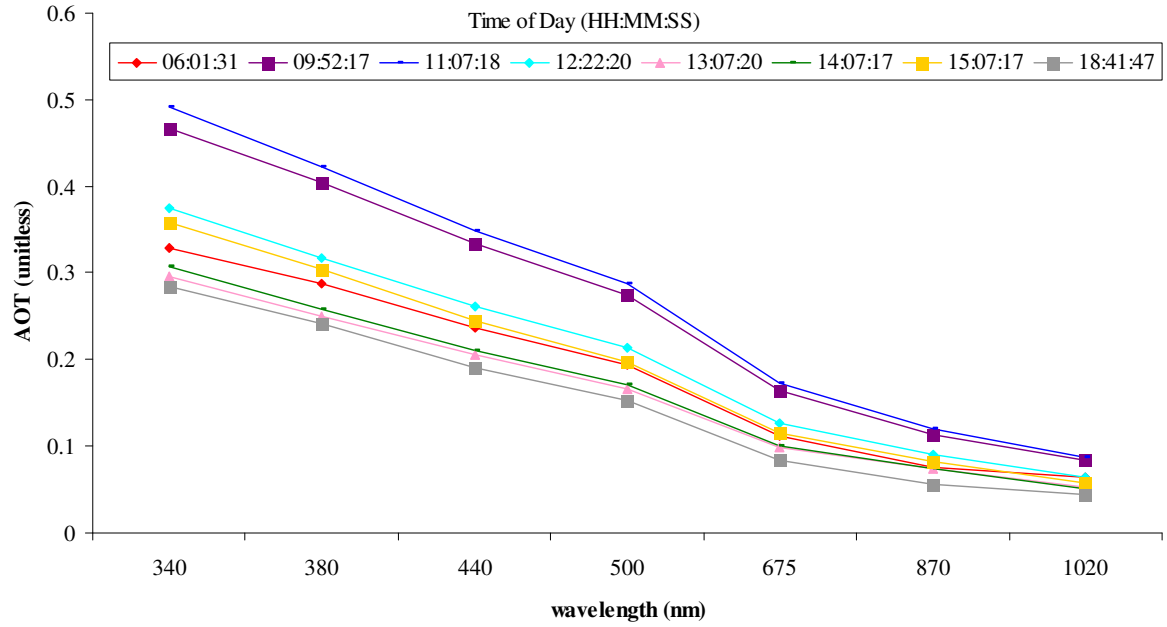

Figure 3-5 Variation of AOT with wavelength at different times of day over the Chilbolton Observatory Site on 17th June 2006.

3.4 Airborne data

The fine spatial and spectral resolution airborne data monitored an area of 9 km × 6 km. Two different aircraft acquired different airborne data between about 10 am to noon on 17th June 2006. The sensors were Compact Airborne Spectrographic Imager (CASI), CASI-2 and CASI-3, an AISA Eagle, a Lidar and a digital camera. The

Environment Agency (EA) acquired CASI-3, Lidar and digital photography data. The Natural Environment Research Council (NERC) Airborne Research & Survey Facility (ARSF) acquired CASI-2 and Eagle data.

Only CASI-3 airborne data were used in this study, a dataset described more fully by Asmat (2009). The aircraft carrying CASI-3 flew at an altitude of 1900 m and monitored the area with the centre coordinate at 51° 8' 42" northern latitude and 1° 26' 12.01" western longitude. CASI-3 data had a spatial resolution of 1 m and 12 bit radiometric resolution and consisted of 32 narrow spectral bands in the visible and near infrared (NIR) regions (Table 3-1 and Table 3-7). The data were acquired in a one and half hour flight, between 9:46 am and 11:16 am local time, in nine parallel flight lines. The direction of flights was mostly North-South, which formed eight out of nine flight lines. The last flight direction was East-West which was perpendicular to the other flight lines and covered the CFARR centre where many ground measurements were recorded. During the flight mission, clouds gradually appeared in the sky which restricted the use of all recorded data. Thus, an area of only 7 km × 2 km was used in this study.

Table 3-1 Spectral characteristics of EA-CASI bands (source: header file)

Band	Central wavelength (nm)	Band width (nm)	Band	Central wavelength (nm)	Band width (nm)
1	400	6.56	17	560	15.54
2	406	6.54	18	576	16.74
3	413	7.08	19	594	18.06
4	420	7.54	20	613	19.52
5	428	7.96	21	633	21.1
6	436	8.38	22	655	22.82
7	445	8.76	23	679	24.66
8	454	9.18	24	704	26.66
9	463	9.62	25	732	28.78
10	473	10.08	26	762	31.02
11	484	10.62	27	794	33.4
12	494	11.22	28	829	35.9
13	506	11.88	29	866	38.52
14	518	12.64	30	906	41.26
15	531	13.5	31	949	44.08
16	545	14.48	32	994	47

Atmospheric correction of the CASI data was achieved using the ATCOR-4 program applied to ground measurements of water vapour, aerosol and spectral reflectance (Asmat, 2009). Two artificial surfaces (asphalt and concrete) were used to measure the directional surface reflectance at the time of the flight over the Chilbolton site. One of the nine flightlines, with a north-south heading, which passed directly over the site was atmospherically corrected. The other flightlines were then corrected for atmospheric effects using an orthogonal flightline which crossed all flightlines and the atmospherically corrected flightline over the site.

3.5 Satellite data

During NFC06, several satellite sensor data were recorded on different days by different operators. The Digital Mapping Camera (DMC) sensor, operated by Ordnance Survey, recorded the data on 9th June 2006. The Système Pour l'Observation de la Terre (SPOT) operated by the Centre National d'Etudes Spatiales (CNES), the French space agency, acquired data on 10th June 2006. The Compact High Resolution Imaging Spectrometer (CHRIS) onboard the Project for On-Board Autonomy (PROBA) operated by the European Space Agency (ESA) acquired data on 17th June 2006. SPOT and CHRIS/PROBA data were used for this study. MODIS data were not acquired as a part of NFC06 but were available for the campaign.

3.5.1 CHRIS/PROBA data

The PROBA is a technology demonstration mission which was launched on 22 October, 2001 (http://earth.esa.int). Since then, this Sun-synchronous satellite has been monitoring the Earth's surface at an altitude of 600 km. It was designed with fully autonomous capabilities needing little involvement from the ground station. There are several instruments onboard the PROBA, of which CHRIS is the prime instrument. CHRIS is a multiple view angle sensor which makes its data valuable in Bidirectional Reflectance Distribution Function (BRDF) and albedo models. CHRIS can operate in five imaging modes that can acquire data in different spatial and spectral resolutions (Table 3-2).

Table 3-2 Characteristics of different acquisition modes of CHRIS/PROBA data (http://earth.esa.int)

Acquisition mode	Spatial resolution	Band range (nm)	Band number	Swath width	Purpose of study
Mode 1	34 m	406-992	62	14 km	Agriculture
Mode 2	17 m	406-1003	18	14 km	Water

Mode 3	17 m	438-1035	18	14 km	Land
Mode 4	17 m	486-788	18	14 km	Chlorophyll
Mode 5	17 m	438-1003	37	7 km	Land

CHRIS data are acquired at five view angles each of them described with a fly-by position (Cutter, 2008). This position on the ground track is determined when the platform zenith angle is minimum, minimum zenith angle (MZA) (Figure 3-6).

Figure 3-6 Illustration of the FZA and MZA (Cutter, 2008)

The acquired FZA are 0°, ±36° and ±55°. Five view angle CHRIS data sets are acquired in a specific order and are recognized with a tag number (Table 3-3).

Table 3-3 Imaging sequence of CHRIS data (Cutter, 2008)

Chronological imaging order	Tag No. order	Scan direction	Nominal FZA
First	3	N-S	+55°
Second	1	S-N	+36°
Third	0	N-S	0°
Fourth	2	S-N	-36°

Last	4	N-S	-55°

The CHRIS datasets used were acquired in hyperspectral mode (mode 1) with 62 spectral bands ranging from 411 nm to 1003 nm (Table 3-4), and an at-nadir spatial resolution of 34 m. The data were recorded at a MZA=7° and different view observation angles (Figure 3-7).

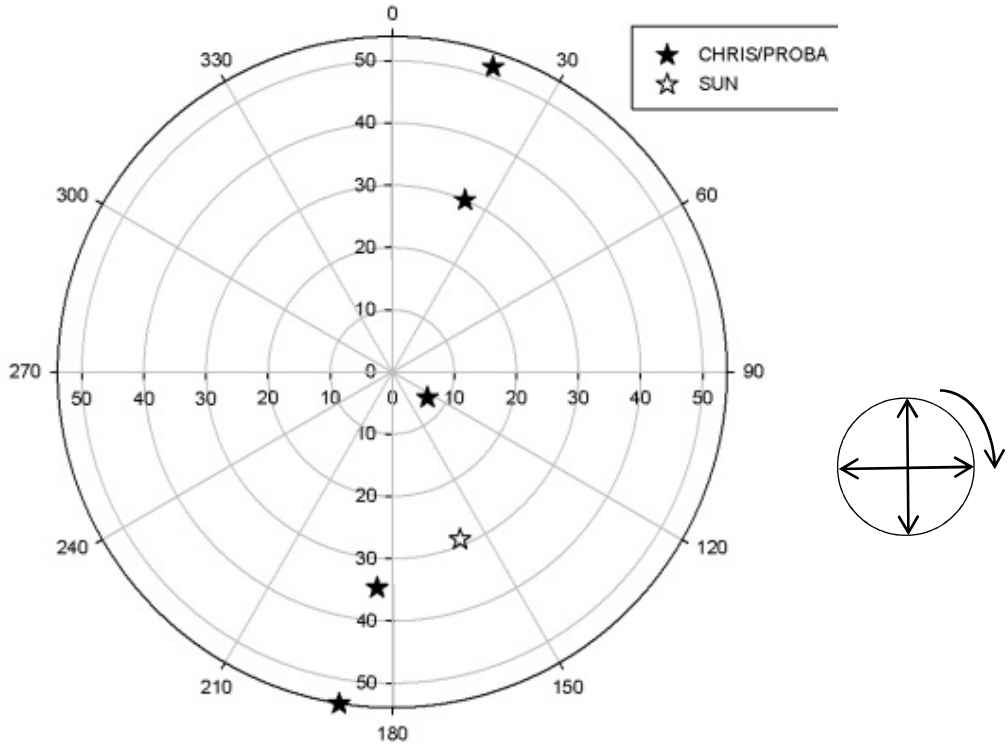

Figure 3-7 The Sun and the five view angles CHRIS geometries over Chilbolton.

Table 3-4 Spectral characteristics of CHRIS/PROBA data (Source: header file of the data)

Band number	Central wavelengths (nm)	Band width (nm)	Band number	Central wavelengths (nm)	Band width (nm)	Band number	Central wavelengths (nm)	Band width (nm)
1	410.5	10.9	22	643.3	9.8	43	796.1	7.8
2	442.4	10.5	23	653.3	10.2	44	803.9	8
3	452.4	9.5	24	663.7	10.6	45	812	8
4	462.1	10	25	674.5	11	46	832.6	16.8
5	472.5	10.6	26	682.9	5.6	47	845.4	8.7
6	482.2	8.9	27	688.6	5.8	48	854.2	8.8

7	491.3	9.3	28	694.4	5.9	49	863.1	9
8	500.9	9.8	29	700.3	6	50	872.1	9.1
9	510.9	10.3	30	706.4	6.1	51	881.4	9.3
10	521.6	10.9	31	712.5	6.2	52	890.7	9.5
11	531.4	8.7	32	718.8	6.3	53	900.2	9.5
12	541.9	12.3	33	725.2	6.5	54	909.7	9.8
13	552.9	9.8	34	731.7	6.6	55	919.5	9.9
14	562.9	10.3	35	738.3	6.7	56	929.6	9.9
15	573.5	10.9	36	745.1	6.8	57	944.7	20.4
16	582.8	7.6	37	752	7	58	960.1	10.4
17	592.5	11.9	38	759	7.1	59	970.6	10.5
18	604.7	12.6	39	766.2	7.2	60	981.1	10.7
19	615.5	8.8	40	773.4	7.3	61	991.8	10.6
20	624.4	9.1	41	780.9	7.5	62	1002.7	10.8
21	633.7	9.5	42	788.4	7.6			

3.5.2 SPOT data

SPOT-5, a Sun-synchronous satellite, was launched on 4th May 2002 and operates at an altitude of 822 km (http://www.satimagingcorp.com). It passes the Equator at 10:30 am local time every 2-3 days, depending on the latitude. The coverage area of each image is 60 km by 60 km to 80 km at nadir. It has different spatial resolutions depending on the spectral band. The Panchromatic band with a spatial resolution of 2.5 m to 5 m covers the spectral region of 480 nm to 710 nm. Multispectral bands cover the green (500 nm to 590 nm), red (610 nm to 680 nm), and NIR (780 nm to 890 nm) wavelengths with a 10 m spatial resolution. The shortwave IR (1,580 nm to 1,750 nm) band has a 20 m spatial resolution. The SPOT data used in this study were acquired on 10th June 2006 and consist of green, red, NIR and shortwave IR bands.

3.5.3 MODIS data

The Moderate Resolution Imaging Spectrometer (MODIS) sensor is onboard the Terra and Aqua satellites. Terra was launched in December 1999 and Aqua was launched a few years later in May 2002. These two Sun-synchronous satellites travel in opposite directions; Terra passes north to south while Aqua passes south to north. They also see an area on the Earth at two different times of day; Terra sees an area at 10:30 am local time while Aqua sees an area at 1:30 pm local time. MODIS has 36 spectral bands ranging from 400 nm to 14.5 µm which cover the visible, NIR shortwave IR and thermal regions. The spatial resolution of MODIS varies depending on the spectral bands; bands 1 and 2 have a 250 m spatial resolution, bands 3 to 7 have a 500 m spatial resolution and other bands have a 1000 m spatial resolution. MODIS has a wide

coverage with a swath width of 2,330 km. MODIS is also provided as different products such as reflectance and albedo products at different spatial, spectral and temporal resolutions.

Table 3-5 Spectral characteristics of MODIS and their application (http://modis.gsfc.nasa.gov)

Band	Bandwidth (nm)	Primary Use	Band	Bandwidth (nm)	Primary Use
1	620 – 670	Land/Cloud/Aerosols Boundaries	20	3.660 – 3.840	Surface/Cloud Temperature
2	841 – 876		21	3.929 – 3.989	
3	459 – 479	Land/Cloud/Aerosols Properties	22	3.929 – 3.989	
4	545 – 565		23	4.020 – 4.080	
5	1230 – 1250		24	4.433 – 4.498	Atmospheric Temperature
6	1628 – 1652		25	4.482 – 4.549	
7	2105 – 2155		26	1.360 – 1.390	Cirrus Clouds Water Vapour
8	405 – 420	Ocean Color/ Phytoplankton/ Biogeochemistry	27	6.535 – 6.895	
9	438 – 448		28	7.175 – 7.475	
10	483 – 493		29	8.400 – 8.700	Cloud Properties
11	526 – 536		30	9.580 – 9.880	Ozone
12	546 – 556		31	10.780 – 11.280	Surface/Cloud Temperature
13	662 – 672		32	11.770 – 12.270	
14	673 – 683		33	13.185 – 13.485	Cloud Top Altitude
15	743 – 753		34	13.485 – 13.785	
16	862 – 877		35	13.785 – 14.085	
17	890 – 920	Atmospheric Water Vapour	36	14.085 – 14.385	

18	931 – 941		
19	915 – 965		

Table 3-6 Spectral characteristics of MODIS bands used in the MODIS reflectance product (Xiong et al., 2006)

Band number	Central wavelength (nm)	Bandwidth (nm)	Equivalent EA-CASI bands	Equivalent SPOT bands	Equivalent CHRIS/PROBA bands
Band 1	645	50	Bands 21,22 and 23	Band 2	Bands 20, 21, 22, 23 and 24
Band 2	858	35	Bands 28 and 29	Band 3	Bands 47, 48, 49, and 50
Band 3	469	20	Bands 8, 9 and 10	-	Bands 4 and 5
Band 4	555	20	Bands 16 and 17	Band 1	Bands 13 and 14
Band 5	1240	20	-	-	-
Band 6	1640	24.6	-	-	-
Band 7	2130	50	-	-	-

The daily reflectance products from 1st June 2006 to 17th June 2006 were downloaded from the MODIS website. The reflectance product is created from the first seven MODIS bands at spatial resolutions of 250 m to 500 m and as daily and 8-day products. Only the first four MODIS bands were used in this study as they have equivalent spectral bands in EA-CASI and CHRIS data.

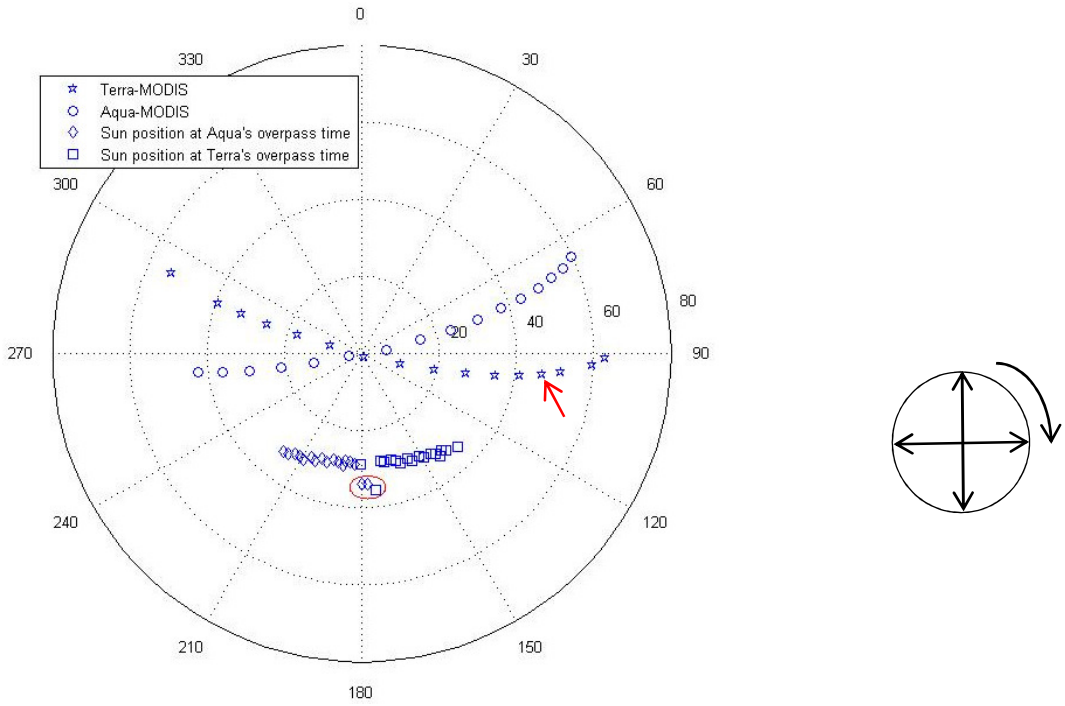

Figure 3-8 View-Sun geometry of the Terra-MODIS and Aqua-MODIS data from 1st June to 17th June 2006 over the Chilbolton area.

Table 3-7 Characteristics of the EA-CASI, SPOT 5 (http://www.satimagingcorp.com/satellite-sensors/spot-5.html), CHRIS/PROBA, and MODIS (http://modis.gsfc.nasa.gov/about/specifications.php).

	EA-CASI	SPOT 5	CHRIS/PROBA	Terra-MODIS	Aqua-MODIS
Launch date	Flying on 17th June 2006	May 2002	Oct 2001	1999	2002
Acquisition date	17th June 2006 (DOY 168)	10th June 2006 (DOY 161)	17th June 2006 (DOY 168)	1st to 17th June 2006 (DOYs 152 to 168)	1st to 17th June 2006 (DOYs 152 to 168)
Acquisition time	9:46 am to 11:16 am	10:30 am	11:20 am	10:30 am	13:30 am
Number of bands	32	4	62	36	36
Spectral range	Visible, and NIR	Visible, and NIR	Visible, and NIR	Visible, NIR, and thermal	Visible, NIR, and thermal
At-nadir	7 km × 2	60 km × 60	14 km × 14	2330 km	2330 km

swath width	km	km	km	(cross track) * 10 km (along track at nadir)	(cross track) * 10 km (along track at nadir)
At-nadir spatial resolution	1 m	2.5 m (Pan) 5 m (Pan) 10 m (bands 1 to 3) 20 m (band 4)	34 m	250 m (bands 1-2), 500 m (bands 3-7), 1000 m (bands 8-36)	250 m (bands 1-2), 500 m (bands 3-7), 1000 m (bands 8-36)
Radiometric resolution	12 bits	8 bits	12 bits	12 bits	12 bits
altitude	1.9 km	822 km	600 km	705 km	705 km
Platform direction	North to south South to north East to west	North to south	North to south	North to south	South to north

The albedo product is produced from the first seven MODIS bands at a spatial resolution of 500 m and as a 16-day product. However, the MODIS albedo product was produced for 17th June 2006 by Boston University for this study. This included the BRDF parameters, black sky albedo, white sky albedo and shortwave albedo. From those, the BRDF parameters and black sky albedo were used in this study.

The differences in the spectra between the Terra-MODIS sensor and EA-CASI and SPOT for green vegetation and non-green vegetation are shown in Figure 3-9 (vegetation) and Figure 3-10 (stubble). Table 3-8 compares the atmospheric variables obtained on DOY 168 2006 by the MODIS, and then input to the MODIS reflectance product, and field measurements.

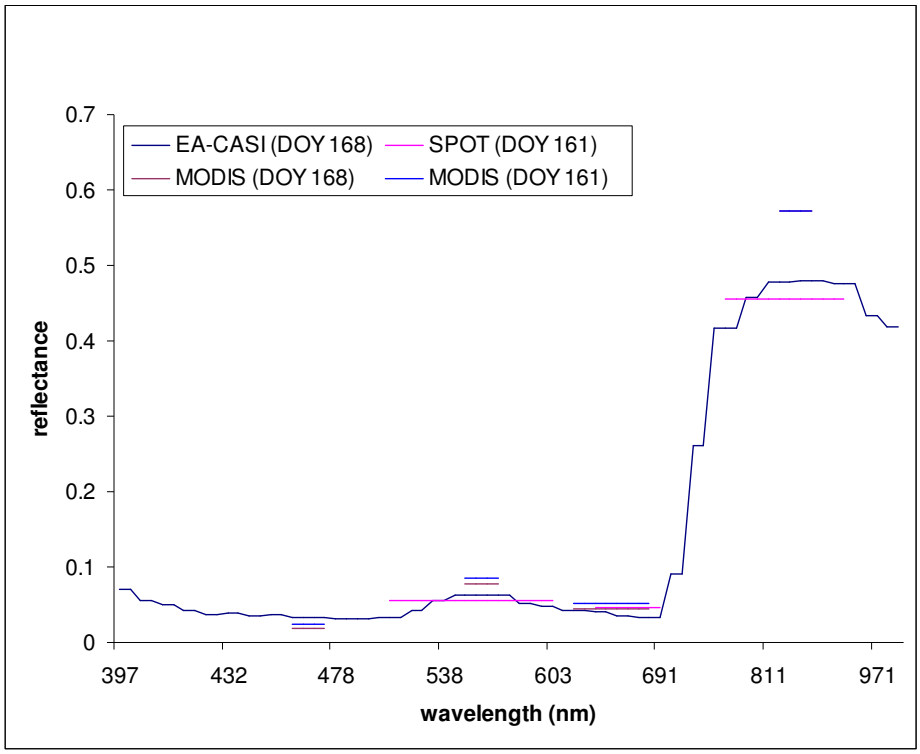

Figure 3-9 Spectral profile of vegetation in EA-CASI, SPOT and MODIS imagery

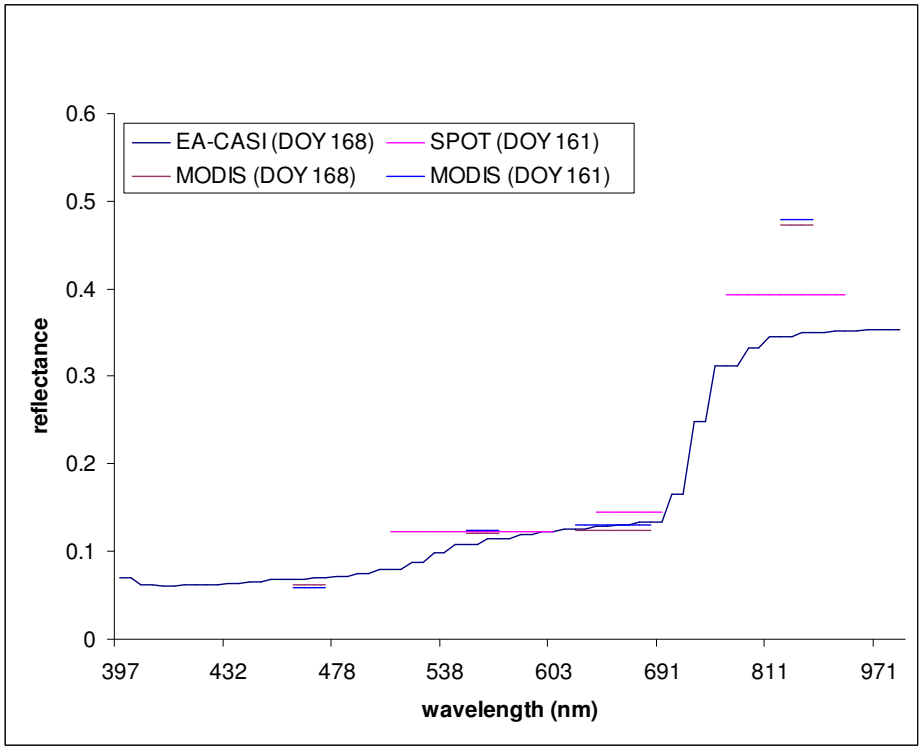

Figure 3-10 Spectral profile of stubble land cover in EA-CASI, SPOT and MODIS imagery

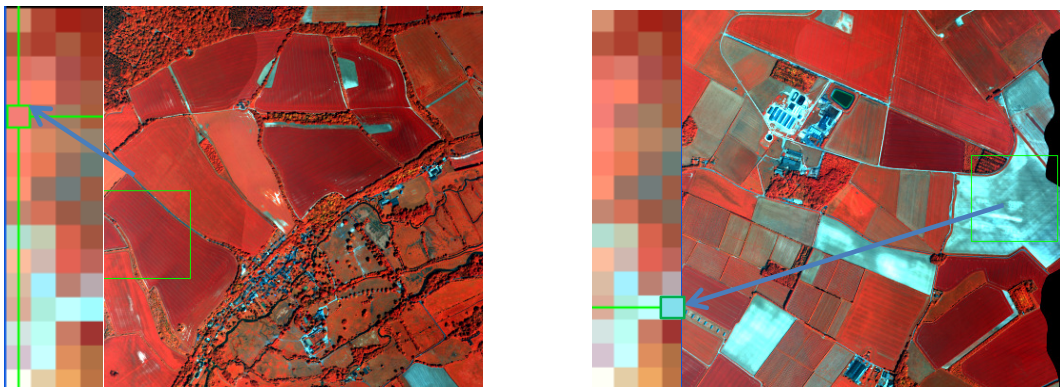

Figure 3-11 Position of the pixels used in Figures 3-9 (the image on the left) and 3-10 (the image on the right). The left part of each image is the up-scaled EA-CASI (500 m) and the right part is the original EA-CASI (1 m).

Table 3-8 Comparison of the atmospheric variables measured in the field site and those estimated by MODIS

	AOT_550 nm	Aerosol type	Water vapour column
Field measurements	0.27	Rural type	2.67
MODIS	0.36 (5-min resolution)	Heavy absorbing smoke (type 4, 5-min resolution)	2.09 (mean daily, 1-deg resolution)

3.6 Methodology

In this study, the validation of the MODIS albedo product as an example of widely used remotely sensed albedo was investigated. Validation is defined here as the determination of the absolute accuracy of the remote sensing products such as atmospherically corrected data and BRDF and albedo estimations using the reliable field/remote sensing measurements.

3.6.1 Accuracy assessment

Congalton and Green (1999) fully explained the methods of the accuracy assessment of remote sensing data. They suggested that the accuracy assessment is usually sought for reasons such as curiosity, increasing the quality of the data by identifying and correcting the source of errors, comparing different algorithms, and knowing the quality of data for decision-making processes.

3.6.1.1 Correlation coefficients

The strength of association between two variables may be shown by the coefficient of correlation (Shaw and Wheeler, 1985). The range of correlation coefficients is between −1 (a perfect negative relationship) and +1 (a perfect positive relationship); a value of 0 shows no correlation between the data. Pearson's correlation coefficient (*r*) is recognized to be the most powerful form of correlation coefficient. It measures the linear relationship between two variables and is based on the covariance term which considers the co-variation of the two variables together.

$$r = \frac{N\sum XY - (\sum X)(\sum Y)}{\sqrt{[N\sum X^2 - (\sum X)^2 * [N\sum Y^2 - (\sum Y^2)}} \qquad \textbf{Equation 3-1}$$

Where *X* and *Y* are the variables and *N* is the number of observations.

A description of the variance explained in *Y* by *X* is given by the square of the correlation coefficient. It measures the proportion of variance explained and is called the coefficient of determination (r^2). In the validation of remotely sensed reflectance, a perfect positive relationship between the reference data and the data that are examined is desired.

3.6.1.2 Linear Regression

A linear regression model measures the form of a relationship between two variables (Shaw and Wheeler, 1985). One variable is the response (*Y*) and the other is the predictor (*X*). Linear regression is calculated based on the least squares concept which fits a line as the squares of the deviations about the line are minimized. It is expressed mathematically as:

$$Y = a + bX + e_i \qquad \textbf{Equation 3-2}$$

Where *a* is the intercept on the *Y* axis, *b* is the slope coefficient and *e* is an error term.

$$a = \frac{\left(\sum Y\right)\left(\sum X^2\right) - \left(\sum X\right)\left(\sum XY\right)}{N\sum X^2 - \left(\sum X\right)^2} \qquad \textbf{Equation 3-3}$$

$$b = \frac{N\sum XY - \left(\sum X\right)\left(\sum Y\right)}{N\sum X^2 - \left(\sum X\right)^2} \qquad \textbf{Equation 3-4}$$

We assumed in this study that the reference data act like the predictor variable and the test data which are examined for their accuracy act like the response.

3.6.1.3 Accuracy

Accuracy is the sum of unbias and precision (Atkinson and Foody, 2002). Bias and precision are both model-based and depend on a statistical model fitted to an ensemble of data values. Bias is an expectation of over- or under-prediction based on some statistical model and may be measured by the mean error. An unbiased model then has a mean error of zero. Precision is an expectation of the spread of errors and may be determined by measuring the standard deviation of the error. A direct estimation of accuracy may then be carried out if there is an independent dataset to assess uncertainty. Accuracy may be measured by the root mean square error (RMSE) which is sensitive to both systematic and random errors:

$$RMSE = \sqrt{\frac{\sum_{i=1}^{n}(z_i - \hat{z}_i)^2}{n}}$$ **Equation 3-5**

Where z_i is the true value and $\hat{z}_i$ is the prediction and *n* is the number of observations. Accuracy is an expectation of the overall error and depends on a statistical model. It is therefore different from error which relates to a single value and is data-based.

3.6.2 Spatial and spectral conversion

To be able to compare different datasets, the data being examined and the reference data should have similar spatial, spectral and radiometric characteristics. Due to the differences in the spectral and spatial resolutions of the data used, some intermediate steps were required. The EA-CASI (and CHRIS/PROBA) data had narrower bands than the MODIS data. Therefore, the equivalent bands of EA-CASI (and CHRIS/PROBA) data with the first four MODIS bands (Table 3-6) were averaged up using a Gaussian function and band widths. The SPOT data had similar spectral bands to the MODIS bands 1, 2, and 4; so the equivalent bands were used (Table 3-6). The EA-CASI (and CHRIS/PROBA and SPOT) data then were upscaled to the MODIS spatial resolution using an average function and nearest neighbourhood resampling method.

The validation process was carried out in several steps (Figure 3-12). The surface reflectance inputs, applied BRDF model and main assumptions were tested. The accuracy of the CHRIS/PROBA albedo as the reference data was also investigated.

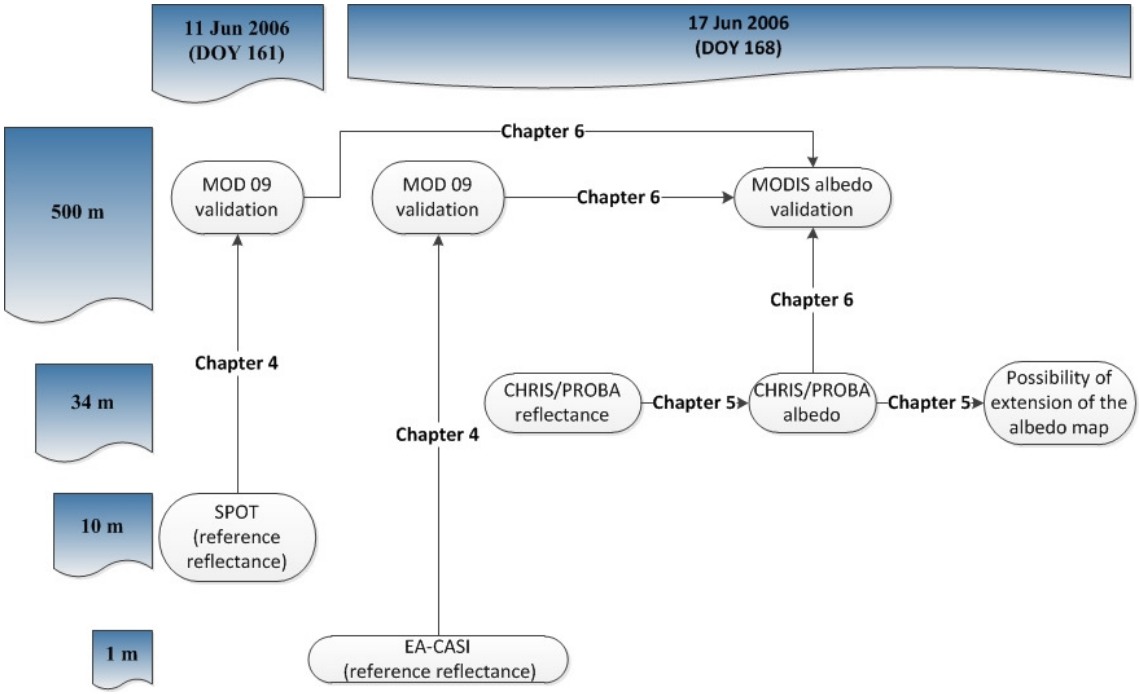

Figure 3-12 Flowchart of methodology

In chapter 4, the process of validating the daily MODIS surface reflectance on DOYs 161 and 168 using the nearly simultaneous EA-CASI and SPOT data will be described. Since the view geometries of the MODIS and EA-CASI were different, a BRDF model was used to obtain the MODIS reflectance at EA-CASI and SPOT view geometries. The accuracy of the BRDF model was assessed by comparing the MODIS reflectance, as the input to the BRDF model, and the estimated BRDF at the same view-Sun geometry. The assumption of invariability of reflectance during the 16-day period was assessed by comparing SPOT and EA-CASI data which had one week time difference.

In chapter 5, the process of obtaining the albedo and the possibility of extension of the obtained albedo map to a larger area will be described. The CHRIS data on DOY 168 was first corrected for atmospheric effects and geometric displacements. The atmospheric correction of the CHRIS data was carried out using two different remote sensing packages, ATCOR-2 and BEAM (Appendix 1). The more accurate results were chosen to be used in the albedo calculation. The resulting albedo map from the CHRIS data is restricted to the common area in all view angles which is smaller than each individual data set. The possibility to extend the albedo map area was assessed using two different methods. The accuracy of estimation of albedo using a land cover map or directional CHRIS reflectance was examined.

In chapter 6, the process of validation of the MODIS albedo will be described. The validation was carried out using two separate methods: a direct method using CHRIS/PROBA albedo and an indirect method assessing the accuracy of the used parameters and variables.

4 Validation of the MODIS reflectance product

4.1 Introduction

Land surface reflectance is the ratio of the reflected to the incident radiation. It is the main input for the estimation of land variables such as surface albedo, vegetation indices (Bonan et al., 2002), the fraction of absorbed photosynthetically active radiation (FPAR), fire scars and snow/ice cover (Vermote et al., 1997a). For example, surface albedo, which is defined as the hemispherical integration of surface reflectance, is required to have an accuracy of 0.02 to 0.05 in climate models (Henderson-Sellers and Wilson, 1983, Sellers et al., 1995). Errors in estimating surface reflectance can introduce large errors in the output surface albedo.

The terminology and definition of surface reflectance have been fully described by Nicodemus et al. (1977) and later Schaepman-Strub et al (2006). The Bidirectional Reflectance Distribution Function (BRDF) is defined as the fraction of incident flux that is reflected at specific sensor geometry within an infinitely small solid angle. It can never be measured. Therefore, an integration of this quantity over a finite solid angle of irradiance and radiance is usually measured (Robinson and Biehl, 1979). The remotely sensed surface reflectance is usually described as a hemispherical-directional reflectance factor (HDRF). This is the ratio of the reflected energy from a surface in one specific sensor geometry to the reflected energy from a lossless and Lambertian surface under the same Sun-view geometry (Schaepman-Strub et al., 2006).

Field measurements of surface reflectance can be taken using a radiometer while satellite sensor observations of surface reflectance are not simply obtained. The remotely sensed surface reflectance is obtained by applying atmospheric correction as well as the correction of adjacency effects and surface-BRDF coupling to radiometrically-calibrated remotely sensed data (Vermote et al., 1997a).

The Moderate Resolution Imaging Spectroradiometer (MODIS) sensor, onboard the Terra and Aqua satellites, observes the Earth's global surface twice a day. The MODIS team applies an atmospheric correction procedure to bands 1 to 7 of the Level 1B MODIS data, centred at 648 nm, 858 nm, 469 nm, 555 nm, 1240 nm, 1640 nm, and 2130 nm, and releases them as surface reflectance products at spatial resolutions of 250 m and 500 m (Vermote et al., 2002). The wide availability of MODIS products and also the attractive spatial, spectral and temporal characteristics of MODIS data have

increased their use worldwide. It is important, therefore, to know how accurate they are. The MODIS Surface-Reflectance Product (MOD09) product has been produced daily and on a global scale since shortly after the launch of Terra-MODIS (December 1999) and Aqua-MODIS (May 2002). The MOD09 is the main input to other MODIS products such as BRDF/Albedo, land cover and evapotranspiration products. It may also be directly applied by scientists from a variety of disciplines, for example, such as phenology (de Beurs and Henebry, 2010), geology (Ballantine et al., 2005) and hydrology (Jia et al., 2009). Again it is, therefore, important to validate the MOD09 product.

The MODIS albedo product's accuracy depends mainly on the input MOD09, the number and distribution of observations and the applied BRDF model. This gives rise to a need for an accurate surface reflectance product whose error should not exceed 0.05, assuming no uncertainty about other factors affecting albedo. Thus, validation of the MOD09 product is essential for BRDF and albedo studies as well as other applications of remote sensing data.

Pre-launch and post-launch validation of the product shows a high accuracy of the MODIS atmospheric correction algorithm, within 0.05 of absolute reflectance values (Vermote and Kotchenova, 2008, Vermote et al., 1997a). Most of the post-launch validation operation is based on analysing one-year, 2003, of AERONET data which includes different view and Sun geometries (Vermote and Kotchenova, 2008). However, these validation efforts were mainly based on a small number of field measurements (using about 150 AERONET sites across the world) with limited geographical extent (Figure 4-1). There is a need for more validation efforts due to the variability of atmospheric conditions and the diversity of land covers across the globe.

The HDRF varies greatly according to parameters such as space, time and view-Sun geometry. Extensive point ground measurements are needed to provide a representative estimate of the relatively large area of a MODIS pixel. Such an extensive coverage would be very expensive and impractical from a logistic point-of-view, especially in spatially heterogeneous areas. Fine spatial resolution remotely sensed data, however, are a suitable intermediary that can be validated using ground measurements; they are also suitable for the validation of coarser spatial resolution data. In this research, fine spatial and spectral resolution airborne (EA-CASI) and Satellite (SPOT) data were used to validate the MODIS reflectance product. Matching the view-Sun geometry of the three data sets, MODIS, EA-CASI and SPOT, was carried out, as well as spatial and spectral upscaling of fine spatial resolution data to the MODIS resolution.

Figure 4-1 Spatial distribution of the AERONET sites used in the validation of the MOD09 product. The colour shows the degree of acceptability of the validation results in band 1 of MODIS (green>80% and red <55%) and the circle size shows the number of the used observations (Vermote and Kotchenova, 2008).

4.2 The MODIS Surface-Reflectance Product

Terra and Aqua are two satellites that carry the MODIS and other instruments. They provide information twice a day for any area. MODIS has 36 spectral bands (ranging from 0.4 to 14.5 μm), a spatial resolution from 250 m to 1000 m, a wide coverage (viewing swath width of 2,330 km) and 16 bit radiometric resolution.

MODIS data are produced at different "levels" of processing: Level 0 (L0) represents the raw data, Level 1 (L1) is the radiometrically-corrected data, Level 2 (L2) is the L1 data atmospherically corrected, Level 2G (L2G) is the gridded L2 data, Level 2G-Lite (L2GL) provides a minimal level of compositing of daily L2G data, Level 3 (L3) is the L2 data projected and composited, and Level 4 data includes additional processing. The data are reprocessed to take into account new refinements in all levels of processing and are called collections. The latest collection is collection 5.

The MODIS Surface-Reflectance Product removes atmospheric effects, such as gases, aerosols and thin clouds, from the at-sensor signals so as to reproduce the target at the Earth's surface with no intervening atmosphere (Vermote and Kotchenova, 2008). MODIS calibrated radiances at bands 1, 2, 3, 4, 5, 6, and 7, centred at 648 nm, 858

nm, 470 nm, 555 nm, 1240 nm, 1640 nm, and 2130 nm, respectively, are those which are corrected for the influence of the atmosphere (Vermote et al., 2002).

Vermote et al. (2011) describe the format of the surface reflectance products. The atmospherically-corrected data are released in different levels of processing as: L2 (MOD09), L2G (MOD09GHK, MOD09GQK, and MOD09GST), L2GL (MOD09GA and MOD09GQ), L3, the 8-day composite product (MOD09A1 and MOD09Q1) and daily L3 CMG (climate modelling grid) (MOD09CMG and MOD09CMA). The collection version of MOD09GHK, MOD09GQK, and MOD09GST are produced up to collection 4 while others are available in the latest collection, collection 5.

MOD09 includes the derived surface reflectance in all reflective MODIS bands (bands 1-16, and 26) at the spatial resolutions of 250 m, 500 m and 1 km. It also includes information about aerosol optical thickness (AOT), water vapour and path radiance, temperature data, geographical coordinates, and finally information about the quality of atmospheric correction in each band and the state of each pixel regarding cloud, aerosol, snow and fire features. MOD09GQ and MOD09GA are the composite daily surface reflectance of L2G data. MOD09GQ includes the 250 m surface reflectance in bands 1 and 2 and band quality information. MOD09GA provides the surface reflectance in the first seven MODIS bands at a 500 m spatial resolution as well as solar-sensor geometry information, reflectance band quality and the state of each 1 km pixel. The 250 m MOD09Q1 and 500 m MOD09A1 products contain the best possible MOD09GQ and MOD09GA data, respectively, during each 8-day period which has a high observational coverage, low view angle, and a clear sky (no cloud and no aerosol). MOD09CMG provides 0.05° surface reflectance in the bands 1 to 7, view-Sun geometry, ozone, brightness temperatures, path radiance, and quality information. The 250 m MOD09GQK and 500 m MOD09GHK provide the best observations during each 24-hour period. Collection 4 of MOD09Q1 and MOD09A1 are the same as their collection 5 equivalent but provide the 8-day composite of MOD09GQK and MOD09GHK.

Surface reflectance is computed using top-of-atmosphere (TOA) reflectance look-up tables and atmospheric parameters (Vermote et al., 1997a). It was initially computed under the Lambertian assumption of the Earth's surface using inversion of the following equation.

$$\rho_{toa}\left(\theta_i, \theta_r, \varphi, P, \overbrace{\tau_A, \omega_0, P_A}^{Aer}, U_{H_2O}, U_{O_3}\right) =$$

$$Tg_{OG}(m, P)Tg_{O_3}(m, U_{O_3})\left[\rho_{atm}(\theta_i, \theta_r, \varphi, P, Aer, U_{H_2O}) +\right.$$

$$Tr_{atm}(\theta_i, \theta_r, \varphi, P, Aer)\frac{\rho_s}{1-S_{atm}(P,Aer)\rho_s}Tg_{H_2O(m,U_{H_2O})}\Big] \quad \textbf{Equation 4-1}$$

Where ρ_{toa} is the TOA surface reflectance, ρ_{atm} is the atmosphere intrinsic reflectance, Tr_{atm} is the total atmosphere transmission, ρ_s is the surface reflectance, S_{atm} is the atmosphere spherical albedo, P is the atmospheric pressure, and Tg_{H_2O}, Tg_{O_3} and Tg_{OG} are the gaseous transmission by water vapour, ozone and other gases, respectively, U_{H_2O} is the integrated water vapour content, U_{O_3} is the integrated ozone content, m is the air mass computed as $1/\cos(\theta_i)+ 1/\cos(\theta_r)$, the parameters describing aerosol properties are τ_A, ω_0, and P_A which are called the aerosol optical thickness, aerosol single-scattering albedo, and aerosol phase function, respectively.

The retrieved surface reflectance was valid only for cloud-free and partially cloudy data (Vermote et al., 1997a). There was, however, no definition of the term 'partially cloudy' which could be, for example, pixels mixed with clouds or cloud-free pixels adjacent to clouds.

The anisotropy of the Earth's surface is then corrected using the ratio between BRDF coupled with the atmosphere and surface-BRDF (Vermote and Vermeulen, 1999). The input surface BRDF can either be obtained from the algorithm used in the MODIS FPAR/LAI algorithm which is based on the relationship between BRDF and land cover stored in LUTs, or from the linear kernel BRDF model applied in the MODIS BRDF/Albedo product.

Neighbouring pixels may have an effect on the reflected sunlight from each pixel (adjacency effect). The adjacency effect is considered up to a distance of 10 pixels around the viewed pixel in MODIS data. The correction algorithm originates from the work by Tanre et al. (1981) and uses the point spread function (PSF) developed for Landsat data (Vermote and Vermeulen, 1999, Ouaidrari and Vermote, 1999).

The inputs to Equation 3-6 are obtained from other MODIS products or climate models. The atmospheric parameters used include aerosol characteristics such as AOT, single scattering albedo (SSA) and particle size distribution, atmospheric pressure, and ozone and water vapour amount (Vermote and Saleous, 2002). Aerosol characteristics and water vapour amount are usually determined using MODIS bands while ozone and atmospheric pressure are obtained from non-remote sensing data.

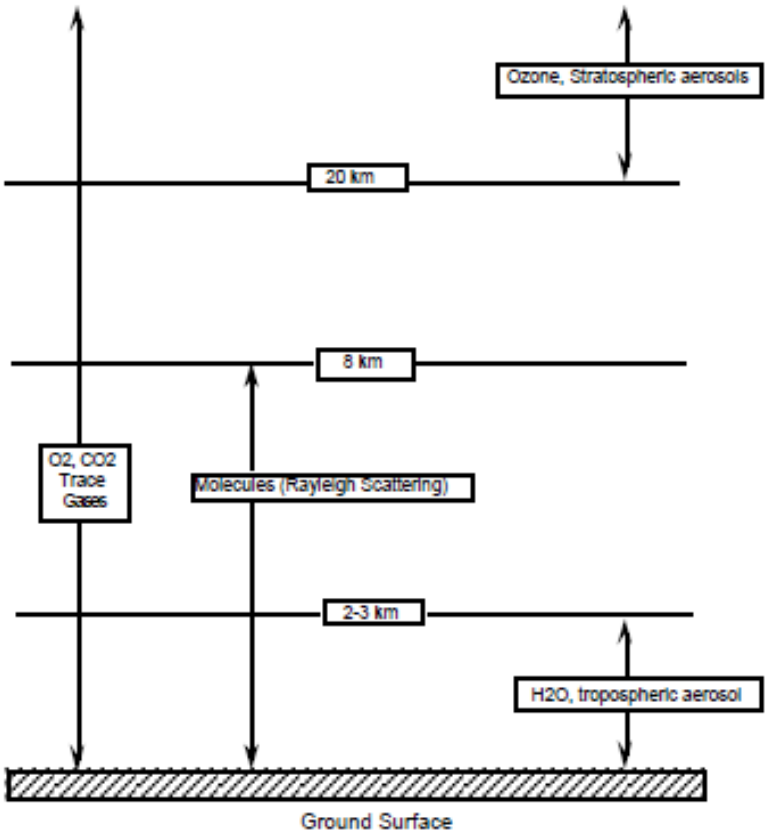

Figure 4-2 The atmospheric components affecting the remote sensing signal in the 0.4 – 2.5 µm range (Vermote et al., 1997a)

Vermote et al. (1997a) and Vermote and Vermeulen (1999) illustrated the effect of atmospheric parameters on the at-sensor signal for Thematic Mapper (TM) and Advanced Very High Resolution Radiometer (AVHRR) sensors (Figures 4-2 and 4-3).

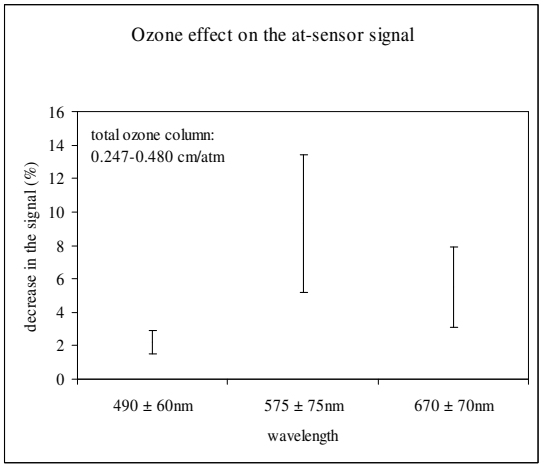

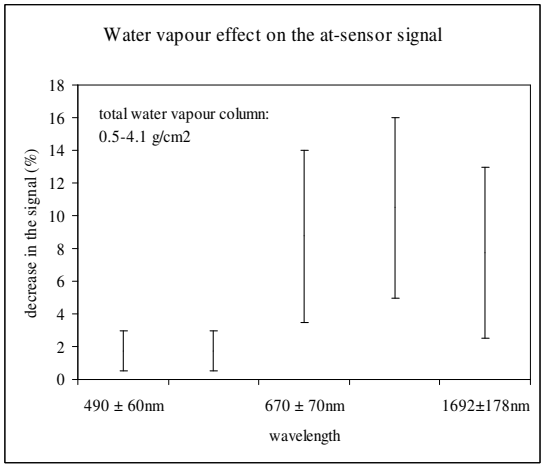

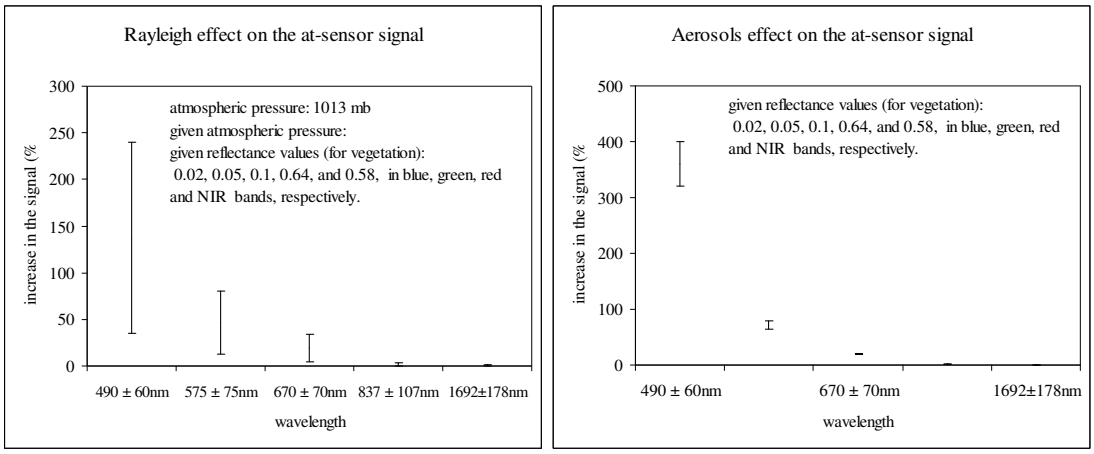

Figure 4-3 Atmospheric effects on the at-sensor signal in the visible and NIR bands (each bar shows the minimum and maximum effect) (values from Vermote et al., 1997a).

Rayleigh scattering is defined as the physical phenomenon of the scattering of light by particles which have a much smaller size than the wavelength of the incident light (Sneep and Ubachs, 2005). It depends on the wavelength, air pressure and temperature profiles (Vermote and Vermeulen, 1999). The radiative transfer code can quantify the Rayleigh effect using the pre-defined values of air pressure and air temperatures of different climates (Vermote and Vermeulen, 1999). The Rayleigh effect has an increasing role on the at-sensor signal with shorter wavelengths (Figure 4-3).

Aerosols are solid or liquid airborne particles with sizes between 0.1 μm to 10 μm which originate either from natural sources (about 90%) such as dust storms or anthropogenic activity (about 10%) (Williamson, S. J. cited in Diner et al., 2008a). They have an increasing role on the at-sensor signal with wavelength, with the maximum effect on the blue band (Figure 4-3). Aerosol characteristics are mapped using an internal aerosol algorithm. The algorithm is based on the dark and dense vegetation (DDV) method which uses an empirical relationship between the visible (centred at 469 nm and 645 nm) and infrared (centred at 2130 nm) bands to predict the surface reflectance in the visible bands. The TOA reflectance is then computed using the estimated surface reflectance in the visible bands for a variety of optical thickness values. The AOT is then computed using a linear interpolation between the actual and the estimated TOA reflectance at a 1 km spatial resolution. Aerosol type is obtained using MODIS bands centred at 490 nm, 443 nm, 412 nm, and 2130 nm and from a set of pre-assigned aerosol models which are based on smoke concentration (Vermote and Kotchenova, 2008).

The water vapour map is retrieved at a 1 km spatial resolution using the two band ratio technique and near infrared (NIR) MODIS bands centred at 936 nm and 940 nm (Vermote and Kotchenova, 2008). It has a decreasing role on the at-sensor signal with wavelength, with the maximum effect on the NIR bands. However, the effect of water vapour on the MODIS bands is small since the bands do not overlap with the water vapour absorption bands (Vermote and Vermeulen, 1999). Only MODIS bands at 645±25 nm (band 1), 858±17 nm (band 2) and 2130±25 nm (band 7) are slightly affected (Figure 4-3).

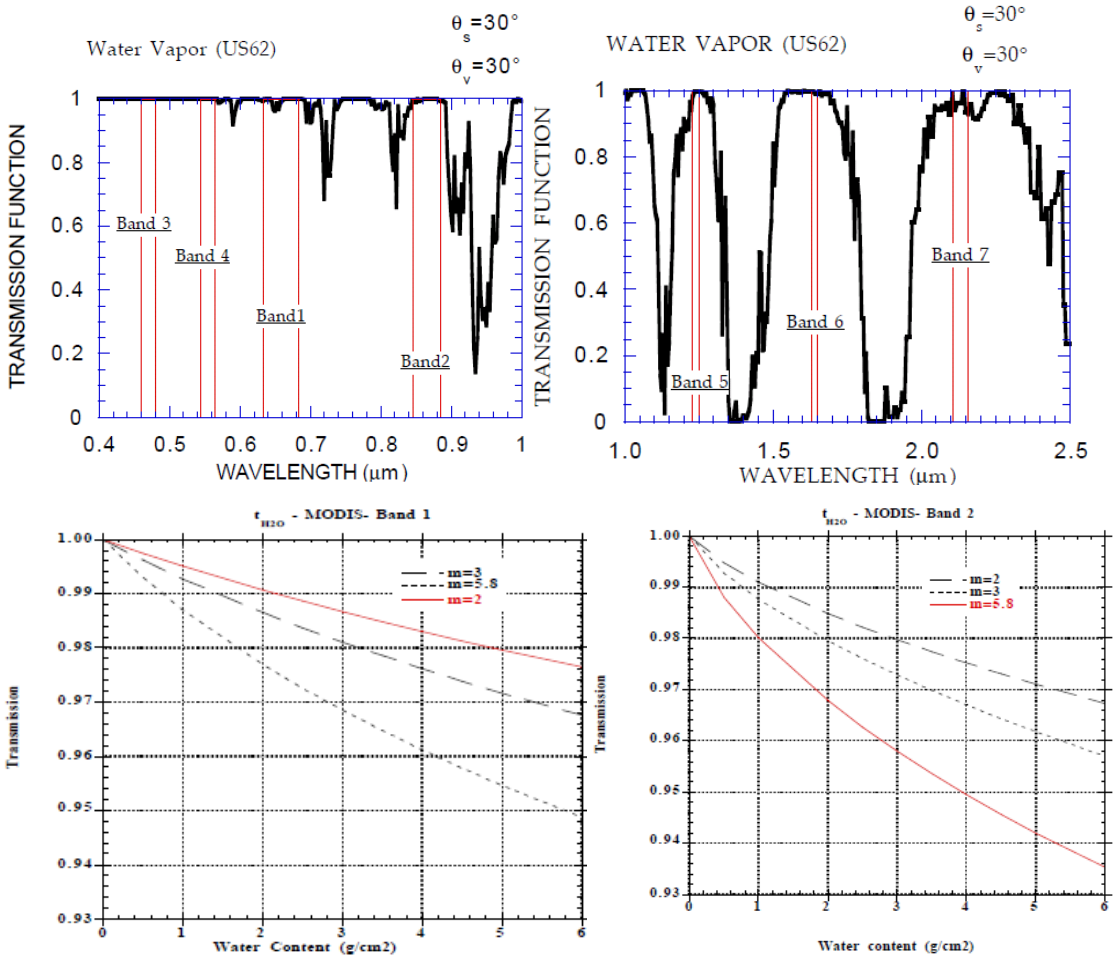

Figure 4-4 Water vapour absorption in the MODIS bands 1 to 7 and the amount of absorption for a set of air masses (m) in bands 1, 2 and 7 (Vermote and Vermeulen, 1999) .

Atmospheric pressure (at 1 km resolution) and ozone concentration (at 1° resolution) are obtained using a numerical weather prediction (NWP) model (and a DEM model) and measurements by an ultra violet (UV) ozone sounder, respectively (Vermote and Kotchenova, 2008). Ozone decreases the at-sensor signal only in the visible bands and has no effect on the NIR bands (Figure 4-3). MODIS bands at 645±25 nm (band 1) and 555±10 nm (band 4) are affected by ozone (Figure 4-5).

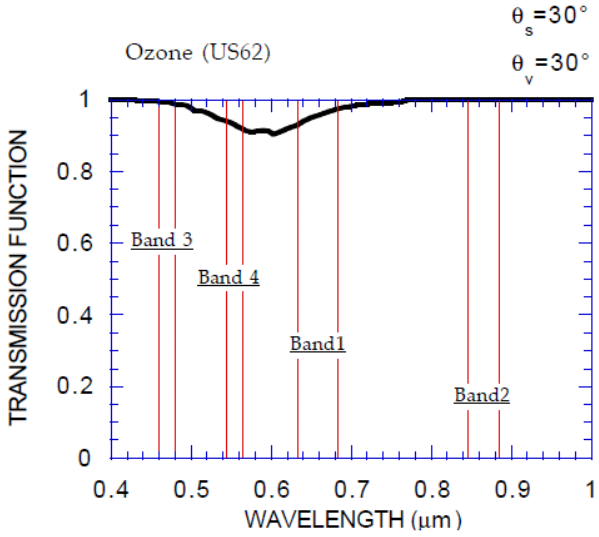

Figure 4-5 Ozone absorbtion in the MODIS bands (Vermote and Vermeulen, 1999).

Gases other than water and ozone transmit sunlight as a function of air mass, *m*, and pressure, *P* (in atm). Figure 4-6 shows how O_2 and CO_2 gases absorb the sunlight in the MODIS bands.

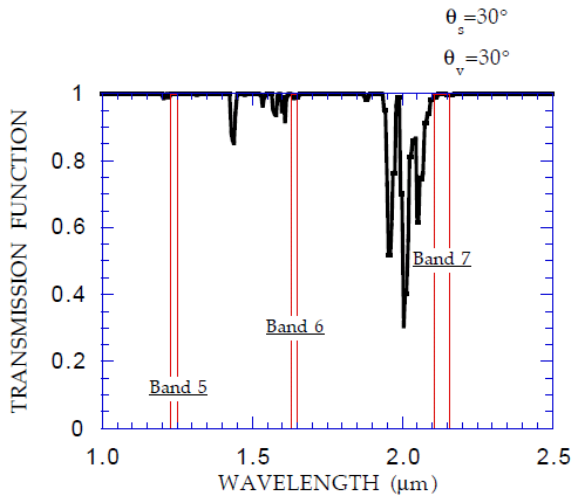

Figure 4-6 Absorptional effect of other gases (O_2 and CO_2) in the MODIS bands (Vermote and Vermeulen, 1999).

The radiative transfer (RT) model used for atmospheric correction of MODIS data is Second Simulation of a Satellite Signal in the Solar Spectrum Vector (6SV) (Kotchenova et al., 2006). The 6SV stems from the scalar version of 6S code which is the higher version of 5S (Simulation of a Satellite Signal in the Solar Spectrum) code developed by Laboratoire d'Optique Atmosphérique (Vermote et al., 1997b). It produces an accurate atmospheric model accounting for the BRDF effect, topography and gaseous absorption. The algorithm uses the LUTs of the path radiance, the diffuse transmittance, BRDF coupling terms and the atmosphere spherical albedo (Vermote and Vermeulen, 1999). Using the LUTs, there is no need to run the code for every pixel which is expensive (Vermote and Vermeulen, 1999). It takes into account the radiation polarization, does an accurate estimate of the highly asymmetric aerosol scattering phase function by varying the number of scattering angles up to 1000, includes an arbitrary variation of the vertical aerosol profile by up to 50 layers, in the height range from 0 to 100 km, can change the number of calculation angles and layers and considers the increase in the number of node wavelengths from 10 to 20 (Kotchenova et al., 2006). It has been extensively validated and its accuracy is claimed to be within 1% (Muldashev et al. as cited in Vermote et al., 2008)

Cirrus correction relies on observations at 1.38 microns which are completely absorbed by water vapour in the lowest 6 km of the atmosphere. Therefore, observed reflectance is assumed to be from high-level clouds (Gao and Kaufman, 1993). The

algorithm assumes that reflectance from cirrus clouds does not vary spectrally and spatially and uses predefined threshold flags to label a pixel with or without cirrus contamination.

The accuracy of the MODIS atmospheric correction algorithm relies on the accuracy of the input atmospheric parameters and the radiative transfer model as well as sensor calibration and BRDF correction (Vermote and Kotchenova, 2008). The MODIS team claim accuracies for atmospheric parameters of 0.01 for AOT, 10 mbar for atmospheric pressure, ±0.02 cm.atm for ozone and 5-10% for column-integrated water vapour content (Vermote and Kotchenova, 2008, Vermote and Saleous, 2002). The pre-computed TOA reflectance is generated by the 6SV radiative transfer model with a claimed accuracy within 1% (Kotchenova and Vermote, 2007, Kotchenova et al., 2006). As the requirements change and the algorithms are modified, the MOD09 data are updated applying the latest collection which is now collection 5. Collection 5 is provided at different spatial resolutions of 250 m (bands 1 and 2), 500 m, 1 km and 0.05° (bands 1 to 7) and uses the latest modified LUT.

The quality of the surface reflectance products is usually assessed using quality assurance (QA) data. Surface reflectance band quality data provide the quality of atmospheric correction in each band at 250 m, 500 m, and 1 km resolutions. The QA information about the state of each MODIS pixel at the 1 km resolution includes information about cloud state, aerosol amount and cirrus existence (Vermote et al., 2011).

Table 4-1 Quality information included in MOD09 (Vermote et al., 2011)

500 km reflectance band quality		1 km reflectance data State QA	
Bits	Description	Bits	Description
0-1	MODLAND QA bits; corrected product produced at 00 – ideal quality all bands 01- less than ideal quality some or all bands corrected product not produced due to 10 – cloud effects all bands 11 – other reasons some or all bands may be fill value	0-1	Cloud state; 00 – clear 01 – cloudy 10 – mixed 11 – not set, assumed clear

	[Note that a value of (11) overrides a value of (01)]		
2-5	Band 1 data quality four bit range; 0000 – highest quality 0111- noisy dector 1000 – dead detector; data interpolated in L1B 1001 – solar zenith >= 86° 1010 – solar zenith >= 85 and < 86° 1011 – missing point 1100 – internal constant used in place of climatological data for at least one atmospheric constant 1101 – correction out of bounds, pixel constrined to extreme allowable value 1110 – L1B data faulty 1111 – not processed due to deep ocean or clouds	2	Cloud shadow; 1 – yes 0 – no
6-9	Band 2 data quality four bit range; Same As Above	3-5	Land/water flag; 000 – shallow ocean 001 – land 010 – ocean coastlines and lake shorelines 011 – shallow inland water 100 – ephemeral water 101 – deep inland water 110 – continental/moderate ocean 111 – deep ocean
10-13	Band 3 data quality four bit range; Same As Above	6-7	Aerosol quantity; 00 – climatology 01 – low 10 – average 11 – high
14-17	Band 4 data quality four bit range; Same As Above	8-9	Cirrus detected; 00 – none 01 – small 10 – average

			11 – high
18–21	Band 5 data quality four bit range; Same As Above	10	Internal cloud algorithm flag; 1 – cloud 0 – no cloud
22–25	Band 6 data quality four bit range; Same As Above	11	Internal fire algorithm flag; 1 – fire 0 – no fire
26–29	Band 7 data quality four bit range; Same As Above	12	MOD35 snow/ice flag; 1 – yes 0 – no
30	Atmospheric correction performed; 1 – yes 0 – no	13	Pixel is adjacent to cloud; 1 – yes 0 – no
31	Adjacency correction performed; 1 – yes 0 – no	14	BRDF correction performed; 1 – yes 0 – no
		15	Internal snow mask; 1 – snow 0 – no snow

Vermote and Vermeulen (1999) described several uncertainties in the MOD09 products, such as absolute calibration, input parameters such as aerosol optical thickness, look-up table interpolation, adjacency effect, cirrus effect, Lambertian approximation error, and the aerosol model. The recent improvements in the aerosol retrieval algorithm and the radiative transfer model have increased the reliability of the product in all reflective bands except band 3 (470 nm) which is used for aerosol inversion (Vermote and Kotchenova, 2008).

4.3 Methodology

In this study, an assessment of the MODIS reflectance product as required for BRDF/Albedo studies is described. EA-CASI and SPOT provided the reference remote sensing data and meteorology and land cover data provided the ancillary data. They were used to assess the accuracy of the MODIS data. The validation was carried out in several ways. The off-nadir MODIS data were validated using the at-nadir reference data. The at-nadir MODIS data were obtained from a BRDF model and were then validated. An assessment of the MODIS BRDF model was then carried out. The MODIS BRDF/Albedo algorithm assumes that the variability of the reflectance with time (during 16 sequential days) is ignorable. The assumption of the temporal invariability of reflectance was assessed by comparing the data for two different days.

The MODIS BRDF model uses only “high quality” (clear sky) observation data. Finding MOD09 data with high quality during the 16-day period was therefore a necessary step. The number of high quality observations as well as the distribution of the view-Sun geometry can affect the accuracy of the retrieved BRDF model. The QA MODIS data, for DOYs 152 to 168, were used to check the reliability of the observations. The distribution of the view-Sun geometry was also checked.

Some similar studies have been done before such as that by Liang et al. (2002). This study, however, had the advantage of using finer spatial resolution data with an accurate atmospheric correction which were more comparable with ground measurements. Also, BRDF values were obtained using the daily MODIS albedo product rather than the operational 16 day MODIS albedo product, which increases the comparability of the data. Furthermore, two reference data sets from two different days were used to validate the MOD09 and the MODIS BRDF model.

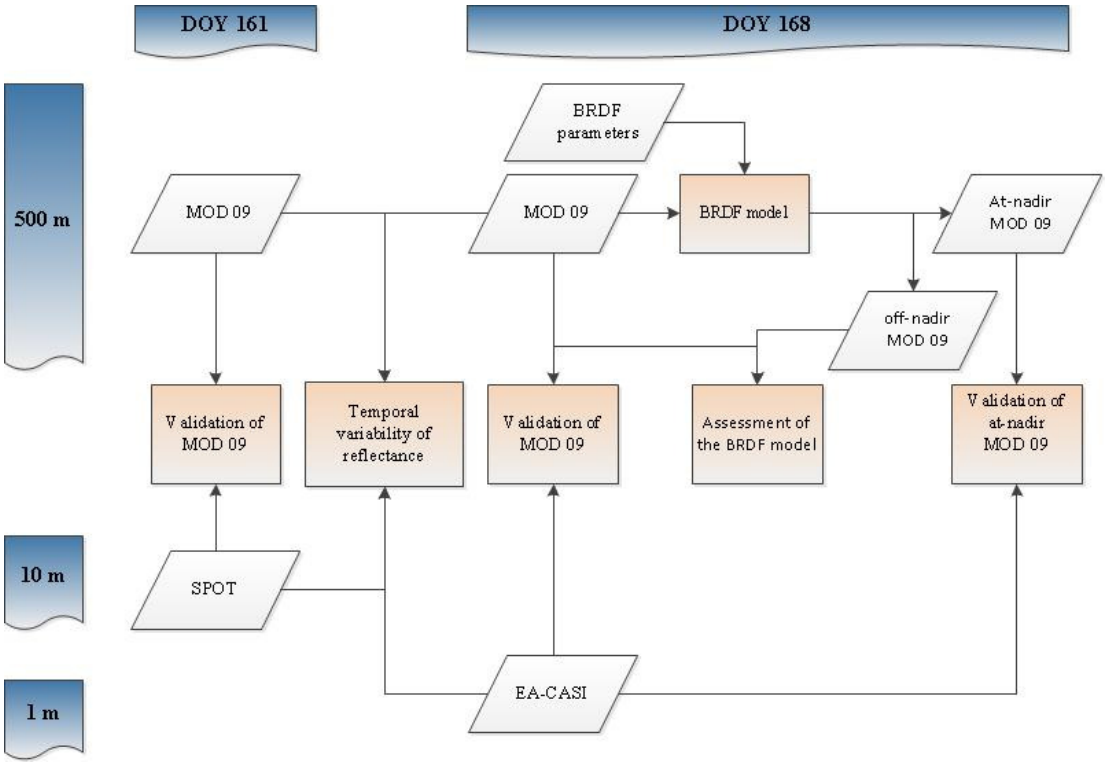

Figure 4-7 Flowchart of the methodology used for validation of MOD09

4.4 Validation of MODIS reflectance

The MODIS reflectance images on DOYs 151 to 168 were downloaded and the view and Sun geometries on the different days were obtained from the data. The data were then assessed, mainly for the appearance of clouds, using the QA flag of the MODIS data as well as the ground measurements. The MODIS reflectance images on DOYs 161 and 168 were selected as these were assessed as being cloud-free and having two available reference images, EA-CASI and SPOT, on those days.

4.4.1 Validation using EA-CASI reflectance

The EA-CASI data on DOY 168 of 2006 were the main source of reference data used for the validation of the MOD09 image on DOY 168. The EA-CASI data were already corrected for atmospheric effects using a radiative transfer model (MODTRAN 4) and validated using ground measurements. The MODIS Reprojection Tool (MRT) was used to subset the MODIS data in HDF format to the EA-CASI area and to reproject the MODIS data to the United Kingdom projection and Ordnance Survey 1936 datum (UKOS36). The equivalent EA-CASI data with MODIS bands 1 to 4 (centred at 645 nm, 858 nm, 469 nm and 555 nm) were chosen and averaged up using a Gaussian function and full width at half maximum (FWHM) model. The EA-CASI data were then upscaled to 500 m spatial resolution using an average function. The MODIS and EA-CASI data were plotted against each other and the correlation coefficient calculated. The results of the validation of MOD 09GA on DOY 168 are seen in Figure 4-8.

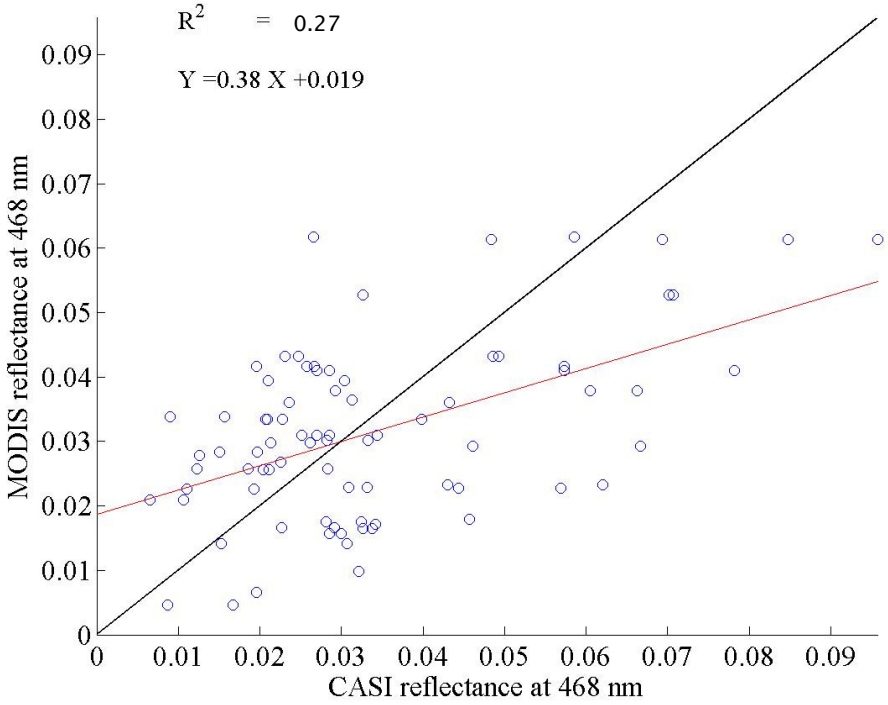
R2 = 0.27
Y =0.38 X +0.019
MODIS reflectance at 468 nm
CASI reflectance at 468 nm
0
0.01
0.02
0.03
0.04
0.05
0.06
0.07
0.08
0.09

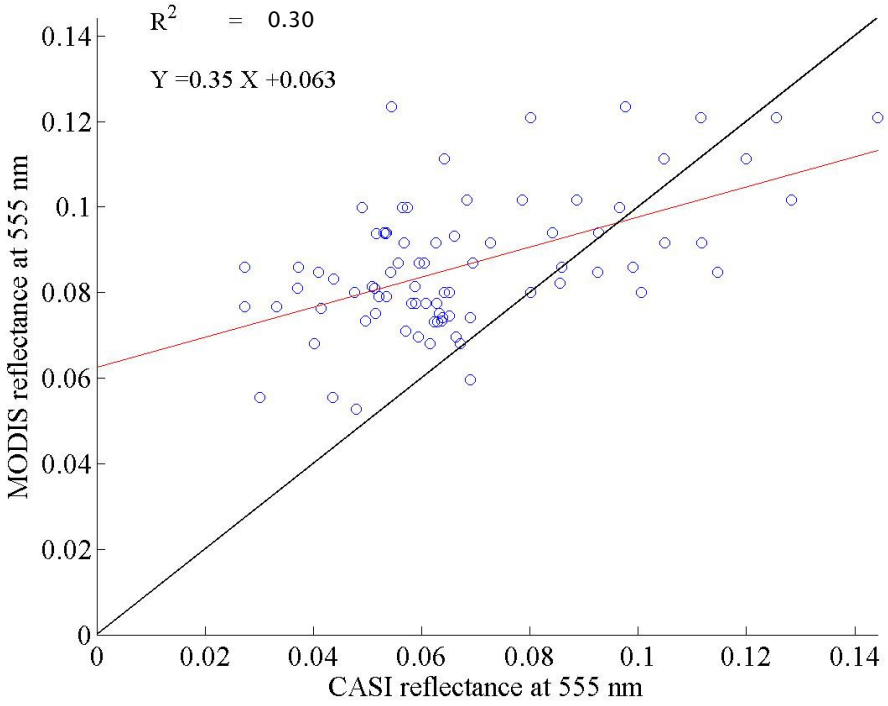
R2 = 0.30
Y =0.35 X +0.063
MODIS reflectance at 555 nm
CASI reflectance at 555 nm
0
0.02
0.04
0.06
0.08
0.1
0.12
0.14

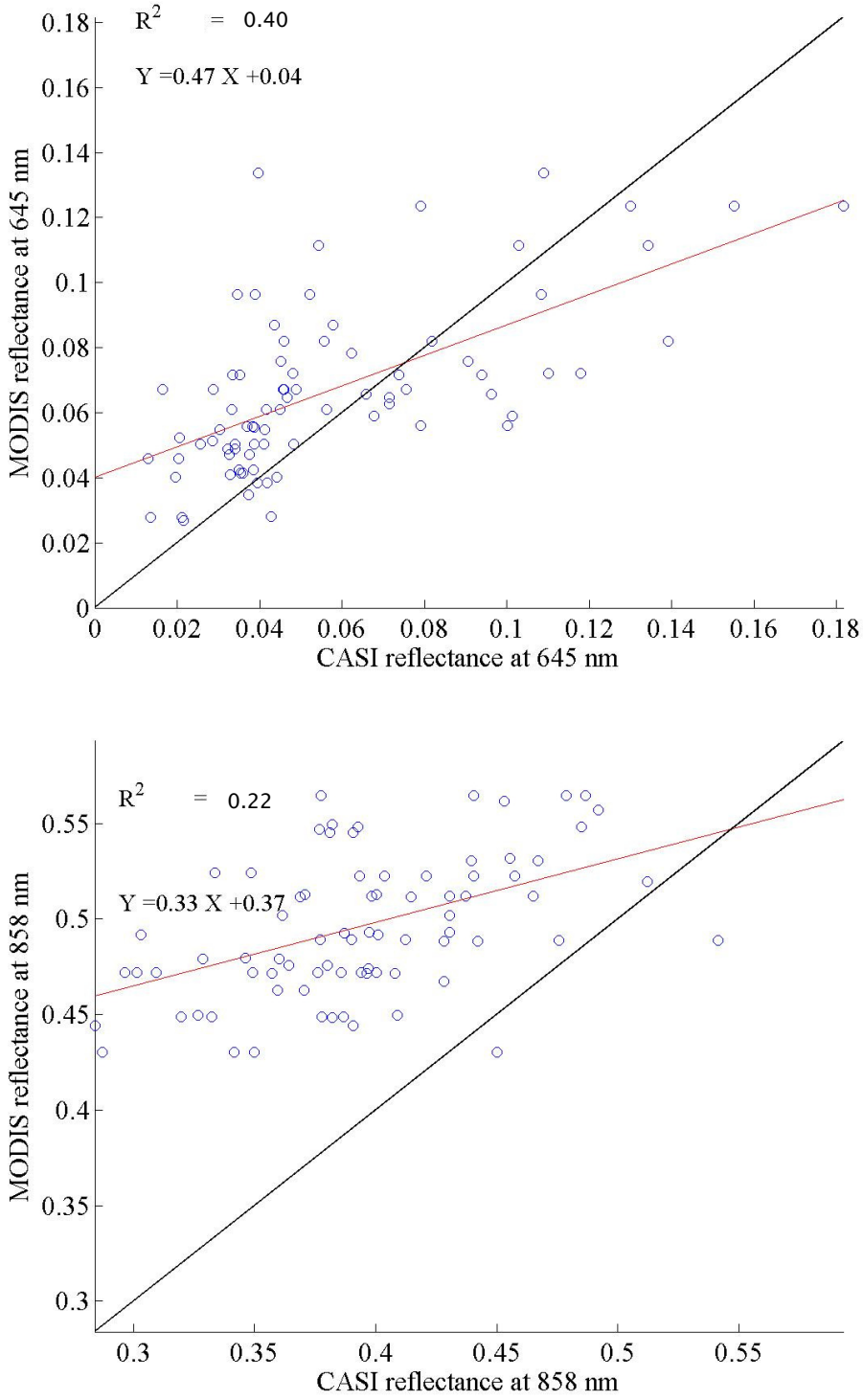

Figure 4-8 Scatterplots of at-nadir EA-CASI reflectance on DOY 168 against off-nadir MODIS reflectance on DOY 168 with view zenith angle (vza) =46°.

The absolute accuracy of the MODIS product was low. In the visible bands, the MODIS product underestimated the reflectance for brighter surfaces and overestimated the reflectance for darker surfaces. In the blue band, there was an overestimation of

reflectance in pixels with ρ<0.03 and an underestimation of reflectance in pixels with ρ>=0.03. In the Green band, there was an overestimation of reflectance in pixels with ρ<0.1 and an underestimation of reflectance in pixels with ρ>=0.1. In the red band, there was an overestimation of reflectance in pixels with ρ<0.08 and an underestimation of reflectance in pixels with ρ>=0.08. In the NIR band, there was an overestimation of reflectance in all pixels with a reflectance less than 0.55. The trend shown for the pixels with ρ>0.6 was a general underestimation of reflectance.

The error in the MODIS reflectance was also derived for each pixel in the first four bands of the MODIS data (Table 4-2). A linear sequence representing all the MODIS image pixels is given in Figure 4-9 and Figure 4-10.

Table 4-2 Error in the MODIS reflectance (percentage) on DOY 168

blue band						green band					
row\column	C1	C2	C3	C4	C5	row\column	C1	C2	C3	C4	C5
R1	-69	-73	-47	97	219	R1	-13	27	84	131	181
R2	-66	-8	17	105	109	R2	10	70	58	118	90
R3	-37	-54	19	89	44	R3	24	11	68	106	56
R4	-49	-43	-27	21	25	R4	16	15	48	52	48
R5	-51	-48	-9	38	120	R5	17	17	19	46	84
R6	-50	-45	7	17	53	R6	2	5	23	41	62
R7	-26	23	15	-9	-17	R7	16	27	33	25	26
R8	-31	9	-10	88	30	R8	7	32	23	81	76
R9	-46	14	40	56	-27	R9	14	39	60	74	3
R10	-60	-12	87	113	62	R10	-13	1	75	104	77
R11	-49	-11	75	133	6	R11	0	12	77	126	26
R12	-61	-25	62	27	-36	R12	-4	6	73	51	-16
R13	-46	-37	-25	-12	-28	R13	0	-13	-7	8	-4
R14	-62	-43	30	115	277	R14	-21	-18	46	130	215
R15	-28	-48	52	60	47	R15	15	-21	49	46	56
R16	-56	-36	44	62	-16	R16	-26	-8	29	44	25
Red band						NIR band					
row\column	C1	C2	C3	C4	C5	row\column	C1	C2	C3	C4	C5
R1	-34	32	105	125	254	R1	9	25	31	50	57
R2	25	106	30	97	80	R2	17	50	45	45	33
R3	24	-9	22	81	33	R3	24	28	44	43	40
R4	21	17	15	25	45	R4	16	13	40	39	23

R5	10	-8	4	47	154	R5	18	24	29	25	27
R6	-7	-3	39	26	68	R6	1	15	14	39	23
R7	43	84	35	-10	-16	R7	3	-4	23	56	62
R8	51	46	8	100	51	R8	-10	26	50	33	46
R9	43	46	51	84	-11	R9	19	17	39	40	35
R10	-42	-24	103	178	148	R10	51	30	19	19	16
R11	-13	-3	114	237	23	R11	13	24	14	10	38
R12	-12	8	105	56	-32	R12	17	32	16	20	59
R13	0	-35	-17	-5	-20	R13	10	30	19	35	57
R14	-32	-39	50	133	306	R14	14	25	19	38	28
R15	0	-41	78	38	47	R15	17	29	19	22	26
R16	-44	-29	47	46	-11	R16	14	21	10	18	53

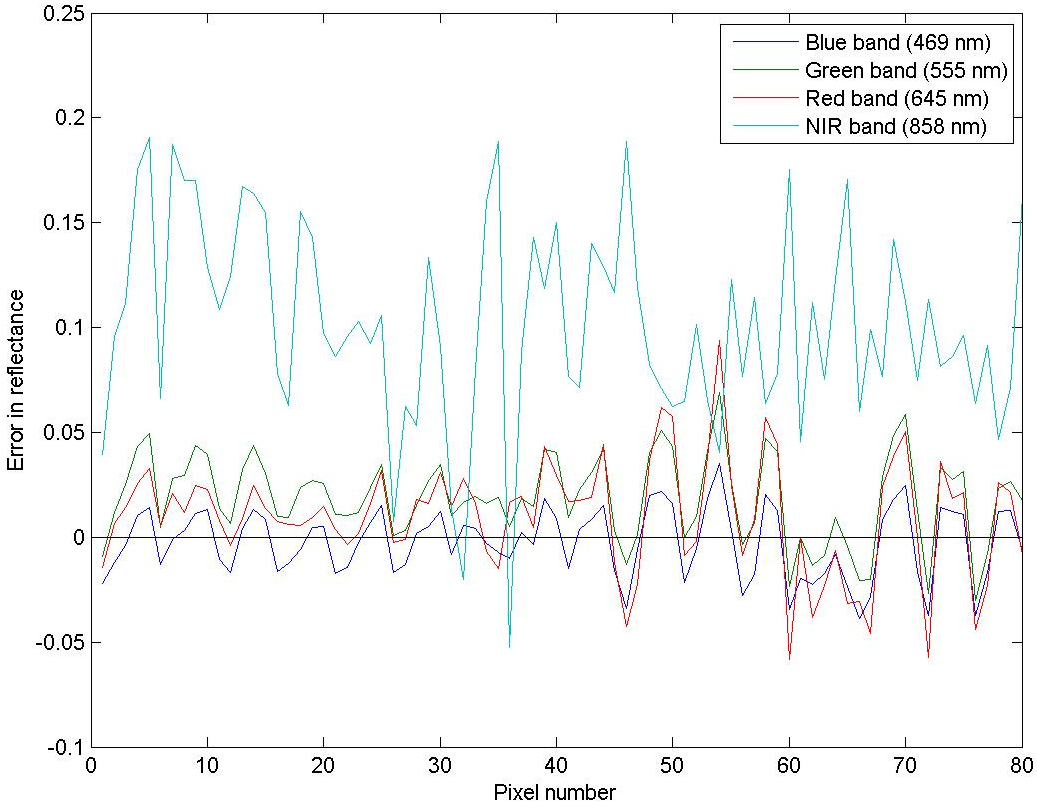

Figure 4-9 Spectral error in the MODIS reflectance (DOY 168).

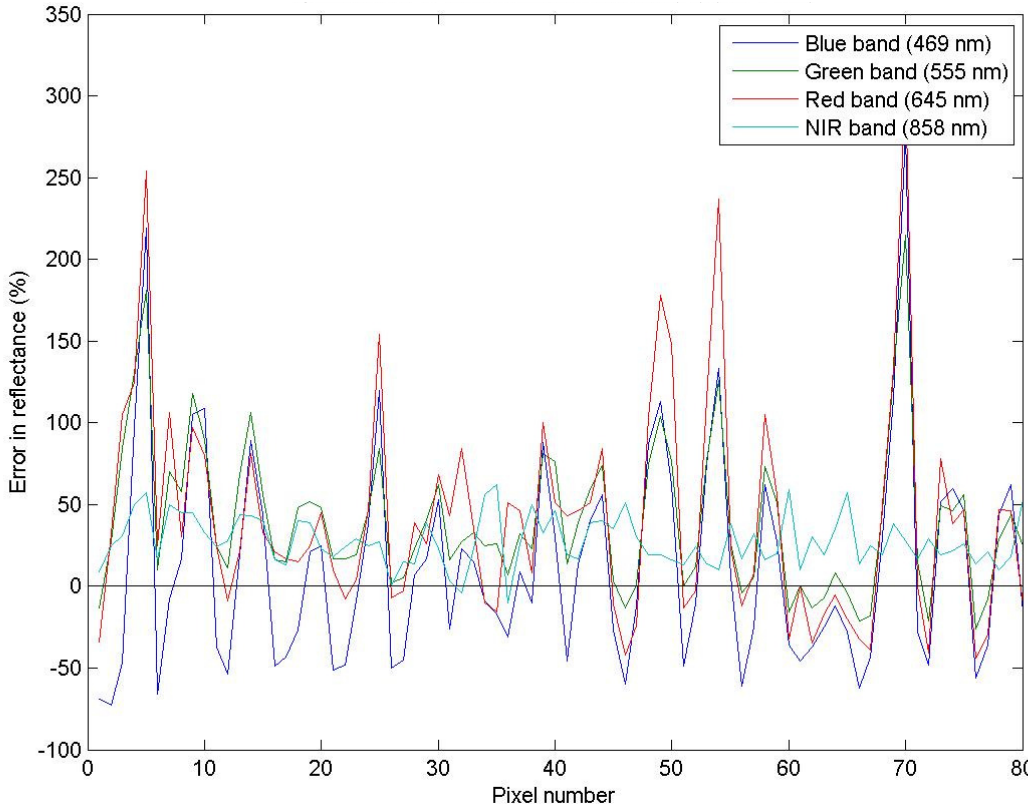

Figure 4-10 Percentage spectral error in the MODIS reflectance (DOY 168).

The errors in the atmospheric correction of the MODIS data in the green band (555 nm) can also be due to uncertainty in the estimation of ozone. In the NIR band, however, MODIS tended to overestimate the reflectance. Since the NIR band is the least affected band by atmospheric effects, an alternative explanation is required, such as uncertainty in the sensor calibration, which can also be the case for the visible bands. Another important source of uncertainty was the difference in the view geometry of the MODIS and EA-CASI data. This issue is considered later in this chapter. Other sources of uncertainties are described in the discussion section of this chapter.

4.4.2 Validation using EA-CASI reflectance in different land covers

The land cover survey undertaken simultaneously with the EA-CASI data provided valuable data for land cover mapping. A supervised classification method, the Spectral Angle Mapper (SAM) algorithm, was applied to the EA-CASI data to derive a land cover map (Figure 4-11). Non-vegetated pixels were classified using a vegetation index mask. Built-up areas and scrublands were classified using visual interpretation and the initial classified land cover from the SAM algorithm. Other classes were determined by the SAM method.

Using the fine spatial resolution land cover map obtained from the EA-CASI data, the reflectance error in the MODIS data was assessed by land cover class (Figure 4-12). Since a variety of land covers may exist at the MODIS spatial resolution, 500 m, then each pixel was labelled based on the largest land cover. As the area covered by the EA-CASI was small (2 km × 7 km), all the surveyed points for the area (107 points) were used to obtain the land cover map. The visual assessment of the obtained land cover map showed it was reliable for the purpose of this work. There were only some uncertainties about the mapped grasslands land cover in the south of the area.

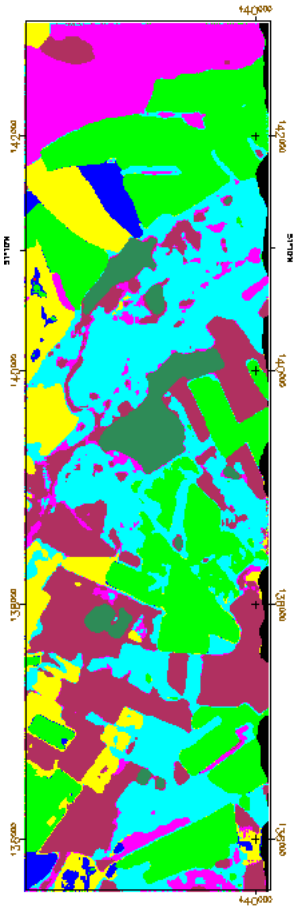

code	class	
LC1	Winter wheat or barley	
LC2	Winter oilseed rape	
LC3	Winter oat	
LC4	Grasslands	
LC5	Woodlands	
LC6	Stubbles	
LC7	Built-up area	

Figure 4-11 Land cover map obtained from the EA-CASI data.

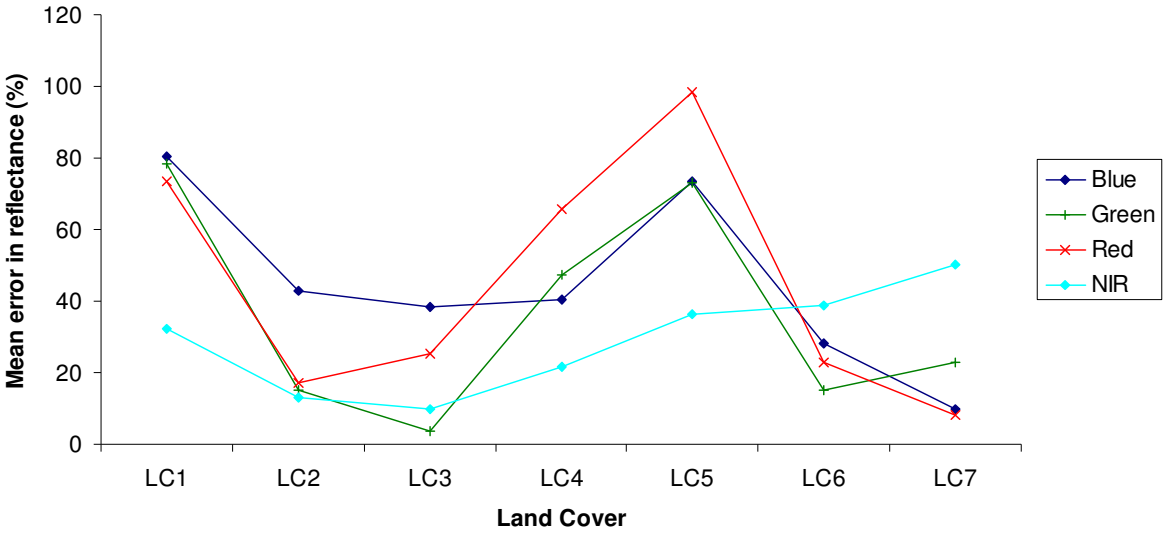

Figure 4-12 Mean percentage error in the MODIS reflectance product (DOY 168). LC1: Winter wheat or barley, LC2: Winter oilseed rape, LC3: Winter oats, LC4: Grasslands, LC5: Woodlands, LC6: Stubble, LC7: Built-up area.

The assessment of the errors in the MODIS reflectance in each land cover (Figure 4-12) showed that winter wheat and barley and woodlands had the maximum error. The reason may be due to higher heterogeneity inside these land covers. The MODIS atmospheric correction may be more suitable for homogeneous land covers due to the assumptions made.

4.4.3 Validation using SPOT reflectance

The existence of SPOT data on DOY 161 in 2006 provided a further opportunity to validate the MOD09 data on DOY 161. The SPOT data were already atmospherically corrected using the MODTRAN 4 model. The MODIS data with Sinusoidal map projection were reprojected to UKOS36 using MRT software and nearest neighbourhood resampling method. The SPOT data were upscaled to the MODIS spatial resolution using an average function. The results of the validation of MOD09GA on DOY 161 are seen in Figure 4-13. Figure 4-14 and Figure 4-15 show the error in the MODIS reflectance for all MODIS pixels, expressed on a line.

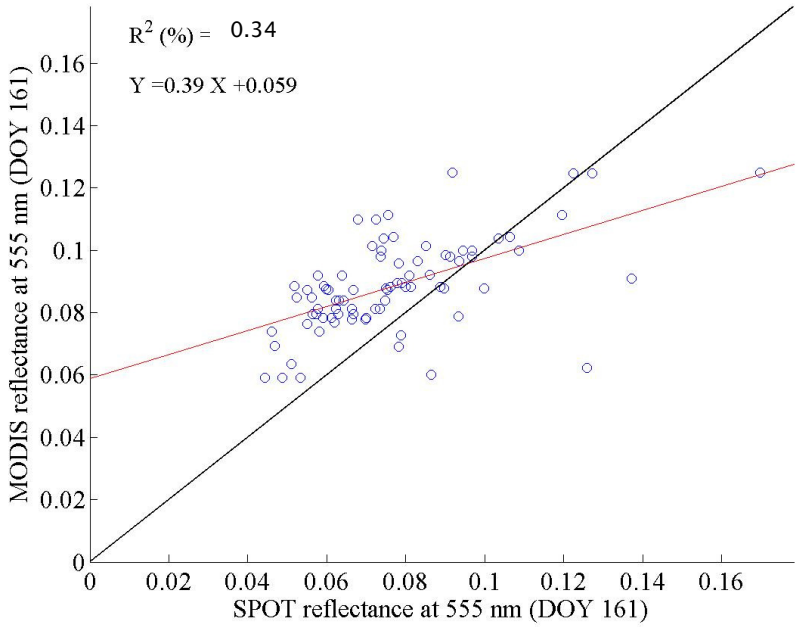
R2 (%) = 0.34
Y =0.39 X +0.059
MODIS reflectance at 555 nm (DOY 161)
SPOT reflectance at 555 nm (DOY 161)
0
0.02
0.04
0.06
0.08
0.1
0.12
0.14
0.16

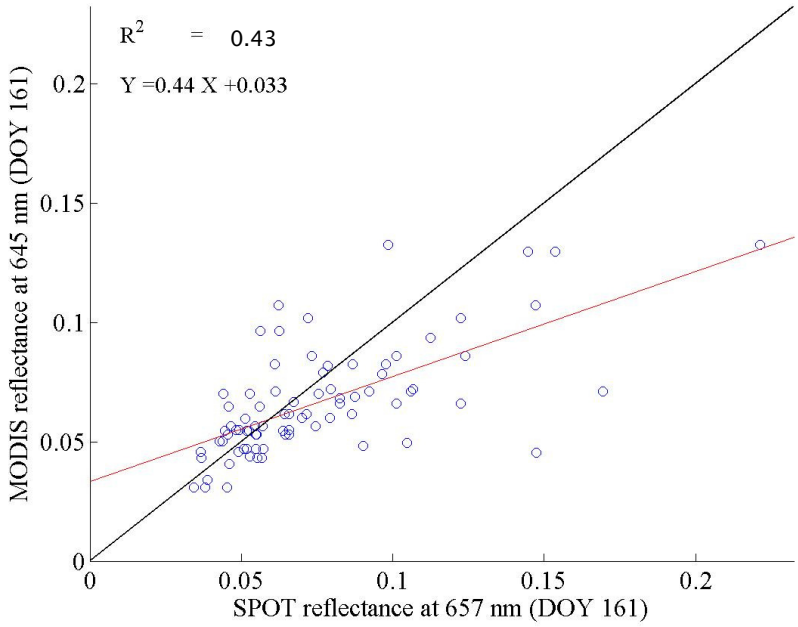
R2 = 0.43
Y =0.44 X +0.033
MODIS reflectance at 645 nm (DOY 161)
SPOT reflectance at 657 nm (DOY 161)
0
0.05
0.1
0.15
0.2

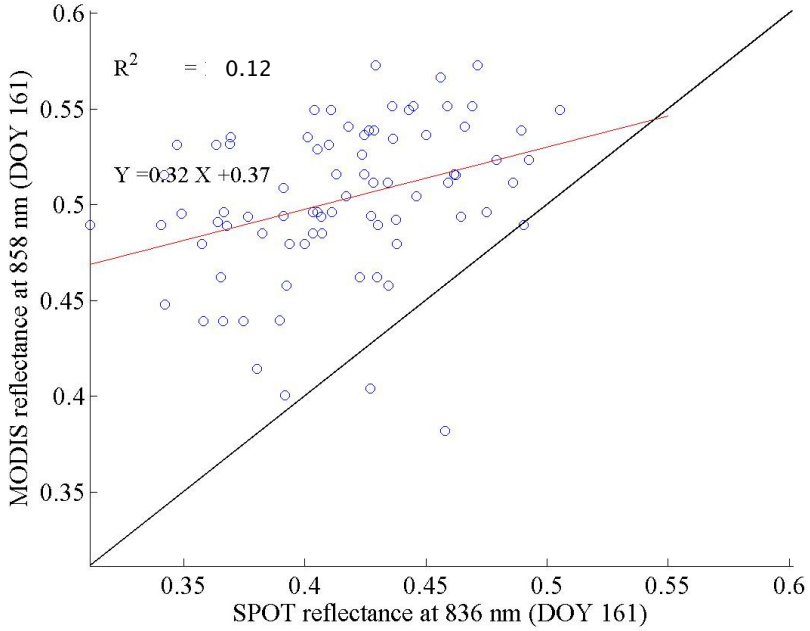

Figure 4-13 Scatterplots between at-nadir SPOT reflectance on DOY 161 and off-nadir MODIS reflectance on DOY 161 with view zenith angle (vza) =51°.

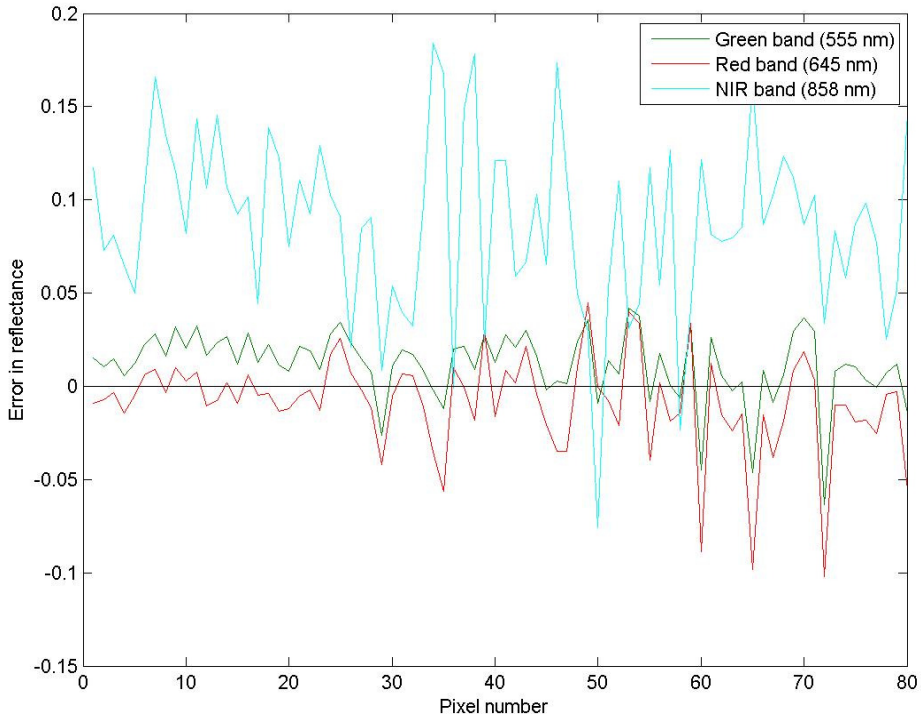

Figure 4-14 Spectral error (bias) in the MODIS reflectance (DOY 161) relative to SPOT.

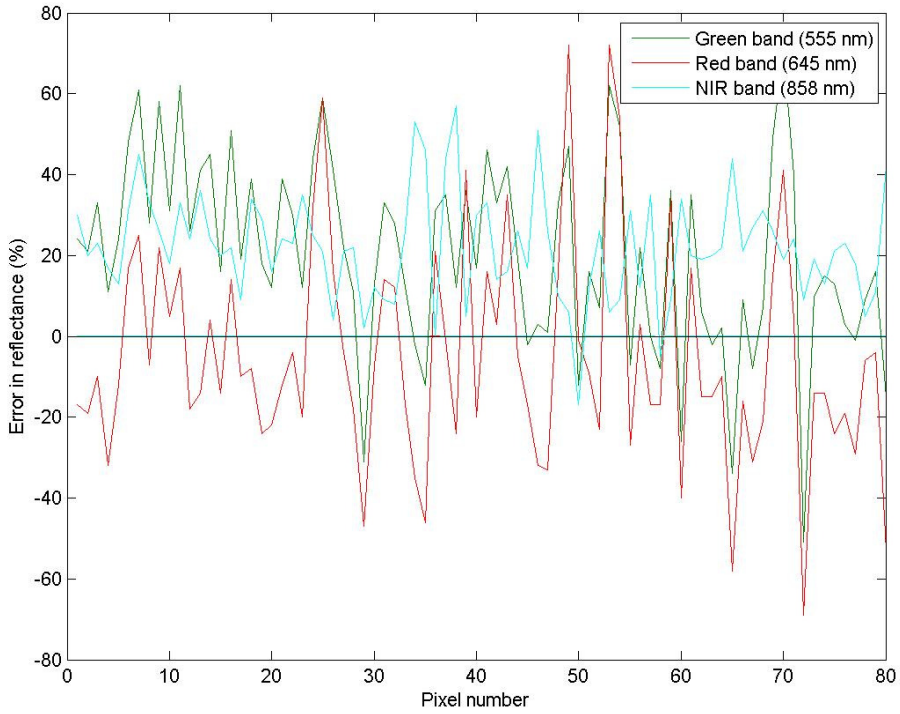

Figure 4-15 Percentage spectral error (bias) in the MODIS reflectance (DOY 161) relative to SPOT reflectance.

The results from the validation of MODIS reflectance using the SPOT data on DOY 161 (Figure 4-13) showed there was almost the same trend as seen in Figure 4-8.

4.5 Validating at-nadir MODIS reflectance estimated from a BRDF model

The MODIS data used had a high view zenith angle while the reference data had an at-nadir view angle. This difference in the view angle may affect the results of the comparison of the MODIS data with the reference data. BRDF parameters for DOY 168, provided by the Boston University team, provided the opportunity to correct the MODIS data for off-nadir effects. Using the BRDF parameters and the MODIS BRDF model, at-nadir MODIS reflectance was estimated. The at-nadir MODIS reflectance from the BRDF model was then compared with the EA-CASI data via scatterplots and the correlation coefficients were estimated (Figure 4-16).

The BRDF parameters were calculated using the MODIS reflectance products over a period of 16 days. The MODIS reflectance products from both Terra and Aqua over the 16 sequential days were recorded with different view and Sun geometries. This helps to introduce a statistical relationship between view-Sun geometry and reflectance. The statistical relationship is usually a linear regression and the regression coefficients are

the BRDF parameters. The BRDF parameters consist of three coefficients, or kernels, which are the isotropic, volumetric and geometric kernels. The reflectance can, thus, be calculated for different view-Sun geometries and can be used in estimating the hemispherical reflectance or albedo.

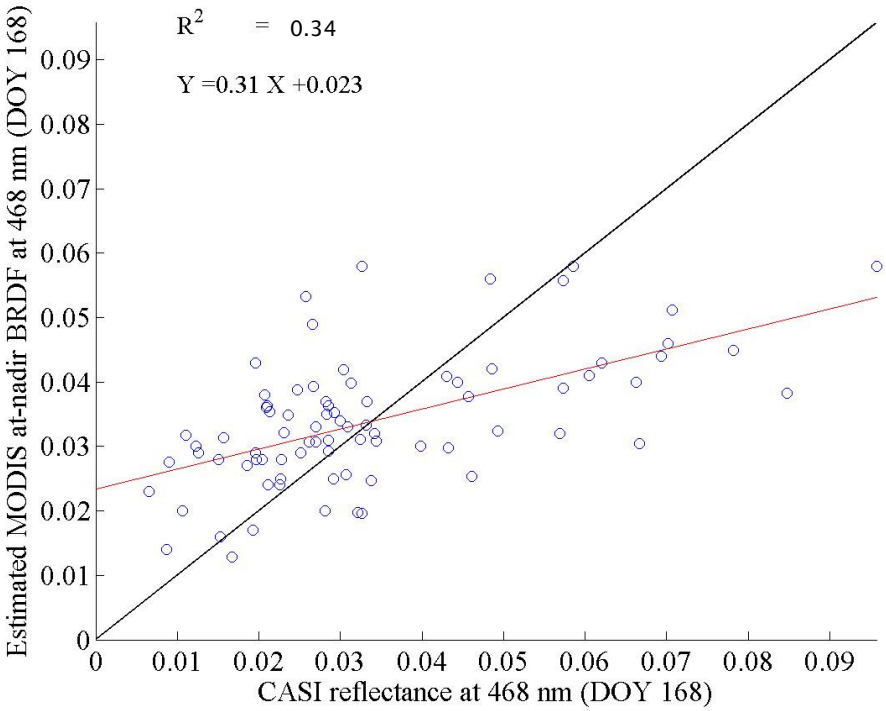

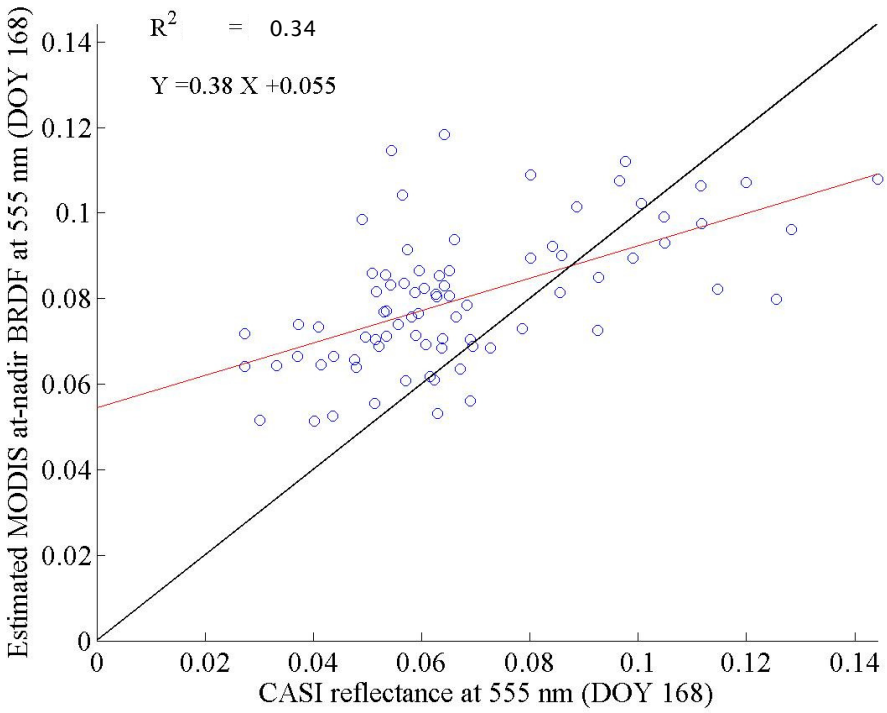

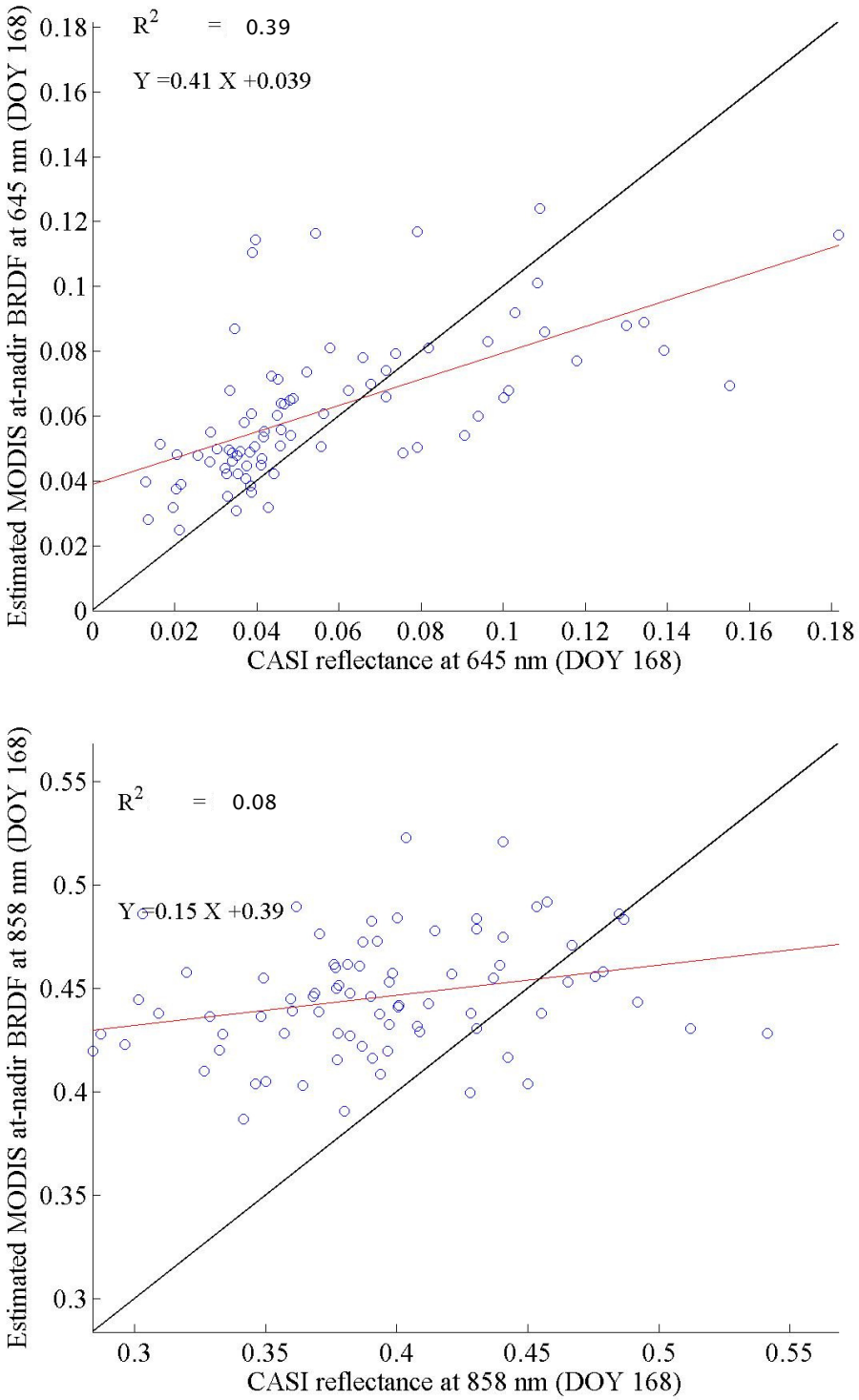

Figure 4-16 Scatterplots of at-nadir EA-CASI reflectance on DOY 168 against at-nadir MODIS reflectance, estimated from the daily MODIS BRDF parameters on DOY 168.

There was no improvement in the validation results after correction of the BRDF effects in the MODIS data. This could be either due to the uncertainty in the applied BRDF model or due to the other uncertainties mentioned in section 4.4.1.

4.6 Validating the BRDF model

An assessment of the MODIS BRDF model was also carried out. Uncertainty about the accuracy of the applied BRDF model was assessed by deriving the input reflectances. Also, the assumption of invariability of reflectance during the 16-day period was investigated.

4.6.1 Capability of the BRDF model in reproducing the input data

Using the MODIS BRDF model and the BRDF parameters for DOY 168, the surface reflectance was retrieved at the MODIS view geometry and spatial resolution. A comparison between the off-nadir data from the BRDF model and the actual off-nadir data was used to demonstrate the accuracy of the BRDF model (Figure 4-17).

As mentioned, MODIS reflectances during the 16 sequential days were used to calculate the BRDF parameters. Given these parameters, we tried to calculate one of the inputs. There was no expectation that a regression model can reproduce the inputs with 100% accuracy since they use all the data and fit the best linear model to the relationship. However, in this study, we used the daily BRDF parameters. The daily BRDF parameters used the 16 sequential reflectance data and the same BRDF model, but gave the largest weight to the day for which reflectance was calculated. Using the daily BRDF parameters for the DOY 168 in the year 2008 the accuracy of the BRDF model was more likely to be challenged.

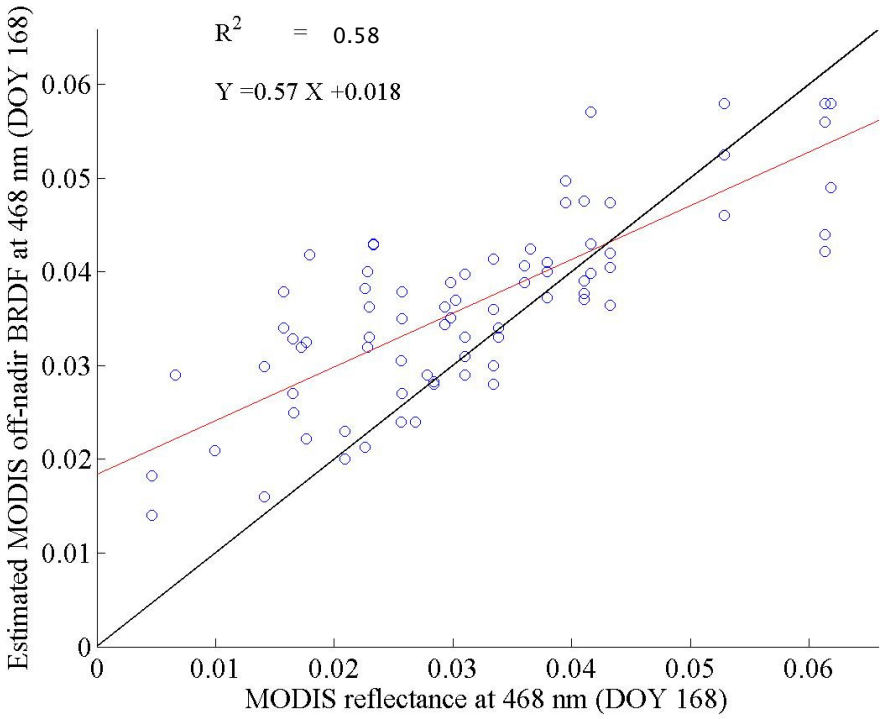
R2 = 0.58
Y =0.57 X +0.018
Estimated MODIS off-nadir BRDF at 468 nm (DOY 168)
MODIS reflectance at 468 nm (DOY 168)
0
0.01
0.02
0.03
0.04
0.05
0.06

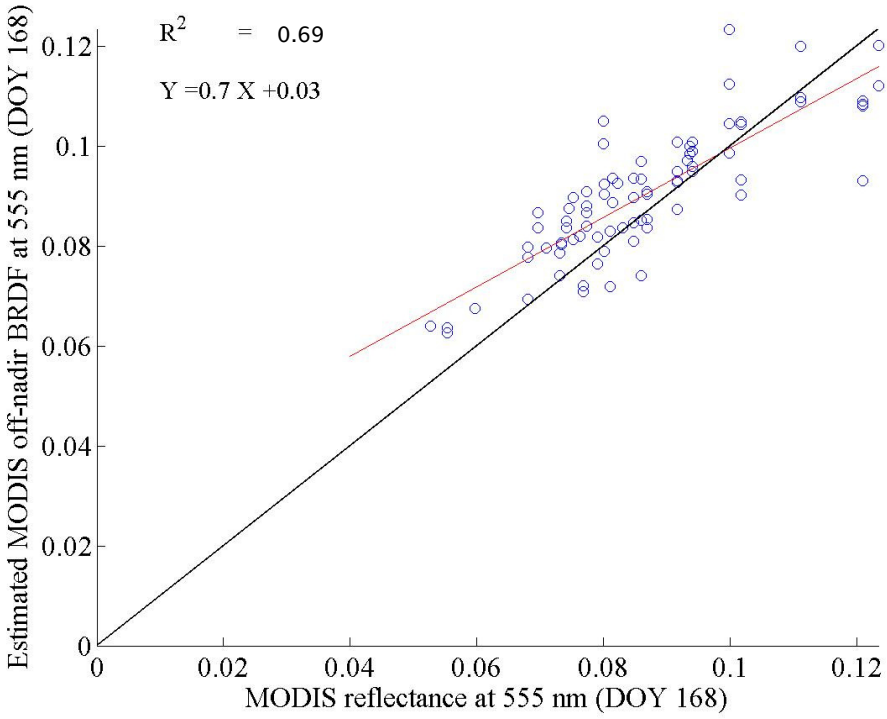
R2 = 0.69
Y =0.7 X +0.03
Estimated MODIS off-nadir BRDF at 555 nm (DOY 168)
MODIS reflectance at 555 nm (DOY 168)
0
0.02
0.04
0.06
0.08
0.1
0.12

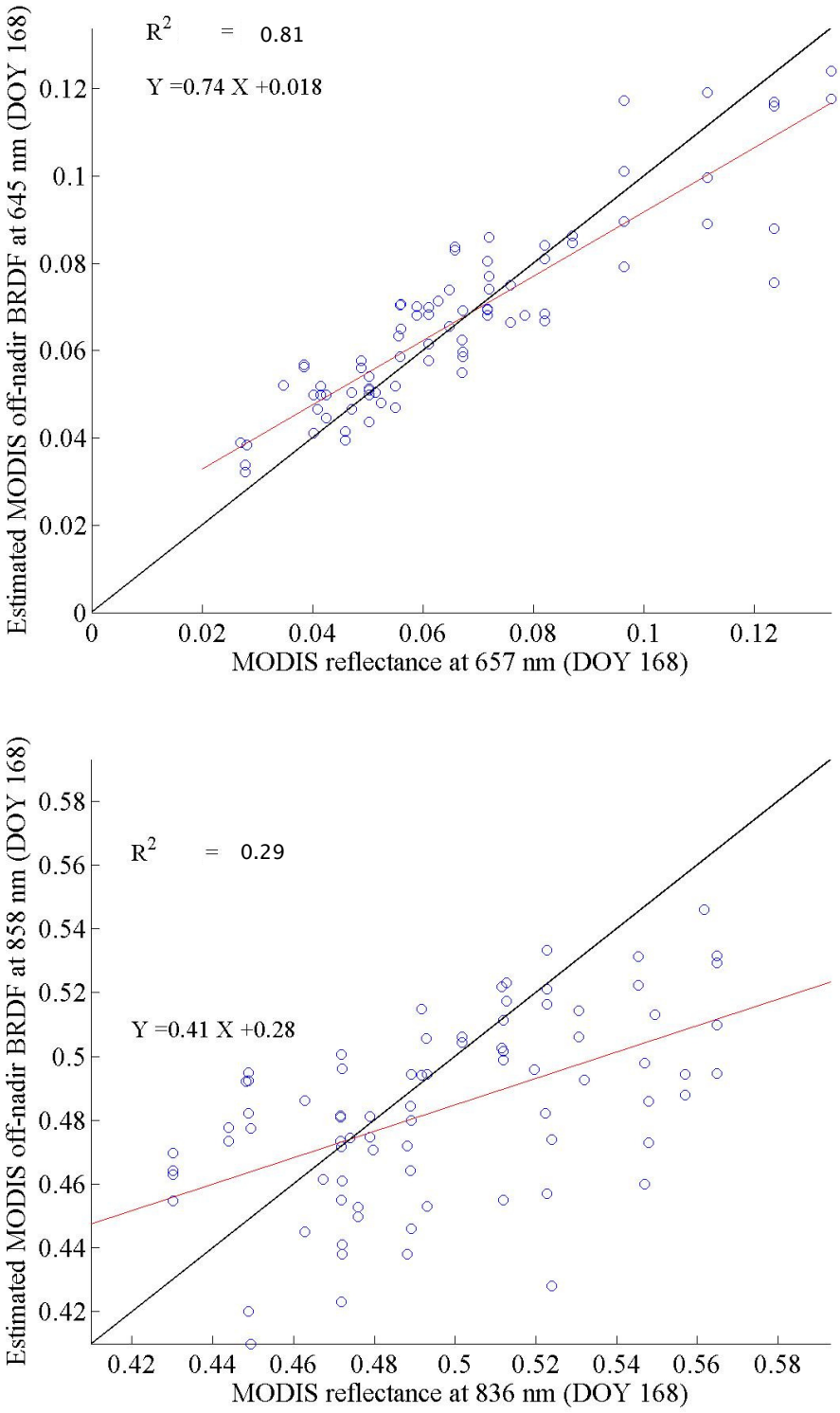

Figure 4-17 Scatterplots of MODIS reflectance on DOY 168 and the reflectance estimated from the daily MODIS BRDF parameters at the same Sun-view geometry.

The results showed that the BRDF model did not reproduce the main input, MODIS reflectance in DOY 168, with high accuracy. The reason may be due to the number and distribution of the observations during the 16-day period. The assessment of the QA data showed that most days (16 out of 24 observations) during the 16-day period were cloudy. This reduces the number of observations. The distribution of the data (Figure 3-8) showed that most of data were in the solar cross-principal plane. This could affect the results from the BRDF model as the variation of reflectance with view geometry is higher in the solar principal plane.

4.6.2 Correctness of the assumption of the invariability of reflectance during 16-day period

In obtaining the BRDF parameters, it was assumed that the surface reflectance varies with only view and Sun geometry. The correctness of this assumption underpins the accuracy of the retrieved BRDF parameters from the surface reflectance of the 16 sequential days. This may then affect the accuracy of the retrieved MODIS reflectance from the BRDF model, i.e. the accuracy of the estimated at-nadir MODIS reflectance in section 4.4 and the estimated off-nadir MODIS reflectance in section 4.5.1. To test this assumption, the variability of the reflectance of the reference data between two different days, DOY 161 and DOY 168, was considered (Figure 4-18). To see how MODIS data reflect the temporal variation in surface reflectance, the MODIS reflectances on DOYs 161 and 168 were also compared (Figure 4-19).

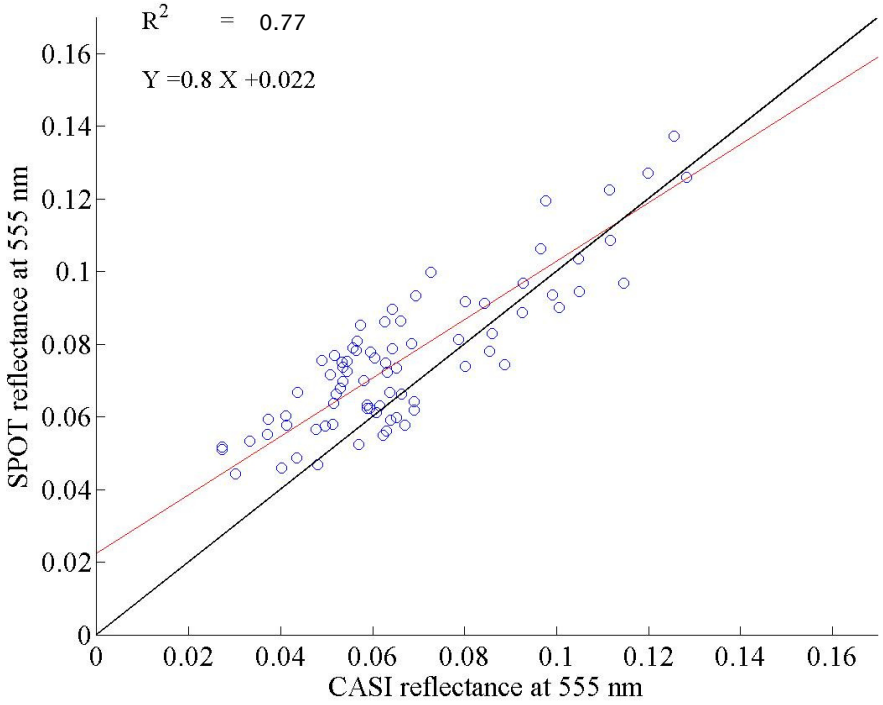
R2 = 0.77
Y =0.8 X +0.022
SPOT reflectance at 555 nm
CASI reflectance at 555 nm
0
0.02
0.04
0.06
0.08
0.1
0.12
0.14
0.16

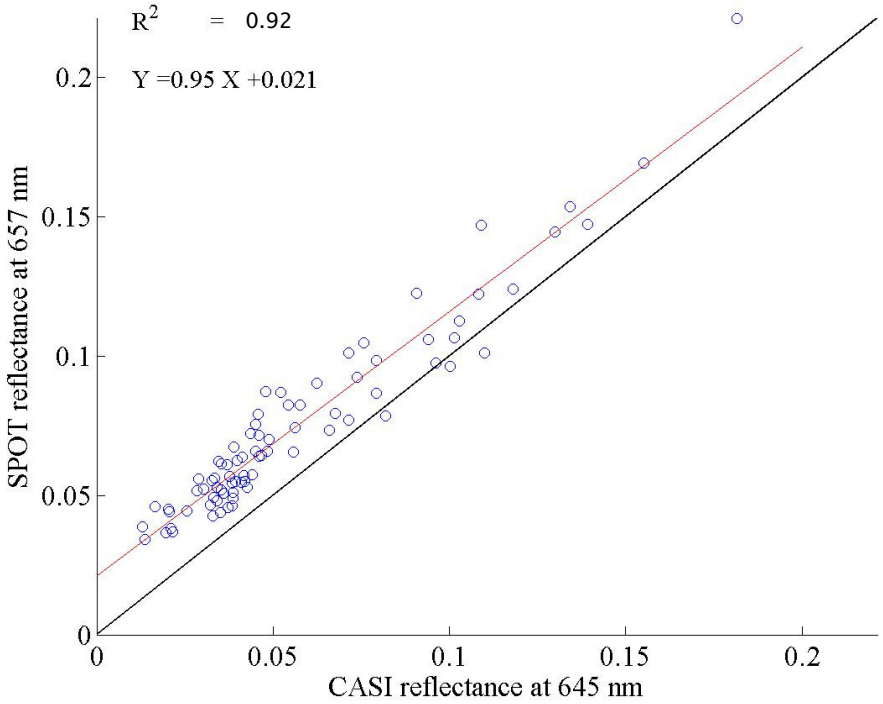
R2 = 0.92
Y =0.95 X +0.021
SPOT reflectance at 657 nm
CASI reflectance at 645 nm
0
0.05
0.1
0.15
0.2

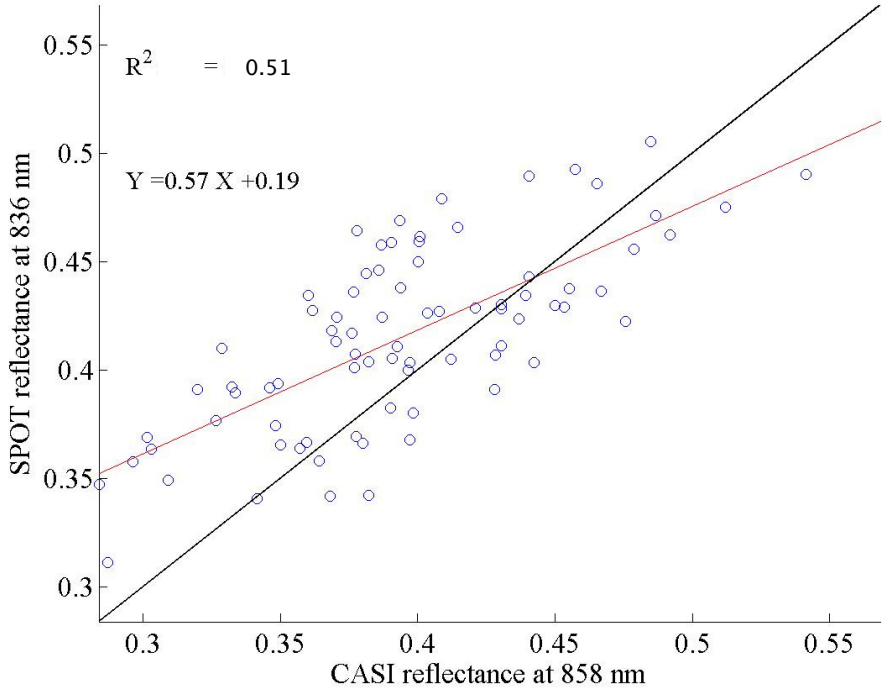

Figure 4-18 Scatterplots of SPOT reflectance on DOY 161 against EA-CASI reflectance on DOY 168 (spectrally resampled to the MODIS bands at 460 m spatial resolution), at a spatial resolution of 460 m.

The results from investigating the temporal variation of reflectance in the reference data (EA-CASI and SPOT) over two days, DOY 161 and DOY 168 (Figure 4-18), showed that the SPOT data had slightly higher reflectance values than the EA-CASI data, especially in the visible bands. In the green band, the reflectance on DOY 161 was higher in the pixels with low reflectance (0.02 to 0.06). In the red band, the reflectance on DOY 161 was higher than for DOY 168. In the NIR band, the reflectance on DOY 161 was higher for the pixels with reflectance 0.3 to 0.4. This may be due to the changes in the central wavelengths and bandwidths or changes in the land cover and NDVI. On the other hand, the differences in the SPOT and EA-CASI reflectance values could be due to differences in these two sensors, mainly differences in spatial and spectral resolution and altitude.

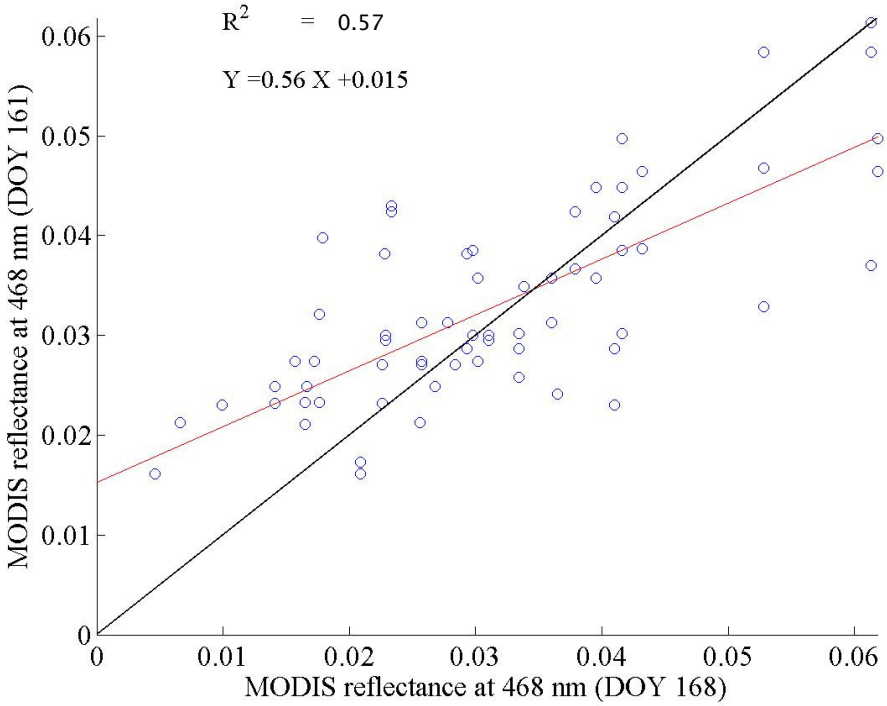
R2 = 0.57
Y =0.56 X +0.015
MODIS reflectance at 468 nm (DOY 161)
MODIS reflectance at 468 nm (DOY 168)
0
0.01
0.02
0.03
0.04
0.05
0.06

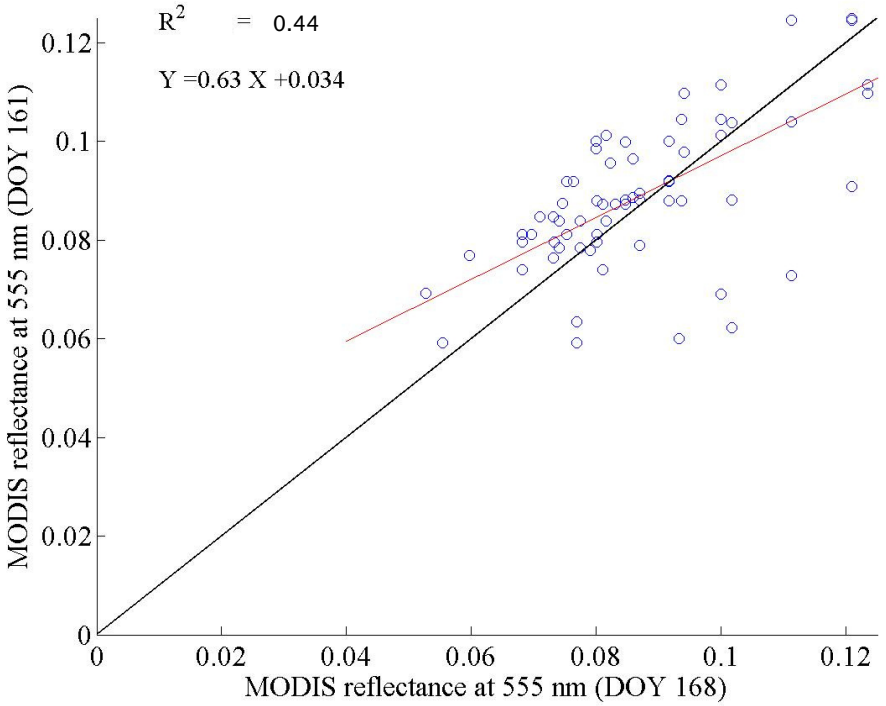
R2 = 0.44
Y =0.63 X +0.034
MODIS reflectance at 555 nm (DOY 161)
MODIS reflectance at 555 nm (DOY 168)
0
0.02
0.04
0.06
0.08
0.1
0.12

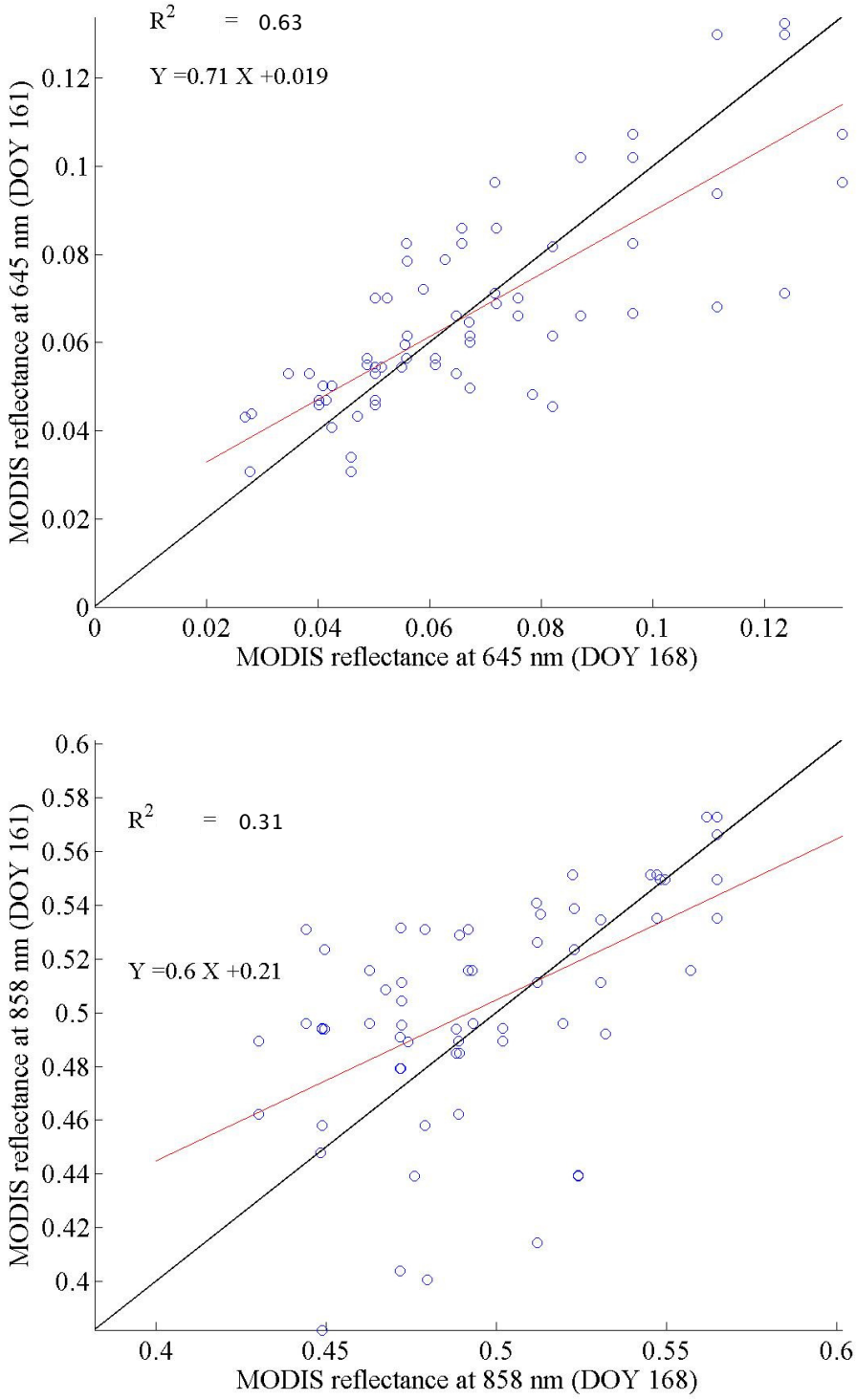

Figure 4-19 Scatterplots of MODIS reflectance on DOY 161 against MODIS reflectance on DOY 168.

The results from investigating the temporal variation of reflectance in the MODIS data over two days, DOY 161 and DOY 168 (Figure 4-19), showed a tendency for an increase in reflectance on DOY 161 in the green band only, but not as large as the one

seen in the reference data. In the blue band, the reflectance on DOY 161 was higher for pixels with reflectance less than 0.045 while for pixels with reflectance higher than 0.045 there was a decrease in the reflectance on DOY 161. In the green band the reflectance on DOY 161 was higher. In the red and NIR bands, there were only small changes in the reflectance.

Temporal comparison of the reflectance in the reference data (Figure 4-18) and in the MODIS data (Figure 4-19) showed that the MODIS reflectance did not increase in the 7-day period, while there was a decrease in the reference reflectance.

4.7 Discussion

The fine spatial resolution EA-CASI data were the main reference data in this study. Accurate atmospheric correction of the data was carried out using simultaneous ground measurements of reflectance and atmospheric parameters. The atmospheric effects were corrected using ATCOR-4 software (Asmat, 2009). Richter (2011) describes the theoretical background used in ATCOR-4. The SPOT data acted as complementary data for validation of the MODIS reflectance, but it also provided assurance about the results from the EA-CASI data; the results of validation were almost the same.

Although the atmospheric correction of EA-CASI data was carried out using ground measurements, there are still several uncertainties which need to be taken into consideration:

There were a small number of valid ground measurements of surface reflectance: the estimated reflectance values were validated using just two ground data locations: one for asphalt and one for concrete.

The results of the comparison of estimated surface reflectance and measured surface reflectance from concrete showed that the errors for the 400-550 nm band were significant (relative error of 10-25%) while, for asphalt, the errors were large at 400-500 nm (relative error of 10%) and 800-1000 nm (relative error of 10-20%) (Asmat, 2009). The region between 550 nm to 800 nm is then reasonably accurate, at least for the two point measurements.

The error in the co-registration of multiple flightlines may be large. Since the data used come from mosaics of several adjacent and orthogonal along-track acquisitions, accurate geo-referencing and co-registration is needed. Asmat (2009) showed that the

errors resulting from co-registration can be large in NIR bands, but high accuracy is achieved in other wavelengths.

There was some uncertainties regarding the atmospheric model used. incident solar light is polarized by the atmosphere's aerosols and Earth's surface and this is not taken into account by scalar radiative transfer models such as MODTRAN (Kotchenova et al., 2006). The errors in surface reflectance resulting from neglecting polarization can be more than 10% (Hulst cited in Kotchenova et al. 2006). Other uncertainties can be introduced by the aerosol model and the use of lookup tables.

The adjacency effect on EA-CASI is quite large due to its fine spatial resolution. Although the data were corrected for the adjacency effect in ATCOR, the accuracy of this correction is not certain. The uncertainty can be greater for boundary pixels, especially those adjacent to built-up and bare soil areas.

However, the above-mentioned uncertainties were mainly minimised when the EA-CASI data were spectrally and spatially resampled to the MODIS spectral and spatial resolution. The results from the validation of the MODIS reflectance using the reference data showed that for the small area studied, there was only a small correlation. A large area, encompassing a wider range of reference values in each band, would provide a more thorough evaluation with the potential to produce a much larger correlation. Some sources of uncertainties in the MODIS reflectance data were either explained or investigated in previous sections of this chapter. Here, other sources of uncertainties in the MODIS data used for the present study are explained:

Small thick clouds: small clouds which may not be identified at the MODIS spatial resolution can introduce a large error in the reflectance product. The studied area was cloud-free at the time of the reference EA-CASI data (between 10:05 am and 10:30 am in DOY 168), but became cloudy shortly afterwards. The acquisition time of the MODIS data started at 10:35 am when the probability of the appearance of clouds increased slightly. The QA of the MODIS data, however, showed a clear sky for the area. Pixels with high reflectance in the visible and near-infrared regions in MODIS, but low reflectance in EA-CASI data may show the effects of cloud. On the other hand, pixels which have low reflectance in visible and near-infrared bands in MODIS, but high reflectance in EA-CASI data may show the effects of cloud shadow.

Thin cirrus clouds: The results of the QA information (State 1 km data) showed that the MODIS data on DOY 168 were affected by cirrus clouds and some pixels had shadow effects as well. Vermote and Vermeulen (1999) mentioned some uncertainties

regarding the use of the MODIS cirrus detection algorithm, such as the adjacency effect, cirrus inhomogeneity and ice clouds effect. Uncertainties in correcting these effects may be another reason for the observed errors.

Atmospheric model: the 6S radiative transfer model used for atmospheric correction of the MODIS data seems to give greater accuracy than other radiative transfer models (Svetlana Y. Kotchenova et al., 2006). However, general uncertainties about these models, such as sensitivity to choosing the aerosol model, whether the aerosol model presents the actual atmospheric state, the Lambertian assumption and Look-Up Table interpolations, still remain (Vermote and Vermeulen, 1999).

AOT and aerosol type retrievals: The algorithm for the estimation of AOT is based on the empirical relationship between the blue (469 nm) and red (645 nm) wavelengths developed on the AERONET sites. This makes the reliability of the estimated AOT for regions with no AERONET sites less certain. Comparison of the aerosol amount and type from the aerosol product (MOD 04) and ground measurements showed that there was an overestimation of the aerosol amount (about 30 %). However, the error in the estimation of aerosol type may introduce larger errors. The aerosol type estimated from the ground measurements was “rural aerosol” which has more scattering effects, while MOD 04 determined “heavy absorbing smoke”. However, MOD09 uses its own aerosol retrieval algorithm which is based on the relationship between the visible and NIR bands. The amount of aerosol at the 1 km spatial resolution was determined from the MODIS QA data (State 1 km data). The aerosol amount for the MODIS data on DOY 168 was determined as a fixed climatology value (0.02) which has an error of more than 90%. Underestimation of the aerosol may result in the undercorrection of the MODIS reflectance product for the aerosol effects and then overestimation of surface reflectance. The aerosol type at the 1 km spatial resolution used in producing the MOD09 product, however, was not part of the information provided by the MOD09GA data. Regarding aerosol modelling, as MODIS uses the visible and NIR bands to model the type and amount of aerosol, there was a possibility of error in the NIR band which may result in introducing errors into the estimated aerosol and aerosol type in the visible bands. The errors in estimating aerosol optical thickness may lead to large errors in the short wavelength bands of MODIS, which is greatest in band 3 (469 nm).

Uncertainties in the BRDF correction: The MODIS data on DOYs 161 and 168 had high view zenith angles of about 50°. This may raise possibilities such as the appearance of thick and thin clouds which do not affect the nadir-based EA-CASI data. The MODIS reflectance product corrects the atmosphere/BRDF coupling using an a

priori estimate of the surface BRDF. The uncertainties in the estimated surface BRDF may introduce errors into the reflectance output.

Spectral integration: The spectral region covered by each band of MODIS and EA-CASI was different. The equivalent EA-CASI bands to those MODIS bands which are used in reflectance retrieval were then chosen and the EA-CASI reflectances were averaged in those bands. Only the first four bands of MODIS, out of seven bands, were assessed since the other three bands were beyond the EA-CASI spectral coverage. Bands 1, 3 and 4 of MODIS were broader than EA-CASI, while band 2 was narrower. The integration in the EA-CASI bands equivalent to the visible MODIS bands was carried out using a Gaussian function. The uncertainty might be greater in the validation of band 2 of MODIS since it compared the broader band of EA-CASI (846.7-885.2 nm) to the narrower band of MODIS (841-876 nm).

Spectral upscaling: The fine spatial resolution EA-CASI and SPOT data were upscaled using a simple average function to the MODIS spatial resolution. A different upscaling method such as using point spread function could slightly change the results. On the other hand, the impact of the upscaling method on the outputs decreases as the size of the output pixel increases. In this study, the pixel size of the output data was 50 to 500 times of the original pixel size. This could significantly minimise the effects of the slight changes between different upscaling methods.

Information included in MOD09GA: MOD09GA is a daily composite product which uses the highest quality observation for each pixel. It was more probable that the used data was recorded at 10:30 am since other times of day were more likely to be cloudy. However, there was a possibility that some pixels had been recorded at different times of the day and with different view-Sun geometries.

Geometric accuracy: It was difficult to visually check the accuracy of the geometric correction of the MODIS data due to the coarse spatial resolution. However, the geometric accuracy of the MODIS data is claimed to be 50 m at nadir (Wolfe et al., 2002, Wolfe and Nishihama, 2009). A coastal line map at scale 1:250,000, from the UK Ordnance Survey, was used to check the overall accuracy of the MODIS data outside of the case study. It showed that the geometric error of the MODIS data was acceptable, about one pixel, although the determination of absolute accuracy was not possible.

Map Projection conversion: The reprojection of the data may also introduce some unintended displacements in the data. The MODIS data were in the Sinusoidal map projection while EA-CASI data were in the United Kingdom Ordnance Survey map

projection. The map projection conversion produced a horizontal and vertical shift (10-100 m). This could be due to differences in the nature of the map projections used. Sinusoidal map projection is an equal-area projection which preserves the area of figures. The UKOS36 map projection, on the other hand, is a conformal projection which preserves the angles of figures.

The results may be summarised as follows:
For the small area studied, the daily MODIS reflectance showed large absolute errors in the first four bands studied. Uncertainty regarding aerosol modelling, cloud detection and sensor calibration may be the main reasons for the observed errors. The reflectance errors in the MODIS data were obtained for each land cover. The vegetated surfaces showed larger errors in the visible wavelengths, while larger errors in the non-vegetated areas were observed in the NIR wavelengths.

BRDF parameters obtained from the daily albedo product were used to transform the MODIS off-nadir product to at-nadir reflectance. Three different comparisons were carried out to test the accuracy of both the BRDF model and the reflectance product. The results showed that there were some uncertainties in the applied MODIS BRDF model and the estimated parameters. The BRDF model was not able to reproduce the observed off-nadir MODIS reflectance. The inaccuracy of the MODIS reflectance product can, thus, be attributed to both the BRDF model used and the atmospheric correction method applied. The atmospheric correction procedure, however, introduced larger errors than the BRDF model. Undetected thin and thick clouds and aerosol optical thickness may, thus, explain the errors observed in the MODIS reflectance for the site analysed.

4.8 Conclusion

Although previous validation studies of the MOD09 product, carried out by the MODIS team, have shown encouraging results, one should bear in mind the limited spatial coverage of the validation sites, which cannot describe the wide variety of climates and land covers across the globe. In this study, fine spatial resolution data were used to validate the daily MODIS reflectance product.

The validation process of coarser spatial resolution MODIS data was supported with two independent high spatial resolution reference datasets. For the small area studied, the daily MODIS reflectance showed large absolute errors in the first four bands studied. The main reason may be the climate conditions of the UK, with high humidity, cloudiness most days, and greater heterogeneity. Under these climate conditions, the

errors in the atmospheric correction of the data with off-nadir view geometry and coarse spatial resolution will be larger. For albedo and climate applications where an absolute reflectance accuracy of greater than 0.05 is required, the use of the MODIS reflectance product may introduce large errors. A higher accuracy of remotely sensed reflectance may be achieved using airborne data that can provide information on cloudy days. Due to the uncertainties in the use of the MODIS BRDF parameters, the use of MODIS data may be restricted to cloud-free days or at-nadir data in partly cloudy days. Further research is currently underway to assess the accuracy of the MODIS albedo product using a range of ground and satellite reference albedo data.

5 Investigation of the spatial variability of albedo

5.1 Introduction

Remote sensing has the advantage of providing synoptic coverage of large areas of the Earth's surface; however, the target is usually imaged from a single view angle which gives insufficient information to calculate albedo. PROBA is an ESA technology demonstration mission which was launched on 22nd October 2001 (http://earth.esa.int) and since then this Sun-synchronous satellite has been monitoring the Earth's surface at an altitude of 600 km. It was designed to be largely autonomous, needing little involvement from the ground station. There are several instruments on PROBA, of which the Compact High Resolution Imaging Sensor (CHRIS) is the most important for this study (Barnsley et al., 2004). CHRIS is a multiple view angle pushbroom sensor which makes its data valuable for Bidirectional Reflectance Distribution Function (BRDF) and albedo modeling. CHRIS can operate in five imaging modes that can acquire data at different spatial and spectral resolutions (Table 3-2). This gives the potential to use data from CHRIS to estimate spectral albedo at fine spatial resolutions over reasonably large areas (24 km × 24 km) and to study spatial variation in albedo. Modeling the spatial variability in albedo is important because, in mid-latitude areas at least, some of the image area can be expected to be affected by clouds, cloud shadow or topographic shadow. CHRIS data from multiple view angles also gives the opportunity to investigate the contribution different view angles make to the estimation of albedo.

5.2 Data used

The Chilbolton test area was again used as the study site (see Chapter 3) and most of the data used in this chapter were acquired during the NCAVEO Field Campaign (Milton et al. 2011). CHRIS/PROBA acquired a full set of five images in Mode 1 from the study area at about 11:20 am on 17th of June 2006 (Figure 5-1). The Sun/sensor geometry is shown in Figure 5-2 and the bands sensed are listed in Table 5-2. Figure 5-2 also shows that the CHRIS/PROBA data were aligned more closely to the solar principal plane than those from MODIS and could, therefore, be expected to provide a more accurate estimate of directional reflectance, and hence albedo. Furthermore, the CHRIS/PROBA data were acquired over a period of about 4 minutes using the along-

track pointing ability of PROBA, unlike the MODIS data which were accumulated over several days.

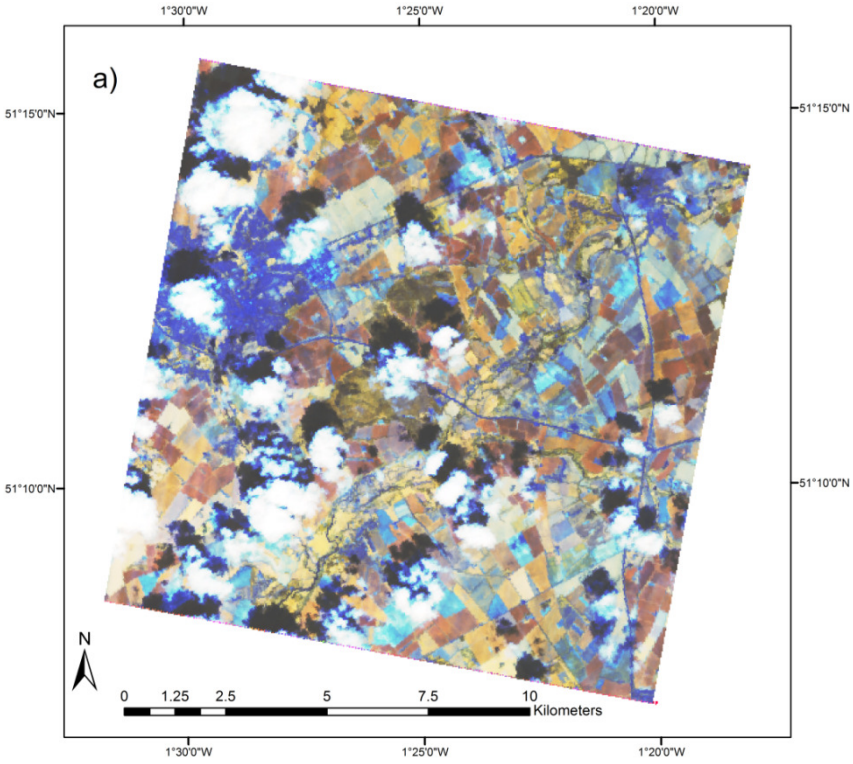

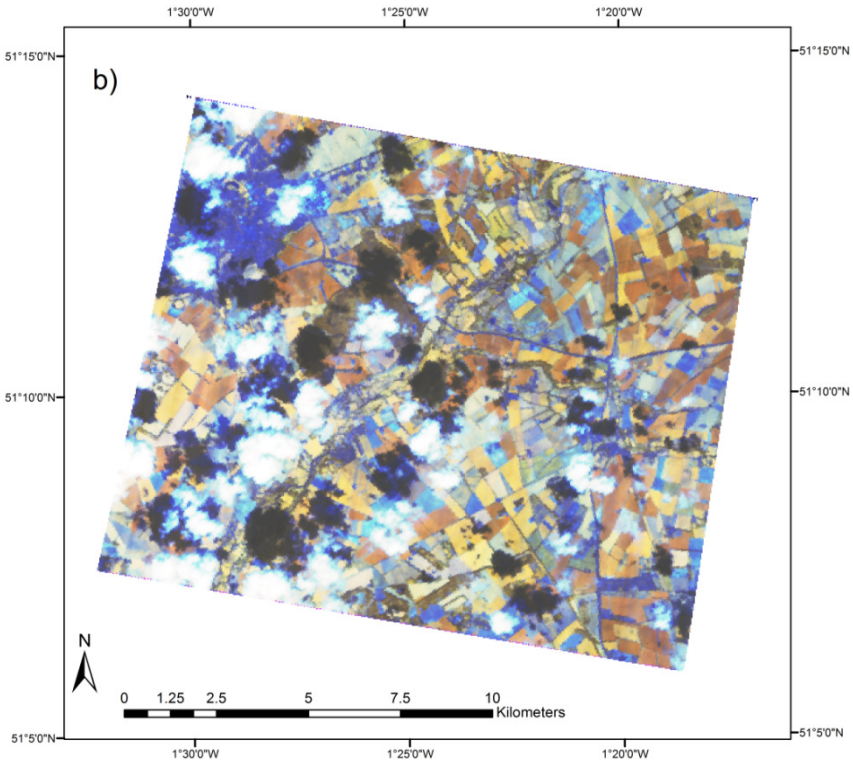

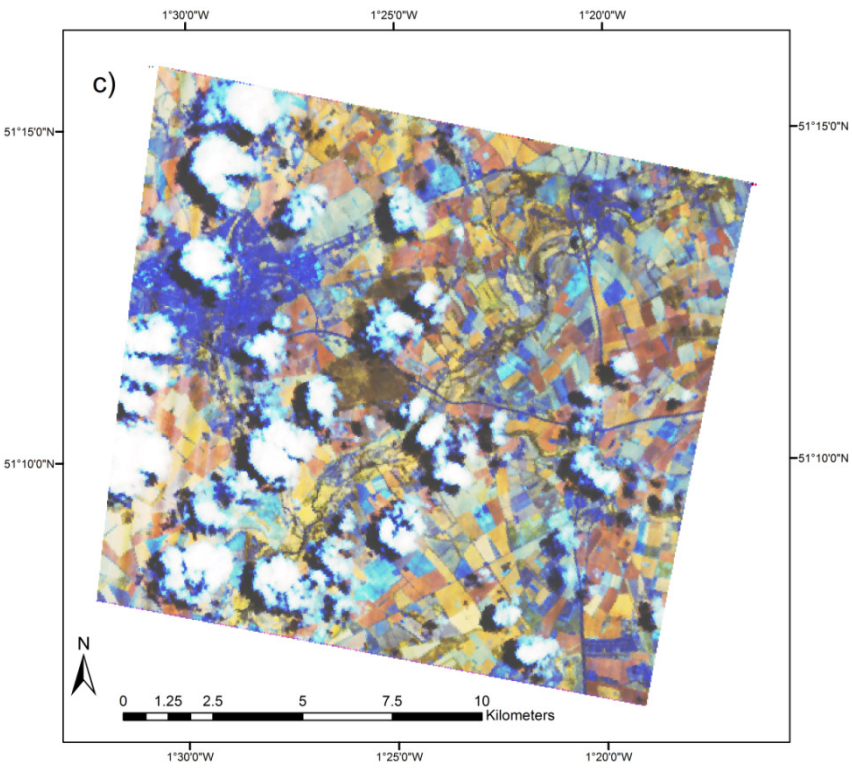
c)
1°30'0"W
1°25'0"W
1°20'0"W
51°15'0"N
51°10'0"N
N
0 1.25 2.5 5 7.5 10
Kilometers

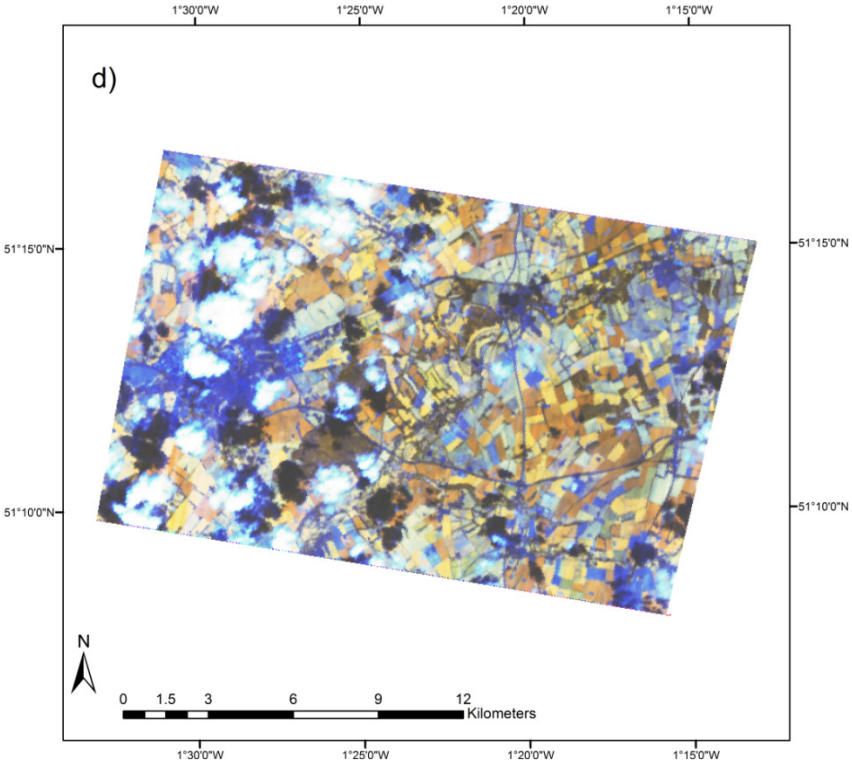
d)
1°30'0"W
1°25'0"W
1°20'0"W
1°15'0"W
51°15'0"N
51°10'0"N
N
0 1.5 3 6 9 12
Kilometers

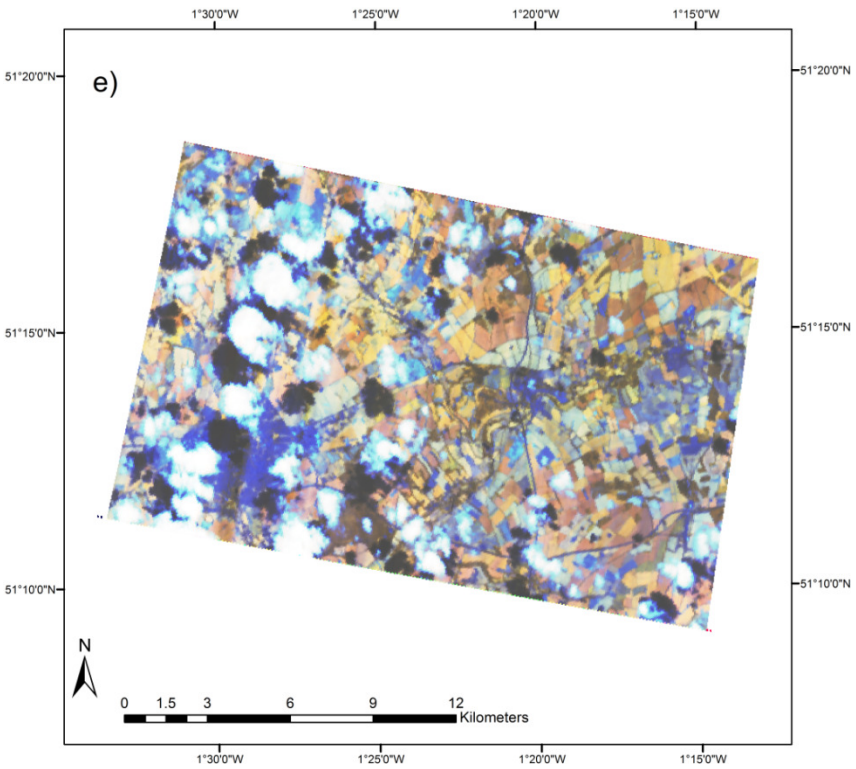

Figure 5-1 CHRIS/PROBA dataset over the Chilbolton site on 17th June 2006. The data were recorded in five fly-by zenith angles (FZA): a) FZA=0°, b) FZA=+36°, c) FZA=-36°, d) FZA=+55°, and e) FZA=-55°. The data were mapped as a false colour composite of bands 48 (red), 33 (green) and 13 (blue).

It is evident from Figure 5-1 that some of the data from some of the view angles were affected by clouds and cloud shadows, so these were excluded from the combined multiple view angles (MVA) data set by manual on-screen digitising. The resulting MVA image is shown in Figure 5-3.

The CHRIS data were converted to surface reflectance using the BEAM software (Fomferra and Brockmann, 2005) provided by ESA, which includes specific corrections for the CHRIS sensor (Alonso et al., 2009). Figures 5-7 to 5-13 show examples of average spectra from each of the seven land covers studied and for each of the five view angles. The spectra from the built-up area show a red edge due to mixing between the vegetated areas (gardens and fields) and the houses and roads being smaller in size than the IFOV. The spectral reflectance in each of the 62 CHRIS bands was averaged to produce broadband reflectance over the spectral regions of interest (Table 5-1). The CHRIS/PROBA bands were averaged based on a Gaussian function in which the bands equivalent to central wavelengths of new spectral regions had the maximum contribution and the bands covering the far end of new spectral regions had the minimum contribution in calculating new reflectance values.

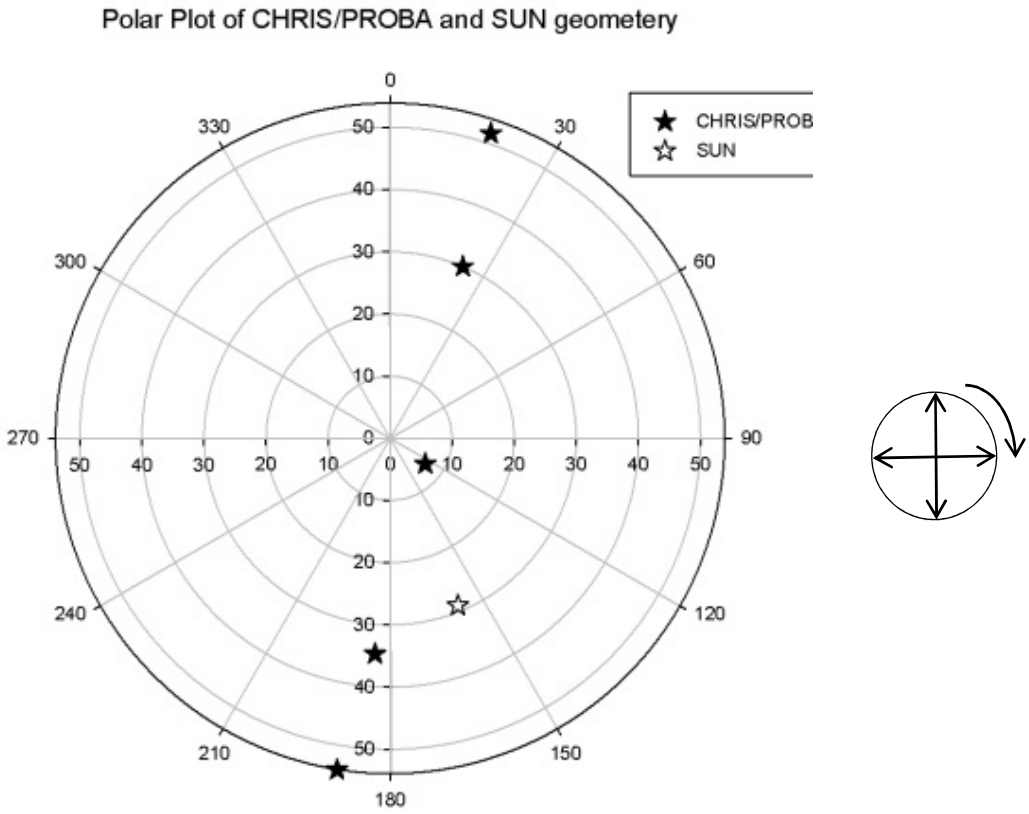

Figure 5-2 The Sun and the five view angles CHRIS geometries over the study site.

Table 5-1 Spectral characteristics of the bands used in the estimated albedo

Spectral region	Central wavelength (nm)	Bandwidth (nm)	Equivalent CHRIS bands
Visible	572	261	Bands 2 to 29 (440 nm- 700 nm)
NIR	856	304	Bands 30 to 62 (700 nm- 1002 nm)
Broadband	725	566	Bands 2 to 62 (440 nm- 1002 nm)

Table 5-2 Spectral characteristics of CHRIS/PROBA data (Source: header file of the data)

Band number	Central wavelengths (nm)	Band width (nm)	Band number	Central wavelengths (nm)	Band width (nm)	Band number	Central wavelengths (nm)	Band width (nm)
1	410.5	10.9	22	643.3	9.8	43	796.1	7.8
2	442.4	10.5	23	653.3	10.2	44	803.9	8
3	452.4	9.5	24	663.7	10.6	45	812	8
4	462.1	10	25	674.5	11	46	832.6	16.8
5	472.5	10.6	26	682.9	5.6	47	845.4	8.7
6	482.2	8.9	27	688.6	5.8	48	854.2	8.8
7	491.3	9.3	28	694.4	5.9	49	863.1	9
8	500.9	9.8	29	700.3	6	50	872.1	9.1
9	510.9	10.3	30	706.4	6.1	51	881.4	9.3
10	521.6	10.9	31	712.5	6.2	52	890.7	9.5
11	531.4	8.7	32	718.8	6.3	53	900.2	9.5
12	541.9	12.3	33	725.2	6.5	54	909.7	9.8
13	552.9	9.8	34	731.7	6.6	55	919.5	9.9
14	562.9	10.3	35	738.3	6.7	56	929.6	9.9
15	573.5	10.9	36	745.1	6.8	57	944.7	20.4
16	582.8	7.6	37	752	7	58	960.1	10.4
17	592.5	11.9	38	759	7.1	59	970.6	10.5
18	604.7	12.6	39	766.2	7.2	60	981.1	10.7
19	615.5	8.8	40	773.4	7.3	61	991.8	10.6
20	624.4	9.1	41	780.9	7.5	62	1002.7	10.8
21	633.7	9.5	42	788.4	7.6			

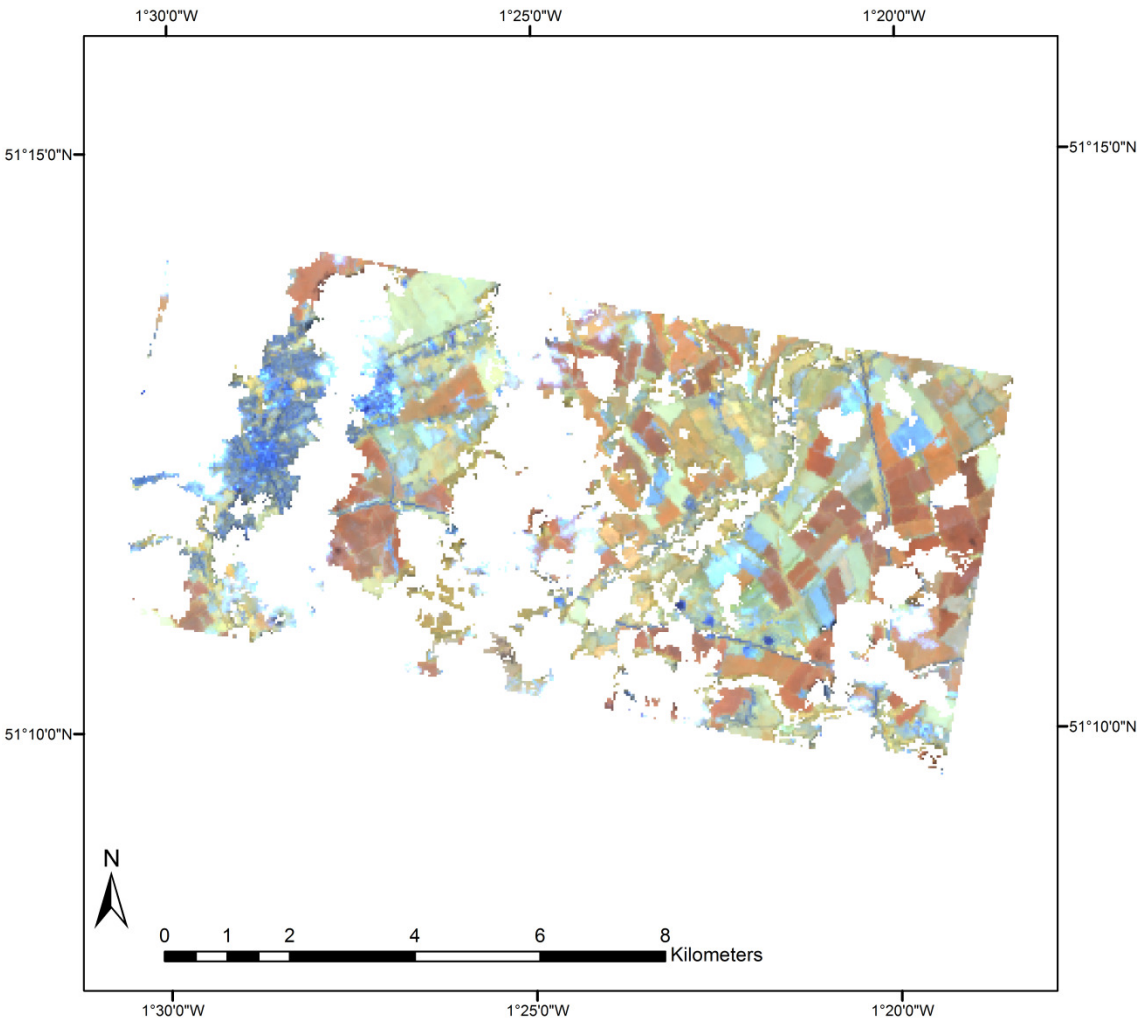

Figure 5-3 The common CHRIS data in all five view angles. The RGB image is a composite of band 48 (854 nm), band 33 (725 nm) and band 13 (553 nm).

5.3 Methodology

Surface reflectance and a kernel-driven BRDF model were used to estimate hemispherical BRDF from the five view angles of the CHRIS data. The possibility of the extension of the albedo map to a larger area was assessed by considering the spatial variability of albedo and the relationship between directional reflectance and albedo.

5.3.1 Albedo estimation

The five view angles of CHRIS/PROBA and the position of the Sun at the time of acquisition of the data were used to calculate the geometric-optical and volumetric components of the RTLSR BRDF model. Surface albedo was calculated by integrating the BRDFs over the full hemisphere. Figure 5-4 shows how the geometric-optical and volumetric kernels were calculated for the CHRIS/PROBA dataset. Using the observed

CHRIS reflectances, f_r, at five view angles, for a pixel in wheat class (Figure 5-7), the linear coefficients of the BRDF model, f_{iso}, f_{vol} and f_{geo}, were obtained for each spectral CHRIS band (Equation 2-21). With the obtained coefficients, the BRDF values in view zenith angles 0-90 and view azimuth angles 0-360° with a 10° interval were then calculated for a particular Sun geometry. The estimated BRDF values were then integrated over the hemisphere for a particular Sun geometry resulting in the black sky albedo, DHR (Equation 2-3). The spectral DHR obtained from the CHRIS dataset was also integrated over the equivalent MODIS bands centred at 465 nm, 555 nm, 659 nm and 858 nm as well as the visible (400-700 nm), NIR (700- 1100 nm) and broadband (400-1100 nm) bands (Table 5-1).

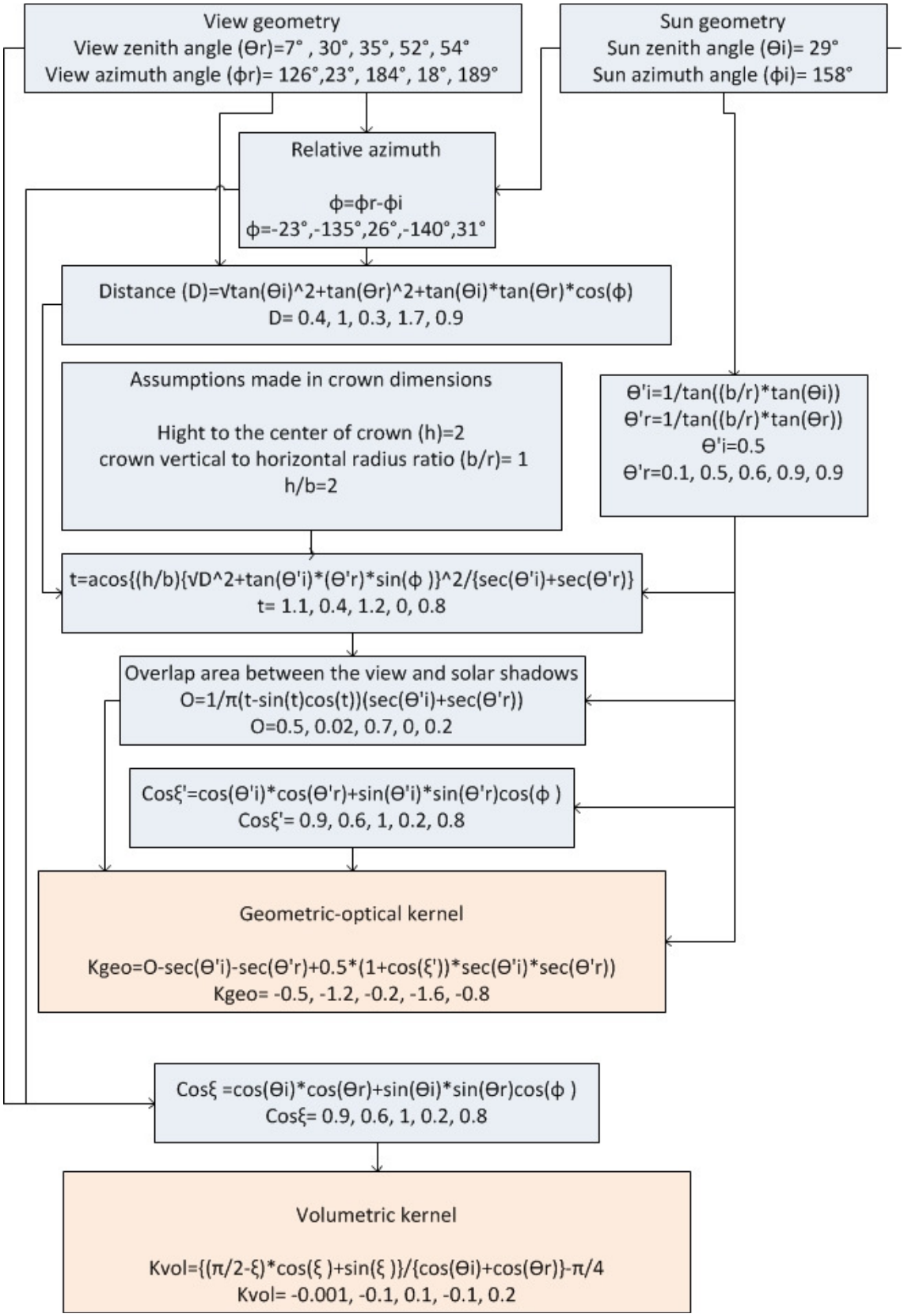

Figure 5-4 The process of calculation of the kernels of RossThick-LiSparseReciprocal BRDF model for the CHRIS/PROBA view geometry on 17th June 2006 over the Chibolton area and the simultaneous Sun geometry.

5.3.2 Extension of the albedo map

The surface reflectance data, a mosaicked image from all five view angles, covered an area of 24 km × 24 km. However, the extent of the obtained albedo map was restricted to an area of 14 km × 8 km (112 km^2): the common area in all five view angles. The appearance of clouds at the time of acquisition of the data caused a further reduction in the size of the area. The final albedo map thus covered an area of about 46 km^2 and due to gaps created by clouds this area was not continuous. Although the obtained albedo map can be a valuable reference to validate coarse resolution data such as the MODIS albedo product, the extent of the albedo map limits the area available for validation. The possibility of estimating albedo for the cloudy parts of the scene and the area outside of the common area in the five view angles was investigated using two different methods. The first was the possibility of using the land cover map from a larger area to estimate albedo. The second method was the possibility of using the directional CHRIS reflectance to estimate albedo.

A land cover map was created using a supervised classification method and visual interpretation (Figure 5-5). The ground sample points were collected as a part of NFC06, nearly simultaneous with the CHRIS/PROBA data. The Spectral Angle Mapper (SAM) classification method was used to classify almost all the land covers. There were 350 training pixels and 180 validation points. A maximum angle of 0.1 radians was used. This is the maximum angle between the spectra of each pixel and the reference spectra. All pixels with angles below this threshold were assigned to the reference class they were closest to. The built-up class was visually classified as it was quite heterogeneous. An accuracy assessment of the classified image was also carried out (Table 5-3). The overall accuracy was calculated by averaging the percentage of correct classifications.

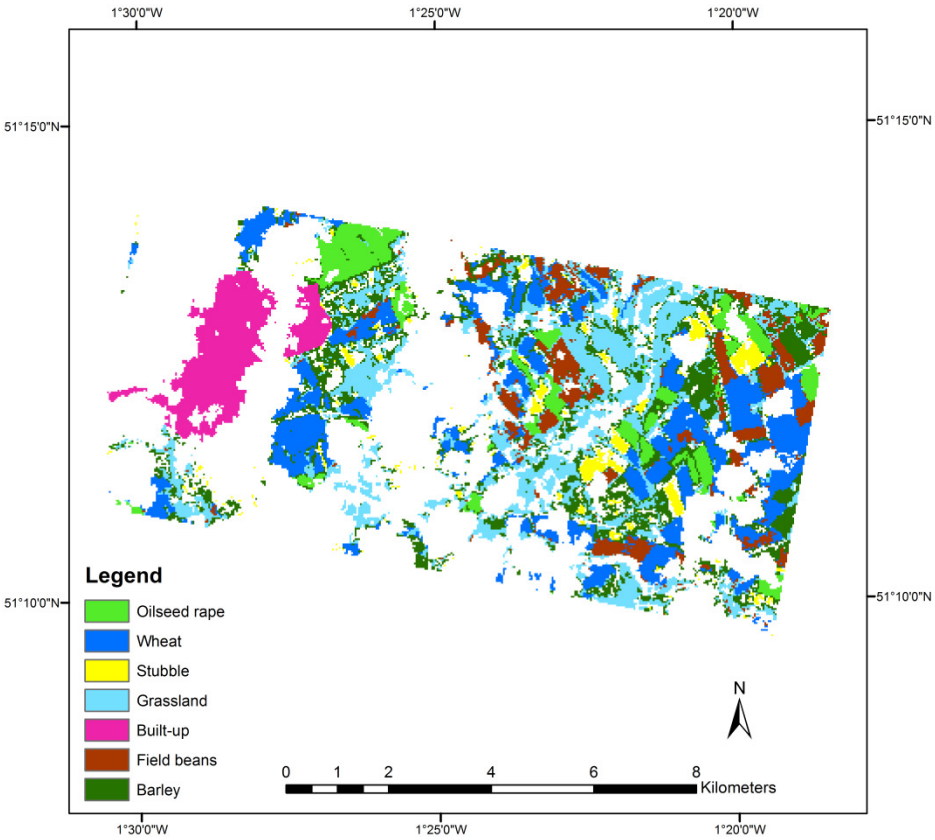

Figure 5-5 Land cover map

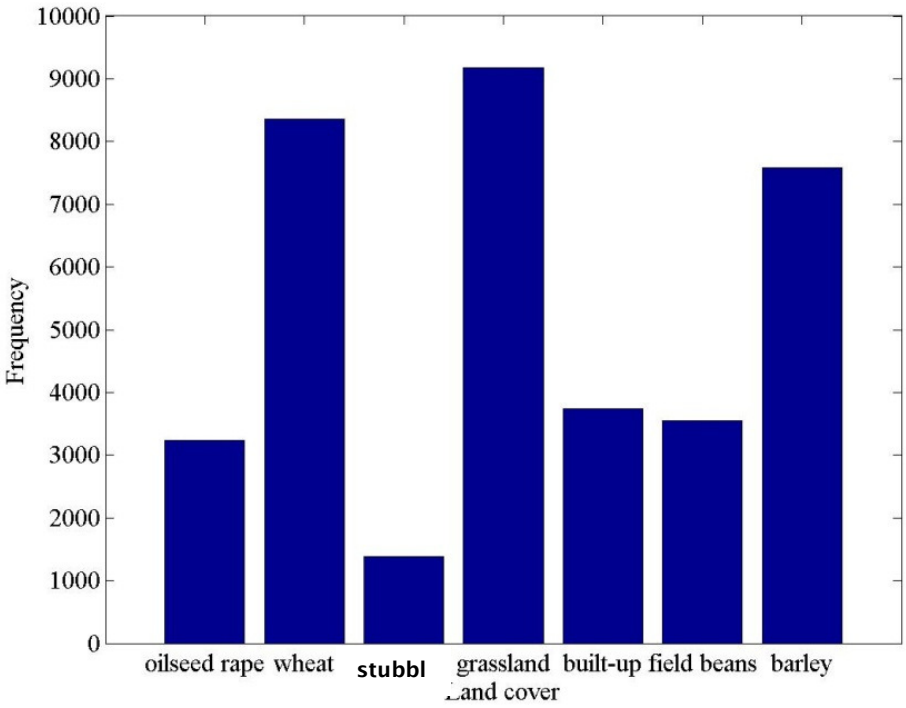

Figure 5-6 Histograms of land covers.

There were several different land covers (mainly crops) in the area (Figure 5-5). Since the crop fields were small (the average field area was approximately 100 m × 30 m), the albedo values of different fields might be affected by neighbouring fields. Grasslands, with an area of 8 km^2, and wheat and barley, each with an area of 7 km^2, were the major land covers in the area (Figure 5-6). Field beans, oilseed rape and built-up area, each with an area of about 3 km^2, and stubble class, 1.3 km^2, made up the other land covers.

The distribution of land covers showed that the built-up area existed only in the western part of the study site whereas the stubble class existed between areas of green vegetation. There was uncertainty about the correctness of the stubble class (which may be bare soil) as the sample data were collected from outside of the area. Distinguishing between bare soil and stubble from remotely sensed data is difficult due to the high level of similarity in the shape of the spectra in the visible and NIR regions (Aase and Tanaka, 1991). The only distinguishable feature is the slope of the reflectance spectra in VIS-NIR that is generally greater for stubble than for bare soil, but this may be affected by soil moisture or stubble age (Goward et al., 1994, Nagler et al., 2000).

Table 5-3 Confusion matrix of the created land cover map

Ground truth (pixels) / Class	Oilseed rape	Wheat	Stubble	Grasslands	Built-up	Field beans	Barely	Total
Oilseed rape	21	0	0	0	0	0	0	21
Wheat	0	25		11	0	0	23	59
Bare soil	3	0	26	0	0	0	0	29
Grasslands	0	0	1	6		0	0	7
Built-up	0	0	0	0	20	0	0	20
Field beans	0	0	0	0	0	35	0	35
Barley	0	0	0	6	0	0	3	9
Total	24	25	27	23	20	35	26	180
Overall Accuracy	130/174=75%							

Although an accuracy assessment of the mapped land cover was produced, there were uncertainties regarding the results obtained. The distribution of training samples was not good since they were all recorded in one part of the study site and not across the entire study site. Therefore, a reliable accuracy assessment was not possible.

The extension of the albedo map using land cover is sensible if the variation inside each land cover is small. The spatial variation of surface albedo inside each land cover was then assessed by examining the deviation of the albedo values in each land cover from the mean albedo value in that particular land cover. It was assumed that the spatial variability between different land covers was greater than that within each land cover. However, this depends on the particular land cover and the homogeneity of the background. Variations in climatology variables, density and structure of vegetation canopy and soil conditions, may also result in spatial variation in albedo (Moody et al., 2008). These conditions usually happen due to the management system in agricultural lands, variation in topography in pastures and grasslands, and greater inhomogeneity in forests. The variation in soil moisture inside each land cover due to the variation in topography, although it can be small, can be the main reason of this variation. The spatial dependency of surface albedo was studied in different aspects. One aspect was to consider the spatial variation of albedo between different land covers. Another was to study the variation of albedo between the same land covers in different parts of the area. Investigating the variation of albedo within each land cover in each part of the area was another area of interest in the spatial dependency of albedo.

The possibility of the extension of the albedo map to a larger area using directional CHRIS reflectance was also assessed. For this, the relationship between reflectance at different view angles and visible, NIR and broadband albedos was studied. Using a linear regression model, the area of the albedo map can be extended to the surrounding area with known directional reflectance. This study also investigates the contribution of each view angle to the estimation of albedo. The critical view angles in the estimation of albedo were then recognized. This may help in modeling the error in the estimation of albedo if the critical view angles are not used. In addition to this, these sensor angles can be considered in future flight missions.

5.4 Assessment of the directional reflectance in different land covers

Figures 5-7 to 5-13 show the reflectance of each land cover type at each of the five view angles, with view angles in the backscatter direction denoted as negative.

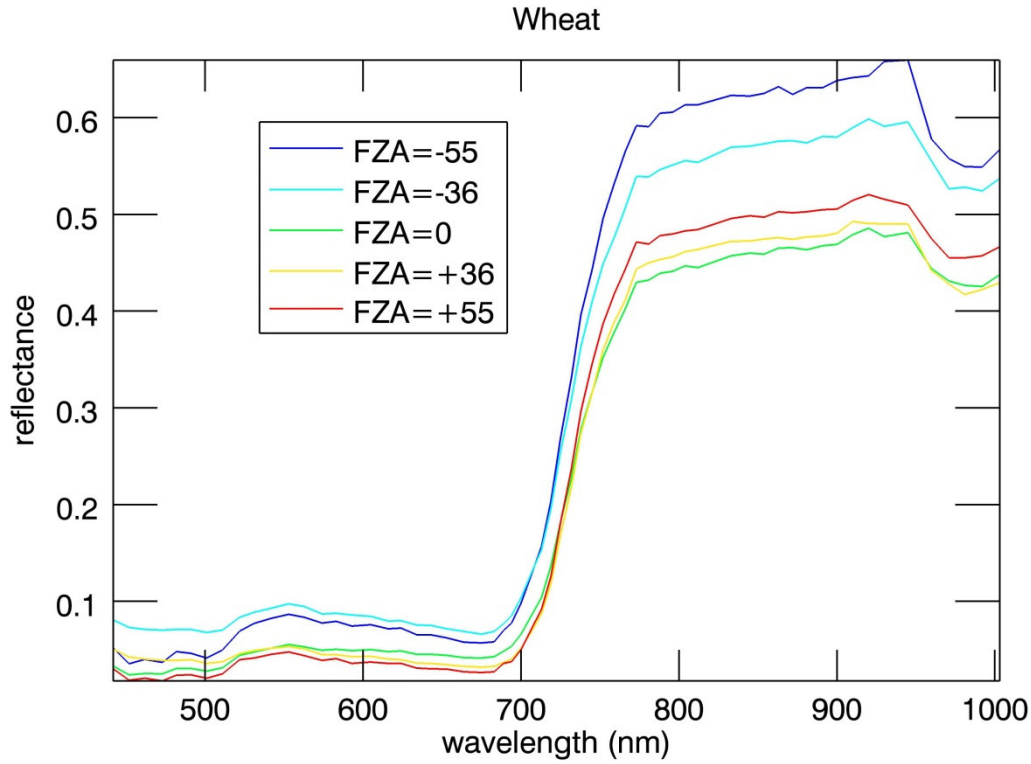

Figure 5-7 Spectral CHRIS reflectance of wheat at all view angles.

Disney et al. (2004) measured wheat's spectra at a test site in the UK. The measurements were carried out using an Analytical Spectral Devices (ASD) Field Spectrometer at the nadir view angle at 10:46 on 17th June 2000. The wheat reflectance was 0.015 (in 450 nm), 0.04 (in 550 nm), 0.02 (in 650 nm) and 0.41 (in 800 nm). The measured reflectance values at FZA=0° in our study site were 0.015 (in 450 nm), 0.05 (in 550 nm), 0.04 (in 650 nm) and 0.038 (in 750 nm). The reflectance values from both measurements were about the same across the entire measured spectra except at the red band (650 nm). As the reflectance at the red band is mainly controlled by the amount of chlorophyll, the difference could be related to the growth stage of wheat.

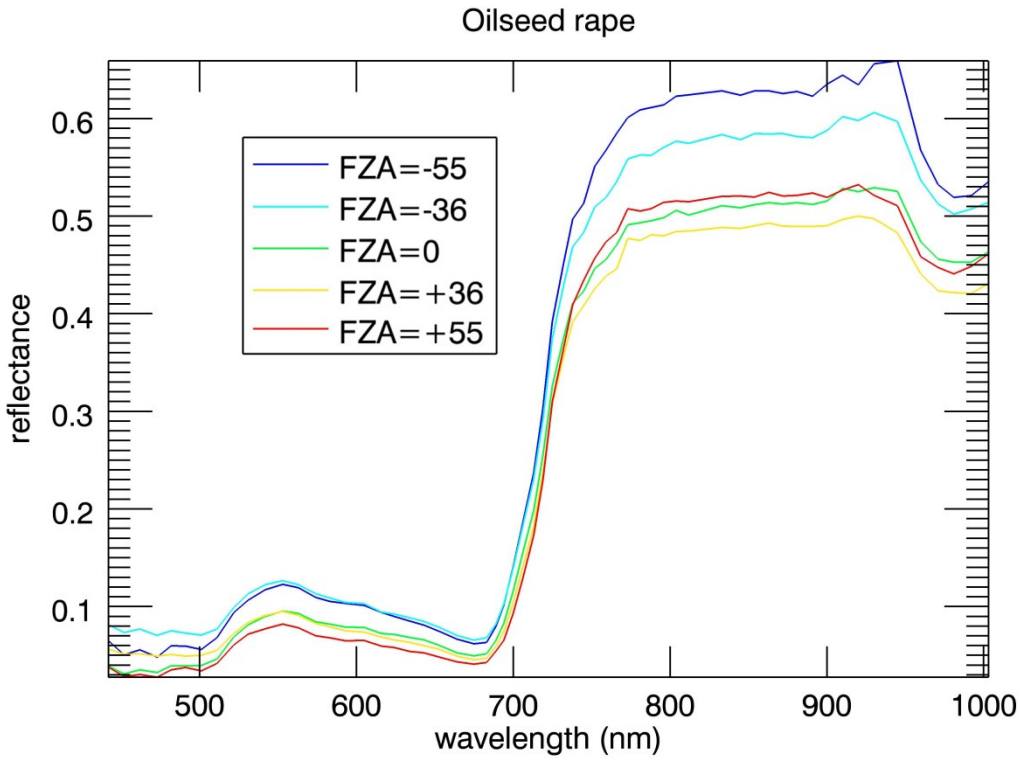

Figure 5-8 Spectral CHRIS reflectance of oilseed rape at all view angles.

Hong et al. (2011) studied the spectra of different varieties of oilseed rape. Visible reflectance varied from 0.08 to 0.12 and NIR reflectance varied from about 0.45 to 0.65. These reflectance values were approximately similar to the range of albedo values in our study site. This may in general show the validity of the obtained reflectances.

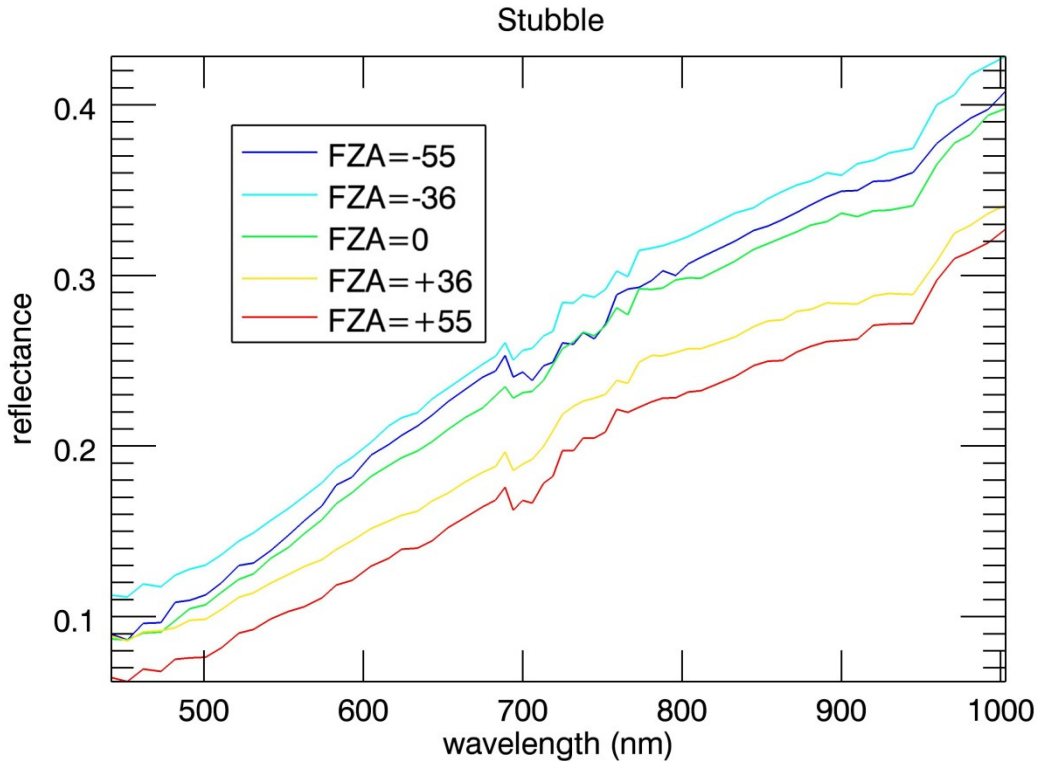

Figure 5-9 Spectral CHRIS reflectance of stubble at all view angles.

Root and Miller as reported by Bowker et al. (1985) measured the spectral reflectance of wheat stubble at a test site in the US. The reflectance values were 0.05 (in 450 nm), 0.11 (in 550 nm), 0.14 (in 650 nm) and 0.23 (in 850 nm). The measured reflectance values at FZA=0° in our study site were 0.07 (in 450 nm), 0.14 (in 550 nm), 0.2 (in 650 nm) and 0.3 (in 850 nm). As the moisture of surface decreases the surface reflectance increases to a greater extent in the NIR than the visible region. Therefore, the higher reflectance values of stubble, compared to that measured by Root and Miller, may be due to the lower surface moisture.

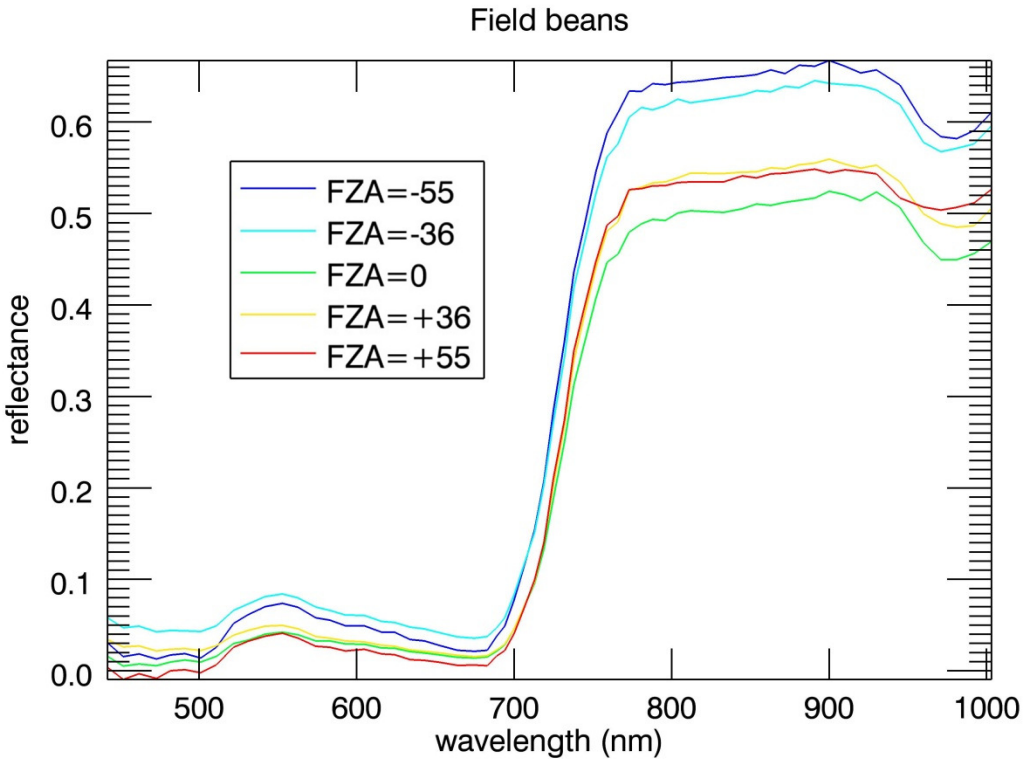

Figure 5-10 Spectral CHRIS reflectance of field beans at all view angles.

Vane et al. as reported by Bowker et al. (1985) measured the spectral reflectance of beans at a test site in the US. The reflectance values were 0.06 (in 450 nm), 0.1 (in 550 nm), 0.08 (in 650 nm) and 0.36 (in 850 nm). The measured reflectance values at FZA=0° at our study site were 0.02 (in 450 nm), 0.05 (in 550 nm), 0.035 (in 650 nm) and 0.5 (in 850 nm). The lower reflectance values in the visible region and higher reflectance in the NIR region may be due to differences in the variety of beans, LAI and soil background conditions.

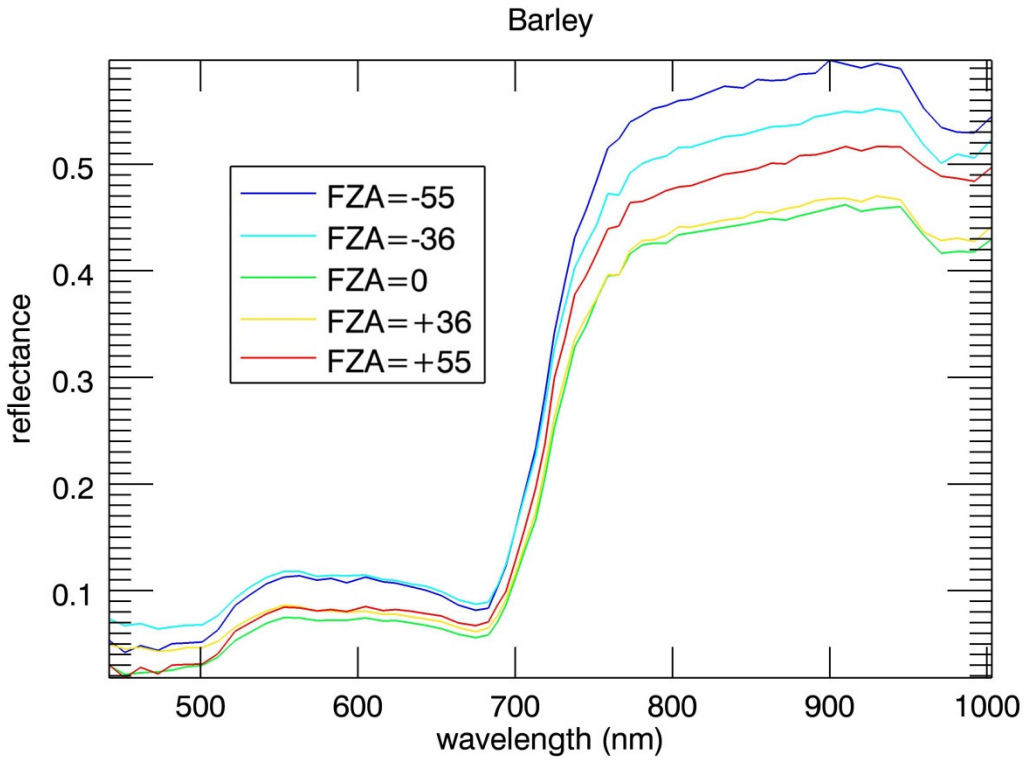

Figure 5-11 Spectral CHRIS reflectance of barley at all view angles.

Vane et al. as reported by Bowker et al. (1985) measured the spectral reflectance of barley at a test site in the US. The reflectance values were 0.06 (in 450 nm), 0.09 (in 550 nm), 0.15 (in 650 nm) and 0.3 (in 850 nm). The measured reflectance values at FZA=0° at our study site were 0.01 (in 450 nm), 0.07 (in 550 nm), 0.05 (in 650 nm) and 0.42 (in 850 nm). The measured values in our case study were lower in the visible and higher in the NIR regions. The reason could be due to differences in barley variety, LAI, density and soil background conditions.

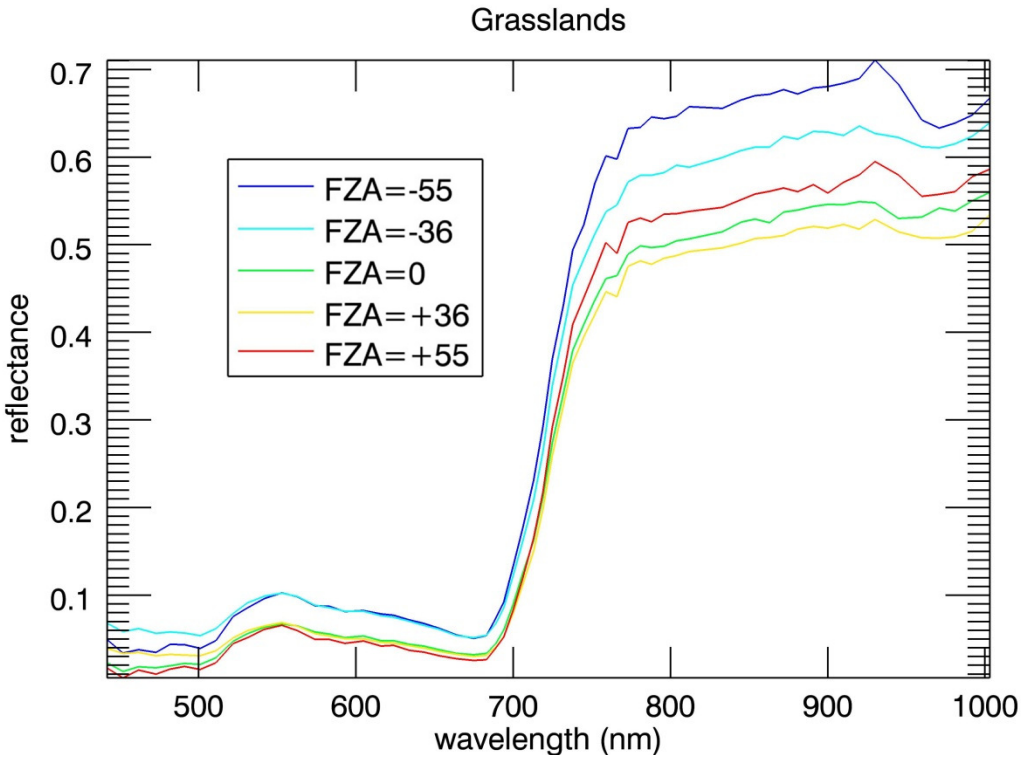

Figure 5-12 Spectral CHRIS reflectance of grass at all view angles.

Root and Miller as reported by Bowker et al. (1985) measured the spectral reflectance of barley at a test site in the US. The reflectance values were 0.03 (in 450 nm), 0.06 (in 550 nm), 0.04 (in 650 nm) and 0.31 (in 850 nm). Siegal et al. as reported by Bowker et al. (1985) measured the spectral reflectance of barley at a different test site in the US. They reported 0.005 (in 450 nm), 0.05 (in 550 nm), 0.04 (in 650 nm) and 0.65 (in 850 nm). The measured reflectance values at FZA=0° in our study site were 0.02 (in 450 nm), 0.07 (in 550 nm), 0.05 (in 650 nm) and 0.5 (in 850 nm). All of these measurements were about the same in the visible band but different in the NIR region. This could be due to differences in grass variety, LAI, density and soil background conditions.

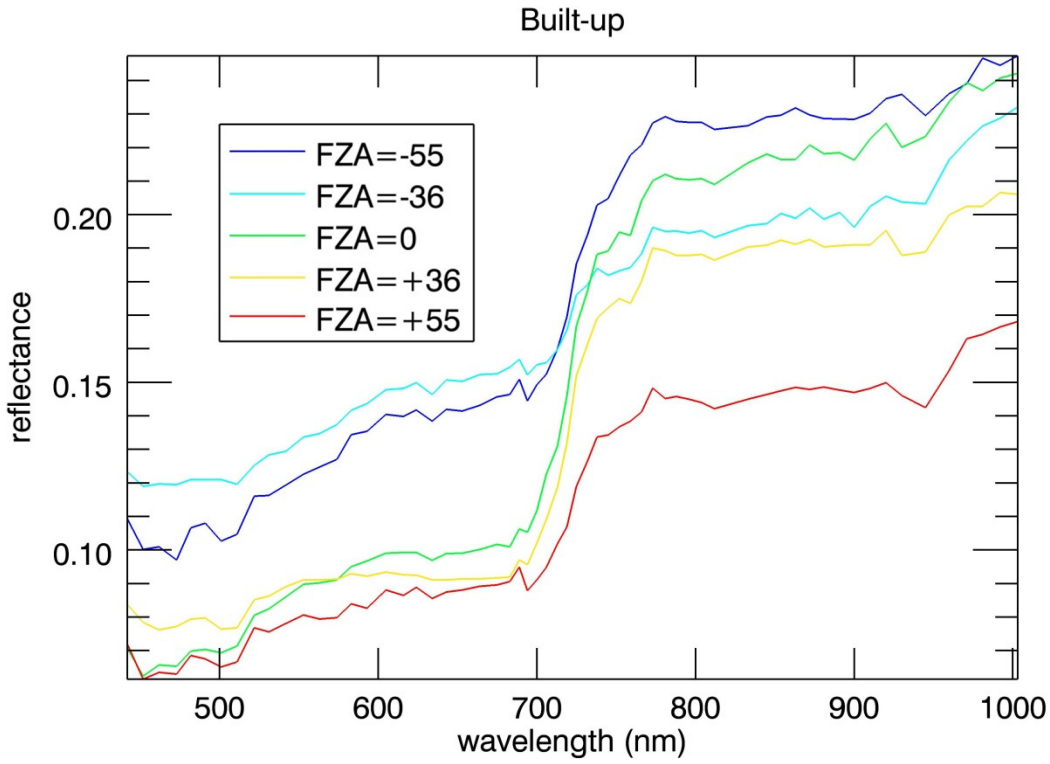

Figure 5-13 Spectral CHRIS reflectance of built-up area at all view angles.

The built-up area was a mixture of asphalt (roads), grass and trees, metals (cars) and granite (house roofs). The measured reflectance was thus a combination of the reflectances of all these surfaces. Root and Miller as reported by Bowker et al. (1985) measured the spectral reflectance of asphalt at a test site in the US. The reflectance values were 0.09 (in 450 nm), 0.11 (in 550 nm), 0.15 (in 650 nm) and 0.2 (in 850 nm). The measured reflectance values at FZA=0° in our study site were 0.02 (in 450 nm), 0.07 (in 550 nm), 0.09 (in 650 nm) and 0.22 (in 850 nm). Vegetation (grass and trees) probably was responsible for the lower reflectance in the visible band and the slightly higher reflectance in the NIR band.

Figure 5-14 and Figure 5-15 compare the reflectance of each land cover type at each of five view angles in two spectral bands, red and NIR. Kimes (1983) related the BRDF effects on remotely sensed data to the canopy geometry, principally the leaf orientation distribution, through gap and backshadow effects. Gap effect (Effect 1) explains that the BRDF effect is the result of the shading of lower canopy layers by components in the upper layers. Therefore, for a complete homogeneous vegetation canopy the minimum reflectance is observed near nadir and the maximum reflectance occurs in the highest off-nadir view angle. In some cases, the minimum reflectance occurs at an off-nadir view angle in the forward scattering direction. This is explained by a backshadow effect whichis usually the case for a dense erectophile canopy with

opaque facets. As leaves are not typically opaque, i.e. lower backshadow effect, at large viewing-illumination angles effect 1 is dominant (Sandmeier et al., 1998). The spectral behaviour of BRDF effects may be explained by multiple scattering (Sandmeier and Itten, 1999, Sandmeier et al., 1998, Kimes, 1983). In green vegetation in the red band, the absorption is high due to the existence of chrolophyll. This reduces the effect of multiple scattering that results in a higher contrast between shaded and illuminated parts. The multiple scattering effect is increased in the NIR band due to lower absorption (higher reflectance) that reduces the BRDF effects. However, both in Kimes (1983) and this study, this is the hot spot effect which varies with wavelength and not the BRDF effect in general.

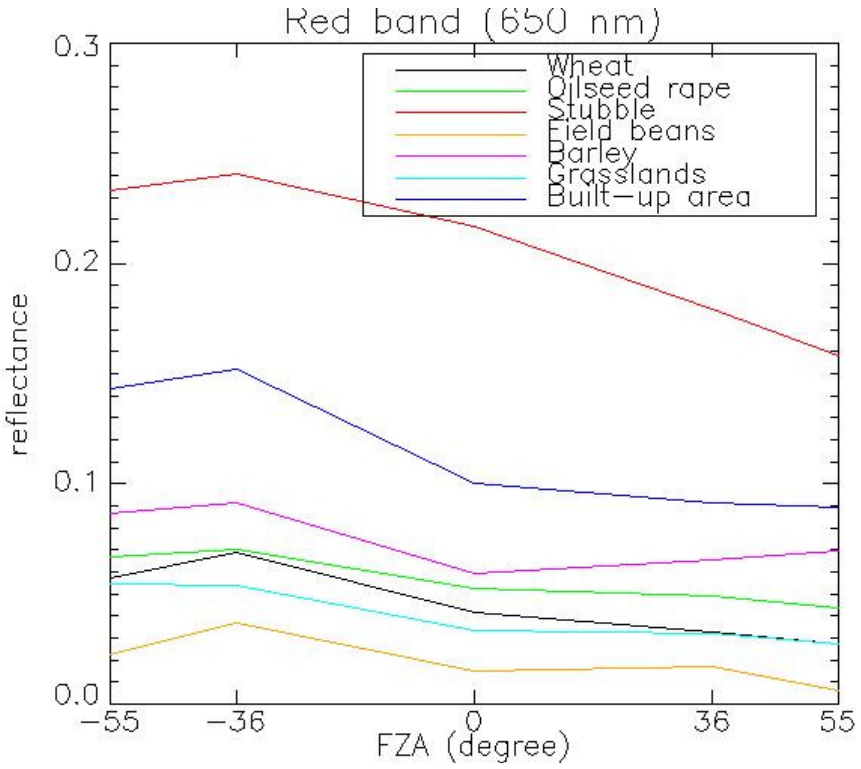

Figure 5-14 Spectral behaviour of different land covers at different CHRIS/PROBA view angles in the red band (650 nm).

All land covers, vegetation and non-vegetation, showed a peak reflectance at FZA=-36°. This was mainly due to the hot spot effect as it was the closest observation to Sun geometry. All land covers, except barley, showed the lowest reflectance at FZA=+55°. This was probably due to the greater effect of shadows at higher view zenith angles in the forward scattering direction. Barley showed the lowest reflectance at FZA=0°. This was probably due to the inhomogeneity of leaf angles which produces the highest shadow at nadir view.

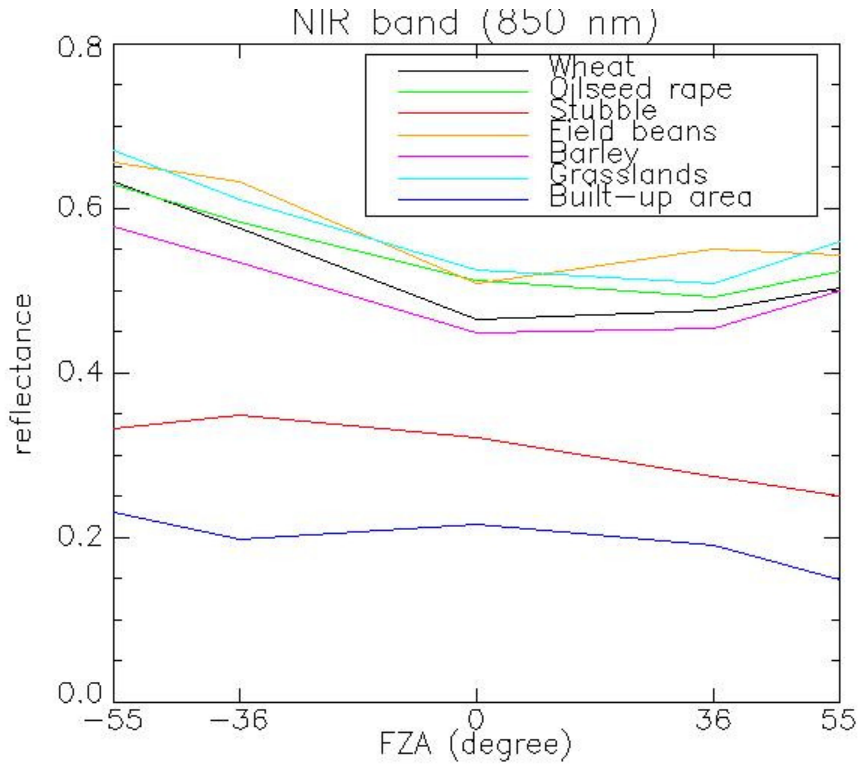

Figure 5-15 Spectral behaviour of different land covers in different CHRIS/PROBA view angles in the NIR band (850 nm).

In the NIR band, the highest reflectance in all land covers, except stubble, was observed at FZA=-55°. This showed that the hot spot effect, which is close to FZA=-36°, was less obvious in green vegetation in the NIR band. The lowest reflectance in vegetation (wheat, barley, field beans, oilseed rape, and grasslands) was at FZA=0° while in land cover with less green vegetation (stubble and built-up area) the minimum reflectance was at FZA=+55°. Another point that needs to be explained is the significance of the differences among the different land covers. Here, the mean reflectance values for each land cover were considered and the observed differences could not be explicit when comparing the reflectance of all pixels in all land covers.

To illustrate the off-nadir effects in a single attribute, an index of isotropy (IA) may be used (Milton and Rollin, 1987).

$$IA = \frac{(Max - Min) + Nadir}{Nadir}$$ **Equation 5-1**

Where Max, Min and Nadir are the spectral reflectances at the hot-spot, the cold spot, and nadir, respectively.

IA may vary for different land covers; IA=1 shows a Lambertian surface whereas IA>1 shows anisotropy of the surface. Figure 5-16 shows the IAs calculated for different

land covers. IA was calculated assuming maximum reflectances at FZA=-55°, minimum reflectances at FZA=+55°, and nadir reflectances at FZA=0°. Stubble land cover was the only land cover which was close to a Lambertian surface in the considered spectrum. Other land covers showed behaviour close to a Lambertian surface in the NIR region whereas in the visible bands (red and blue bands) there was a departure from a Lambertian surface. This spectral behaviour of the anisotropy of the surfaces was probably due to the spectral chlorophyll absorbance role which is maximum in the red and blue bands.

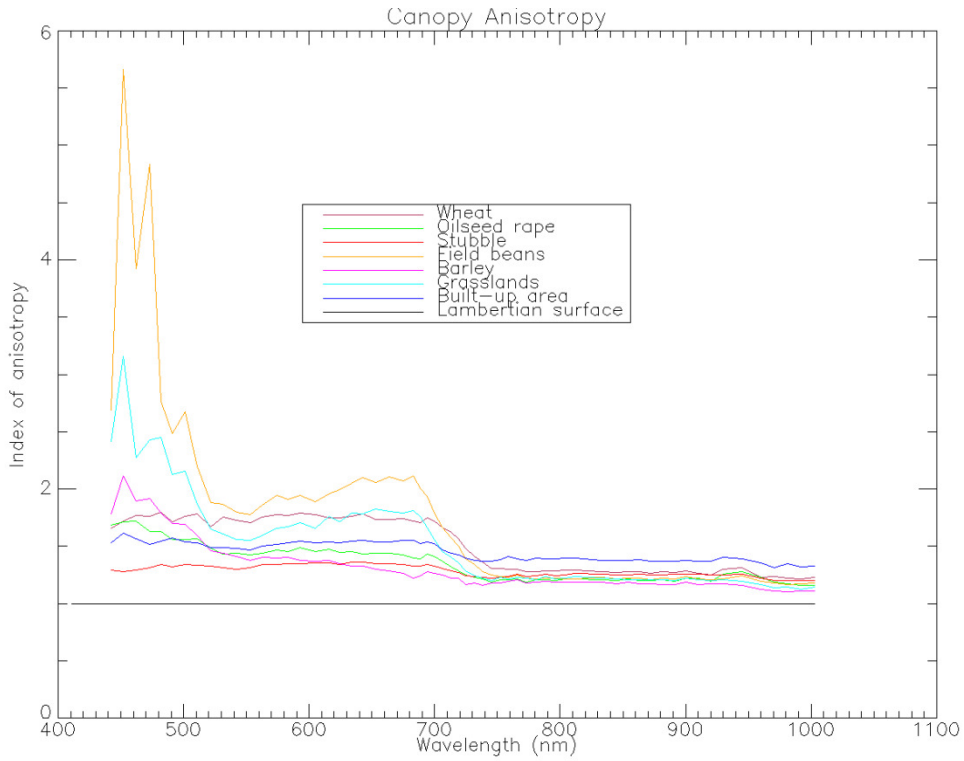

Figure 5-16 Index of anisotropy for different land covers.

It is evident from these results that the MVA characteristics of the land cover classes fall into three broad response types. First, the vegetated surfaces (wheat, oilseed rape, grass, barley and beans) all have highest reflectance in all wavelengths in the backscatter direction, especially at -55°. The reflectance of the vegetated classes at nadir and forward-scatter geometries is lower and less variable with view angle. The second type of response comprises the stubble class. In this, the contrast between backscatter and forward scatter responses is less systematic. The highest reflectance at all wavelengths is found for -36° and -55°, with that from +36° and +55° being markedly lower. The third type of response is found from the built-up class. The spectra from this class are the most variable with view angle, probably due to the

different proportions of vegetation and bare surface presented to the sensor at each view angle.

5.5 Albedo maps

Figures 5.17 to 5.22 show the distribution of the categorised visible, NIR and broadband albedos across the study site. Albedo, may vary according to factors such as wavelength, the transmissibility of the leaf, leaf arrangement and inclination, plant density and the Sun angle (Dickinson, 1983). Here, the changes in albedo due to the transmissibility of the canopy were discussed.

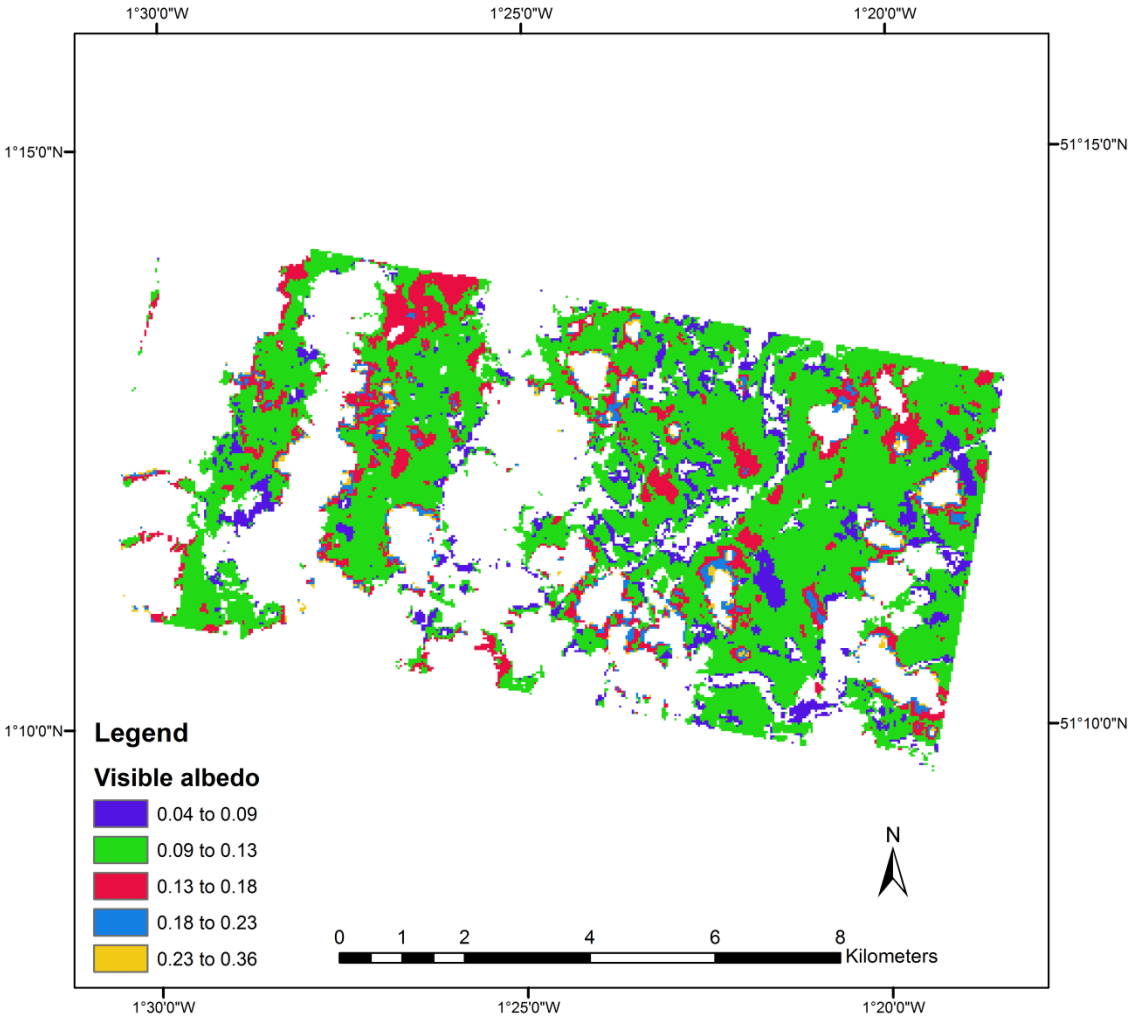

Figure 5-17 Visible albedo map

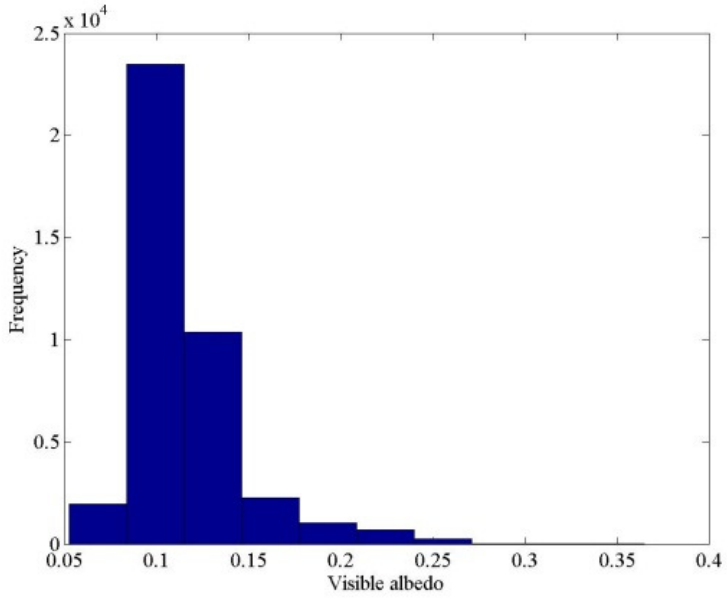

Figure 5-18 Histogram of visible albedo.

Although there was a wide range of visible albedo values (0.04-0.36), most of the area showed a low visible albedo of 0.09-0.13 (Figure 5-17 and Figure 5-18). The pixels with visible albedo greater than 0.23 were most likely undetected clouds.
The low visible albedo values can be due to an increase in the biomass of vegetation cover (Bray et al., 1966) which causes an increase in the chlorophyll a+b content. Chlorophyll absorbs most of the incident irradiance in blue and red bands (Mavi and Tupper, 2004). However, factors such as the light saturation of chlorophyll and the exposure of the soil background may mask this effect. The effect of these factors on the study site can be explored using remote sensing indexes that show the effect of soil background such as vegetation fractional cover (North, 2002) and chlorophyll such as the MERIS terrestrial chlorophyll index (MTCI) (Dash and Curran, 2004).

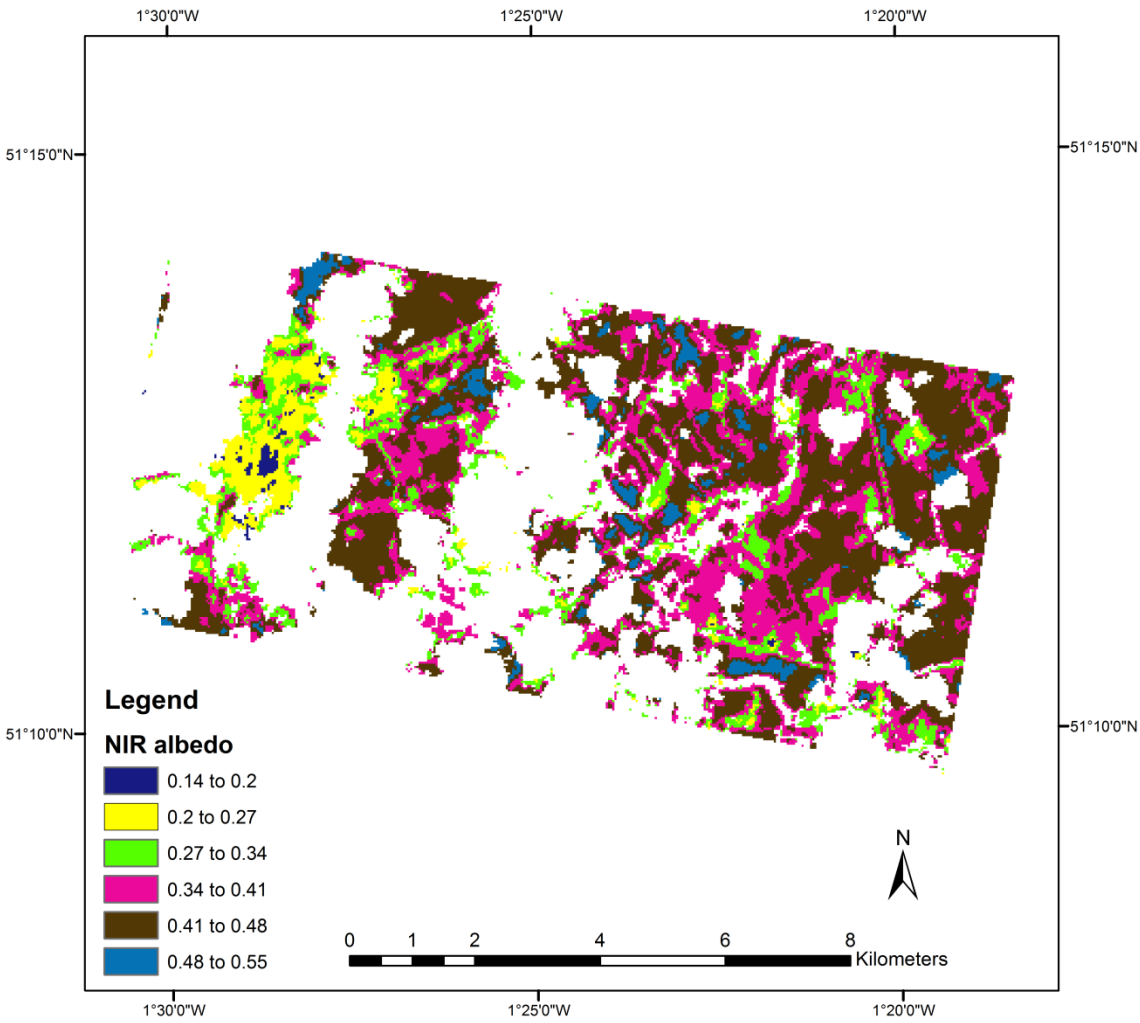

Figure 5-19 NIR albedo map

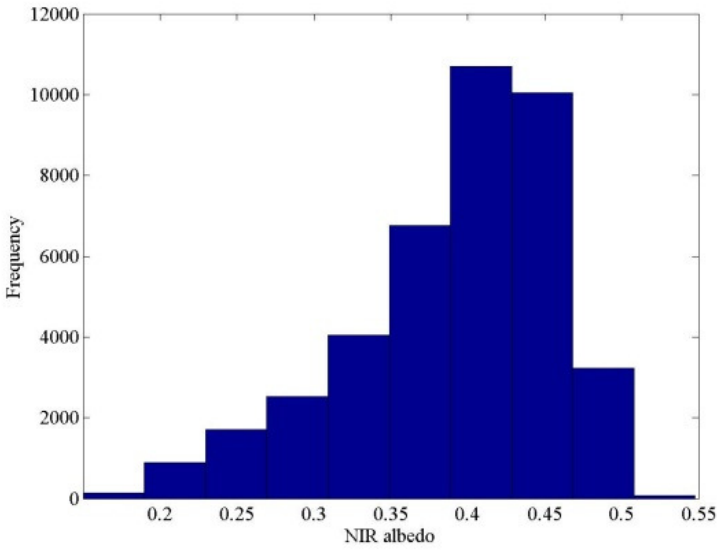

Figure 5-20 Histogram of NIR albedo.

Most of the area had a NIR albedo of 0.34 to 0.45 (Figure 5-19 and Figure 5-20). Green vegetation showed higher NIR albedo (greater than 0.3) than the built-up area and stubble (less than 0.3) land covers. This is mainly due to the cellular structure of the leaves in the plant canopies which controls the amount of air space inside the leaves (Atazadeh, 2011). NIR albedo had a wider range of values than visible albedo. This can be due to the variation in the cellular structure of different vegetation types and/or surface moisture.

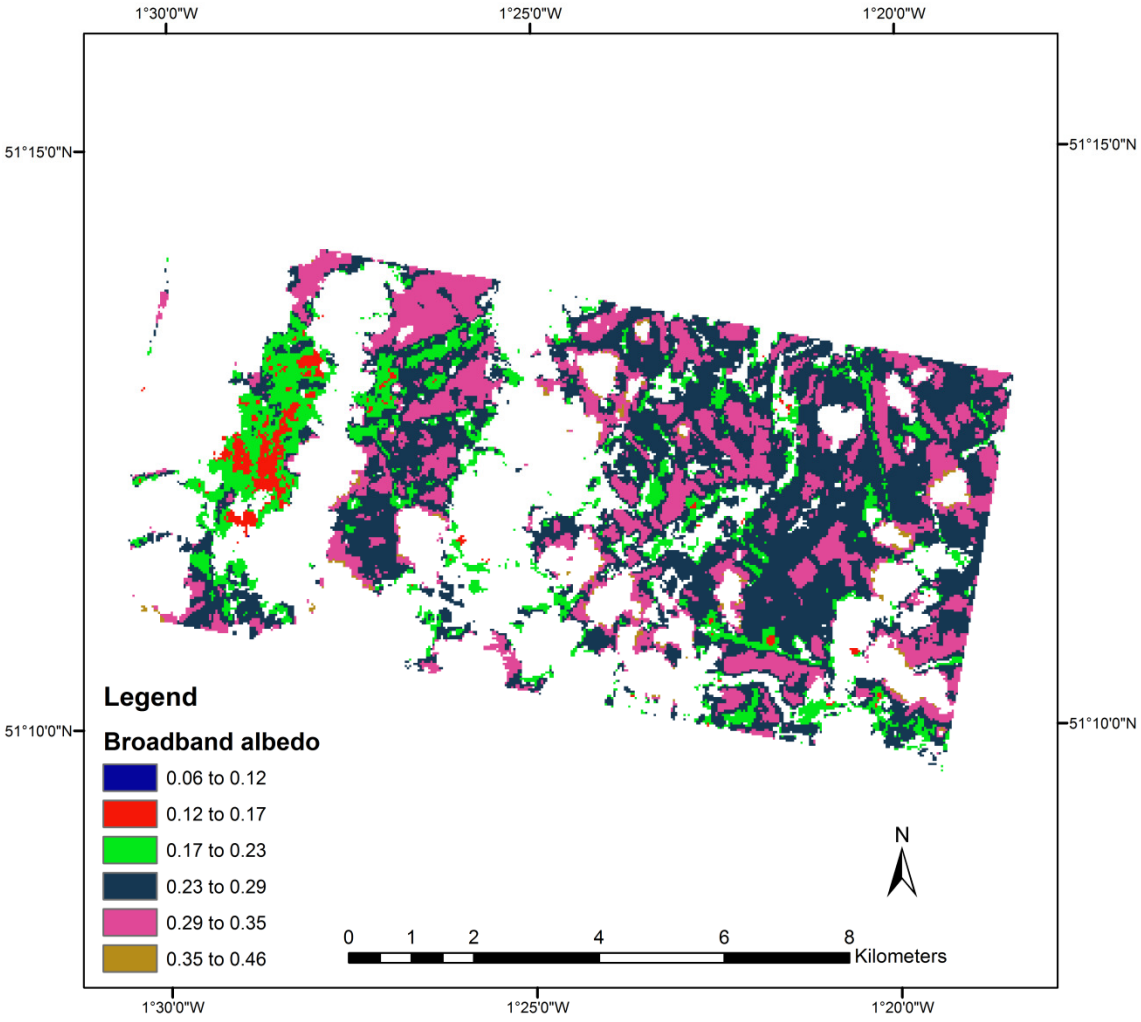

Figure 5-21 Broadband albedo map

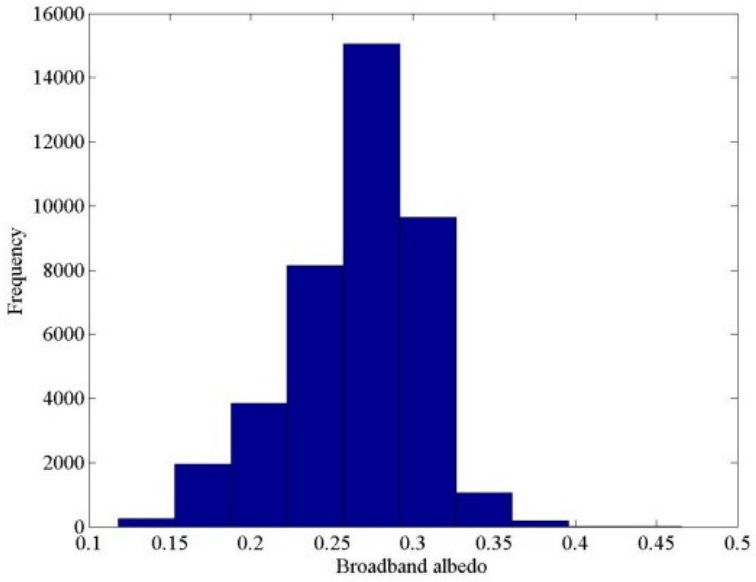

Figure 5-22 Histogram of broadband albedo.

The broadband albedo showed values ranging from 0.06 to 0.46 (Figure 5-21 and Figure 5-22). Built-up area had lower albedo values (mostly less than 0.23) while vegetation showed higher albedo values (0.23 to 0.35). Albedo values greater than 0.35 were probably undetected clouds.

5.6 Relationship between directional reflectance and albedo

5.6.1 Relationship between directional reflectances and albedo without using a land cover map

Appendix 2 shows the scatterplots of CHRIS/PROBA reflectance and spectral black sky albedo in different view geometries. Figure 5-23 summarises the obtained results comparing the R-squared and RMSE values of the applied linear regression model.

Table 5-4 RMSE (and linear regression parameters) of the estimated albedos with respective to directional reflectances in different spectral bands.

FZA	Band	R-squared (%)	slope	intercept	RMSE	RMSE (%)
0	Visible	10	0.27	0.09	0.04	40
0	NIR	27	0.64	0.16	0.07	19
0	Broadband	11	0.36	0.18	0.05	21
36	Visible	19	0.40	0.07	0.04	38

36	NIR	62	0.89	0.09	0.07	19
36	Broadband	42	0.71	0.10	0.05	20
-36	Visible	12	0.27	0.08	0.05	36
-36	NIR	55	0.82	0.04	0.06	13
-36	Broadband	29	0.56	0.10	0.05	16
55	Visible	33	0.72	0.05	0.04	42
55	NIR	83	0.84	0.10	0.06	16
55	Broadband	71	0.80	0.08	0.04	19
-55	Visible	85	0.61	0.03	0.03	24
-55	NIR	84	0.90	0.00	0.05	12
-55	Broadband	80	0.79	0.03	0.04	13

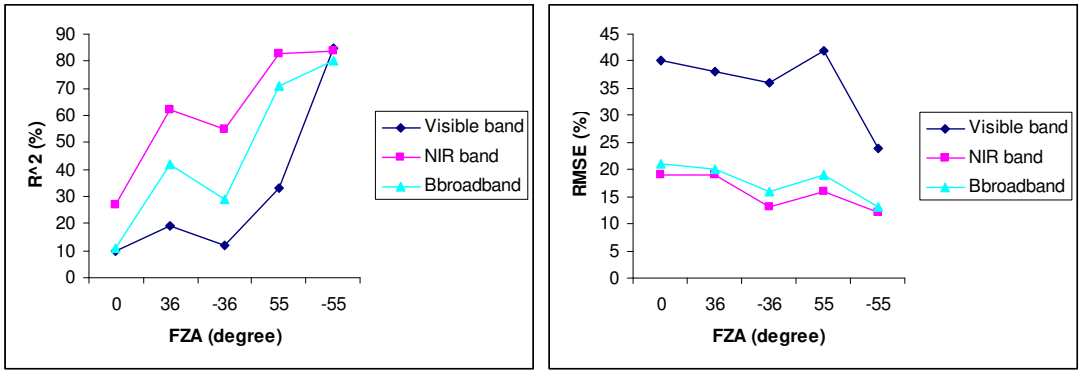

Figure 5-23 R-squared and percentage of median RMSE of estimated albedo with respect to directional reflectances in different spectral bands.

The following points are then derived:
As the view zenith angle increases, the correlation between reflectance and albedo increases. The at-nadir reflectance and the reflectance at FZA=-55° have the minimum and maximum linear relationship with albedo, respectively. The agreement also depends on the azimuth view angle. From among all five view angles, the best agreement between reflectance and albedo was observed at the backscattering direction, FZA=-55°. Although the R-squared value for FZA=-36° is lower than that for FZA=36°, the distribution of the data (Appendix 2) shows a slightly better agreement at FZA=-36° (less RMSE).

The amount of error in the predicted albedo was minimal at the backscattering direction (FZA=-36° and FZA=-55°), about 15% in broadband albedo. This shows that albedo can be retrieved with higher accuracy, up to 5%, at higher view zenith angles in the back scattering direction.

The better agreement between the albedo and reflectance at FZA=-55° was probably due to the higher contribution of the reflectances observed at this view angle in calculating albedo. Reflectances at the backscattering direction were higher than albedo whereas it was opposite in the forward scattering direction. This higher contribution can be due to having higher reflectances. If this is true, then more observations at higher view zenith angles are required in albedo calculations.

The relationship between reflectance and albedo varied in different spectral bands. The agreement was higher in the NIR than the visible region. This was mainly due to the higher variations of albedo values in NIR. The agreement might have been higher in the visible bands if there were a variety of land covers with a wider range of reflectances such as water, bare soils, crops, and forest.

The amount of error in the predicted albedo using the NIR bandwas about half of the observed errors in the visible band. This showed that, although the agreement of albedo and reflectance was lower in the visible than NIR band, the retrieved visible albedo had a higher accuracy in the visible band.

5.6.2 Relationship between directional reflectances and albedo using a land cover map

Appendix 3 shows the scatterplots of different directional CHRIS/PROBA reflectance and spectral black sky albedo values in different land covers. Figure 5-24 summarises the obtained results comparing the R-squared and RMSE values of the applied linear regression model for different land covers.

Table 5-5 RMSE (and linear regression parameters) of the estimated albedos with respective to directional reflectances in different land covers and different spectral bands.

FZA	Band	Land cover	R-squared	Slope	Intercept	RMSE	Median RMSE (%)
0	Visible	Oilseed rape	3	0.54	0.07	0.03	120
0	NIR	Oilseed rape	5	0.30	0.31	0.04	61
0	Broadband	Oilseed rape	6	0.36	0.20	0.03	67
36	Visible	Oilseed rape	9	0.46	0.08	0.03	64
36	NIR	Oilseed rape	34	0.67	0.18	0.06	66
36	Broadband	Oilseed rape	30	0.65	0.13	0.04	67
-36	Visible	Oilseed rape	1	0.10	0.11	0.03	52
-36	NIR	Oilseed rape	17	0.46	0.22	0.04	48

-36	Broadband	Oilseed rape	8	0.31	0.20	0.04	53
55	Visible	Oilseed rape	25	0.63	0.06	0.03	58
55	NIR	Oilseed rape	64	0.62	0.19	0.05	42
55	Broadband	Oilseed rape	56	0.62	0.13	0.04	47
-55	Visible	Oilseed rape	84	0.59	0.04	0.03	26
-55	NIR	Oilseed rape	60	0.68	0.11	0.05	46
-55	Broadband	Oilseed rape	63	0.64	0.08	0.04	44
0	Visible	Wheat	2	0.41	0.08	0.04	158
0	NIR	Wheat	5	0.27	0.33	0.09	95
0	Broadband	Wheat	5	0.30	0.21	0.06	106
36	Visible	Wheat	6	0.32	0.08	0.04	63
36	NIR	Wheat	30	0.60	0.22	0.08	78
36	Broadband	Wheat	21	0.51	0.16	0.06	79
-36	Visible	Wheat	2	0.10	0.10	0.05	43
-36	NIR	Wheat	21	0.45	0.23	0.04	39
-36	Broadband	Wheat	5	0.19	0.23	0.04	44
55	Visible	Wheat	12	0.59	0.06	0.04	78
55	NIR	Wheat	61	0.71	0.16	0.06	48
55	Broadband	Wheat	44	0.70	0.11	0.05	62
-55	Visible	Wheat	90	0.57	0.03	0.03	23
-55	NIR	Wheat	71	0.72	0.09	0.05	37
-55	Broadband	Wheat	78	0.65	0.08	0.04	35
0	Visible	Bare soil	20	0.49	0.07	0.04	41
0	NIR	Bare soil	37	0.62	0.13	0.05	33
0	Broadband	Bare soil	38	0.54	0.11	0.04	28
36	Visible	Bare soil	40	0.68	0.05	0.03	31
36	NIR	Bare soil	57	0.81	0.10	0.06	38
36	Broadband	Bare soil	50	0.72	0.09	0.04	36
-36	Visible	Bare soil	35	0.49	0.06	0.05	40
-36	NIR	Bare soil	51	0.68	0.08	0.06	34
-36	Broadband	Bare soil	40	0.56	0.08	0.05	42
55	Visible	Bare soil	57	0.92	0.04	0.03	41
55	NIR	Bare soil	78	0.91	0.07	0.05	34
55	Broadband	Bare soil	69	0.89	0.06	0.04	40
-55	Visible	Bare soil	89	0.68	0.03	0.03	24
-55	NIR	Bare soil	87	0.81	0.02	0.05	28
-55	Broadband	Bare soil	87	0.74	0.03	0.04	30
0	Visible	Grassland	2	0.30	0.08	0.03	87

0	NIR	Grassland	8	0.37	0.25	0.06	47
0	Broadband	Grassland	8	0.36	0.17	0.04	49
36	Visible	Grassland	6	0.21	0.09	0.03	41
36	NIR	Grassland	43	0.72	0.14	0.06	42
36	Broadband	Grassland	28	0.55	0.13	0.04	43
-36	Visible	Grassland	3	0.13	0.09	0.05	45
-36	NIR	Grassland	33	0.66	0.10	0.07	47
-36	Broadband	Grassland	16	0.41	0.14	0.05	52
55	Visible	Grassland	19	0.60	0.06	0.03	61
55	NIR	Grassland	75	0.72	0.14	0.06	29
55	Broadband	Grassland	63	0.70	0.10	0.04	36
-55	Visible	Grassland	85	0.57	0.04	0.03	22
-55	NIR	Grassland	73	0.83	0.03	0.06	35
-55	Broadband	Grassland	72	0.73	0.05	0.04	34
0	Visible	Built-up	11	0.22	0.10	0.08	42
0	NIR	Built-up	37	0.41	0.16	0.08	27
0	Broadband	Built-up	29	0.32	0.14	0.08	32
36	Visible	Built-up	43	0.53	0.07	0.04	26
36	NIR	Built-up	54	0.70	0.10	0.06	26
36	Broadband	Built-up	48	0.60	0.10	0.04	25
-36	Visible	Built-up	52	0.48	0.06	0.06	29
-36	NIR	Built-up	66	0.62	0.08	0.07	27
-36	Broadband	Built-up	60	0.55	0.08	0.06	30
55	Visible	Built-up	62	0.86	0.05	0.04	35
55	NIR	Built-up	80	0.93	0.07	0.06	29
55	Broadband	Built-up	73	0.92	0.06	0.05	33
-55	Visible	Built-up	85	0.64	0.04	0.04	19
-55	NIR	Built-up	89	0.75	0.04	0.06	23
-55	Broadband	Built-up	89	0.70	0.04	0.05	23
0	Visible	Field beans	0	0.21	0.09	0.03	144
0	NIR	Field beans	1	0.11	0.40	0.07	80
0	Broadband	Field beans	0	0.07	0.27	0.05	90
36	Visible	Field beans	6	0.39	0.07	0.03	65
36	NIR	Field beans	48	0.75	0.15	0.06	52
36	Broadband	Field beans	37	0.72	0.11	0.04	59
-36	Visible	Field beans	2	0.13	0.09	0.04	45
-36	NIR	Field beans	23	0.55	0.19	0.05	41
-36	Broadband	Field beans	9	0.31	0.19	0.04	47

55	Visible	Field beans	17	0.69	0.05	0.03	72
55	NIR	Field beans	75	0.77	0.13	0.05	33
55	Broadband	Field beans	63	0.77	0.09	0.04	43
-55	Visible	Field beans	91	0.59	0.03	0.03	21
-55	NIR	Field beans	72	0.84	0.04	0.04	32
-55	Broadband	Field beans	74	0.75	0.05	0.03	32
0	Visible	Barley	1	0.17	0.10	0.03	72
0	NIR	Barley	16	0.59	0.17	0.06	53
0	Broadband	Barley	12	0.48	0.14	0.04	53
36	Visible	Barley	10	0.29	0.09	0.03	39
36	NIR	Barley	52	0.83	0.11	0.07	42
36	Broadband	Barley	36	0.64	0.11	0.05	43
-36	Visible	Barley	7	0.24	0.08	0.04	46
-36	NIR	Barley	46	0.75	0.07	0.06	36
-36	Broadband	Barley	26	0.55	0.10	0.05	45
55	Visible	Barley	26	0.65	0.06	0.03	53
55	NIR	Barley	80	0.82	0.11	0.06	29
55	Broadband	Barley	69	0.78	0.09	0.04	36
-55	Visible	Barley	83	0.60	0.03	0.03	23
-55	NIR	Barley	81	0.88	0.00	0.05	30
-55	Broadband	Barley	78	0.77	0.03	0.04	31

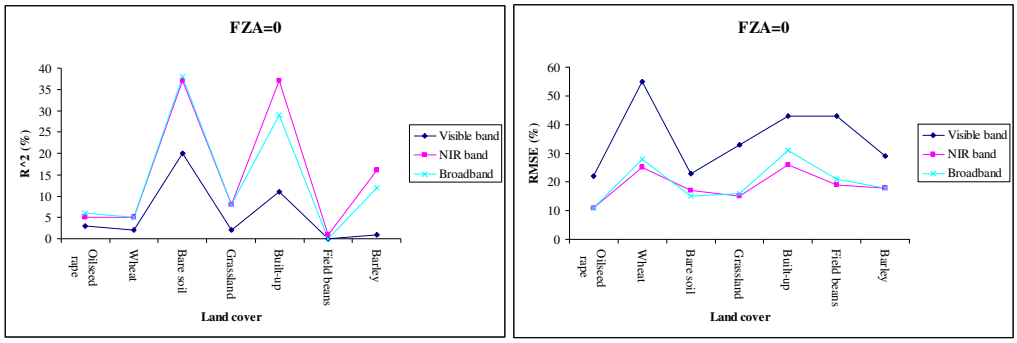

Figure 5-24 R-squared and percentage of median RMSE of estimated albedo with respect to reflectance at FZA=0° in different spectral bands and in different land covers.

The agreement between albedo and reflectance at FZA=0° was low in all land covers. This shows a higher dependence of the accuracy of the obtained albedo on view geometry than land cover type. Non-green vegetation land covers, stubble and built-up area, had a greater level of agreement with albedo than with green vegetation. This

was partly due to the higher variation in reflectance/albedo values in stubble and built-up land covers.

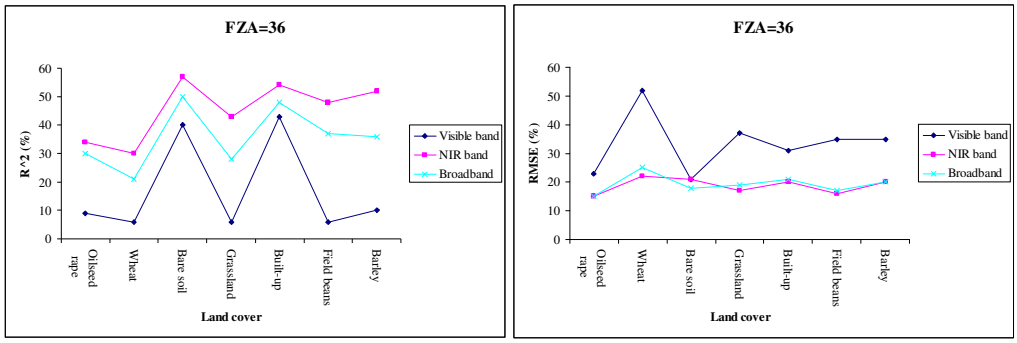

Figure 5-25 R-squared and percentage of median RMSE of estimated albedo with respect to reflectance at FZA=36° in different spectral bands and in different land covers.

The agreement between albedo and reflectance at FZA=36° was higher than FZA=0°. This was probably due to slightly higher reflectance values at this view angle. Here, as was also seen at FZA=0° as well, non-green vegetation land covers, stubble and built-up area, had greater agreement with albedo than with green vegetation. However, despite what was seen at FZA=0°, the levels of agreement between the albedo and reflectance seen in stubble and built-up areas were quite similar. The agreement between NIR albedo and reflectance in some land covers, field beans and wheat, considerably increased in relation to the observed agreement at FZA=0°. This was most likely due to higher reflectance values which show albedo can be quite sensitive to slight variations in the reflectance in the NIR band. This caused a higher level of agreement between broadband albedo and reflectance, despite a low level of agreement in the visible band. The RMSE of estimated broadband albedo and reflectance was similar in all land covers, about 20%, despite different RMSEs in the visible band. This was probably as a result of lower variation in the agreement between NIR albedo and reflectance at this view angle.

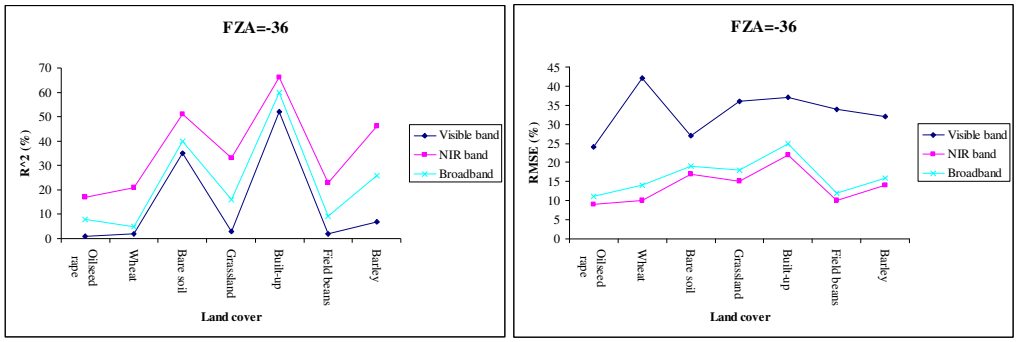

Figure 5-26 R-squared and percentage of median RMSE of estimated albedo with respect to reflectance at FZA=-36° in different spectral bands and in different land covers.

The agreement between albedo and reflectance at FZA=-36° was slightly higher than FZA=36°, probably due to higher reflectance values. Non-green vegetation land covers, stubble and built-up area, had greater levels of agreement with albedo than green vegetation (Figure 5-26). The agreement was slightly higher in built-up areas than stubble, in contrast to that seen at FZA=0°. This may be due to the effect of green vegetation, which was part of the built-up area, in this view angle. The RMSE of the NIR albedo with respect to reflectance was higher in non-green vegetation. This was probably due to higher variation of reflectance values at this view angle in stubble and built-up areas. The RMSE of visible albedo, however, was low in stubble land cover, probably caused by higher reflectance values when compared to those of green vegetation.

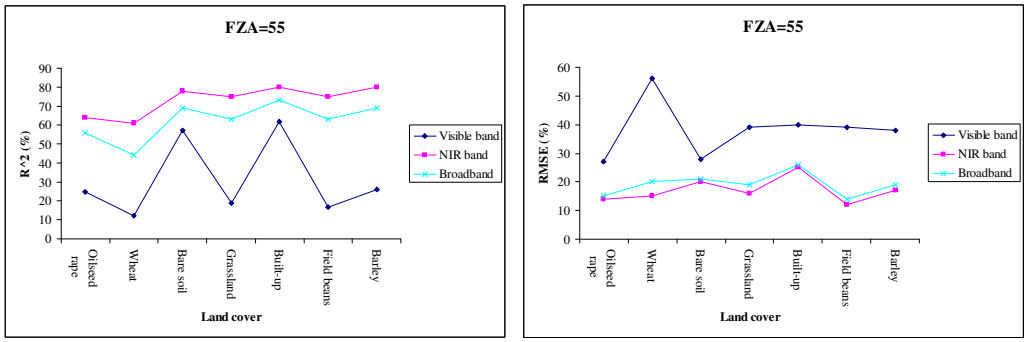

Figure 5-27 R-squared and percentage of median RMSE of estimated albedo with respect to reflectance at FZA=55° in different spectral bands and in different land covers.

The agreement between albedo and reflectance at FZA=55° was higher than those with lower view zenith angles (Figure 5-27). The agreement was quite high in the NIR band in all land covers. to the most likely reason for this was the higher variation of reflectance values in the NIR band. Non-green vegetation land covers showed higher

agreement between visible albedo and reflectance, probably due to greater variation of the reflectance values.

The RMSE of NIR albedo with respect to reflectance showed a difference of up to 10% in different land covers. Among green vegetation, field beans had the least RMSE, about 10%, while the highest RMSE belonged to built-up areas.

The RMSE of visible albedo was highest in wheat. As Appendix 3 (Figure A3.10) shows reflectances with magnitudes of 0.05 to 0.1 were responsible for this high RMSE. The pixels with those reflectances had higher reflectance values when observed at FZA=-55° while having lower reflectances at other view angles.

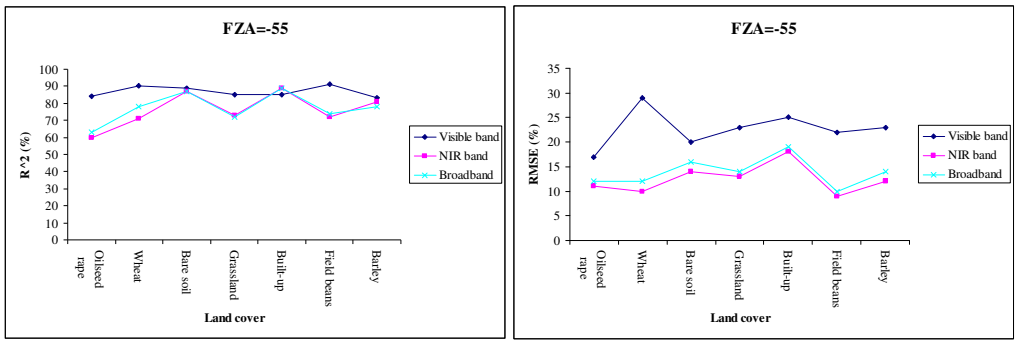

Figure 5-28 R-squared and percentage of median RMSE of estimated albedo with respect to reflectance at FZA=-55° in different spectral bands and in different land covers.

The agreement between albedo and reflectance at FZA=-55° was the highest among all five view angles (Figure 5-28). Despite other view angles, the agreement in the visible band was higher than the NIR band, particularly for in green vegetation. This was due to higher observed reflectance values for those pixels, especially in green vegetation but also in non-green vegetation, which had lower reflectances at other view angles. Lower reflectance values in these pixels were the main reason for the lower levels of agreement and higher RMSE of the obtained albedo at other view angles. Greater exposure of the surfaces with higher reflectance such as dry background soil, dried or yellow stems etc., may explain this behaviour. The agreement in the NIR band was the lowest in green vegetation, oilseed rape, and was highest in non-green vegetation. The lower agreement in oilseed rape was due to the pixels with lower reflectance values at this view angle, 0.3-0.4. These pixels showed higher reflectance values at the lower view zenith angles. The obtained albedo apparently had a higher agreement with the directional reflectances with higher reflectance values. The RMSE of the NIR albedo in respect to reflectance varied from 8%, in field bean, up to 15%, in built-up area.

The following points can be derived from the results:
The agreement between albedo and reflectance in all spectral bands and in all land covers was highest at FZA=±55°. This was probably due to the higher intensity of reflectance at higher view zenith angles. The agreement was slightly better at FZA=-55°.

The agreement between albedo and directional reflectance was slightly improved when the agreement was sought in the individual land covers. The land cover map served principally to obtain a better knowledge of the errors in the data. The assessment of the applied linear model showed that some classes, wheat and built-up land covers, had larger RMSEs which caused a higher general RMSE when a land cover map was not used. There was therefore a decrease in the deviations from the obtained linear regression model in some classes when a land cover map was used.

The agreement between albedo and directional reflectance in vegetation was higher in the NIR albedo than the visible and broadband regions. This was mainly due to the higher range of values in NIR as well as higher reflectance intensity.

The broadband albedo, here, resulted from the integration of spectral albedo in the visible and NIR bands (400 nm- 1000 nm) and may be different with the shortwave albedo which covers wavelengths 200 nm to 3000 nm. Considering the spectra of vegetation and bare soil, which have spectral behaviour approximately similar to that of stubble, in the range of 200 nm to 3000 nm from the literature (http://www.aai.ee/bgf/ger2600/), the actual broadband albedos of vegetation (200 nm- 3000 nm) may be about 20% higher than the estimated albedo in the spectral range of 400 nm to 1000 nm. The calculated broadband albedo of bare soil, as well as stubble, (400 nm- 1000 nm) may be about 40% lower than the actual broadband albedo (200 nm- 3000 nm).

5.7 Spatial variability of albedo

The results from the comparison of the albedo in different land covers showed that the spectral behaviour of surface albedo was similar to the surface reflectance (Figure 5-7 to Figure 5-15).

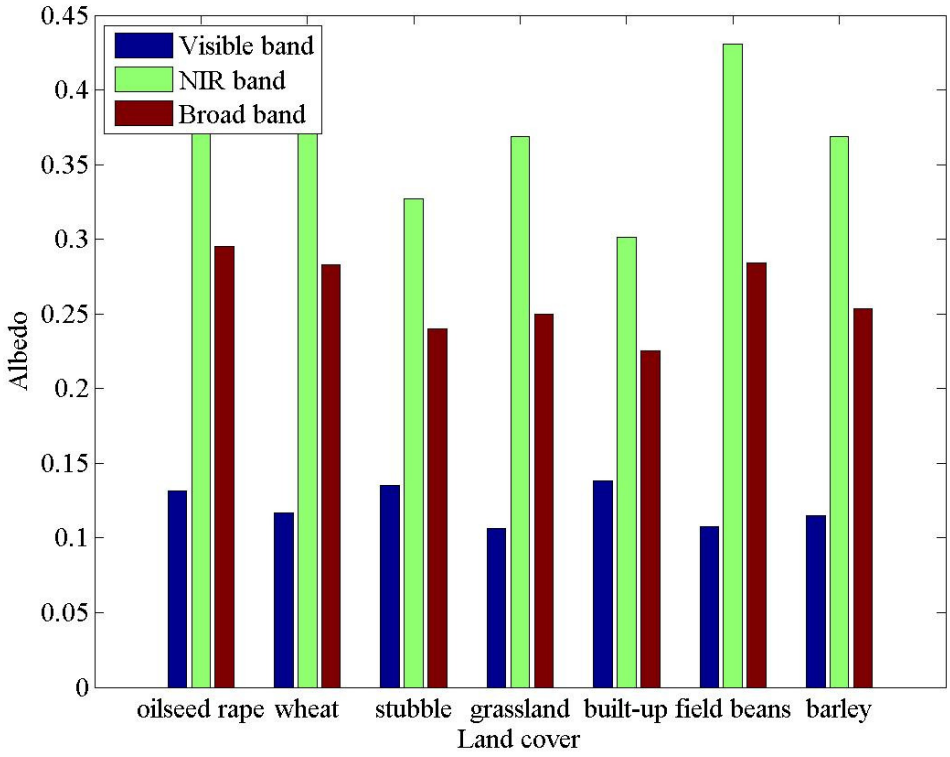

Figure 5-29 Mean values of visible, NIR and broadband albedo in different land covers.

The stubble and built-up land covers showed higher visible albedos but lower NIR and broadband albedos relative to the green vegetation (Figure 5-29). The oilseed rape and field beans land covers had the maximum albedo in the NIR band while the built-up class had the minimum NIR albedo.

Broadband albedos were higher in green vegetation than land covers with no vegetation due to higher NIR reflectances. While in the visible and NIR bands, the albedo values were different in the stubble and grassland land covers, the broadband albedos of these two classes were similar. This showed that for classification purposes, the use of broadband albedo can be less useful than spectral albedo.

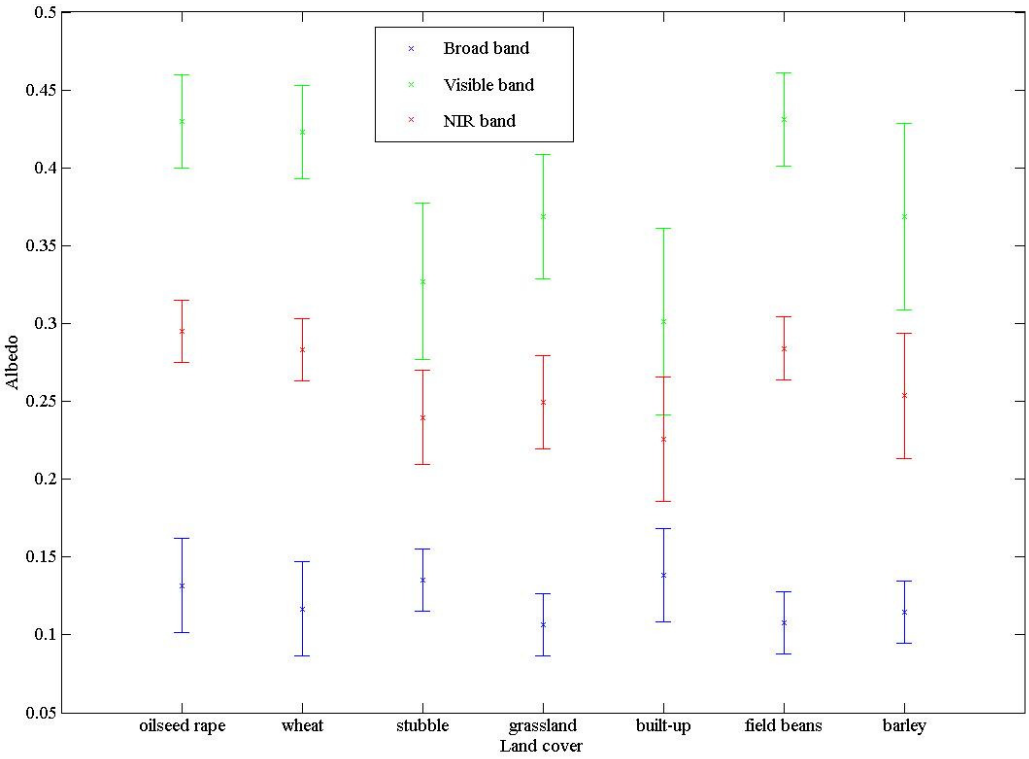

Figure 5-30 The error in the visible, NIR and broadband albedos in different land covers. The error bars show ±1 standard deviation.

The deviation from the mean values of NIR and broadband albedos was highest in the barley and built-up classes and lowest in the field beans, oilseed rape and wheat land covers (Figure 5-30).

Table 5-6 Mean and standard deviation (SD) values of visible, NIR and broad bands albedo in different land covers.

Land cover	Visible		NIR		Broadband	
	Mean	SD	Mean	SD	Mean	SD
Oilseed rape	0.13	0.03	0.43	0.03	0.30	0.02
Wheat	0.12	0.03	0.42	0.03	0.28	0.02
Stubble	0.14	0.02	0.33	0.05	0.24	0.03
Grassland	0.11	0.02	0.37	0.04	0.25	0.03
Built-up	0.14	0.03	0.30	0.06	0.23	0.04
Field beans	0.11	0.02	0.43	0.03	0.28	0.02
Barley	0.11	0.02	0.37	0.06	0.25	0.04

Figures 5-31 shows how visible, NIR and broadband albedos vary between the different fields of each land cover. A field consists of adjacent pixels with the same land cover.

The albedo value for most crops at full cover was reported as 0.26 (Monteith, 1959, Piggin and Schwerdtfeger, 1973). However, this may vary for each land cover. Surface spatial heterogeneity may be due to the variation in soil depth (Kershaw, 1959), topography (Greig-Smith, 1961), soil nutrients (Galiano, 1985), positions of subsurface rocks (Usher, 1983), crop height, leaf area index (LAI), rainfall, soil moisture (Piggin and Schwerdtfeger, 1973) and so on.

Due to the small size of the study site, the main reason for the spatial variation in the albedo can be misclassification and/or the slight variation in topography and soil moisture. To minimise the misclassification error, only large fields, greater than 4.5 hectares in size, were assessed for the spatial variability of albedo. It was assumed that the accuracy of the classification of larger fields was higher due to a better visual assessment as well as being close to the size of the actual fields.

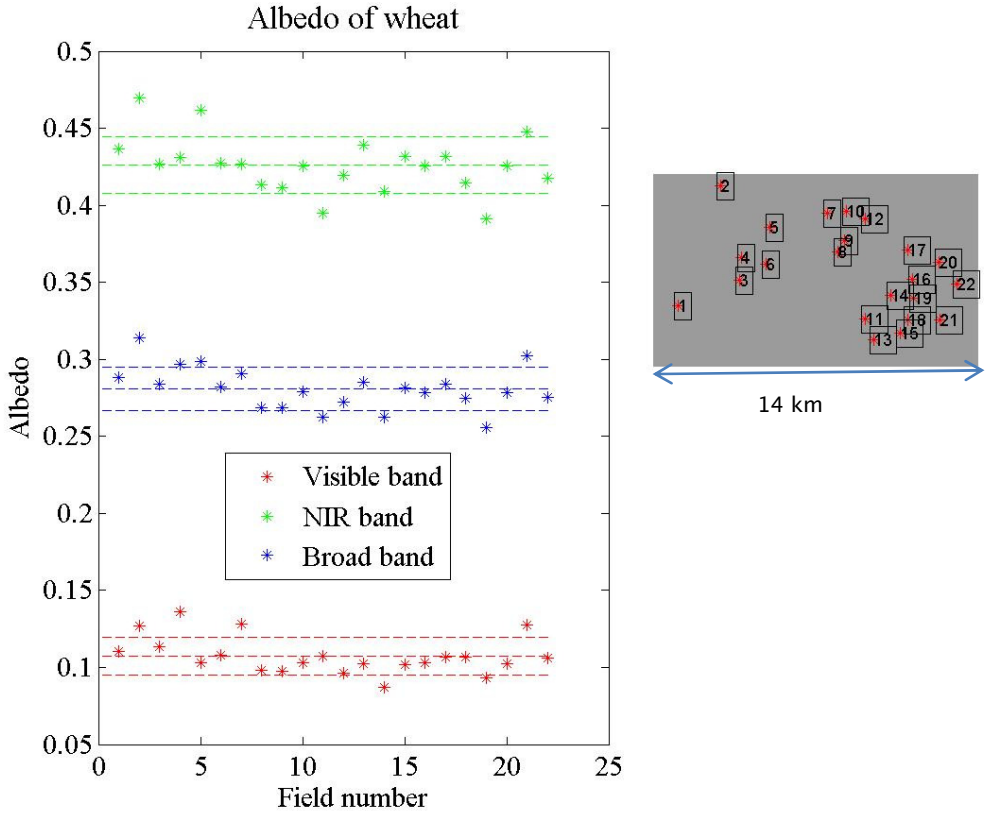

Figure 5-31 Albedo of different fields of wheat class in visible, NIR and broad bands. The dotted line shows the mean and one standard deviation from the mean value. The image on the right shows the distribution of fields on the image.

Monteith as reported by Piggin and Schwerdtfeger (1973) measured the albedo of winter wheat in different seasons in England. He observed an increase in albedo as LAI increased with maximum albedo, 0.27, at the end of May. This was quite similar to the obtained mean broadband albedo, 0.28 on 17 July 2006, in our study site. Huawei et al. (2004) studied the temporal variation of winter wheat albedo in China. The albedo

values varied from 0.1 on DOY 150 to 0.23 on DOY 125; the albedo value on DOY 168, the same day as the retrieved albedo map in Chilbolton, was 0.17. The albedo values in the wheat class in this study on DOY 168 varied from 0.25 to 0.32. This may indicate that the albedo was overestimated in our study. However, the variations of climate conditions, surface moisture, topography, and variety type may cause high variations in albedo values. The computed albedo by Huawei et al. was mean daily albedo while the computed albedo at our study site was a snapshot at the time of satellite overpass. In addition, as the spatial variation of the albedo showed, even in a small study site, albedo may vary by as much as 0.07. Regarding the adjacent cloud/shadow clouds effects, only fields 2, 4, 7 and 21 were adjacent to clouds, in almost all view angles, which may explain the slight increase in the albedo values. The spectra of wheat and barley are very similar, however, the albedo value would probably be lower for wheat than barley in full cover conditions (Piggin and Schwerdtfeger, 1973). This is due to the difference in the shape of these crops when they ripen. Ripe wheat stands upright exposing a greater soil area whereas ripe barley tends to bend over at the top covering the ground more effectively. Wheat, however, showed slightly higher albedo values than barley. This was probably due to the different growth speeds of these two crops.

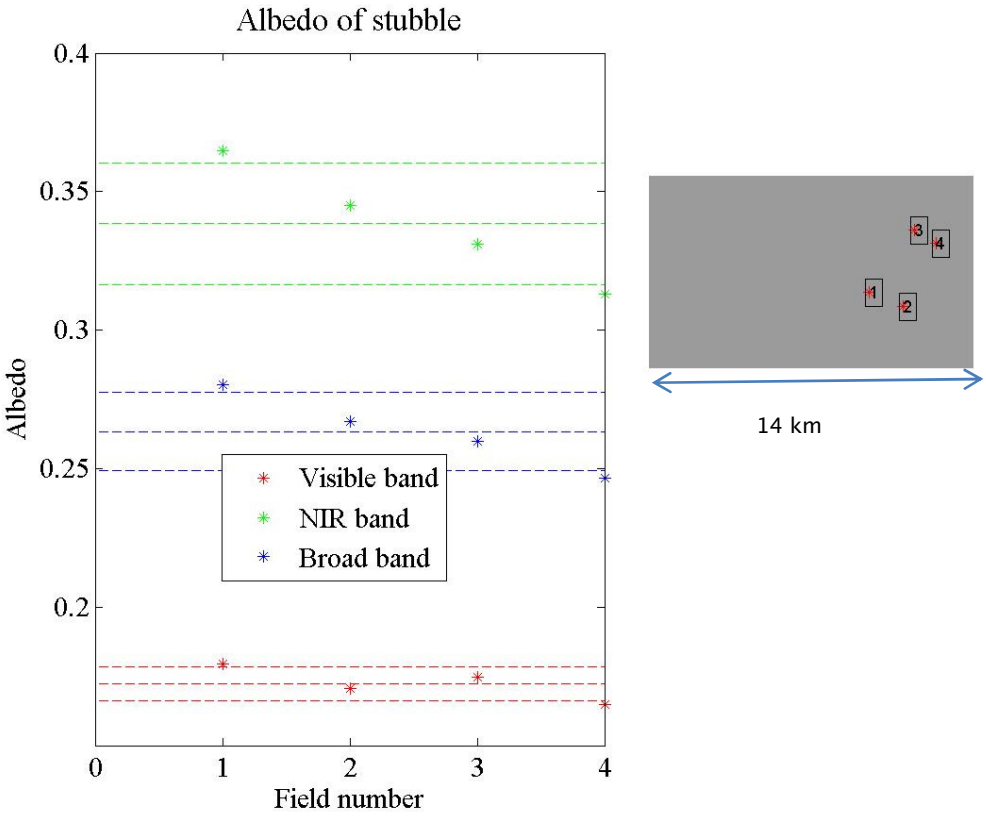

Figure 5-32 Albedo of different fields of stubble class in visible, NIR and broad bands.

The mean broadband albedo value of the stubble class was 0.26. Piggin and Schwerdtfeger (1973) measured a higher albedo value, 0.34, for the barley stubble in late December after harvesting, while other studies reported lower albedo values, 0.15 to 0.2, for stubble (Barry and Chambers, 1966, Wijk, 1963). Different Sun geometry, measuring of albedo at the time of satellite overpass instead of daily mean albedo, and different spectral range may be the reasons for observing different albedos. The spatial variation in stubble albedo in our case study may be due to the variation in surface moisture and the variation in the coverage of stubble due to winds and cattle grazing. Other reasons may be the adjacency of the different fields with clouds/shadow clouds. Although fields 1 and 2 were nearly adjacent to each other, they had a high variation in albedo values. A visual assessment of these fields in all five view angle datasets showed adjacent pixels are cloud-free in all view angles with the exception of FZA=-55°. Field 1 was adjacent to clouds while field 2 was adjacent to cloud shadows. Since the image data taken at FZA=-55° showed a stronger relationship to the resulting albedo, the adjacency to the cloud/shadow clouds can have a greater effect on the resulting albedo. Other fields, 3, 4 and 5, were adjacent to clouds at FZA=+55°. The image taken at FZA=+55° had also a significant effect on the resulting albedo but the effect is less than the reflectance taken at FZA=-55°. This showed the actual albedo value of stubble land cover was probably slightly lower than the mean albedo value.

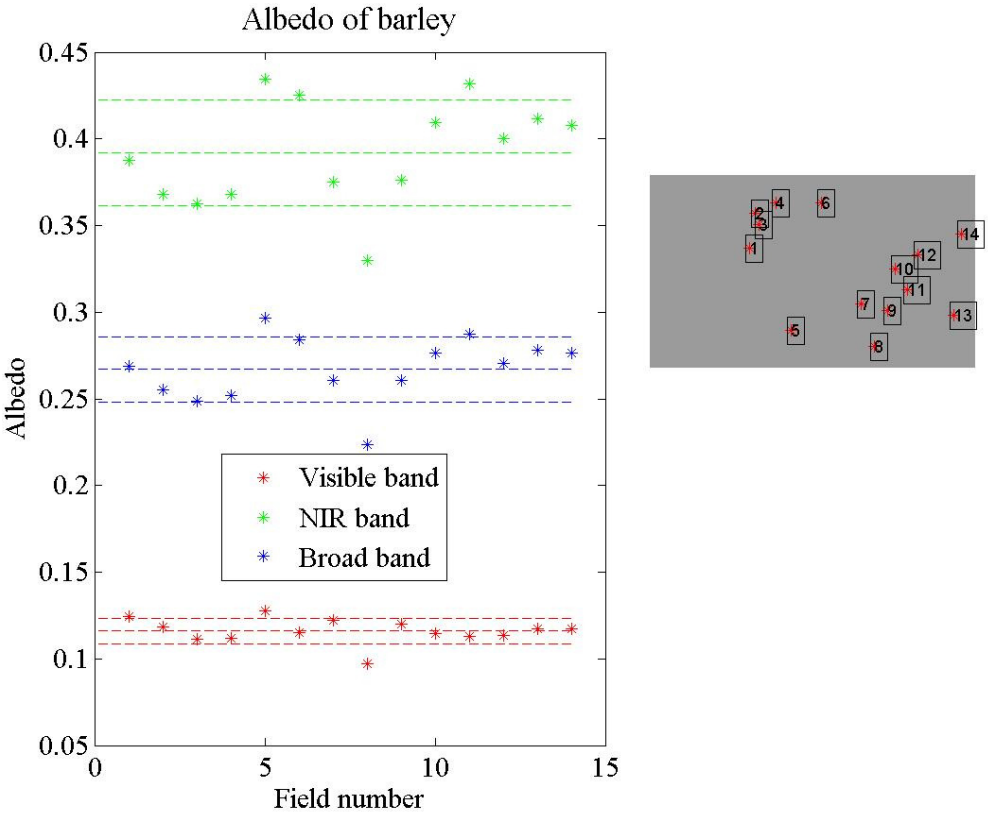

Figure 5-33 Albedo of different fields of barley class in visible, NIR and broad bands.

The mean broadband albedo value for barley was 0.27. Piggin and Schwerdtfeger (1973) measured a similar albedo value, 0.26, for full cover barley. The spatial variation of barley may be due to changes in surface moisture or adjacency to clouds/shadow clouds. As the spatial distribution of albedo in the barley class shows, there are some fields, for example field 11, which do not follow the spectral behaviour of vegetation in the visible and NIR bands. This can be due to changes in the density of vegetation cover or misclassification errors. The other source of uncertainty regards the adjacency of fields with clouds/shadow clouds. In fields 1 and 7, adjacent clouds were only seen at FZA=-55° which can be the reason for showing a closer value to the mean albedo. Field 2 was not adjacent to any cloud/shadow clouds which makes the retrieved albedo value more reliable. The adjacent clouds and cloud shadows were seen in all view angles in fields 4 and 5. Field 8 was adjacent to grass and wheat land covers that had a lower mean value than barley; this may be the cause for a decrease in the albedo value. Fields 7, 11 and 12 showed a different spectral behaviour than other fields, i.e. as the NIR albedo decreased/increased, the visible albedo did not show the same changes. These may be due to misclassification errors.

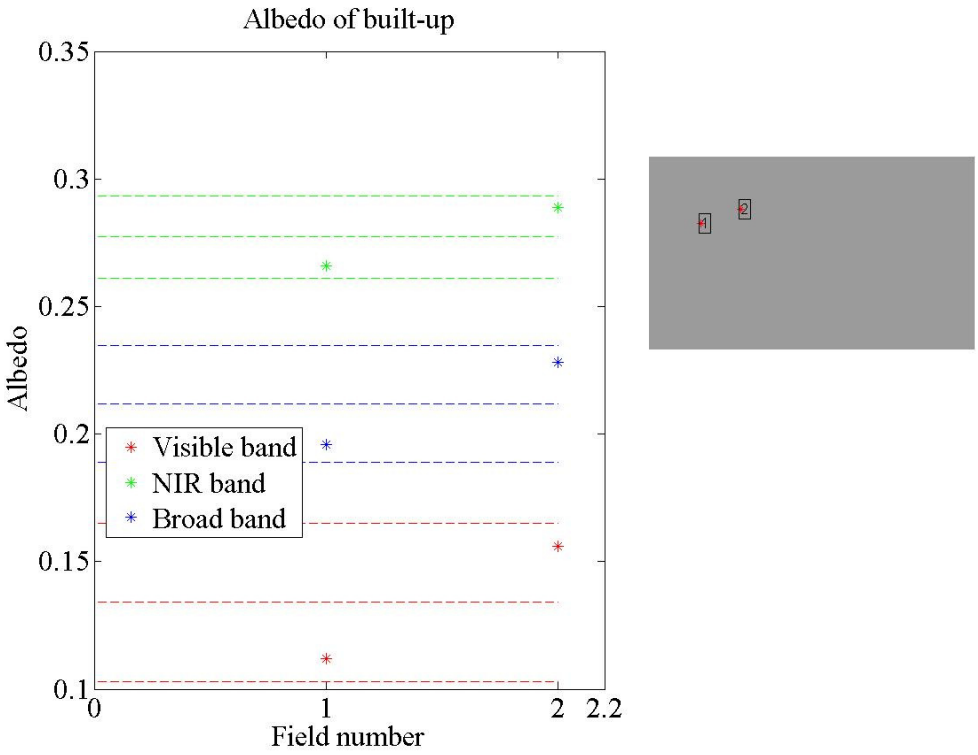

Figure 5-34 Albedo of different fields of built-up class in visible, NIR and broad bands.

Field 1 was adjacent to clouds and some cloud shadows but its larger size was probably the reason for being less affected by clouds/shadow clouds. Field 2 was adjacent to clouds at FZA=0° and ±55° which could explain its higher albedo value than field 1.

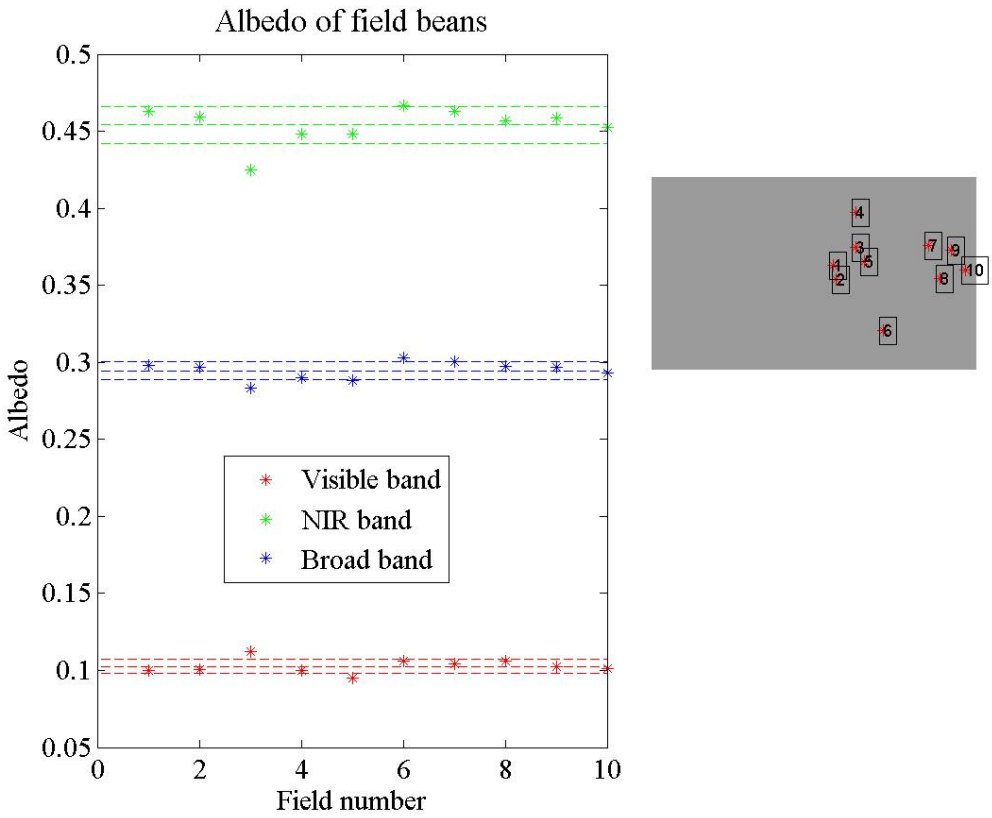

Figure 5-35 Albedo of different fields of field beans class in visible, NIR and broad bands.

The field beans class is shown by the colour maroon. Only field 3 was affected by clouds at FZA=-55° which may have caused an increase in visible albedo. However, the NIR albedo decreased which suggests that the different spectral behaviour in field 3 relative to other fields may be due to a misclassification error. Field 3 spectra were closer to grasslands and wheat.

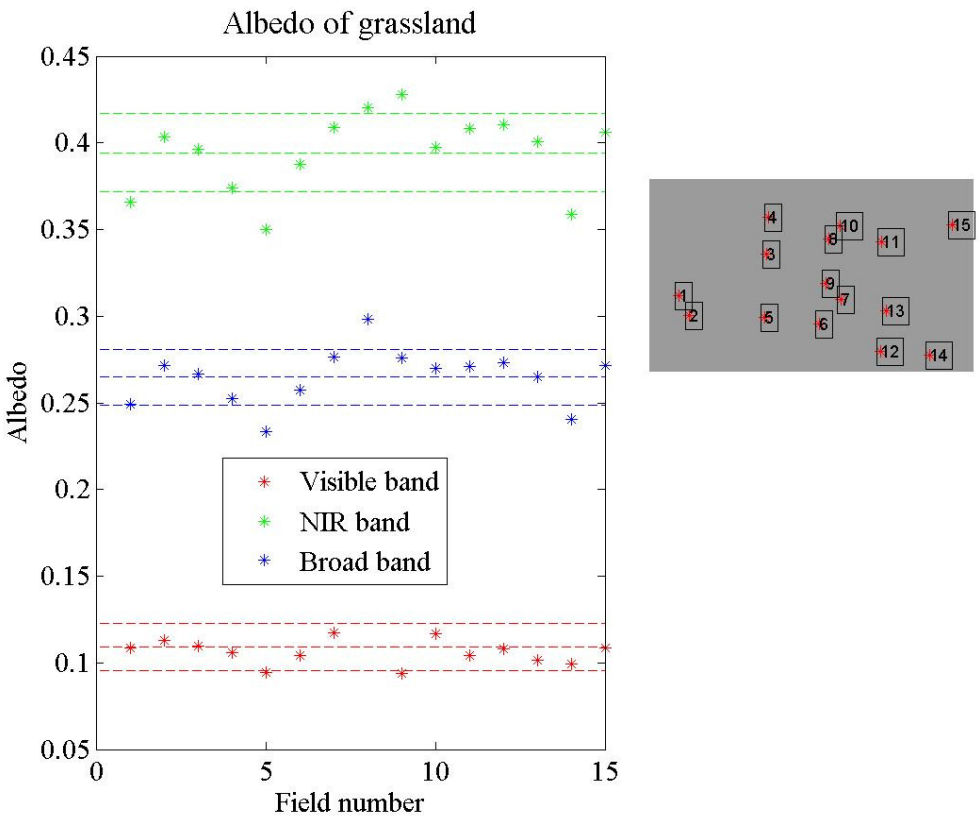

Figure 5-36 Albedo of different fields of grasslands class in visible, NIR and broad bands.

The grasslands fields are shown by the colour cyan. Field 1 was adjacent to cloud shadows in all view angles which may explain a lower value than the mean albedo. Field 2 was affected by clouds at FZA=-36° and -55° which could be the reason for a slightly higher value than the mean albedo. Field 8 was affected by clouds at FZA=-55° which may explain a higher value than mean albedo. Field 5 was affected by clouds in all view angles except FZA=0° and should show a higher albedo value than mean. However, it showed a lower albedo value than mean, which may be due to misclassification errors.

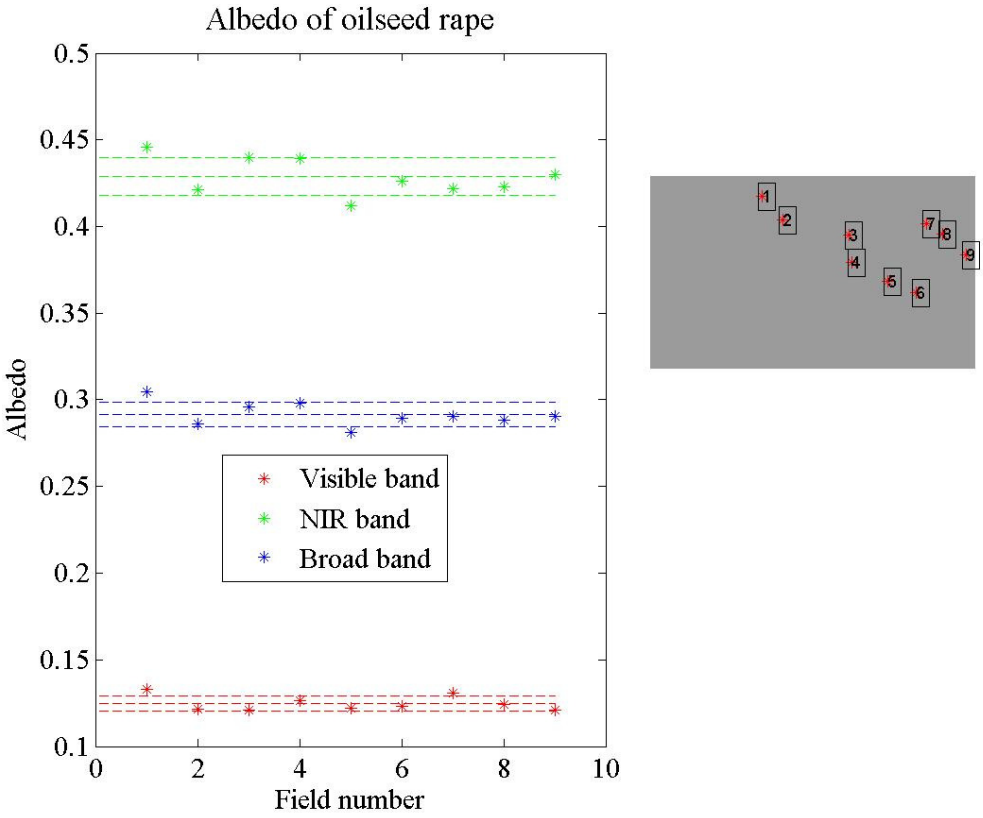

Figure 5-37 Albedo of different fields of oilseed rape class in visible, NIR and broad bands.

The oilseed rape class is shown by the colour green. With the exception of field 2, the other fields did not appear to be adjacent to clouds/cloud shadows. Field 2 was adjacent to cloud shadows in all view angles, except at FZA=0 which was adjacent to clouds. This probably caused a decrease in the albedo value relative to the mean value.

Albedo varied greatly between different fields of the same land cover. However, the magnitude of the variation was not the same in all land covers. Barley had a higher spatial variation in albedo than other land covers. The main reason for the observed variations could be the variation in the physical and chemical characteristics of the surface in the study site, while a small proportion of the variation in albedo could be due to other effects such as clouds/cloud shadows. An estimation of albedo for each land cover may then be made using the mean value of albedo for that class. The error may be as high as one standard deviation from the mean value that is different for each land cover. Regarding the estimation of broadband albedo, some land covers, the field beans and oilseed rape, showed errors of up to 7%, while others, the barley and built-up, showed higher errors of up to 17%. The magnitude of the errors also varied with the spectral band. The errors were higher in the visible band (about 15% in the wheat class to 25% in the stubble class).

The spatial variation of visible, NIR and broadband albedo over all the pixels in each land cover was also examined (Appendix 3). The results showed that the mean value in each field was affected by extreme albedo values, probably affected by clouds/cloud shadows. Therefore, this could be another explanation for the variation of albedo in different fields.

5.8 Conclusion

Albedo was calculated based on the MODIS BRDF model and CHRIS/PROBA reflectances observed at five view angles close to the solar principal plane. The results showed that surface albedo may be obtained using reflectances with high view zenith angles in the backscattering direction. This makes it possible to extend the albedo area to a larger area (area covered by FZA=-55°) with errors of up to 13%. Using a land cover map may increase the accuracy of the obtained albedo in some land covers. This also indicates that for calculating albedo, a sensor with high view zenith angles in backscattering direction is critical. Albedo varied between the different crop types in the area, from 0.25 in barley to 0.3 in field beans. This showed that assuming a fixed albedo value for agricultural lands map introduced errors of up to 17% of the albedo values. Therefore, a land cover map that shows a different variety of vegetation may increase the accuracy of the applied models such as evapotranspiration modelling. The variation of albedo between different fields of the same land cover showed errors of up to 17% of the albedo values if a fixed value for specific land cover is used. A further classification of the land cover map which uses maps of surface moisture, cloud/cloud shows, and topography (slope, aspect and elevation) seems valuable especially in large heterogeneous areas. This will result in a hyperclass land cover map which may greatly increase the accuracy of the obtained albedo based on the land cover map.

Further study to examine the relationship between albedo and directional reflectance and land cover is recommended. Such study should measure field albedo in a variety of land covers, using aerial sensors with a higher number of view angles which cover both solar and cross principal planes, and using a hyperclass land cover map.

6 Validation of Albedo product of MODIS

6.1 Introduction

There are a variety of remote sensors which have been/are being used to produce a map of the Earth's surface albedo. Some examples are AVHRR, MISR, MERIS, and POLDER. There are some restrictions about using these sensors to estimate albedo that relate mainly to their availability, knowledge and the time required to calculate albedo, and spatial, spectral and temporal resolutions. The MODIS albedo and reflectance anisotropy product is increasingly being used by the modelling community to both evaluate and refine a number of climatological and biogeochemical models (Schaaf et al., 2011). The MODIS instrument has the advantages of daily coverage of the Earth, moderate spatial resolution and spectral bands placed to be used in cloud detection, atmospheric correction, and thermal applications. A significant effort is also being carried out to develop different MODIS products, including the albedo product, and to provide outreach to scientists. The MODIS albedo product uses the other MODIS products such as the aerosol and water vapour products, as well as some ancillary data such as climatology data. There is the possibility of introduction of errors within the MODIS products, which could either be due to instrument errors, incomplete transmission of the data to ground stations, geolocation uncertainties, errors in the ancillary data and so on (Masuoka et al., 2011). Information about the appearance of these errors could be obtained by assessing the quality assurance (QA) of the MODIS products which provide the user community with an indication of the reliability of the data. On the other hand, there are other sources of errors such as the accuracy of atmospheric correction, the assumptions used in the production of the MODIS albedo product, and the BRDF model used. Although some validation efforts have been carried out by MODIS, their frequency and spatial distribution are limited. The uncertainty regarding the accuracy of the MODIS albedo product is therefore a concern, particularly in those areas with different climate and surface conditions to the validation sites used by the MODIS team. Here, the results of previous chapters, the errors in the MODIS atmospheric correction and the CHRIS/PROBA albedo map, are used to quantify the probable errors in the MODIS albedo product.

6.2 Method

6.2.1 Statistical model

Some statistical parameters used here, such as correlation and RMSE, have been explained previously (Chapter 3). Land surface albedo applications at the global scale,

such as large scale general climate models (GCMs), may use albedo values at a coarser spatial scale than the MODIS albedo resolution. Thus, the validation of the MODIS albedo product may be required at a much coarser resolution, for example coarser than 1°. A comparison between the mean albedo values of the whole area may then be interesting. A statistical hypothesis test, a t-test, was then used. The t-test is a two-sample test (Shaw and Wheeler, 1985) for continuous data such as those from remote sensing. It measures significant differences between two datasets considering the differences in the means and standard deviations.

$$t = \frac{\overline{X} - \overline{Y}}{\sqrt{\left(\frac{s_{X^2}}{n_{X-1}} + \frac{s_{Y^2}}{n_{Y-1}}\right)}}$$ **Equation 6-1**

Where $\overline{X}$ and $\overline{Y}$ are the mean values of the *X* and *Y* datasets, respectively, s_{X^2} and s_{Y^2} are the variances of the *X* and *Y* datasets, respectively, n_X and n_Y are the sample sizes of the *X* and *Y* datasets, respectively, and t is the test statistic.

The correctness of a null hypothesis is assessed in the t-test. The null hypothesis assumes there is no significance difference between the two datasets H_0: $\overline{X} - \overline{Y} = 0$ (or P ($\overline{X} > \overline{Y}$) =0.5). The calculated *t* value (from Equation 6-1) is compared with a tabulated *t* value at the required level of significance which is usually 0.05. If the probability (p) of $t_{tabulated} <= t_{calculated}$ is high (close to 1) then the null hypothesis is true. This test is parametric which mean the data need to have a normal distribution. A test of normality of the datasets is therefore required.A normal probability plot graphically assesses whether or not the data could come from a normal distribution (Chambers et al., 1983). If the data are normal, the plot will be linear. Other distribution types will introduce curvature in the plot.

Where the data do not have a normal distribution, the t-test may not be an appropriate test (Shaw and Wheeler, 1985). The Mann-Whitney U test may be applied to non-parametric data that can be ranked. It has the advantage of being applicable to a small group of data. The two datasets need to be combined into one group and ranked from the lowest to highest value. The data are then separated into the two original groups which are now ranked. The U statistic is calculated using the following formula:

$$U = n_1 n_2 + \frac{n_1(n_1+1)}{2} - R_1$$ **Equation 6-2**

Where n_1 and n_2 are the sizes of the smaller and larger groups, respectively, R_1 is the sum of ranks in the smaller group and *U* is the Mann-Whitney test statistic.

U is assumed to have a normal distribution for large samples. The standardized value, z, which is approximately a standard normal deviate, is then used:

$$z = \frac{U - m_U}{\sigma_U} \qquad \textbf{Equation 6-3}$$

Where m_U and σ_U are the mean and standard deviation of U.

A statistical table for the Mann-Whitney U test is then used to determine if the probability of the calculated U is the same as or lower than the one in the table. The same hypothesis (H_0 and H_1), explained for the t-test, is used in this test.

6.3 Methodology

Validation of the daily MODIS albedo product on DOY 168 2006 was carried out by examining the errors in the input reflectance and BRDF model as well as comparison with the CHRIS/PROBA albedo (Figure 6-1).

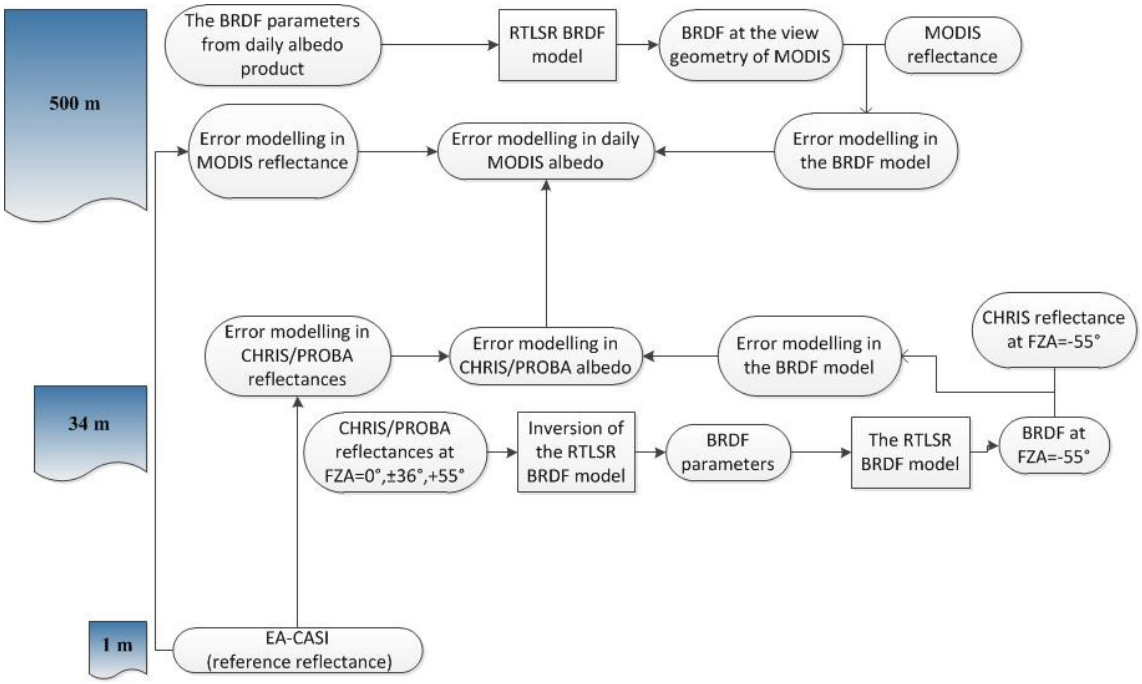

Figure 6-1 Methodology of the validation of the MODIS albedo product

6.4 Validation of the CHRIS/PROBA albedo

The CHRIS/PROBA albedo values needed to be validated before using them as a reference to validate the MODIS albedo product. Although they were not field albedo measurements, nearly simultaneous field reflectance measurements provided a valuable reference dataset to validate the input reflectances to the albedo model.

Airborne EA-CASI reflectance data were used as reference data to validate the CHRIS/PROBA reflectances at FZA=0°. The 32 bands of the EA-CASI data and 62 bands of the CHRIS/PROBA data were averaged using a Gaussian function and band widths to four MODIS bands centred at 469 nm, 555 nm, 645 nm and 858 nm. The spatial resolutions of the EA-CASI data, 1 m, and the CHRIS/PROBA data, 34 m, were then averaged up to the MODIS spatial resolution, 500 m. A linear regression model was then used to model the error in the CHRIS/PROBA data. A more detailed validation of the CHRIS/PROBA data is described in Appendix 1.
The accuracy of the calculated CHRIS/PROBA albedo was assessed by testing the accuracy of the input reflectances and the applied BRDF model.

6.4.1 Accuracy of the CHRIS surface reflectance

The accuracy of the CHRIS/PROBA atmospheric correction, aggregated over 32 EA-CASI bands and at a spatial resolution of 34 m, was assessed in Appendix 1. Here, the CHRIS/PROBA reflectances, corrected using the BEAM software, were spectrally and spatially aggregated to the first four MODIS bands. The CHRIS data were then validated using the spectrally and spatially aggregated EA-CASI data to MODIS bands (Figure 6-2). The errors in the CHRIS data were also quantified (Table 6-1).

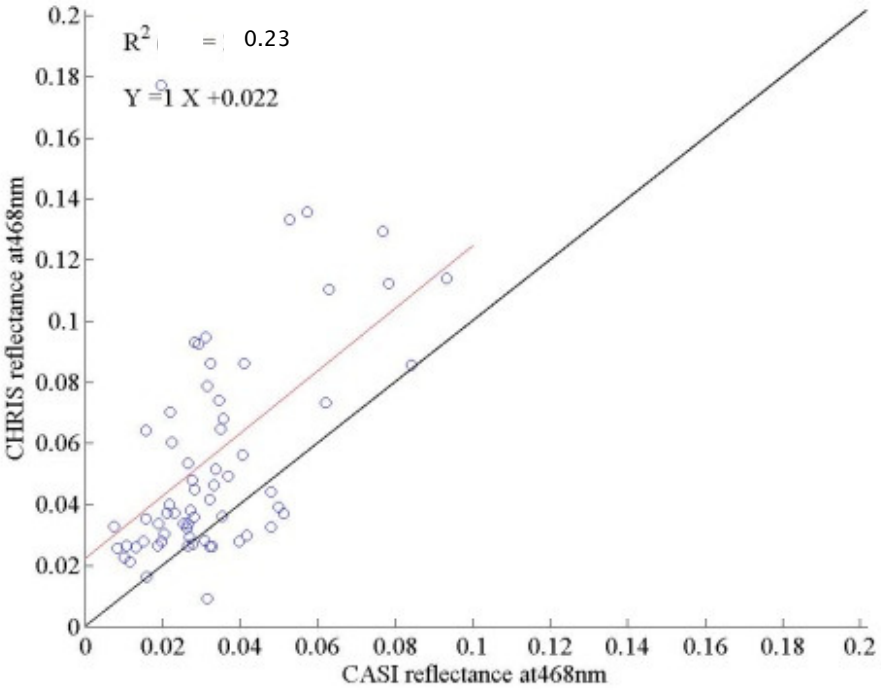
R2 = 0.23
Y =1 X +0.022
CHRIS reflectance at468nm
CASI reflectance at468nm
0
0.02
0.04
0.06
0.08
0.1
0.12
0.14
0.16
0.18
0.2

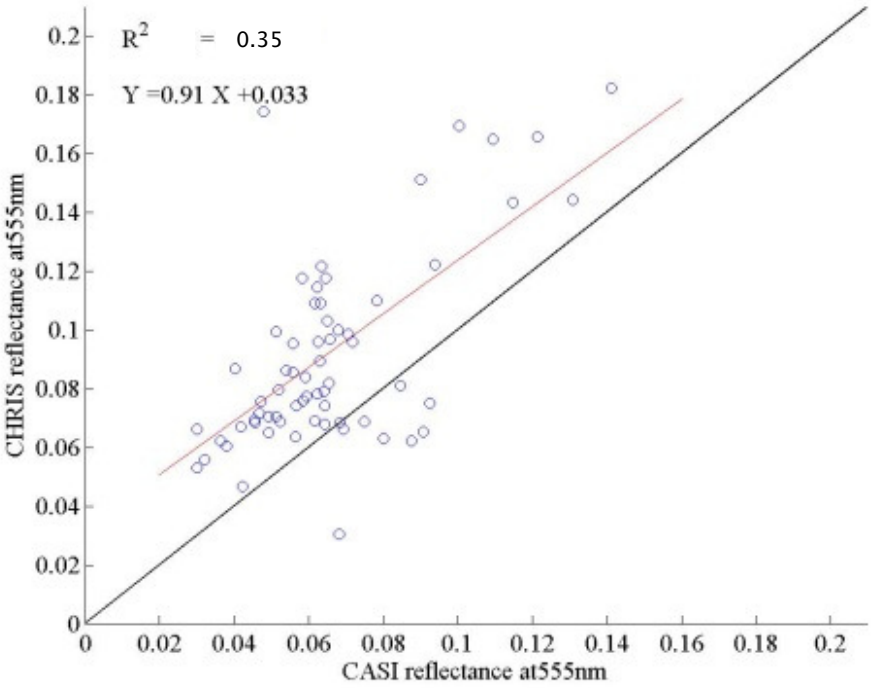
R2 = 0.35
Y =0.91 X +0.033
CHRIS reflectance at555nm
CASI reflectance at555nm
0
0.02
0.04
0.06
0.08
0.1
0.12
0.14
0.16
0.18
0.2

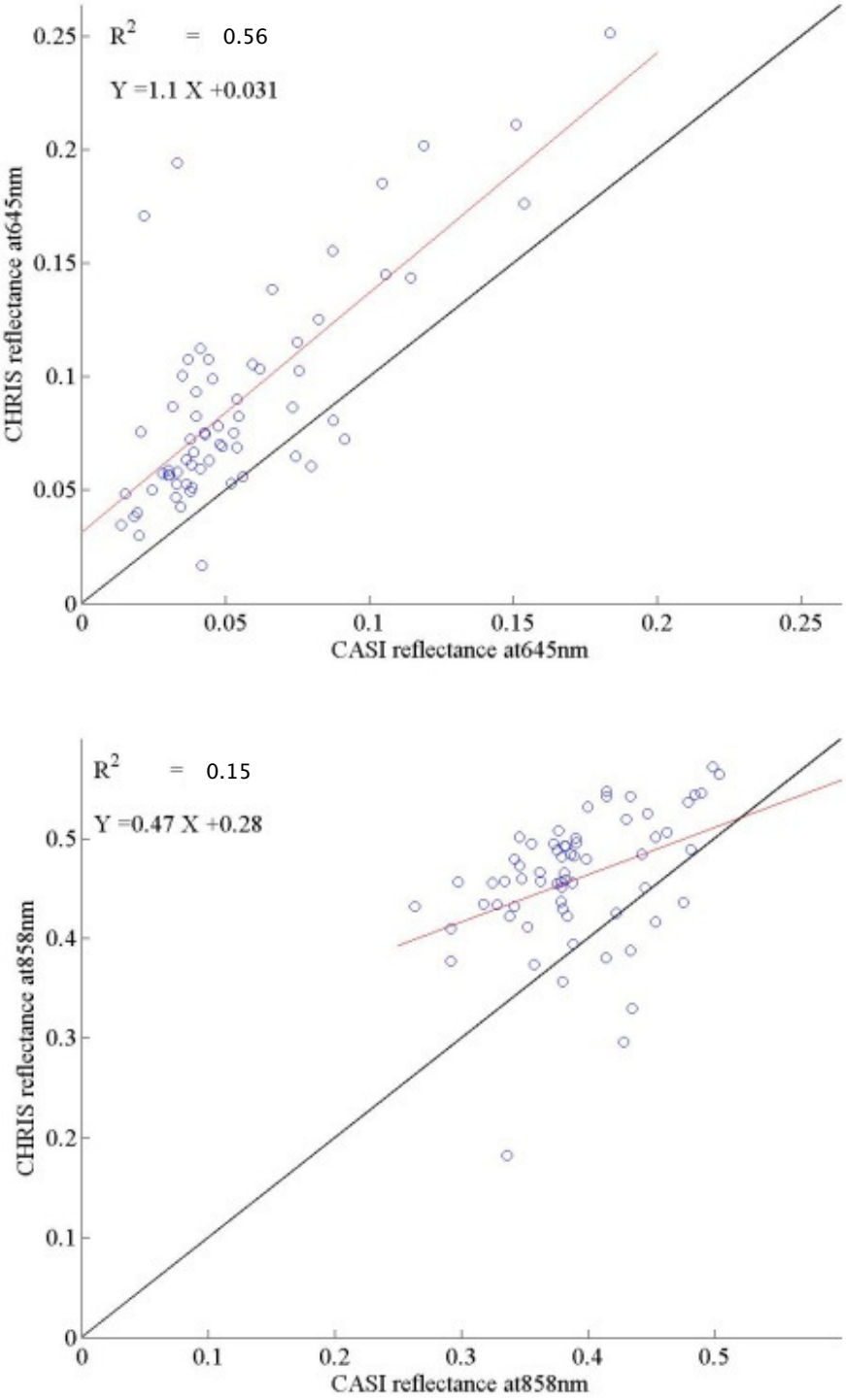

Figure 6-2 Scatter plots showing the relationship between EA-CASI reflectance and at-nadir CHRIS reflectance.

Table 6-1 Errors in the at-nadir CHRIS reflectance (and some statistical parameters shown in Figure 6-2)

band	R-squared	slope	intercept	RMSE	%RMSE
468	0.23	1	0.02	0.04	142
555	0.35	0.91	0.03	0.04	63
645	0.56	1.1	0.03	0.05	110
858	0.15	0.47	0.28	0.10	25

The absolute errors in the CHRIS reflectance data were higher than those seen in the MODIS data (Table 6-1 and Table 6-5). However, the errors in the CHRIS data seem systematic whereas MODIS showed random errors. The CHRIS reflectances were overestimated in all bands. In the visible band, this was probably due to uncertainties in the applied AOT. The results of the atmospheric correction of the CHRIS data using the BEAM software and the actual AOT value, 0.27, caused negative reflectance values. A lower AOT value, 0.15, was then used to avoid the negative reflectances. This value was suggested by Luis Guanter, who developed the atmospheric correction algorithm for CHRIS/PROBA data in BEAM, as I mentioned the problem by email. This caused an undercorrection of the CHRIS data for aerosol effects which resulted in higher reflectance values in the visible band (Appendix 1). Overestimation of reflectance in the NIR band may be due to an underestimation of water vapour calculated by the BEAM software. The probable errors in the sensor calibration may be another reason for overestimated reflectance in NIR, which may also be the case in the visible bands. The uncertainties in the reference EA-CASI reflectances could be another explanation for the observed reflectance overestimation in the NIR region. Asmat (2009) mentioned uncertainties in the absolute accuracy of NIR reflectances and co-registeration errors. However, these errors will have been minimised by upscaling the data to 500 m.

The validation carried out on the CHRIS data was for the at-nadir view geometry. If the errors in the CHRIS data are systematic and the same in all view angles, then the resultant albedo may show the same errors. The errors, however, could be different (higher or lower) in off-nadir CHRIS reflectances which might have caused a further source of uncertainties in the calculated albedo.

6.4.2 The accuracy of the applied BRDF model.

The uncertainty in the BRDF model and its effect on albedo was also investigated. The BRDF parameters of the BRDF model were calculated using four out of five view angles CHRIS reflectances. CHRIS data sets at FZA=0°, ±36° and 55° were used in the BRDF

modelling and the data at FZA=-55° were used as control data to check the uncertainty in the BRDF model.

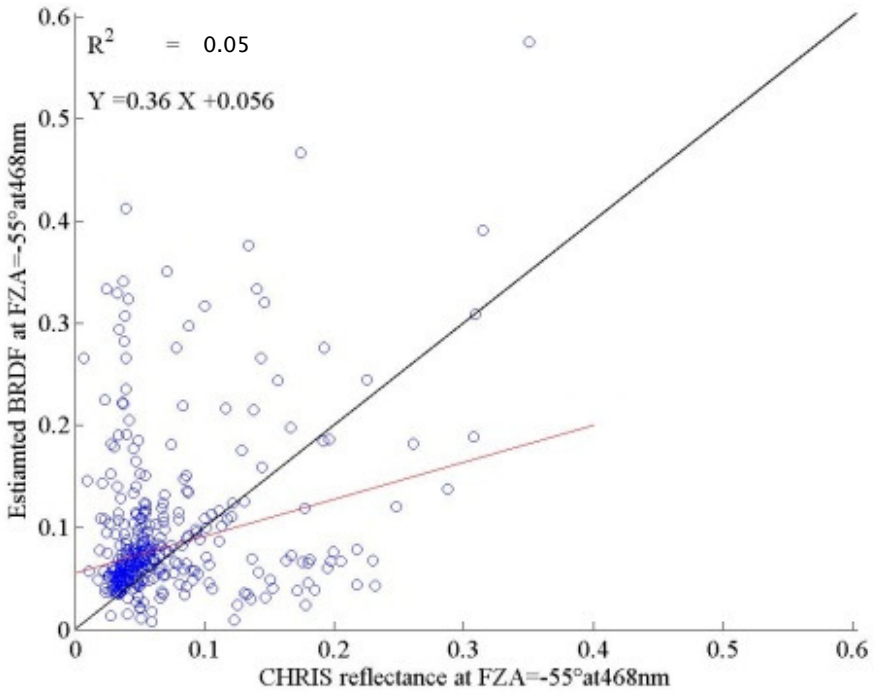

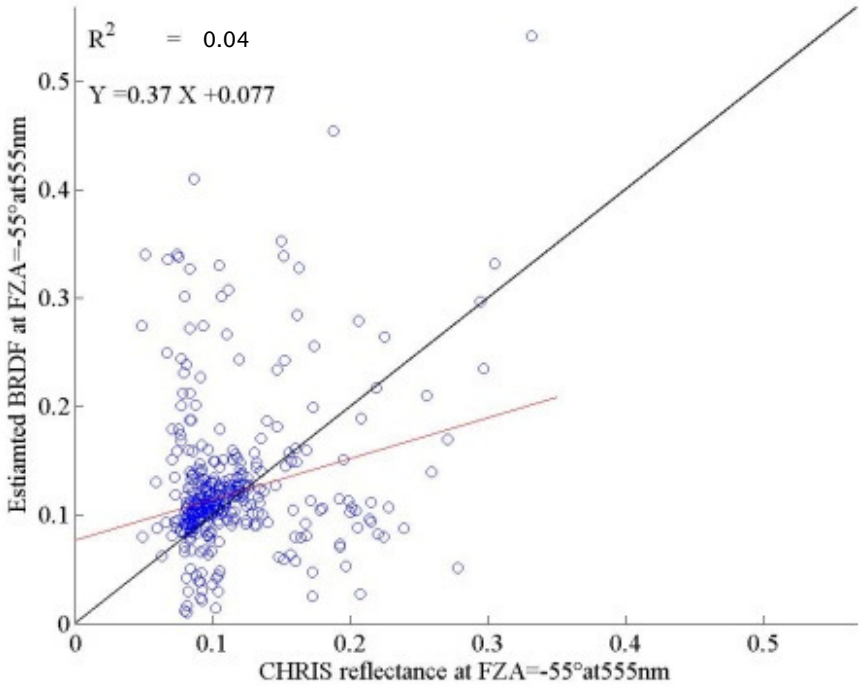

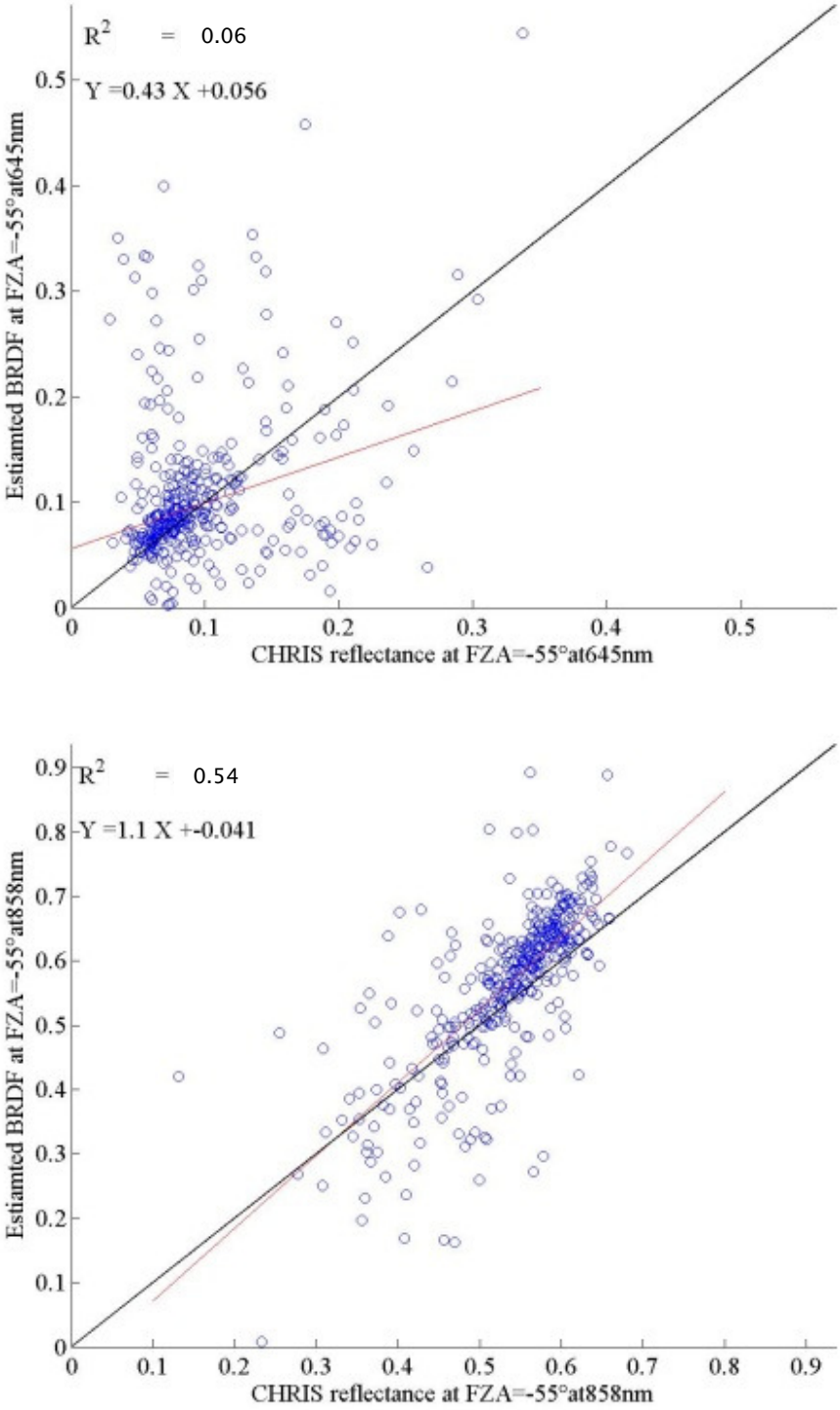

Figure 6-3 Scatter plots showing the relationship between CHRIS reflectance at FZA=-55° and the estimated BRDF at FZA=-55° which was calculated using all view angles except at FZA=-55°.

Table 6-2 Errors in the estimated BRDFs relative to the actual CHRIS reflectances at FZA=-55° (and some statistical parameters shown in Figure 6-3)

band	R-squared	slope	intercept	RMSE	%RMSE
468	0.05	0.36	0.06	0.10	198
555	0.04	0.37	0.08	0.08	85
645	0.06	0.43	0.06	0.09	111
858	0.54	1.10	-0.04	0.09	16

The results demonstrated that removing the critical view geometry FZA=-55° from the albedo calculation may introduce large errors in the output albedo. This indicated that the applied BRDF model may not obtain the absolute BRDF values accurately especially off-nadir data in the backscattering direction. On the other hand, the magnitude of errors may decrease when spatial resolution of the obtained albedo decreases such as those in climate models.

The magnitude of the effect of the uncertainty in the BRDF parameters and the BRDF model in the estimated albedo depends on the distribution of errors in the hemispherical BRDF. The worst case scenario is if all the errors are positive or negative but they may also neutralize each other.

There were also some other uncertainties which may have affected the CHRIS albedo:
Geometric accuracy: Uncertainties regarding geometric correction are higher at CHRIS spatial resolution at higher view zenith angles. However, the uncertainty is reduced at coarse MODIS spatial resolution.

Radiometric correction: CHRIS bands, particularly by those with shorter wavelengths, are affected by vertical stripes and drop-outs. Although these errors are dealt with in the CHRIS toolbox of the BEAM software, they are not completely removed. There are also some uncertainties regarding the replaced data.

Distribution of geometry of data: The five view angle data are well distributed with approximately 20-30 degree intervals. However, these data are in the solar principal plane and there was no information about the cross-track principal plane. In addition, there was no information about view zenith angles above 50° which have a greater contribution to the computation of albedo due to the assumed higher reflectance values.

Number of observations: There were only five view angles. The number of observations needs to be high enough to cover both the solar principal and cross-principal planes as well as covering different view zenith angles.

It was concluded that there was uncertainty in the accuracy of the obtained CHRIS/PROBA albedo resulting from errors in the input reflectance data and the applied BRDF model. Therefore, the validation of the absolute values of the MODIS albedo using the CHRIS albedo was not possible. On the other hand, the errors in the CHRIS/PROBA looked systematic; the changes in the CHRIS and EA-CASI reflectance were synchronous. This showed that the CHRIS/PROBA data were able to show the changes in the surface reflectance, and the resulting albedo, although the absolute reflectance and albedo values were uncertain. In addition, the better distribution of the view geometries in the solar principal plane, and simultaneous observations in all five view angles, make the relative albedo values more reliable than MODIS albedo. For this, the resulting CHRIS/PROBA albedo could be used to validate the MODIS albedo in a different way. The accuracy of presenting the changes in the surface albedo using the MODIS albedo product (the relative albedo values) could be measured by using the CHRIS/PROBA albedo as a reference albedo map.

6.5 Validation of the MODIS albedo

Since the reference CHRIS/PROBA albedo data were produced from the one-day observations, DOY 168 2006, it may not be comparable with the operational 16-day MODIS albedo product. The MODIS daily albedo product produced by Boston University was used in this study. This product still uses 16 days reflectance data as input, like the operational 16-day albedo product, but gives the greatest weight to the day closest to when the daily albedo is produced. The DOY 168 albedo product was then produced using surface reflectance data from DOY 152 to DOY 168, the RTSLR BRDF model and a weighting table which gave the greatest weight to the data in DOY 168 and the least weight to the data in DOY 152. The MODIS albedo was validated using two different methods, direct and indirect. In the direct method, the CHRIS albedo was used as the reference albedo (Figure 6-4) whereas in the indirect method, the accuracy of the MODIS albedo was related to the accuracy of the input reflectances and the BRDF model.

The MODIS albedo was validated earlier in this thesis using the indirect method. In chapter 4, the validation of the daily MODIS surface reflectance product (MOD09 GA) was carried out using airborne EA-CASI and satellite SPOT-5 data. Therefore, in this

chapter, the effect of the errors in the MODIS reflectances and BRDF model on the estimated albedo was considered.

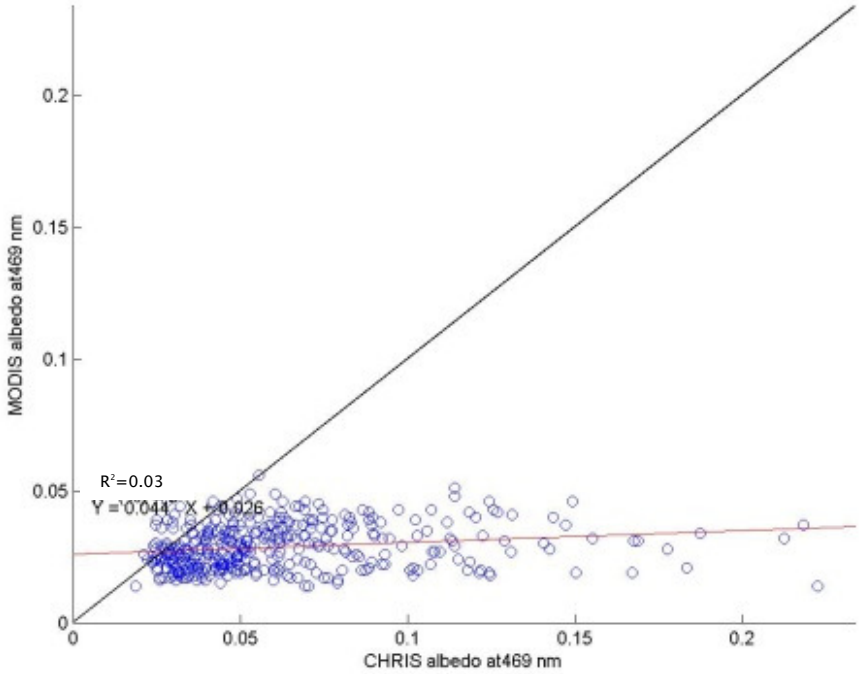

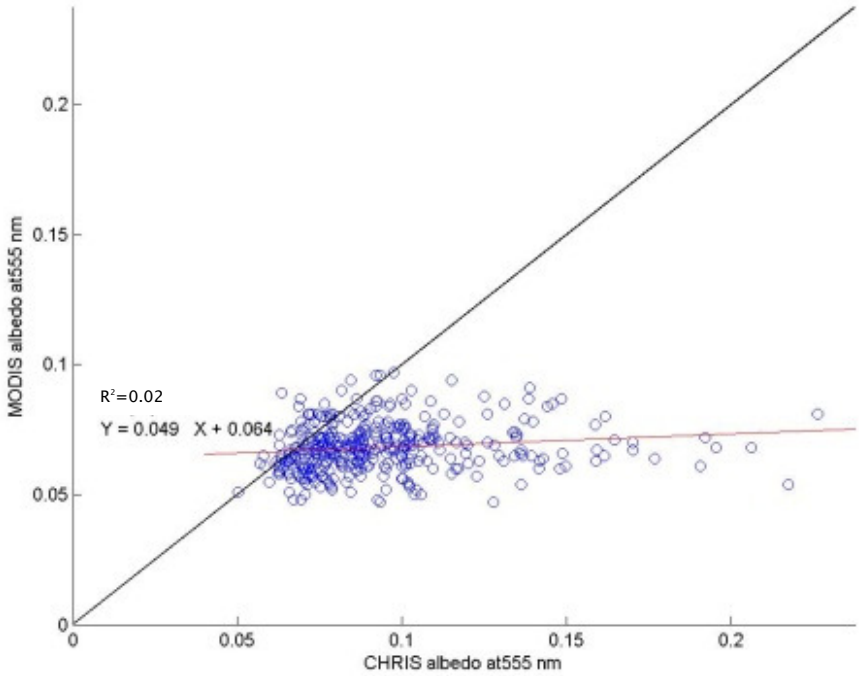

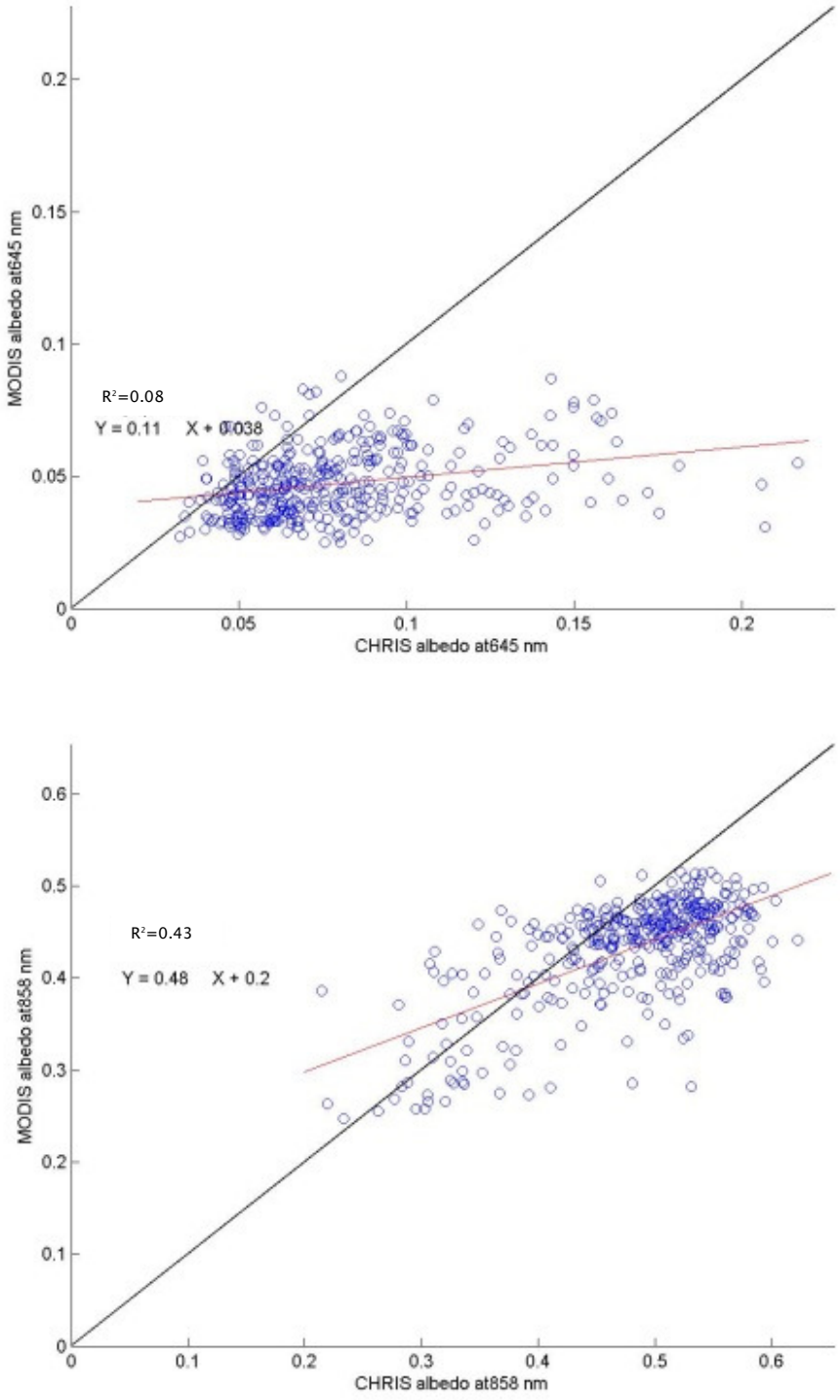

Figure 6-4 Scatter plots showing the accuracy of the MODIS albedo product

Table 6-3 Statistical parameters of Figure 6-4

Wavelength (nm)	R-squared	slope	intercept	mean_x	mean_y	RMSE	%RMSE

469	0.03	0.04	0.03	0.06	0.03	0.05	93
555	0.02	0.05	0.06	0.09	0.07	0.04	43
645	0.08	0.11	0.04	0.08	0.05	0.04	62
858	0.43	0.48	0.20	0.48	0.43	0.07	15

From the results the following points are made:
The MODIS albedo product showed lower albedo values than the CHRIS/PROBA albedo. Since the errors in reflectance have a direct effect on the resulting albedo, this may be due to the lower MODIS reflectances. The reflectance values observed by CHRIS/PROBA were higher than those observed by the reference EA-CASI data (Figure 6-2). This showed that the CHRIS/PROBA albedo may have overestimated the albedo due to an overestimation in reflectances or that MODIS may have underestimated the albedo.

The MODIS albedo had less variation than the CHRIS albedo. This may be due to the use of reflectance data only in the solar cross-principal plane (Figure 5.9 in chapter 5) which have less variation with view geometry. Another reason could be the coarser spatial resolution of the MODIS data. The spatial resolution decreases as view zenith angle becomes larger; thus the MODIS data at off-nadir have a coarser spatial resolution than 500 m. Most of the MODIS observations used in the considered 16 day period were off-nadir (Figure 5.9). The MODIS observations on DOY 168, which had the highest effect in producing the applied daily MODIS albedo, had a high zenith angle (46°), which was in the cross-principal plane (azimuth angle of 96°).

In studies that require coarse spatial resolution albedo, such as those are used in climate models, the accuracy of the MODIS albedo product may be sought in coarser resolution. A comparison of the mean albedo values was also carried out to assess the validity of MODIS albedo over larger areas. The statistical t-test was used to test the null hypothesis that there is no significant difference between the mean albedo values of the CHRIS and MODIS albedo. However, since the results of this test are valid for parametric data, the normality of the distribution of both the CHRIS and MODIS data were assessed (Figure 6-5 and Figure 6-6). The mean values of albedo were obtained from an area of 46 km^2.

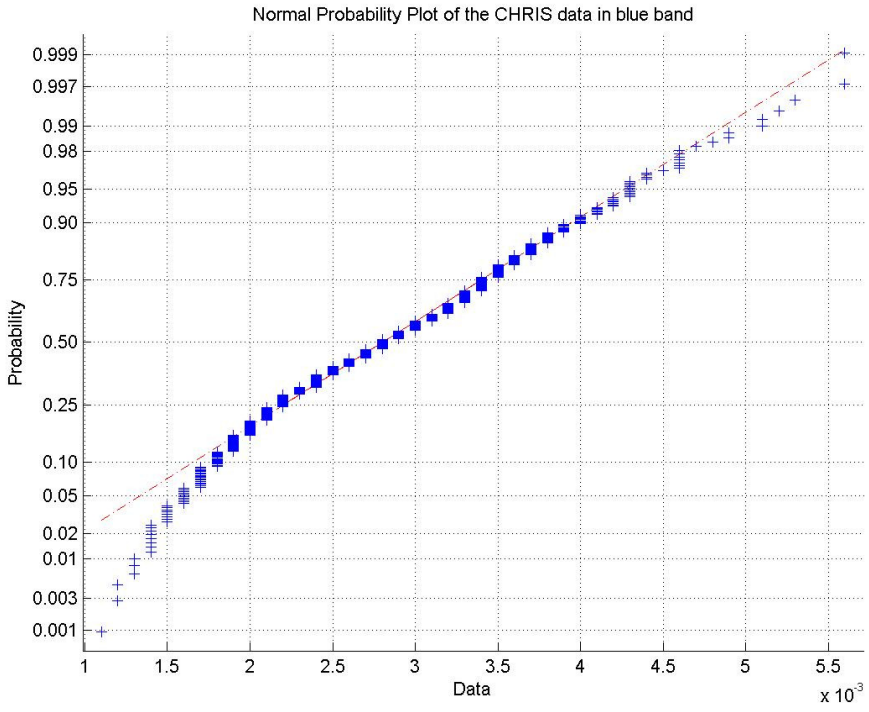
Normal Probability Plot of the CHRIS data in blue band
Probability
0.999
0.997
0.99
0.98
0.95
0.90
0.75
0.50
0.25
0.10
0.05
0.02
0.01
0.003
0.001
1
1.5
2
2.5
3
3.5
4
4.5
5
5.5
Data
x 10-3

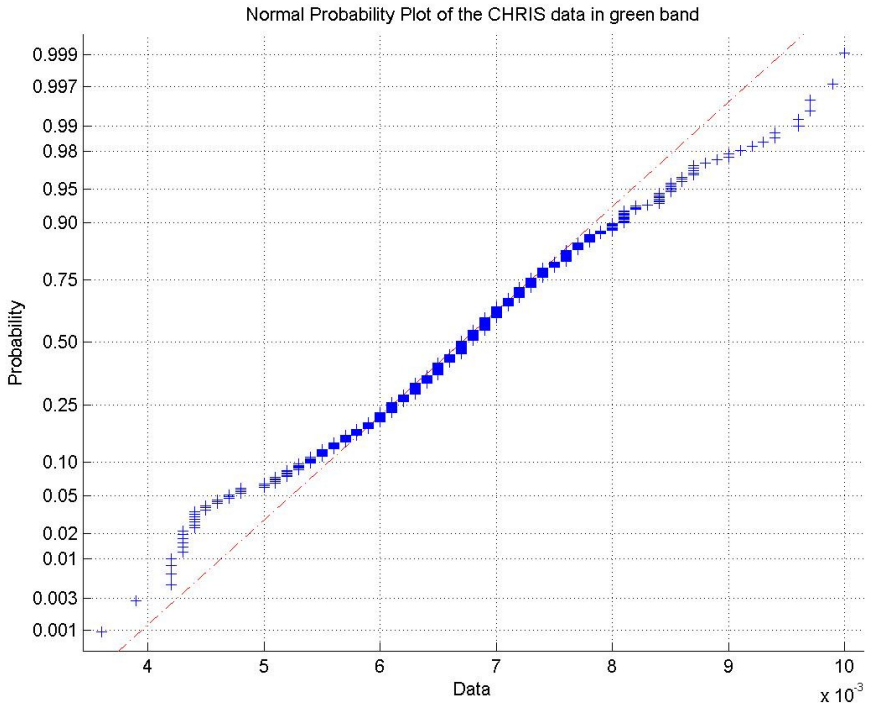
Normal Probability Plot of the CHRIS data in green band
Probability
0.999
0.997
0.99
0.98
0.95
0.90
0.75
0.50
0.25
0.10
0.05
0.02
0.01
0.003
0.001
4
5
6
7
8
9
10
Data
x 10-3

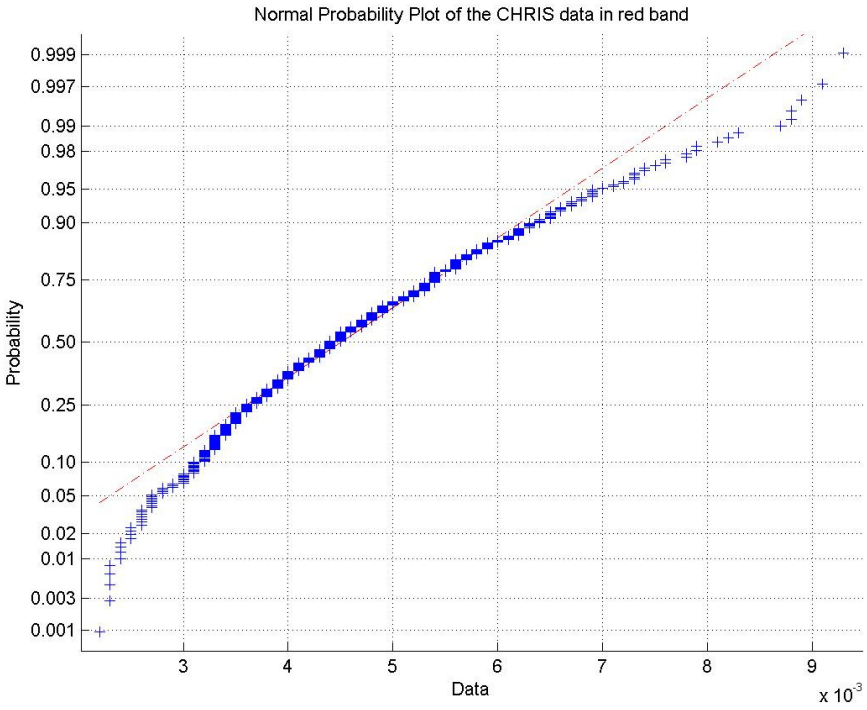

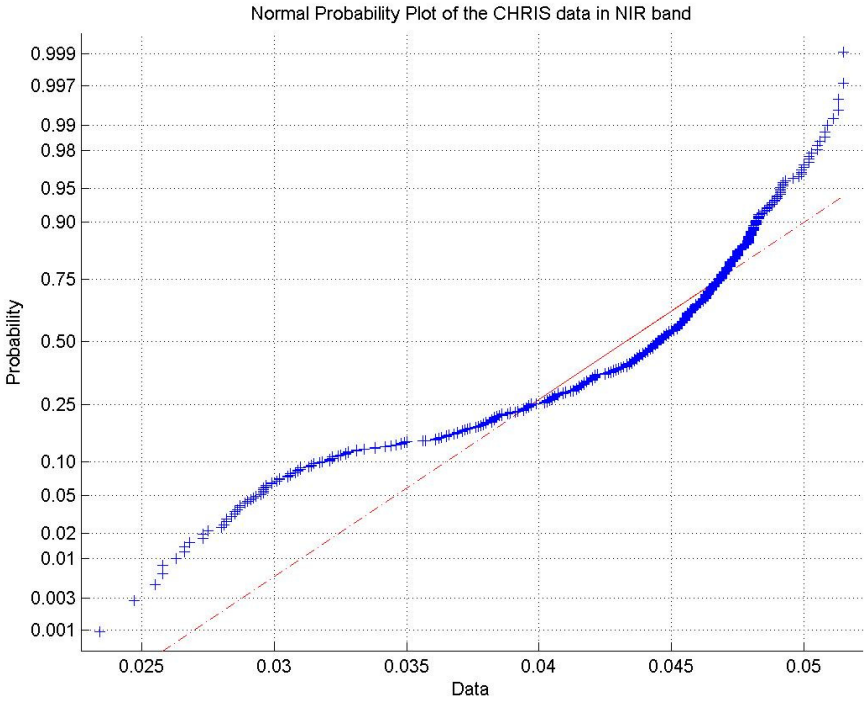

Figure 6-5 Normal probability plot of CHRIS data.

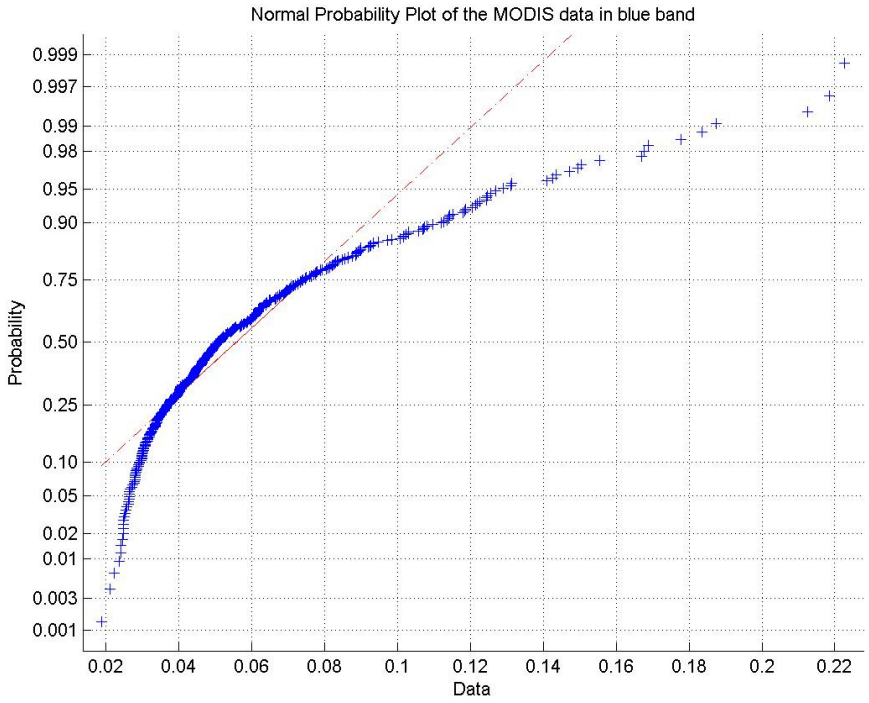
Normal Probability Plot of the MODIS data in blue band
Probability
0.999
0.997
0.99
0.98
0.95
0.90
0.75
0.50
0.25
0.10
0.05
0.02
0.01
0.003
0.001
0.02
0.04
0.06
0.08
0.1
0.12
0.14
0.16
0.18
0.2
0.22
Data

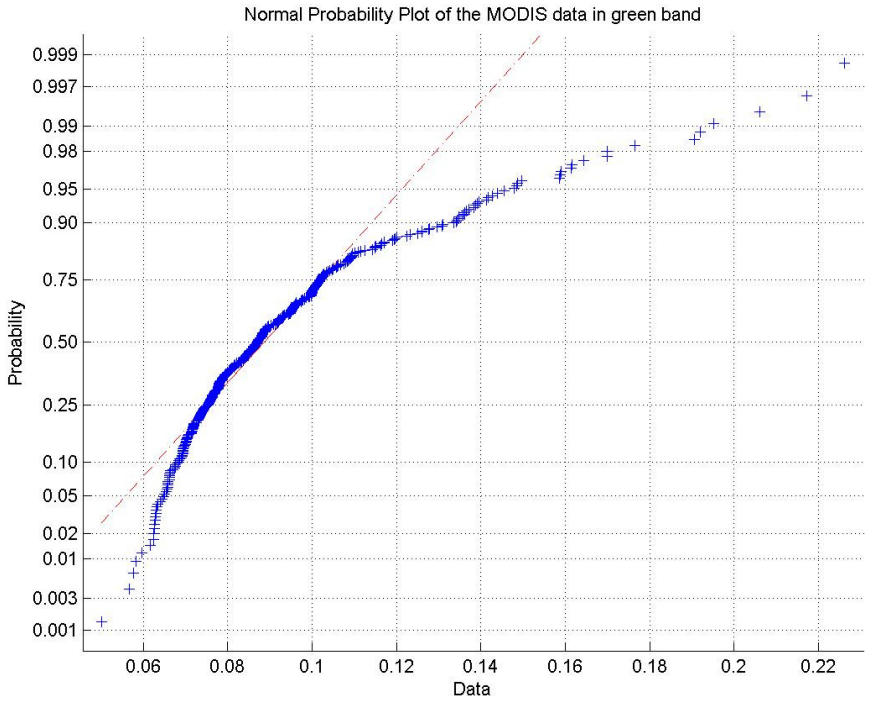
Normal Probability Plot of the MODIS data in green band
Probability
0.999
0.997
0.99
0.98
0.95
0.90
0.75
0.50
0.25
0.10
0.05
0.02
0.01
0.003
0.001
0.06
0.08
0.1
0.12
0.14
0.16
0.18
0.2
0.22
Data

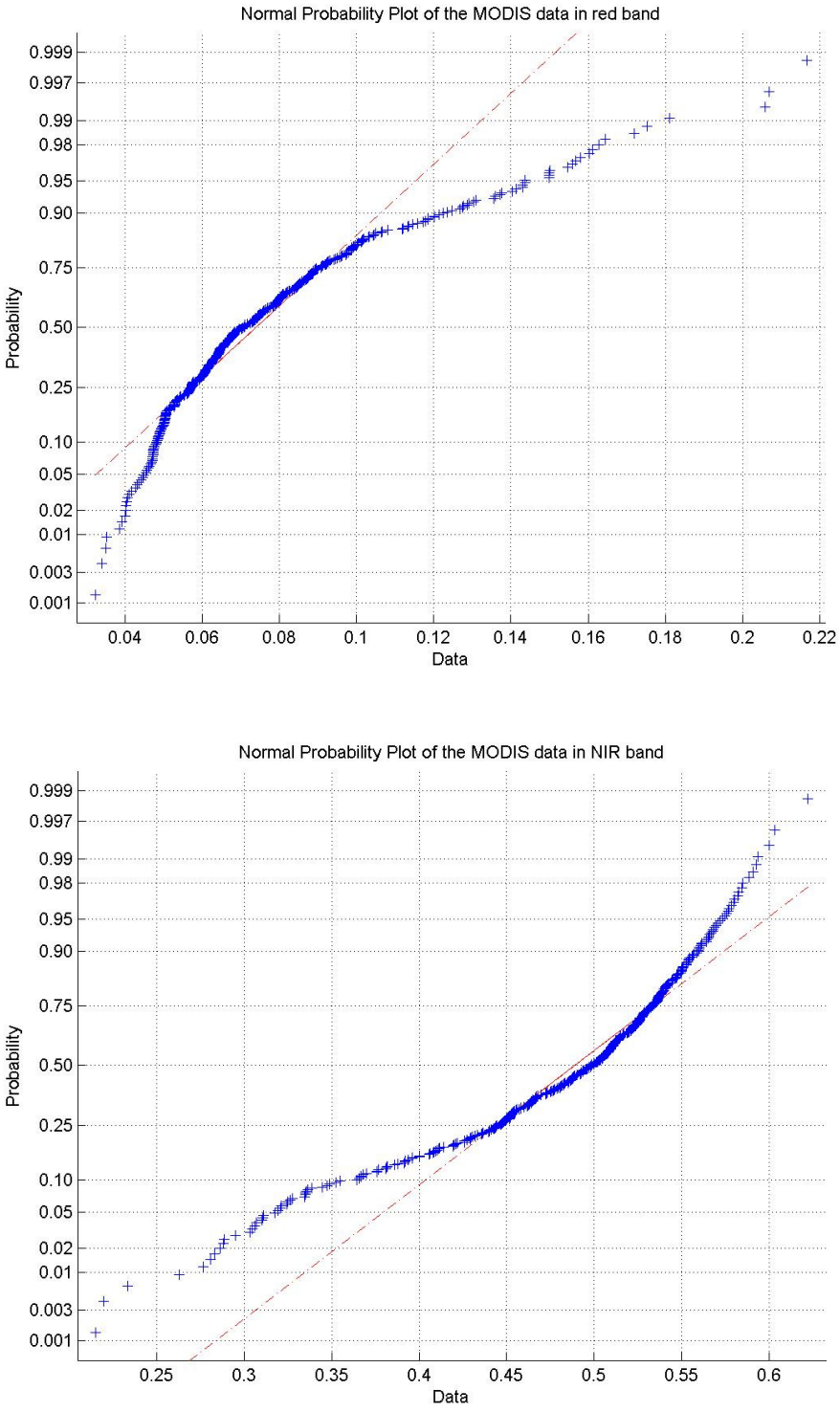

Figure 6-6 Normal probability plot of MODIS data.

The normal probability plots of the CHRIS and MODIS data showed that an assumption of normality of the data was not correct as the plots were not linear. The Mann-Whitney U test, designed for non-parametric data, was therefore used. The hypotheses used were:

Null hypothesis: The median of the CHRIS albedo equals the median of MODIS albedo. Alternative hypothesis: The median of the CHRIS albedo is greater (or less) than the median of the MODIS albedo.

Table 6-4 Mann-Witney U test results

Test	Blue band	Green band	Red band	NIR band
Mann-Witney U	16995	20544	19127	37427
Z	-18.029	-16.837	-17.312	-11.167
probability (p)	0.00	0.00	0.00	0.00

It then can therefore concluded that there is a statistically significant difference between the median of the CHRIS/PROBA albedo and that of the MODIS albedo in the visible and NIR bands. This may demonstrate an uncertainty in using the MODIS albedo product, even in models which require a coarse spatial resolution.

The main uncertainties in MODIS albedo are:
Accuracy of MODIS surface reflectance: The validation of the MODIS reflectance on DOYs 161 and 168 were explained in Chapter 5. Assessment of the surface reflectance product showed errors which were quite significant in the case study. The errors were at a minimum in the NIR band (%RMSE=19) and at a maximum in the red band (%RMSE=56). As explained above, this may introduce the same magnitude of errors in the albedo. The uncertainty regarding aerosol modelling, cloud detection and sensor calibration were assumed to be the main reasons for the observed errors.

Table 6-5 Errors in the at-nadir estimated BRDF

Band	Mean_CASI	Mean_MODIS	RMSE	%RMSE
468	0.034	0.034	0.01	46
555	0.068	0.08	0.02	36
645	0.057	0.062	0.02	56
858	0.394	0.446	0.07	19

Geometric accuracy: As explained in Chapter 4, the geometric error in the MODIS albedo could be approximately one MODIS pixel. This might change the results of the validation of the reflectance and albedo MODIS products. A further comparison was carried out comparing the reflectance and albedo values in a larger area (Table 6-3 and Table 6-5). The results still showed errors greater than 5% of absolute mean

values. This demonstrated that, even if there was no uncertainty about the accuracy of the geometric correction of the MODIS data, the uncertainties in the accuracy of the MODIS reflectance and albedo products would still remain.

Distribution of the geometry of data: The applied observations were distributed in the solar cross-principal plane. The lower variability of BRDF with view geometry in this region and the lack of information in the solar principal plane make the results from the BRDF model less certain. This could explain the lower variability of the MODIS albedo in comparison with the CHRIS/PROBA albedo.

Number of observations: Although the MODIS albedo product uses 16-day period observations of both Terra-MODIS and Aqua-MODIS, in this case study most of the days in the period, about 75% of observations, were cloudy which dramatically reduced the number of observations.

Variability of reflectance during the 16-day period: In the use of sequential multi-date observations it is assumed that the variation of surface reflectance is mainly due to the changes in Sun-view geometry. However, in this case study, changes in the wetness of the land covers, due to rain on the 4th, 12th and 13th, introduced some uncertainties regarding the stability of reflectance at different times.

Clouds and cloud shadows: There were some uncertainties regarding the small clouds or thin clouds which may not have been detected by the MODIS cloud detection algorithm. There were ground observations of cloud appearances on DOY 155 at the time of Terra/Aqua-MODIS overpass when the MODIS QA data recorded clear observations.

The accuracy of the used BRDF model: The assessment of the RTLSR BRDF model showed errors of about 100% in the blue band, 20% in the green band, 30% in the red band and 15% in the NIR band in the resulting BRDF (Figure 6-7). This undermines using this BRDF model at local scales.

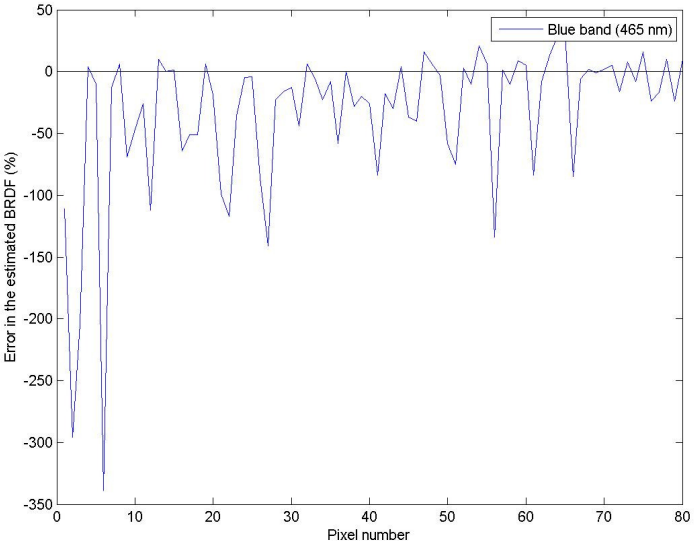
Blue band (465 nm)
Error in the estimated BRDF (%)
Pixel number

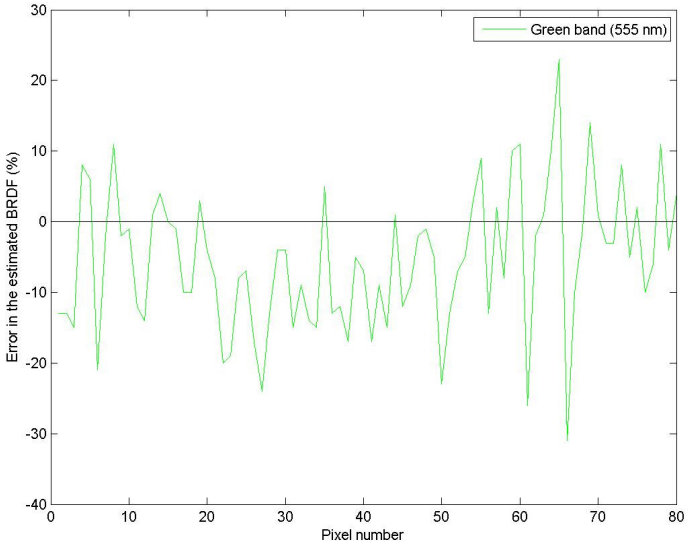
Green band (555 nm)
Error in the estimated BRDF (%)
Pixel number

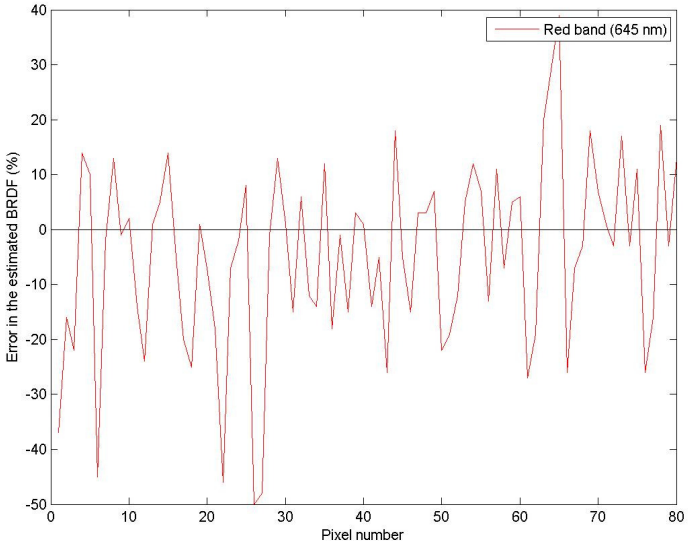
Red band (645 nm)
Error in the estimated BRDF (%)
Pixel number

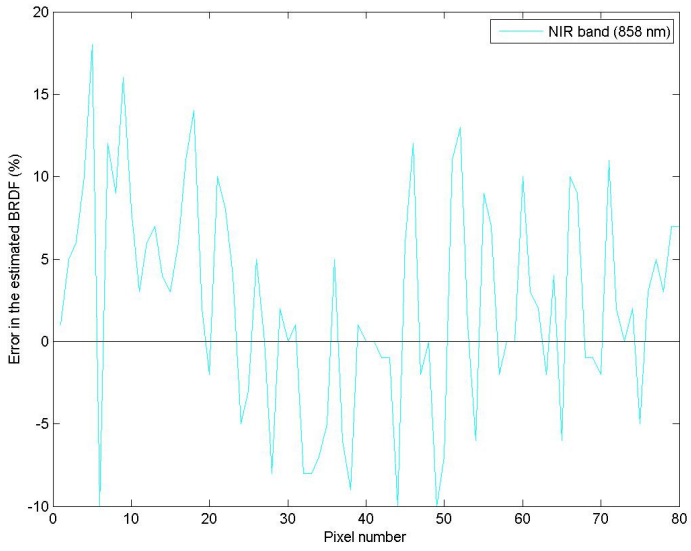

Figure 6-7 The error in the estimated BRDF. This shows the differences in the actual MODIS observations and those from the BRDF model.

Quality control: The quality information of the daily albedo product (DOY 168) showed that almost all the data are of good quality and a full BRDF inversion was carried out. However, the quality information of the MODIS reflectance product showed that most of the daily MODIS reflectance products (more than 75% of observations) during the studied 16-day period, were cloudy and were therefore not valid for entering into the BRDF model.

6.6 Conclusion

This study considered the possibility of the validation of the MODIS albedo values using the CHRIS/PROBA albedo. There were uncertainties regarding the accuracy of the atmospheric correction of the CHRIS data and the applied BRDF model. These uncertainties limited the use of the CHRIS albedo to validate the absolute accuracy of the MODIS data. However, the CHRIS albedo was determined to be valid for assessment of the relative accuracy of the MODIS albedo. The MODIS albedo had less spatial variation than the CHRIS albedo, mainly due to the assumptions used in producing the MODIS albedo product and poor distribution of the observations. This study therefore highlighted a concern about the accuracy of the MODIS albedo product in the UK for applications at local scales. The accuracy of the product seems questionable even when the spatial resolution decreases, as required for climate models.

7 Discussion and Conclusion

Surface albedo is one of the key parameters required in climate/climate change models and surface energy balance studies. Field measurements of albedo are expensive due to the spatial heterogeneity of land surface and climate variables. Remote sensing offers a way of overcoming this barrier by providing continuous information at the global scale. On the other hand, the process of calculating albedo from remotely sensed observations may not be easy or desirable for scientists who need information about surface albedo. The BRDF/Albedo product of MODIS is probably the only remote sensing data that provides routine global coverage of the Earth's surface albedo, every 16 days, at a moderate spatial resolution of 500 m. These characteristics of the product as well as their availability have made it widely used across the globe. Information about the accuracy of such a widely used product is critical for the applications for which it is employed. The MODIS land team reported a high accuracy for the MODIS albedo product, within 5% of the field measured albedo. However, this accuracy was obtained principally under optimal atmosphere and surface conditions such as clear sky, and large homogenous surfaces. This may then not be true for the UK with suboptimal conditions (i.e. a cloudy atmosphere and land surfaces which are heterogeneous in the MODIS spatial resolution). The validation of the MODIS albedo product thus seems critical for the UK.

Validation of the MODIS albedo product was carried out using independent data and methods. A variety of field measurements and high spatial resolution data were used in this study to examine the validity of the MODIS albedo product over a heterogeneous cloudy area in southern England. The data were collected mainly during the NCAVEO field campaign in 2006. The main advantage of the NCAVEO dataset was that the field and remote sensing measurements were nearly simultaneous. This is crucial in surface reflectance and albedo studies as they are highly variable in space and time. The diversity of the NCAVEO datasets was another advantage in the validation of remote sensing data. However, this study used only a subset of the remote sensing dataset, CHRIS/PROBA, SPOT, and EA-CASI, and field measurements, land cover survey, main atmospheric variables and spectra of the surface, which were the most appropriate data for validation of the MODIS albedo product. Comprehensivity of the dataset could help significantly in the study of a variety of variables which affect surface albedo. The dataset included measurements of a variety of atmospheric variables at different atmosphere depths, surface spectra, vegetation structure and growth. The datasets could be used to validate remotely sensed atmospheric correction data, investigate spatial influences on data, as well as the intercomparison of remote sensing observations. Two methods were used: direct and indirect comparisons. The direct

comparison method used a fine resolution albedo from CHRIS/PROBA whereas the indirect method used the fine resolution reflectance data to assess the accuracy of the inputs to the albedo model. As the direct method may quantify the absolute errors in the MODIS albedo the indirect method may help to better understand the probable source of errors. In the indirect method, the fine resolution airborne EA-CASI and SPOT reflectances were used to validate the accuracy of the MODIS atmospheric correction.

One of the advantages of this study was the use of the multiple view angle CHRIS/PROBA datasets to obtain albedo. As there was no field measurement of albedo, the obtained albedo map was validated by testing the accuracy of the atmospherically corrected data. The errors observed in the CHRIS reflectance varied from 20% in the NIR band to more than 60% in the visible bands. The errors may increase, particularly for larger view zenith angles. The atmospheric correction model used for both the reference EA-CASI data and CHRIS data was the same, MODTRAN4. Therefore, the sources of errors in the CHRIS/PROBA reflectance data could be due to errors in the sensor calibration, radiometric and clouds. The investigation of CHRIS/PROBA reflectance (Appendix 1) showed an offset error in the visible region, ranging from +0.02 (in the red band) to +0.07 (in the blue band). The cause of the error may be due to the analogue electronic offsets as reported by Cutter and Johns (2005). The CHRIS toolbox in the BEAM software seemed to correct this error using the latest calibration information for the data. The radiometric errors were due to vertical noise and drop-outs. These errors were also corrected using the CHRIS toolbox in the BEAM software. However, the degree of correctness of these errors, especially in the off-nadir data, could not be determined.

The main issue could be the cloudiness of the day. Although the clouds and cloud shadows were masked before atmospheric correction, the clouds may affect the scattering of light in the clear parts which is not taken into account in current radiative transfer models such as MODTRAN4. This effect can be greater in the off-nadir data as the clear line of sight decreases. The amount of error resulting from this effect may increase as the spatial resolution decreases. In order to minimise the errors in the atmospheric correction, the main source of errors as well as the magnitude of the errors need to be determined. The above-mentioned errors for the CHRIS data were based on the conditions of the study site. Reducing the sources of uncertainties, such as validating the clear sky data for another site in the UK, can result in the determination of the main source of errors. The validation process carried out in this study was restricted to the at-nadir CHRIS data due to the lack of the off-nadir ground measurements of reflectance. BRDF measurements of the same view-Sun geometries at the CHRIS data can provide data for the validation of off-nadir data. However, the BRDF

measurements of the view-Sun geometries can also help in validating the BRDF model. The ground measurements should cover the CHRIS pixels and, if possible, they should be made for different land covers.

The albedo product of MODIS is computed using reflectance data from Terra-MODIS and Aqua-MODIS over a period of 16 sequential days and the RossThickLiSparseReciporacal (RTLSR) BRDF model (Schaaf et al., 2011). The accuracy of the input reflectance data has a direct effect on the accuracy of the albedo product. The atmospheric correction of the MODIS data is carried out using simultaneously measured atmospheric variables created by other MODIS products and the 6SV radiative transfer model (Vermote et al., 2002). The accuracy of the atmospheric correction of the MODIS data, which includes all observations during a 16-day period which are used in producing the albedo product, depends greatly on the climate state. The greatest accuracy may be achieved in the data collected in clear skies, which may be the case in dry areas such as the Sahara desert in summer, although this may be affected by sand-carrying winds which are typical of deserts. Conversely, the lowest accuracy may occur in areas with a large amount of aerosol and water vapour in the atmosphere, which may be the case in coastal areas. He et al. (2010) showed that the aerosol estimated by MODIS was in good agreement with ground measurements but also mentioned errors in the urban areas and some systematic errors which led to underestimation of aerosol when the aerosol amount was high. They mentioned aerosol models and surface reflectance estimations as the main source of errors in the MODIS data. Jin et al. (2003) tested the accuracy of the reflectance product by assessing the Quality Assurance (QA) of the product on an area in southern Africa. Looking at NDVI and neighbouring pixels, they found some cloudy and hazy pixels, although the QA values showed they were clear and cloud-free.

An investigation was carried out regarding the errors in the MODIS reflectance data and how they may affect the resulting albedo. The errors observed in the MODIS reflectance varied from 15% of absolute reflectance values in the NIR band to 66% in the visible band (93% in blue, 43% in green and 62% in red band). The changes in view geometries of the MODIS and the EA-CASI data (about 50°) may introduce some errors in the validation. The RTLSR BRDF model and the daily BRDF parameters were used to correct the BRDF effects in the MODIS data. Correction of the BRDF effect mainly increased the accuracy of the MODIS reflectance in the visible bands. The errors in the MODIS reflectance after the correction of BRDF effects were 19% in the NIR band to 46% in the visible band (46% in blue, 36% in green and 56% in red band). The uncertainties regarding the BRDF parameters employed, the BRDF model and atmospheric correction can offer some explanation for the observed errors. The errors in the atmospheric

correction could be due to undetected small thick clouds or thin cirrus clouds in the MODIS pixel size as well as cloud-shadow effects, uncertainty in the estimated aerosol and aerosol type. Another issue as mentioned above, could be uncertainty in the atmospheric models used for partly cloudy data.

The RTLSR uses the weighted sum of an isotropic parameter, a volumetric kernel which is derived from radiative transfer models (Ross, 1981), and a geometric-optical kernel which is based on surface scattering and geometric shadow-casting theory (Li and Strahler, 1992). The volumetric kernel applies a single-scattering radiative transfer model for a uniform dense leaf canopy with a Lambertian background. The use of this kernel is usually limited to close dense canopies (LAI >3), where the spatial distribution of leaves is random, such as corn, soybean and grass (Yongqin, 2011). The geometric-optical component, the 'LiSparse-R' kernel, considers the shadow-casting effect on reflectance, based on the height and the shape of objects, for a sparse canopy with a Lambertian background. The operational MODIS albedo uses a fixed preselected value for parameters defining the height and shape of the canopy, i.e. crown relative height (h) and vertical to horizontal radius ratio (b/r) (Strahler et al., 1999). This means assuming that all surfaces are spherical crowns that are separated from the ground by half their diameter. This assumption may be true for a forest canopy but not for vegetation such as crops and grass. There are also other uncertainties such as the accuracy of the modelled hot spot effect (Kawata, 2008, Verger et al., 2004), and the high probable effect of the ignored characteristics of vegetation (Rochdi et al., 2006). Therefore, the assumptions used in the BRDF models, which were developed and validated under certain environmental states, may introduce greater uncertainties if the model is used in a different environment. Although the validity of the MODIS BRDF model has been widely tested for a variety of land covers at the global scale, the use of broad classes of land covers, for example using a single definition of land cover class for crops which include a wide variety of crop types may introduce different uncertainties in different land covers. Therefore, the MODIS BRDF model may not be suitable at local or regional scales for which different land covers or more specific land covers may be of interest. The accuracy of the BRDF model could not be assessed in this study due to the lack of sufficient directional ground measurements. However, a simple investigation of the BRDF model using CHRIS/PROBA data showed large errors in the retrieved BRDFs. The investigation was based on the accuracy of the retrieved BRDF at FZA=-55° using the other four view geometries of the CHRIS data. The errors varied from 16% in the NIR band to 131% in the visible band (198% in blue, 85% in green, and 111% in red band). The BRDF model first needs to be validated for different land covers in the study site using the directional BRDF measurements, either extensive ground measurements or using multiple-

sensor/multiple-flightlines airborne data. Uncertainties regarding insufficiency of the number of observations and poor distribution of data can be minimised using observations from other sensors such as MISR.

Problems regarding BRDF and albedo retrieval using remote sensing data also arise from an insufficient number of view angles, which causes the estimated albedo to rely more on the prediction of reflectance from models than on measurements of actual BRDF. The distribution and number of observations may then have a large effect on the estimated BRDF parameters which will affect the resulting albedo. Most of the MODIS observations were collected from the solar cross-principal plane, which are less variable with view geometry. Most days at the study site were cloudy which introduces large errors both upon inclusion of those data, which increases the unreliability of the results, or upon their exclusion, which decreases the number of observations. In brief, the errors in the MODIS BRDF model could also be due to uncertainties in the obtained BRDF parameters resulting from the poor distribution of observations and decreases in the number of cloud-free reflectances.

An assessment of the most critical view geometry for the estimation of albedo was carried out using five view geometries of the CHRIS data. The view geometry of the largest view zenith angle in the backscattering direction, FZA=-55°, had the strongest agreement with the estimated albedo. The errors (percentage median RMSE) in the estimated albedo using this single view geometry, FZA=-55°, were 24% (in the visible band, 0.4-0.7 μm) and 12% (in the NIR band, 0.7-1.1 μm). The error in the broadband albedo (0.4-1.1 μm) was closer to the albedo in the NIR region, 13%, as the NIR covered most of the broadband region. Using a land cover map showed larger errors may appear in the land covers for which albedo is more variable, such as the built-up class for which the errors in the visible and NIR bands were 25% and 15%, respectively. Smaller errors may occur in those land covers with less variability of albedo, such as field beans where the errors in the visible and NIR bands were 17% and 11%. The advantage of using a land cover map is that the modelling of the errors can be more precise. Using nadir view reflectance to calculate albedo, the errors in the estimated albedo went up to 40% in the visible region, 19% in the NIR region and 21% in the broadband region. The errors in estimating albedo were highest for the built-up class, 43% (in the visible region), 26% (in the NIR region) and 31% (in the broadband region), and lowest for oilseed rape, 22%, 11% and 11% in the visible, NIR and broadband bands, respectively. This showed it may be possible, from single view geometries, to calculate broadband albedo with errors of less than 20%. However, the error is higher than the required accuracy for climate models.

The operational MODIS albedo product is claimed to have the required accuracy for the climate models, an absolute accuracy of 0.05 if the quality assurance (QA) data show the best state of the estimated albedo. There was no mention if the claimed accuracy is for the spatial resolution of the operational product, 500 m, or for climate models which have coarser spatial resolutions. This study considered the accuracy of the MODIS albedo at a spatial resolution of 500 m.

In producing the MODIS albedo, it is assumed that the variability of reflectance over a period of 16 sequential days is mainly related to variation in view-Sun geometry. The assumption of invariability of surface reflectance during a 16-day period (Wanner et al., 1997) is the most problematic issue of the albedo product. The reflectance can change based on the moisture of the surface, which is controlled by climate or by humans, in the case of agricultural fields. Wind may also change the surface moisture substantially and thus have an indirect effect on surface reflectance. Wind also controls the amount of aerosol and water vapour in the atmosphere, which affects the atmospheric correction. Schaaf et al. (2011) also mentioned some uncertainties that this assumption may introduce in the albedo product during periods of strong phenological change such as vegetation greenup, senescence, or harvesting and ephemeral snowfall. This study examined the variability of reflectance. The difference in the reflectance of the reference data with the same view-Sun geometry in two days with a one-week difference (EA-CASI and SPOT) was from 11% (in the NIR band) to more than 24% (in the visible bands). The difference in the reflectance in the MODIS data with about the same view-Sun geometry in the same two days was from 7% (in the NIR band) to more than 15% (in the visible bands). This showed that, for the study site, firstly the differences in the sequential 16-day period may not be due to the BRDF effect, secondly, the differences in the reflectance in the 16-day period can be large, and finally, there was an uncertainty in the enhancement of the variations in the MODIS reflectance during 16-day period. The differences in the reflectance can be due to the differences in the soil moisture as the most of the days were cloudy.

An albedo map may be estimated using a land cover map such as the one produced by the MODIS backup algorithm. When the amount and distribution of clear views is insufficient to build the BRDF parameters, a backup algorithm (Strugnell et al., 2001, Strugnell and Lucht, 2001) is used which uses a look-up table of BRDF parameters from previous good days and a land use map. However, the estimation of albedo based on each land cover type can only be true for that surface if the spatial variation of albedo is small within that land cover type. Ignorance of this issue may introduce uncertainties, the magnitude of which depends on the heterogeneity of the area. This study examined the spatial variability of albedo for a variety of land covers (mostly

croplands) using a fine resolution albedo map created from the CHRIS/PROBA data. The size of each land cover field was usually smaller than a MODIS pixel size and therefore each MODIS pixel represented an area with mixed land covers. The investigation of the variation of albedo with land cover showed that the albedo values can greatly vary within each land cover type. The variation was higher in the visible albedo than the NIR and broadband albedos. The error resulting from the point measurements of albedo within each land cover was quantified. The error varied with land cover type and spectral band, ranging from 14% (in stubble) to 25% (in wheat) in visible albedo values and from 7% (in oilseed rape, field beans and wheat) to 16% (in barley) in NIR and broadband albedos. A land cover map may also be used to fill gaps in an albedo map.

Gaps in the albedo map may occur due to clouds. A mean value of albedo for each land cover may be used to fill the gaps in the albedo map provided that the spatial variability of albedo is small. As the spatial variation of albedo increases, the errors in using the mean albedo of land cover increase. The errors ($\alpha_{stdv}*100/\alpha_{mean}$) from using the mean value of visible albedo for each land cover ranged from 14% (in wheat land cover) to 23% (in oilseed rape); the errors decreased in the estimated NIR albedo which ranged from 7% (in oilseed rape, wheat and field beans) to 15% (in barley and stubble). The errors in the broadband albedo (0.4 µm to 1.1 µm) were highest in the built-up class (17%) and lowest in oilseed rape, wheat and field beans (7%). This showed it may be possible to obtain the albedo for most crops with an error within 10%.

As albedo is obtained using all multiple view angle data, the albedo map is restricted to the cloud-free area in all view angles. However, each of the single view geometries may provide some information for the cloudy part of the albedo map. Another method of gap filling can therefore use the relationship between albedo and the directional reflectances used in estimating albedo. However, as mentioned before, the accuracy of the obtained relationship may not be the same as some view geometries may have a poor relationship with albedo such as the nadir view with RMSE of 21% in broadband albedo; while some may have a better relationship, such as those with high view zenith angles in the solar principal plane with RMSE of 13% in broadband albedo. Using a land cover map may help to model the uncertainties with greater accuracy.

The albedo from both sensors, MODIS and CHRIS/PROBA, showed some uncertainties. The question is which sensor is better for use in albedo studies. Choosing the best method to measure albedo depends on sensor properties, the method used for measuring albedo, and climate conditions. MODIS covers most spectral bands used for calculating broadband albedo, while due to restrictions in the spectral bands in the

CHRIS data in the visible and NIR regions (0.4 to 1.1 micron) there are more uncertainties regarding producing broadband albedo (0.3 to 5 micron) from CHRIS data. However, albedo from CHRIS can be valid if visible or NIR albedo is required, which have applications in vegetation studies. CHRIS data has the advantage of a higher spatial resolution, which can make it a better option if an albedo map for each land cover is required. Sensor calibration is probably more accurate in MODIS data than CHRIS data, as some errors in the CHRIS radiances were observed most likely due to the sensor calibration issue. MODIS provides albedo information at different times of year while CHRIS may not; this makes MODIS data more useful to track the changes in albedo during different times of the year. The MODIS albedo uses more observations, in a cloud-free state of sky, to calculate albedo, and also includes the variation in the Sun geometry the calculation of albedo. This can be an advantage for MODIS in areas with clear sky. CHRIS may be used to provide information from cloudy areas, but not on cloudy days, as it obtains all the observations to calculate albedo at the same time. Thus, if the area monitored by CHRIS is cloud-free at a specific time, a more reliable albedo map may be obtained. The distribution of sensor geometry is also in favour of CHRIS data as it covers the solar principal plane. As the changes in albedo are higher in the solar principal plane, more observations from this area can increase the accuracy of the obtained albedo. So, in brief, the CHRIS data can provide a good source of information for validation of the albedo product of MODIS, especially where most of the days are cloudy.

Some previous studies examined the validation of the MODIS albedo product under suboptimal conditions. However, the methodology used in this study showed specific advantages. Disney et al. (2004) examined the accuracy of the MODIS albedo product over agriculture land in UK which was one of the MODIS core validation sites. This study had the advantage of using field measurements of albedo and a variety of airborne and satellite sensor data. However, the albedo product studied was produced by using the observations from Terra only, while the product studied in this thesis used the latest MODIS albedo algorithm which uses both Terra and Aqua observations which use a greater number of observations to run the BRDF model. In this study the MODIS albedo with a 500 m resolution was used whereas Disney et al. (2004) used the MODIS product with a 1 km resolution. However, the spatial resolution of fine resolution remote sensing data which acted as intermediate data to scale up the field measurements were about the same as our data, up to about 30 m. This means the fine resolution intermediate data were upscaled to a coarser spatial resolution which theoretically should have been less representative of the heterogeneous area covered. Disney et al. (2004) used the point field measurements of albedo to compare with the 1-km MODIS albedo product. Although they used some other high spatial resolution

remote sensing data as intermediate data, those data were obtained at the nadir view angle and could not capture the anisotropy of the surface. They simply assumed a Lambertian surface for the studied area whereas this thesis showed this assumption would have introduced larger errors in the resulting albedo. The anisotropy of the surface was captured by the CHRIS/PROBA observations due to relatively well-distributed multiple view angle observations in the solar principal plane. The available high spatial resolution data were also used to validate the inputs to the MODIS albedo product which is a robust method. There are also other uncertainties in the method used by Disney et al. (2004) such as using the albedo product obtained by a backup algorithm, which is based on land cover, due to insufficient cloud-free observations, and using the 16-day albedo product and assuming it was equivalent with the daily albedo observations.

Validation of remotely sensed albedo could be a straightforward process if there were optimal conditions in environmental, climate and surface conditions, and if dataset werecomprehensive, cloud-free, with a reliable sensor calibration, atmospheric correction and more. For the study site in the UK with suboptimal conditions in the environment and dataset, validation of the MODIS albedo was not an easy task. In addition, most previous validation studies were for optimal conditions so there was a lack of literature for areas with suboptimal conditions particularly in the UK. The methodology was mainly developed as the data were processed and analysed and had to be modified several times at each stage. For example, the validation of the MODIS albedo was carried out using the first version of the atmospherically-corrected CHRIS/PROBA datasets; however, an investigation of the reflectances obtained from the CHRIS/PROBA datasets identified some uncertainties.

Further studies are required to validate remotely sensed albedo under UK conditions. Field measurements of narrow band albedo, using instruments such as a goniometer, as well as total shortwave albedo, using instruments such as a pyranometer, may lead to a better way of modelling the errors in the estimated broadband albedo from remote sensing data. As albedo may vary significantly with land cover, point field measurements may not provide enough reference albedo information in the MODIS pixel size. Multiple scale observations of albedo may be used to overcome this barrier. Fine spatial resolution airborne data, of a few metres resolution, may be comparable with field measurements. These data may be collected simultaneously with the other satellite observations, can be programmed to cover desired spectral bands, and designed to provide multiple view angle observations either using multiple view sensors or multiple flight lines which cover critical view geometries in albedo estimation. Multiple view angle CHRIS/PROBA datasets are valuable in albedo studies

as their well distribution in solar principal plane. Developing downscaling and upscaling methods may help greatly in the validation of coarse spatial resolution data. A detailed land cover map may provide information to develop algorithms for albedo estimation especially in cloudy areas such as the UK.

The assumptions used in producing the MODIS albedo product, the accuracy of atmospherically corrected input data to the BRDF/Albedo model, and the accuracy of the BRDF model all contribute to the observed uncertainties in the MODIS albedo product. It was shown that the accuracy of the MODIS albedo product was much lower than the 5% claimed by the MODIS team under UK conditions. The observed errors in the MODIS reflectance data under the best conditions at the study site (least cloudy days) were 40% in the visible band and 20% in the NIR band. As most days were cloudy, the accuracy of the atmospheric correction of the MODIS data could be worse. As the errors in the reflectances used have a direct effect in the resulting albedo, the errors in the broadband MODIS albedo product could be 20% to 30%. The accuracy, however, increased as spatial resolution decreased. The error in the broadband MODIS albedo could be 10% to 15%. This is not good news for climatologists who wish to have an albedo with accuracy within 5%. The MODIS albedo product was also less sensitive to the spatial variations of albedo due to variations in surface and climate conditions with space. This could be disappointing news for the hydrologists who are interested in mapping albedo variations over agricultural lands. Improvements in atmospheric correction methods and BRDF modelling could largely minimise the error in estimated albedo. Airborne data are particularly useful as we may be able to plan in advance the minimisation of errors by covering the critical view geometries, the most important spectral regions and so on.

A1 Appendix 1

This appendix assesses the performance of the BEAM and ATCOR softwares for the atmospheric correction of CHRIS/PROBA data.

A1.1 Introduction

CHRIS/PROBA monitors the target on the Earth in both across track and along track directions. It provides five consecutive images from five different angles which yield valuable information for BRDF and albedo studies. The target is viewed when the sensor has fly-by zenith angles of 0°, ±36° and ±55°. The fly-by zenith angle is the sensor zenith angle respect to the closest point to the target on the satellite's ground track. The spatial and spectral resolution varies according to the acquisition mode which is defined based on the purpose of the study.

The accurate atmospheric correction of the CHRIS data is an important step in modelling surface albedo. Radiometrically corrected satellite data are usually corrected for atmospheric correction. However, in the case of CHRIS data a further step to investigate the correctness of the data is required, since CHRIS/PROBA was originally designed for demonstrational purposes. Some issues regarding the CHRIS data such as the offset errors introduced by the analogue electronic offsets were reported (Cutter and Johns, 2005). The radiative transfer MODTRAN4 code is a physical atmospheric correction model which is claimed to have a high accuracy. However, running the model on remote sensing data can be a difficult task since it is a forward model. ATCOR2 and BEAM softwares use MODTRAN4 to perform an accurate atmospheric correction on satellite data. However, off-nadir view angle satellite data require specific consideration due to the coupling surface-atmosphere BRDF effect. In this study, the accuracy of the atmospheric correction performed by these softwares was assessed. A more accurate surface reflectance was then chosen for further study.

Table A1- 1 Characteristics of the different acquisition modes of CHRIS/PROBA data

Acquisition mode	Spatial resolution	Band range (nm)	Band number	Swath width	Purpose of study
Mode 1	34 m	406-992	62	14 km	Agriculture

Mode 2	17 m	406-1003	18	14 km	Water
Mode 3	17 m	438-1035	18	14 km	Land
Mode 4	17 m	486-788	18	14 km	Chrolophyl
Mode 5	17 m	438-1003	37	7 km	Land

A1.2 Method

In this section, the theoretical basis of atmospheric correcting using the ATCOR-2 and BEAM softwares is described. The atmospheric correction of EA-CASI data and the validation method were described in the previous chapter.

ATCOR-2 is a commercial software for the atmospheric correction of satellite imagery with a small to medium Field Of View (FOV) from a flat terrain. It uses the atmospheric database calculated by the MODTRAN4 radiative transfer model. The database is produced as look-up tables (LUTs) which contain pre-calculations of the typical atmospheric states and is then corrected by ATCOR. Visibility is calculated for dark reference pixels and aerosol optical thickness is then obtained from a non-linear relationship with visibility which has been defined by MODTRAN. Aerosol is modelled by choosing an appropriate aerosol type from four basic aerosol types, rural, urban, desert and maritime. Water vapour is obtained using a differential absorption method which uses bands between 940 and 1130 nm.

The BEAM software was developed by the European Space Research Institute (ESRIN), which is a part of European Space Agency (ESA), for processing of remote sensing data and in particular those data provided by the ESA. The CHRIS toolbox was added to the BEAM software to overcome the difficulties in the pre-processing of CHRIS/PROBA data (Alonso et al., 2009). It includes modules for performing noise reduction, cloud screening, and atmospheric correction. The atmospheric correction algorithm used in the CHRIS toolbox is based on work by Guanter et al. (2005). It uses a Look-Up Table (LUT) generated by the MODTRAN4 radiative transfer model and retrieves the required information from the image itself. Dependingthe mode of the CHRIS/PROBA data, the quality of atmospheric correction varies. The best quality is expected in modes 1 and 5 where the spectral resolution is sufficient for deriving different atmospheric variables. The columnar water vapour estimation, a top threshold of AOT at 550 nm, spectral calibration and spectral polishing can be carried out in these modes. The data are corrected for vertical stripes and cloud effects before atmospheric correction using the Noise Reduction and Cloud Screening modules.

There are two kinds of noise in the CHRIS data: vertical noises and dropouts. The former derives from irregularities of the entrance slit and Charge-Coupled Device (CCD) elements. This is due to changes in the sensor temperature in the across track direction. The latter comes from problems in the transmission of band 2 of CHRIS. Firstly, dropout pixels are corrected using spatial and spectral information of the wrong pixel and its neighbours. Vertical noises are then corrected in two steps: first they are corrected using the lookup tables (LUTs) of the noise pattern and its relationship with the sensor temperature; then the remaining strips for each band are corrected using the information from the image and the method presented by Fomferra and Brockmann (2005).

BEAM removes the cloudy pixels using a Cloud Screening (CS) module before the atmospheric correction. The CS algorithm transforms TOA reflectance into a set of features taking into account illumination, atmosphere and surface effects. Then an unsupervised classification method is applied to produce the cloud probability for each pixel. Spectral unmixing can also be applied to produce the cloud fraction per pixel.

For atmospheric correction, first the CHRIS data are corrected for spectral displacement, then aerosol optical thickness and columnar water vapour are retrieved and finally the obtained surface reflectance is corrected for spectral systematic errors. Since there are some uncertainties regarding the calibration of the CHRIS data (Cutter and Johns, 2005), a physical radiative transfer method leads to some errors. A combined atmospheric correction method using both empirical and physical methods is then used for the CHRIS/PROBA data. The empirical line method only corrects the image for the miscalibration of data while the MODTRAN 4 radiative transfer method is responsible for the atmospheric correction of CHRIS data. There is no need for ground measurements and the necessary information is obtained from the image. Five reference pixels with a high spectral contrast provide a means of inverting the TOA radiances and obtaining AOT, water vapour content, and updated calibration coefficients. The selection of the five reference pixels should be from the dark dense vegetation to bare soil to find reliable calibration coefficients. In contrast to the general empirical line method, the calibration coefficients are not used to obtain surface reflectance but to correct the radiometric calibration errors.

A1.3 Case study and data

Chilbolton is approximately 45 km north of Southampton in southern England and is the site of the STFC Chilbolton Facility for Atmospheric and Radio Research (CFARR)

(latitude 51° 8' 41.57" N, longitude 1° 26' 18.00" W, and altitude 88 m). The area around CFARR was used for a field campaign organized in June 2006 by the Network for Calibration and Validation in Earth Observation (NCAVEO). The area around the research station is mainly composed of agricultural fields, conifer and broadleaf woodlands and grasslands. In June 2006 the main crops were barley, wheat, oats and oilseed rape.

During the NCAVEO field campaign 2006 (NFC06), a variety of ground measurements and satellite and airborne data were collected. Ground measurements included surface reflectance from several artificial and natural land covers, AOT and water vapour. The full data set is described by Milton et al. (2008), from which EA-CASI and CHRIS/PROBA data were used in this research.

The Compact High Resolution Imaging Spectrometer (CHRIS) onboard ESA's PROBA satellite is a hyperspectral instrument which operates in five different modes that differ from each other in spectral bands sensed (18 to 62 bands), and spatial resolution, from 17 m to 34 m. The NFC06 data were acquired in Mode 1 which has a full swath width, 62 spectral bands ranging from 405 nm to 1009 nm, and nadir spatial resolution of 34 m.

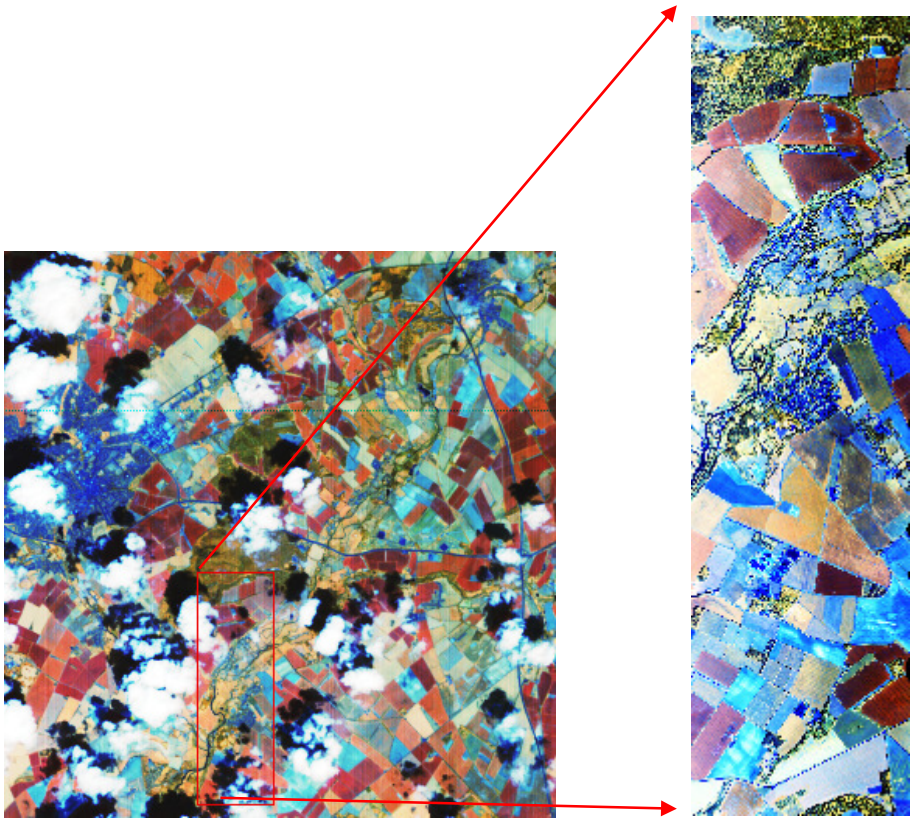

Figure A1- 1 The Level 1B CHRIS/PROBA data at nadir view (on the left) and EA-CASI data (on the right) from the Chilbolton area on 17th June 2006.

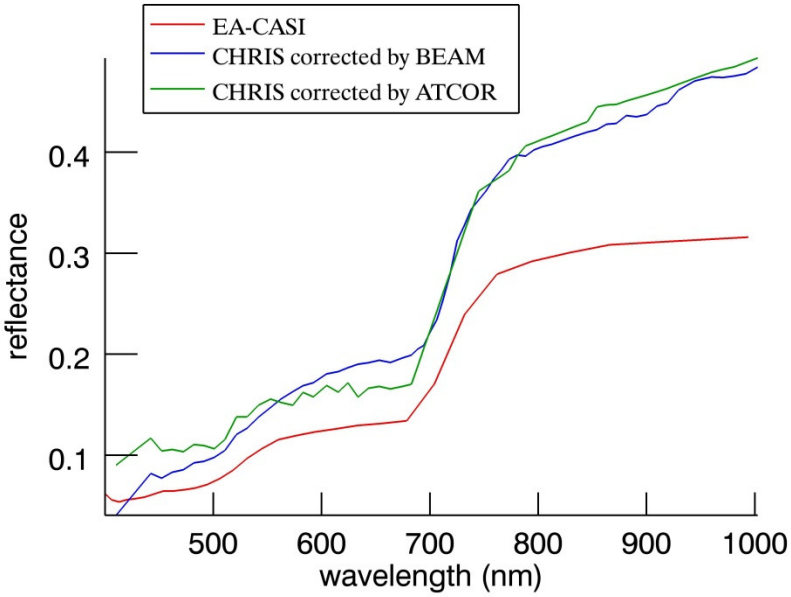

Figure A1- 2 Spectral profile of the reflectance of a set-aside land cover (sparse vegetation) in EA-CASI data, CHRIS data corrected by BEAM software and CHRIS data corrected by ATCOR software

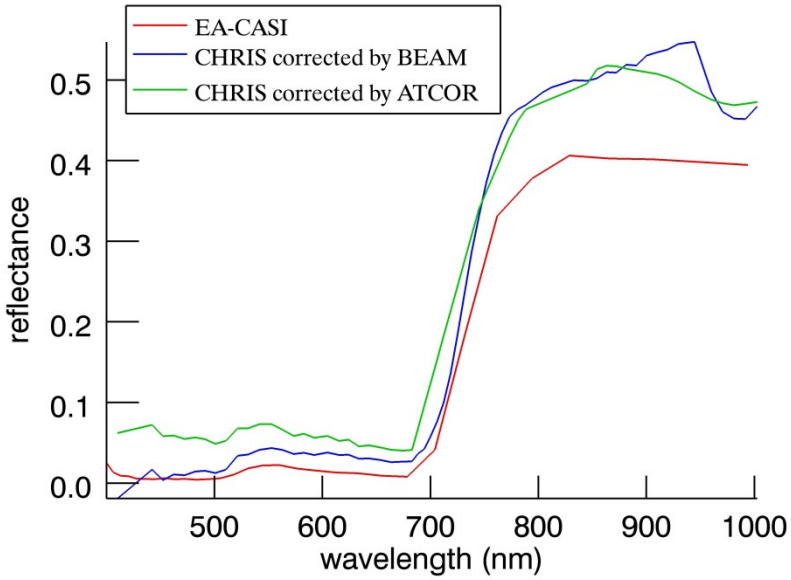

Figure A1- 3 Spectral profile of the reflectance of a vegetation land cover in EA-CASI data, CHRIS data corrected by BEAM software and CHRIS data corrected by ATCOR software

A1.4 Methodology

Surface reflectance was obtained using the ATCOR-2 software and Beam-CHRIS toolbox. The data were then geometrically corrected using the Ground Control Point (GCP) method and an Ordnance Survey Map (1:25000) with Ordnance Survey of Great Britain 1936 datum and Transfer Mercator projection. The results were compared against the EA-CASI surface reflectance already validated with ground measurements. The CHRIS and EA-CASI data were upscaled spatially and spectrally to a coarser resolution. Higher spatial resolution EA-CASI data were also spatially upscaled to CHRIS's spatial resolution while the higher spectral resolution CHRIS data were spectrally resampled to the EA-CASI bands 3 to 32. The spectral resampling was carried out using a Gaussian spectral response function and the full-width half-maximum of each band. The spatial upscaling was performed using an aggregation function.

The CHRIS data were destriped using a program provided by the ESA called HDFclean, and then atmospherically corrected using ATCOR-2. The reflectance data were then registered to the Ordnance Survey National Grid using GCPs. This was difficult due to the large proportion of cloud and cloud shadows, especially for the extreme off-nadir view angles (± 55° nominal).

The CHRIS data were also corrected for noise, clouds and atmosphere effects using BEAM software. The data were then geocorrected using the Ground Control Points (GCPs) method. The optimal cloud screening was carried out using 14 clusters, 30 iterations and 31415 random seeds. Pixels with brightness greater than 37% were recognised as clouds and those with brightness less than 8% as shadow. The atmospheric correction was then run using the initial values for AOT at 550 nm, 0.27, and water vapour column, 2.67 g cm^{-2}, from the ground measurements. The default cloud product threshold of, 0.05 was used. The adjacency correction, spectral polishing and water vapour mapping options were checked to be performed.

A1.5 Results of the validation of CHRIS reflectance from BEAM

The CHRIS/PROBA data at nadir view were atmospherically corrected using BEAM software. The CHRIS data were then resampled to EA-CASI spectral bands while the EA-CASI data were upscaled to the CHRIS spatial resolution. The CHRIS surface reflectance was then validated against the reference EA-CASI data.

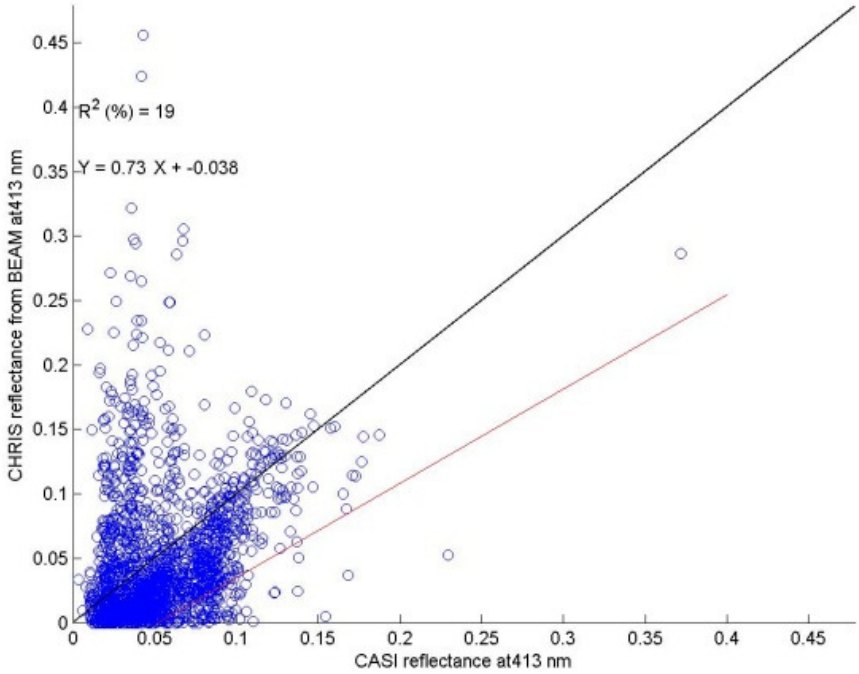

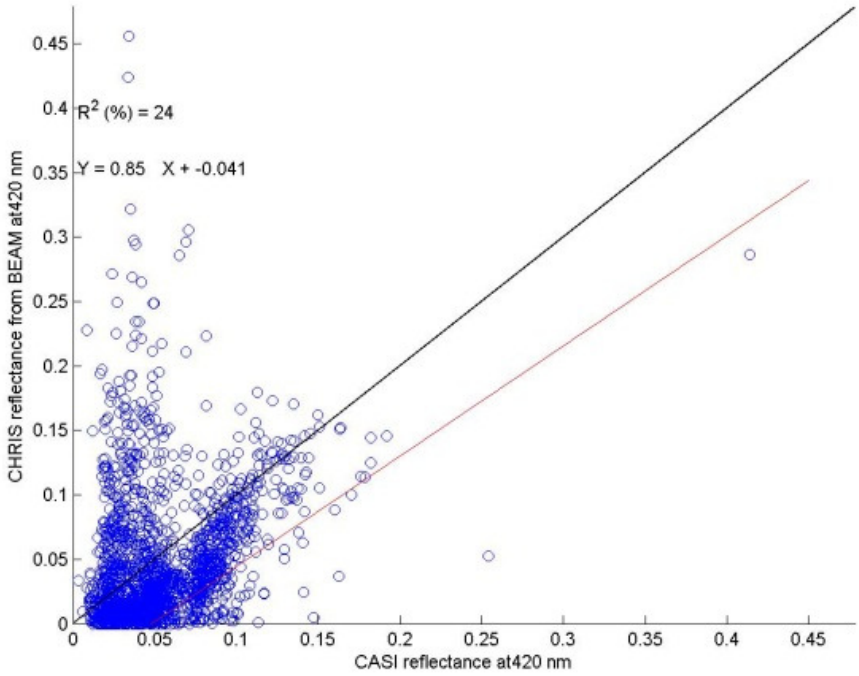
R2 (%) = 24
Y = 0.85 X + -0.041
CHRIS reflectance from BEAM at420 nm
CASI reflectance at420 nm
0
0.05
0.1
0.15
0.2
0.25
0.3
0.35
0.4
0.45

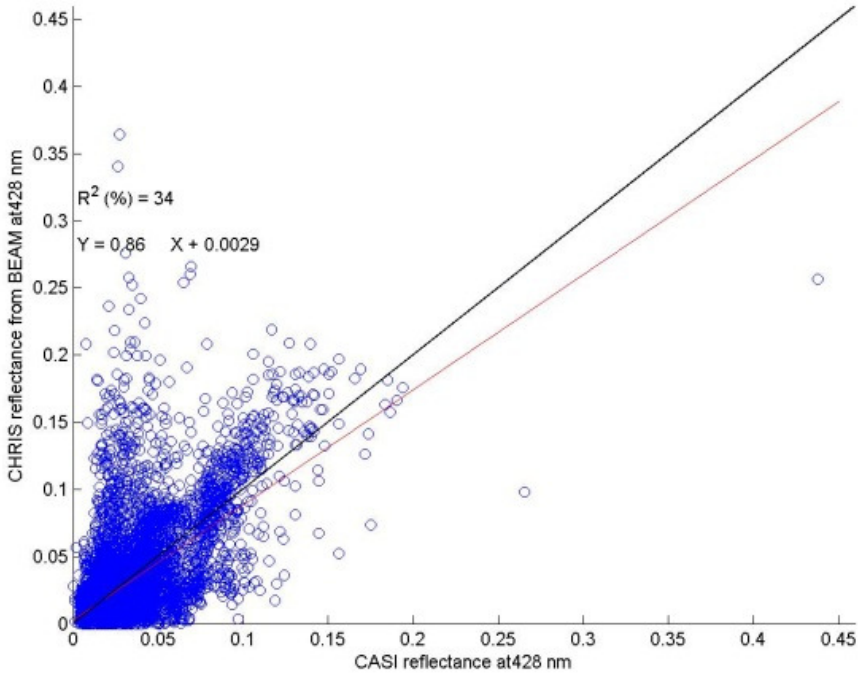
R2 (%) = 34
Y = 0.86 X + 0.0029
CHRIS reflectance from BEAM at428 nm
CASI reflectance at428 nm
0
0.05
0.1
0.15
0.2
0.25
0.3
0.35
0.4
0.45

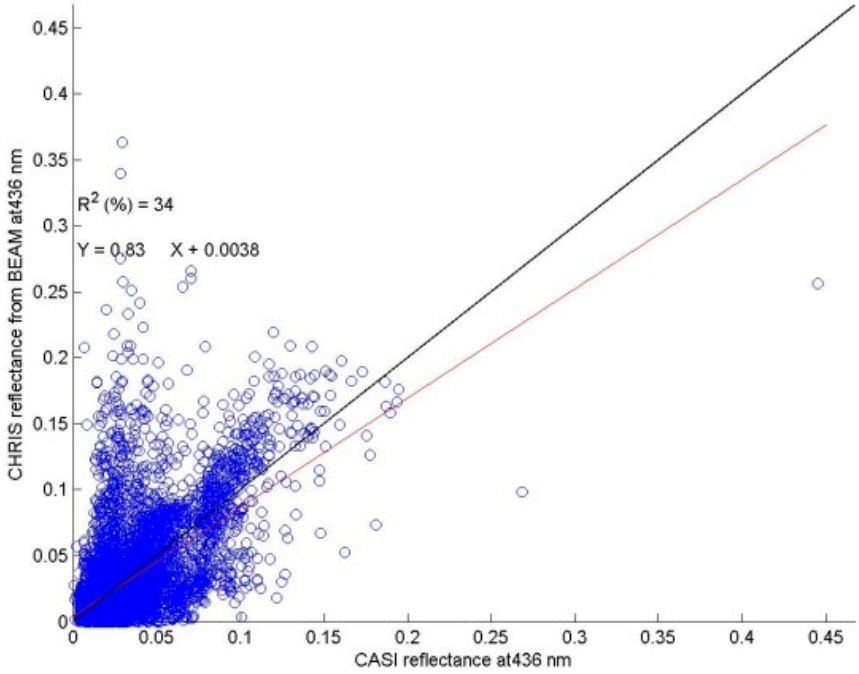
CHRIS reflectance from BEAM at436 nm
CASI reflectance at436 nm
R2 (%) = 34
Y = 0.83 X + 0.0038
0
0.05
0.1
0.15
0.2
0.25
0.3
0.35
0.4
0.45

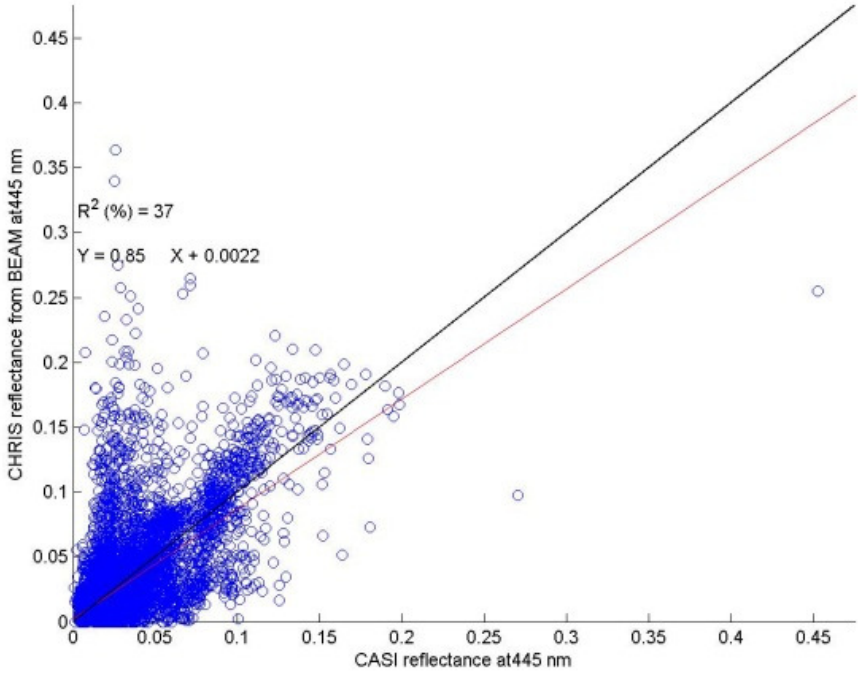
CHRIS reflectance from BEAM at445 nm
CASI reflectance at445 nm
R2 (%) = 37
Y = 0.85 X + 0.0022
0
0.05
0.1
0.15
0.2
0.25
0.3
0.35
0.4
0.45

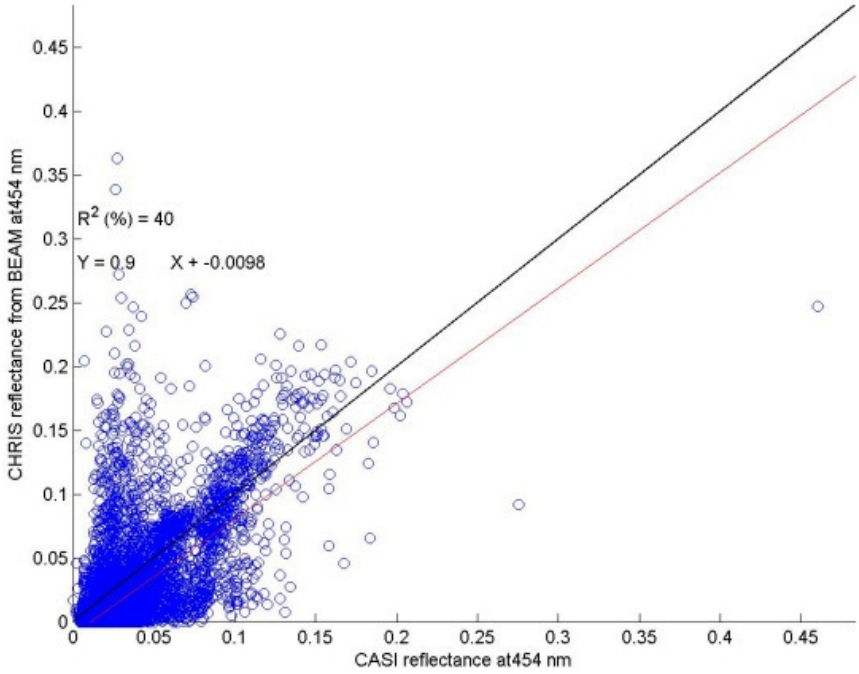
CHRIS reflectance from BEAM at454 nm
CASI reflectance at454 nm
R2 (%) = 40
Y = 0.9 X + -0.0098
0
0.05
0.1
0.15
0.2
0.25
0.3
0.35
0.4
0.45

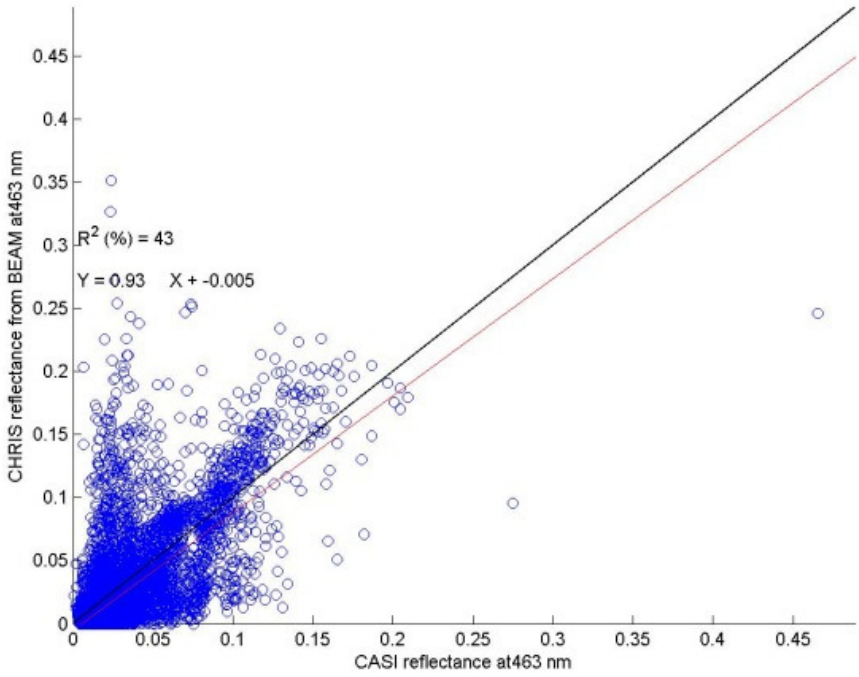
CHRIS reflectance from BEAM at463 nm
CASI reflectance at463 nm
R2 (%) = 43
Y = 0.93 X + -0.005
0
0.05
0.1
0.15
0.2
0.25
0.3
0.35
0.4
0.45

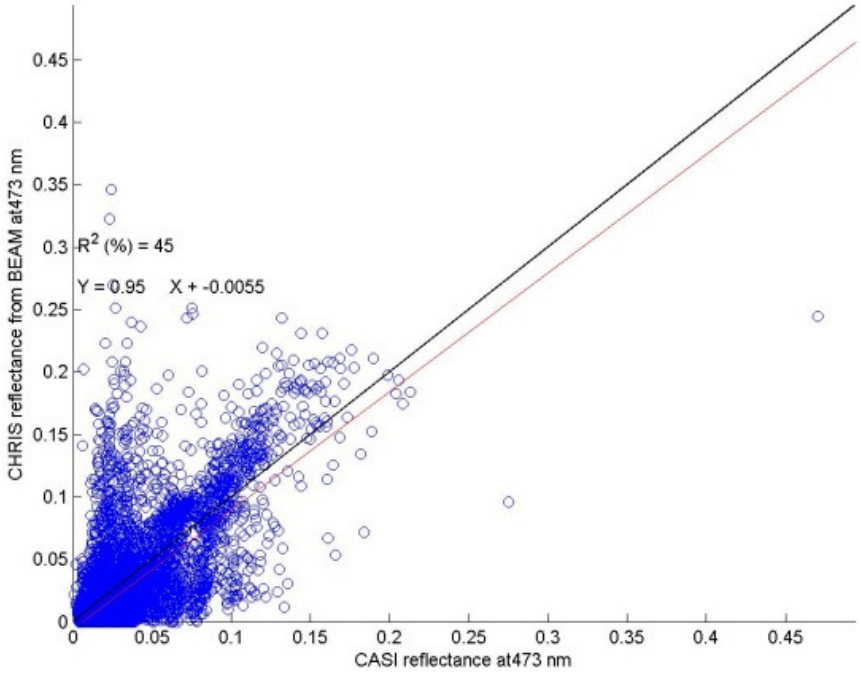
CHRIS reflectance from BEAM at473 nm
CASI reflectance at473 nm
R2 (%) = 45
Y = 0.95 X + -0.0055
0
0.05
0.1
0.15
0.2
0.25
0.3
0.35
0.4
0.45

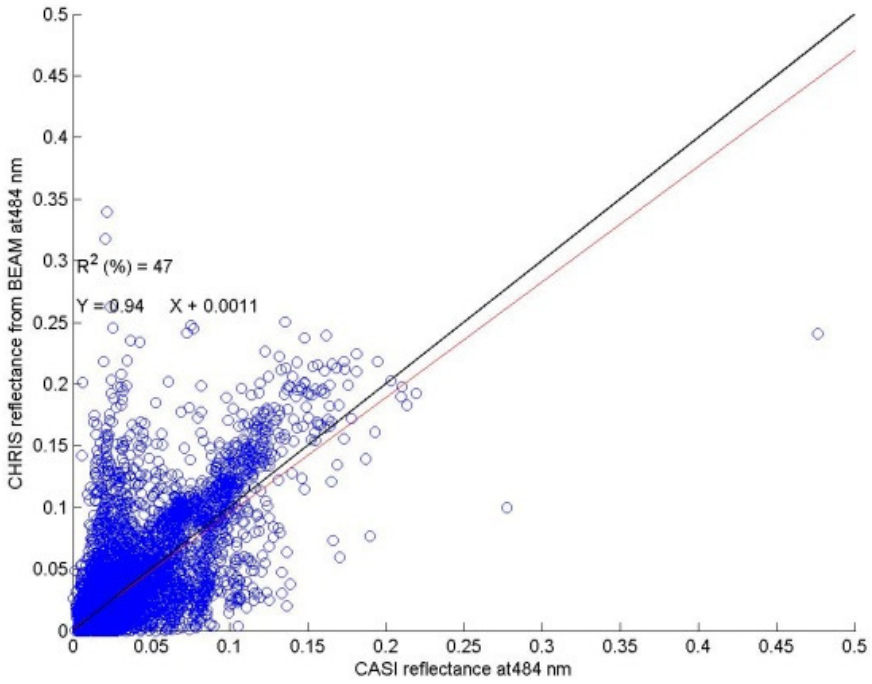
CHRIS reflectance from BEAM at484 nm
CASI reflectance at484 nm
R2 (%) = 47
Y = 0.94 X + 0.0011
0
0.05
0.1
0.15
0.2
0.25
0.3
0.35
0.4
0.45
0.5

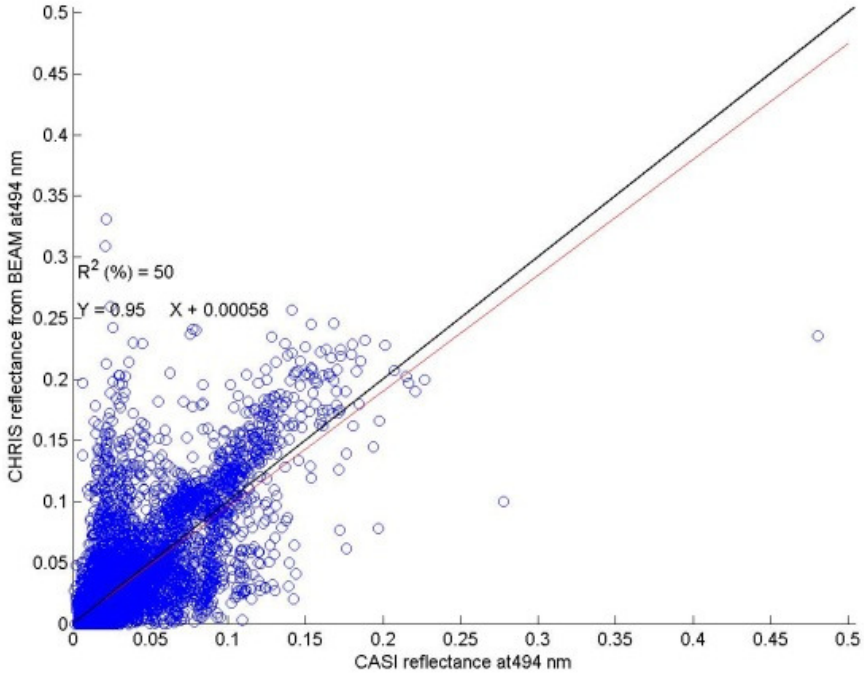
CHRIS reflectance from BEAM at494 nm
CASI reflectance at494 nm
R2 (%) = 50
Y = 0.95 X + 0.00058
0
0.05
0.1
0.15
0.2
0.25
0.3
0.35
0.4
0.45
0.5

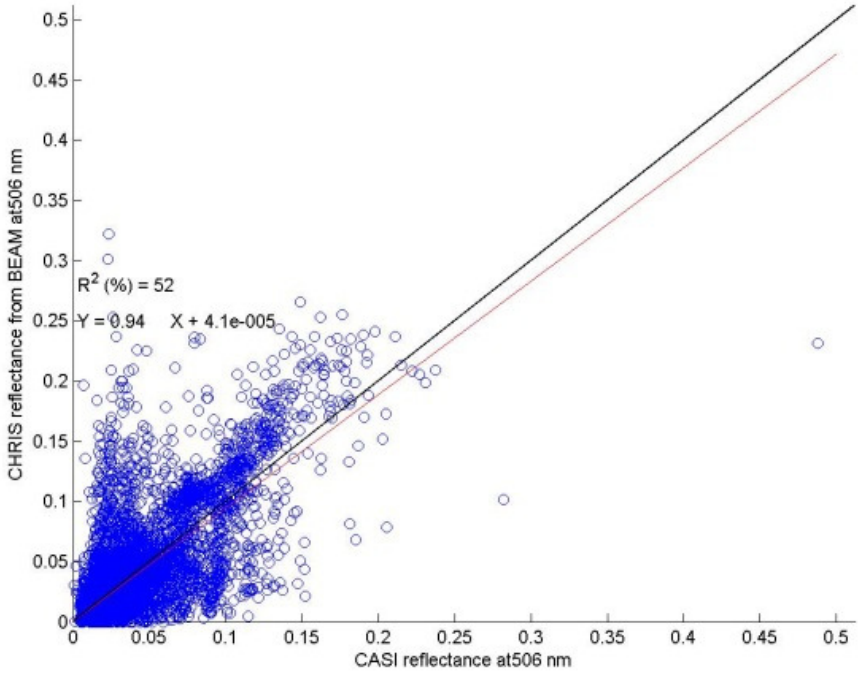
CHRIS reflectance from BEAM at506 nm
CASI reflectance at506 nm
R2 (%) = 52
Y = 0.94 X + 4.1e-005
0
0.05
0.1
0.15
0.2
0.25
0.3
0.35
0.4
0.45
0.5

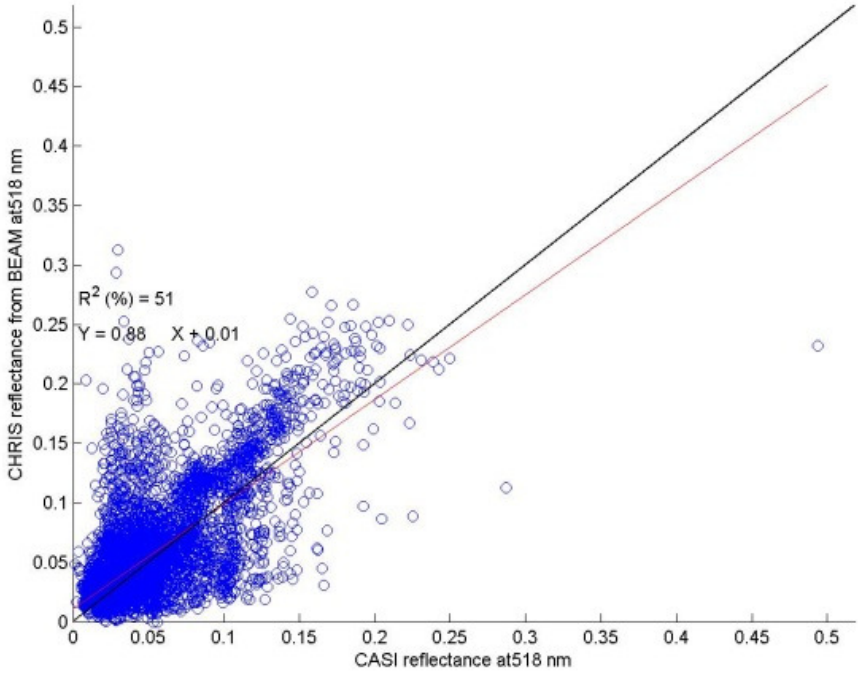
CHRIS reflectance from BEAM at518 nm
CASI reflectance at518 nm
R2 (%) = 51
Y = 0.88 X + 0.01
0
0.05
0.1
0.15
0.2
0.25
0.3
0.35
0.4
0.45
0.5

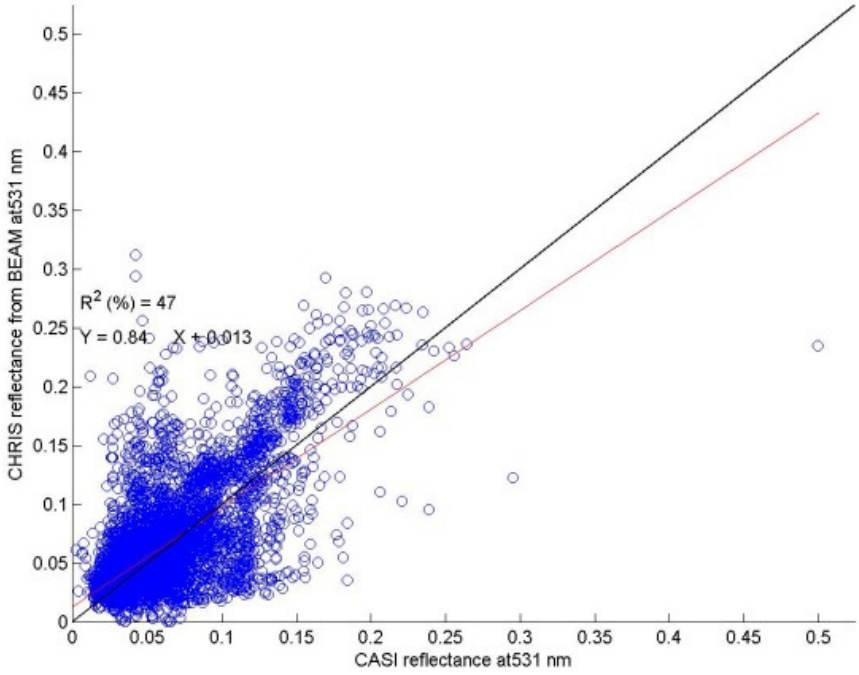
CHRIS reflectance from BEAM at531 nm
CASI reflectance at531 nm
R2 (%) = 47
Y = 0.84 X + 0.013
0
0.05
0.1
0.15
0.2
0.25
0.3
0.35
0.4
0.45
0.5

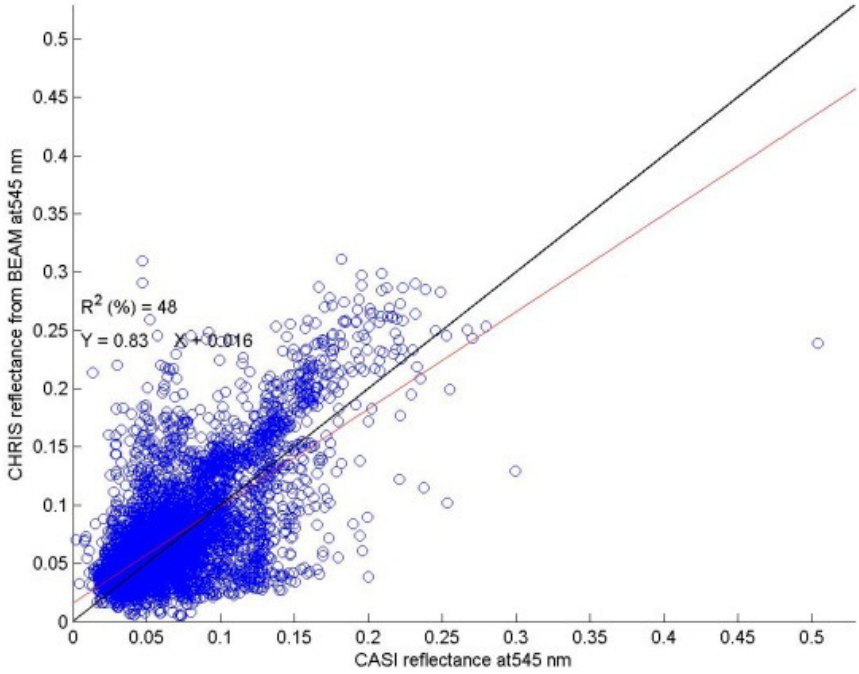
CHRIS reflectance from BEAM at545 nm
CASI reflectance at545 nm
R2 (%) = 48
Y = 0.83 X + 0.016
0 0.05 0.1 0.15 0.2 0.25 0.3 0.35 0.4 0.45 0.5

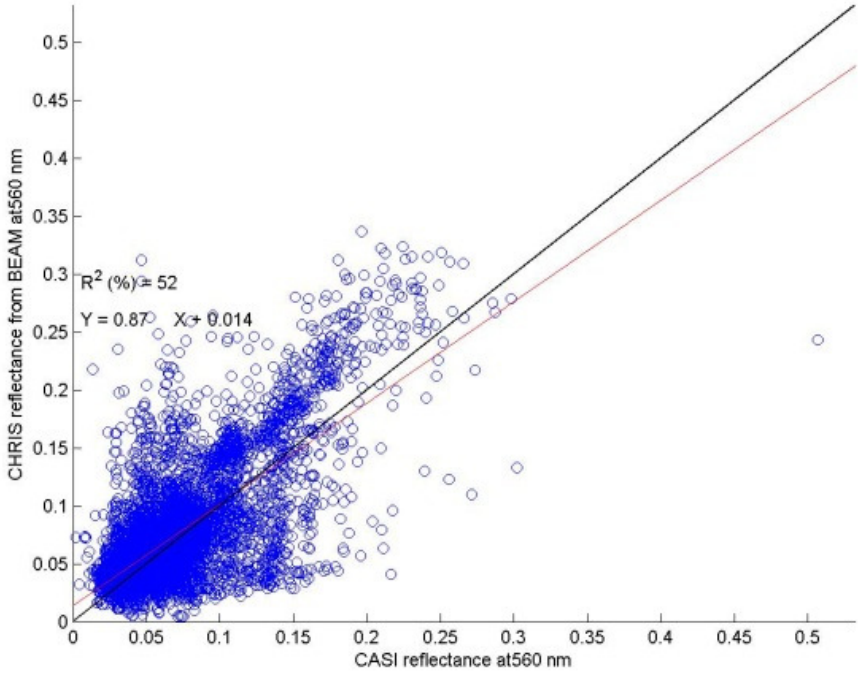
CHRIS reflectance from BEAM at560 nm
CASI reflectance at560 nm
R2 (%) = 52
Y = 0.87 X + 0.014
0 0.05 0.1 0.15 0.2 0.25 0.3 0.35 0.4 0.45 0.5

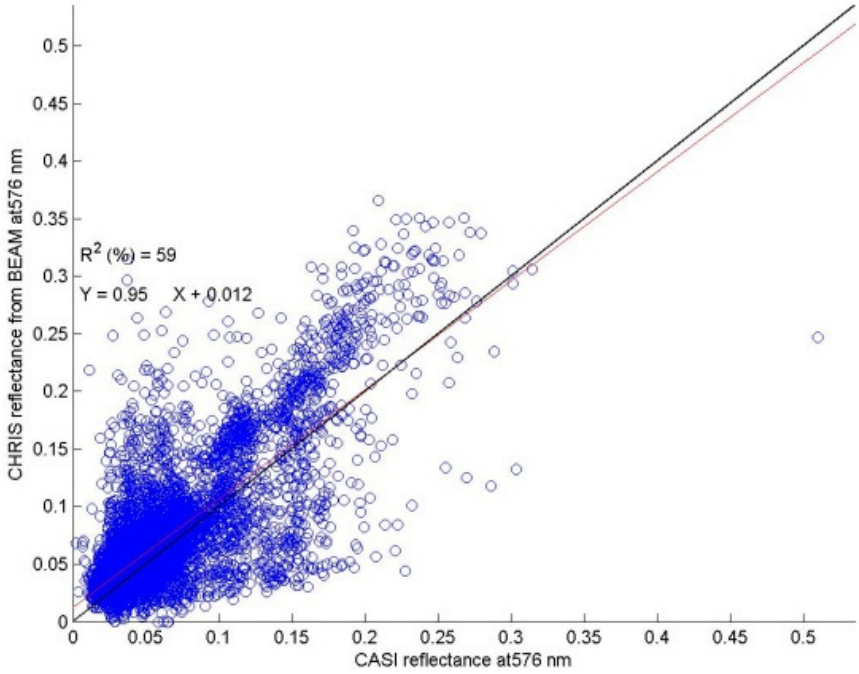
CHRIS reflectance from BEAM at576 nm
CASI reflectance at576 nm
R2 (%) = 59
Y = 0.95 X + 0.012
0
0.05
0.1
0.15
0.2
0.25
0.3
0.35
0.4
0.45
0.5

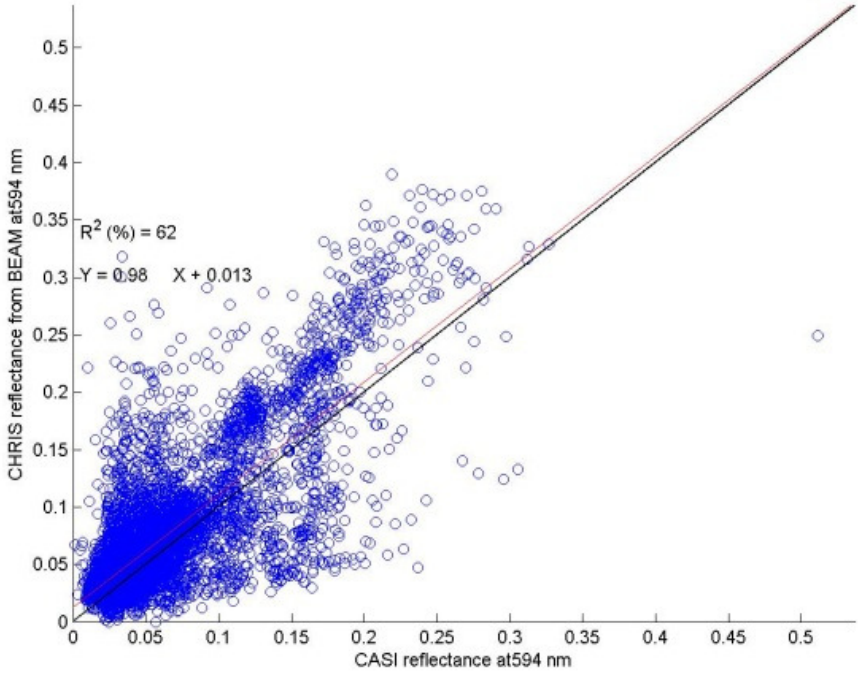
CHRIS reflectance from BEAM at594 nm
CASI reflectance at594 nm
R2 (%) = 62
Y = 0.98 X + 0.013
0
0.05
0.1
0.15
0.2
0.25
0.3
0.35
0.4
0.45
0.5

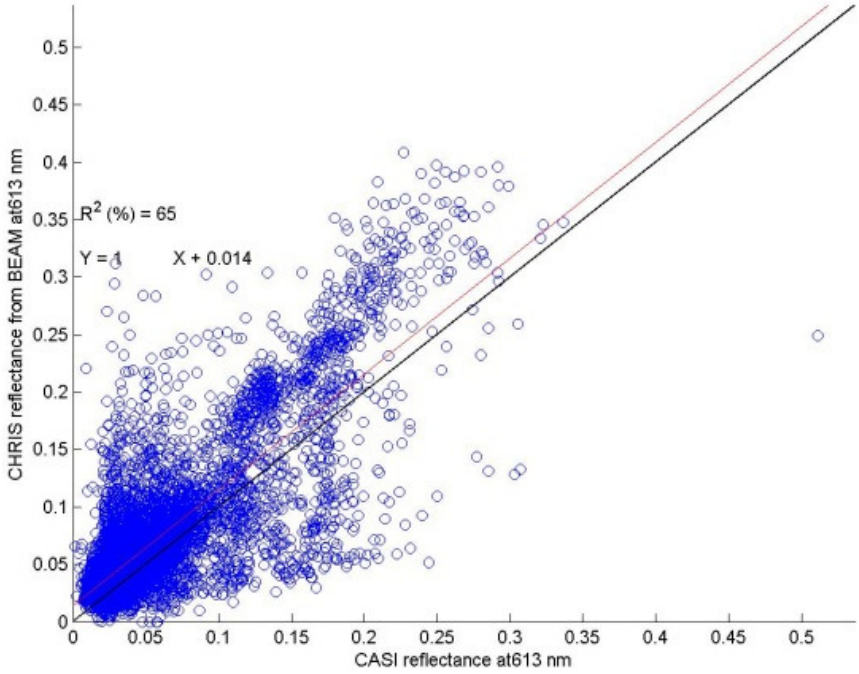
CHRIS reflectance from BEAM at613 nm
CASI reflectance at613 nm
R2 (%) = 65
Y = 1 X + 0.014
0 0.05 0.1 0.15 0.2 0.25 0.3 0.35 0.4 0.45 0.5

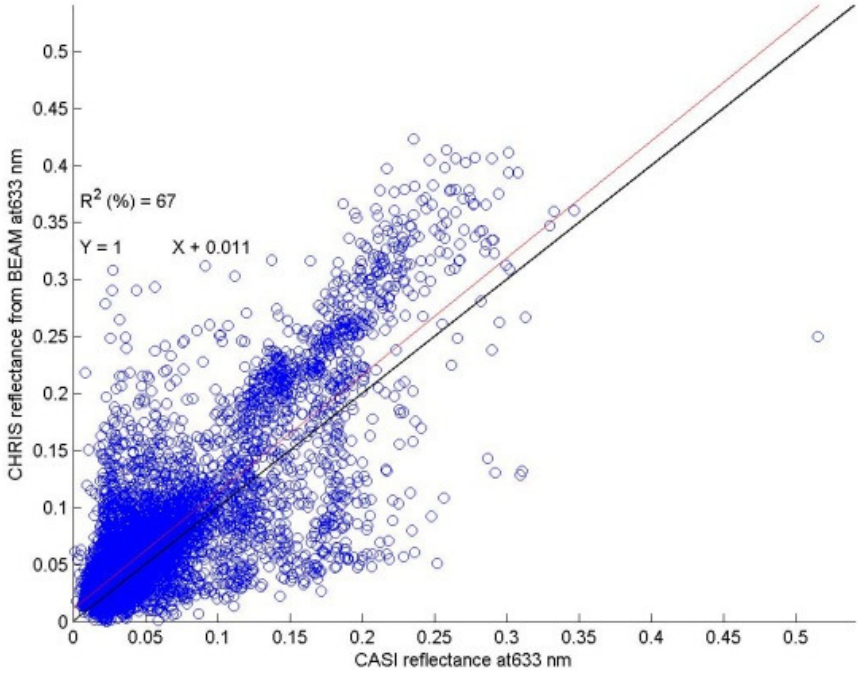
CHRIS reflectance from BEAM at633 nm
CASI reflectance at633 nm
R2 (%) = 67
Y = 1 X + 0.011
0 0.05 0.1 0.15 0.2 0.25 0.3 0.35 0.4 0.45 0.5

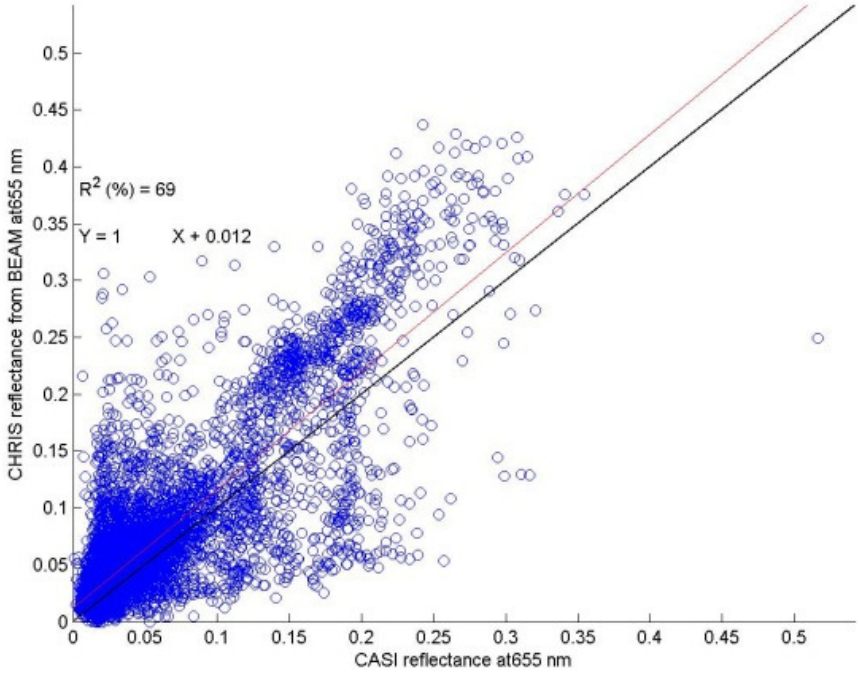
CHRIS reflectance from BEAM at655 nm
CASI reflectance at655 nm
R2 (%) = 69
Y = 1 X + 0.012
0 0.05 0.1 0.15 0.2 0.25 0.3 0.35 0.4 0.45 0.5

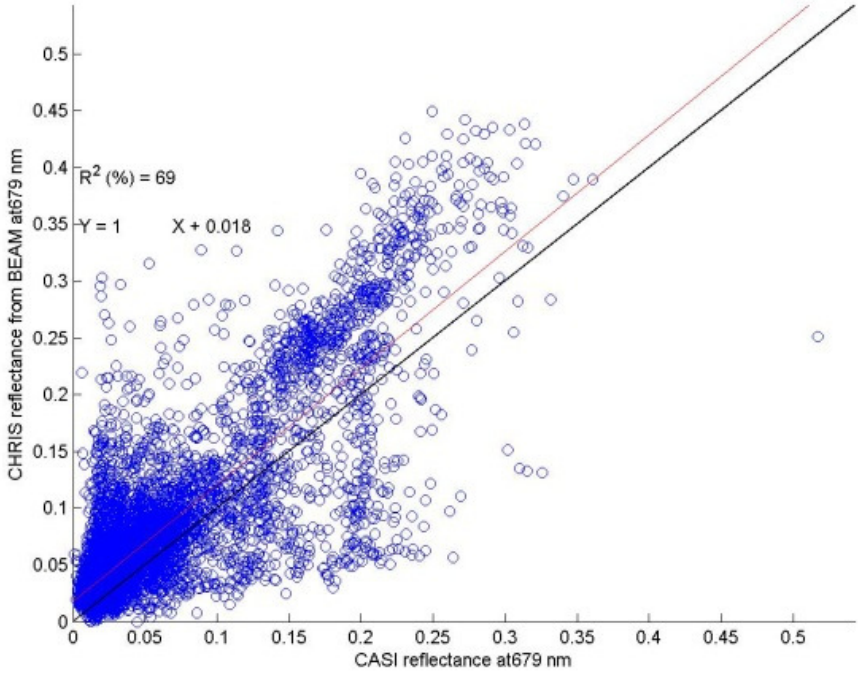
CHRIS reflectance from BEAM at679 nm
CASI reflectance at679 nm
R2 (%) = 69
Y = 1 X + 0.018
0 0.05 0.1 0.15 0.2 0.25 0.3 0.35 0.4 0.45 0.5

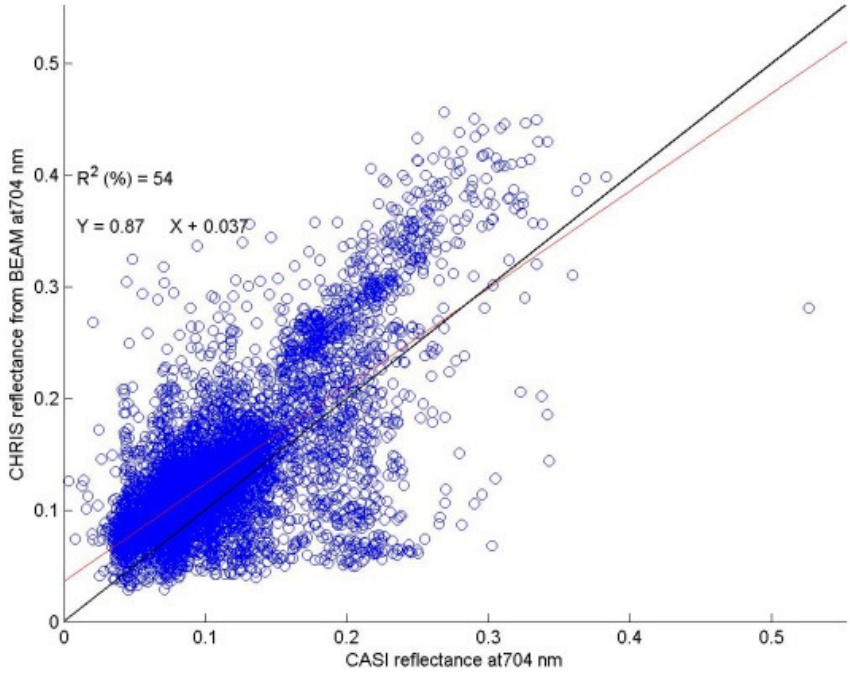
R2 (%) = 54
Y = 0.87 X + 0.037
CHRIS reflectance from BEAM at704 nm
CASI reflectance at704 nm
0
0.1
0.2
0.3
0.4
0.5

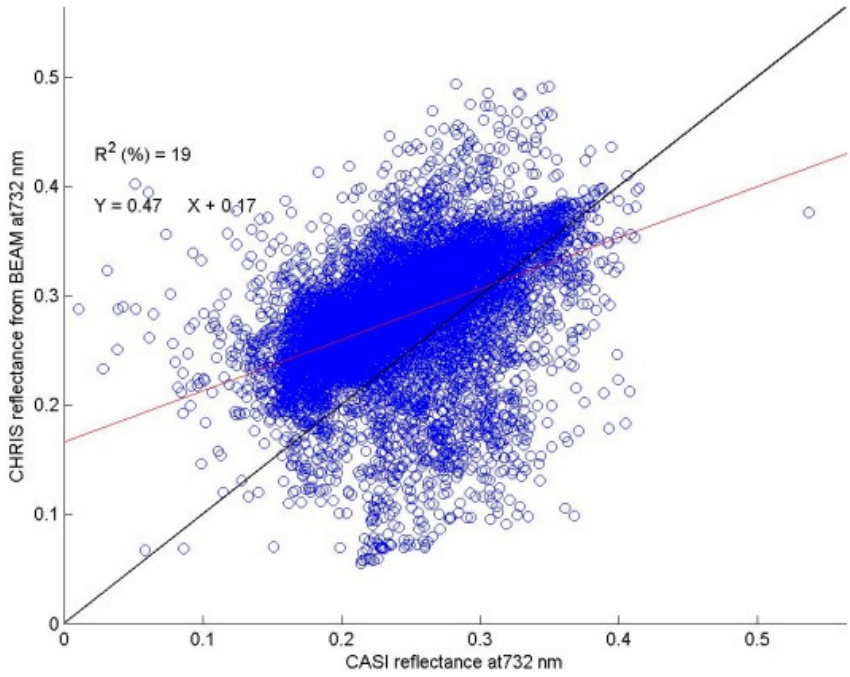
R2 (%) = 19
Y = 0.47 X + 0.17
CHRIS reflectance from BEAM at732 nm
CASI reflectance at732 nm
0
0.1
0.2
0.3
0.4
0.5

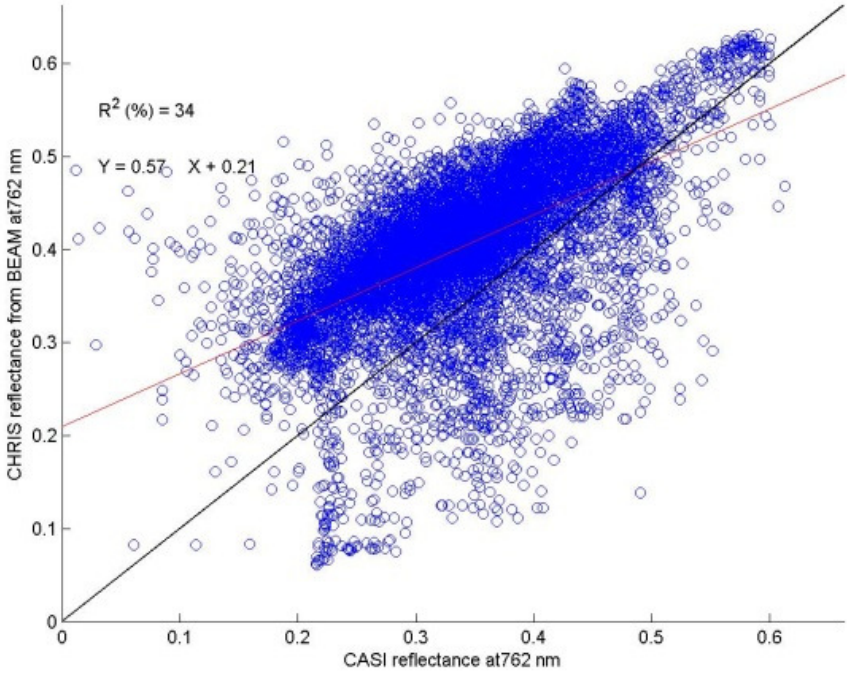
R2 (%) = 34
Y = 0.57 X + 0.21
CHRIS reflectance from BEAM at762 nm
CASI reflectance at762 nm
0
0.1
0.2
0.3
0.4
0.5
0.6

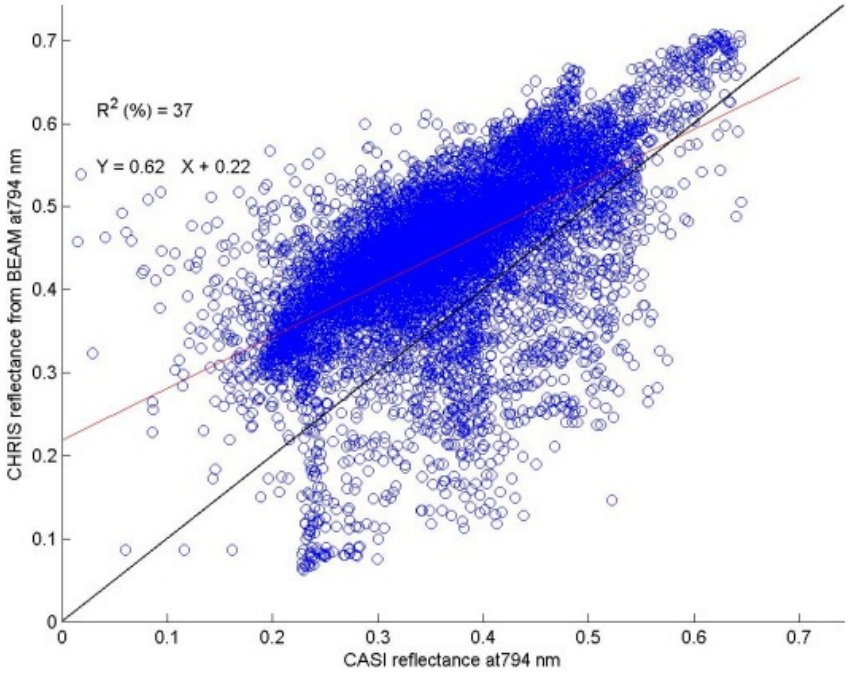
R2 (%) = 37
Y = 0.62 X + 0.22
CHRIS reflectance from BEAM at794 nm
CASI reflectance at794 nm
0
0.1
0.2
0.3
0.4
0.5
0.6
0.7

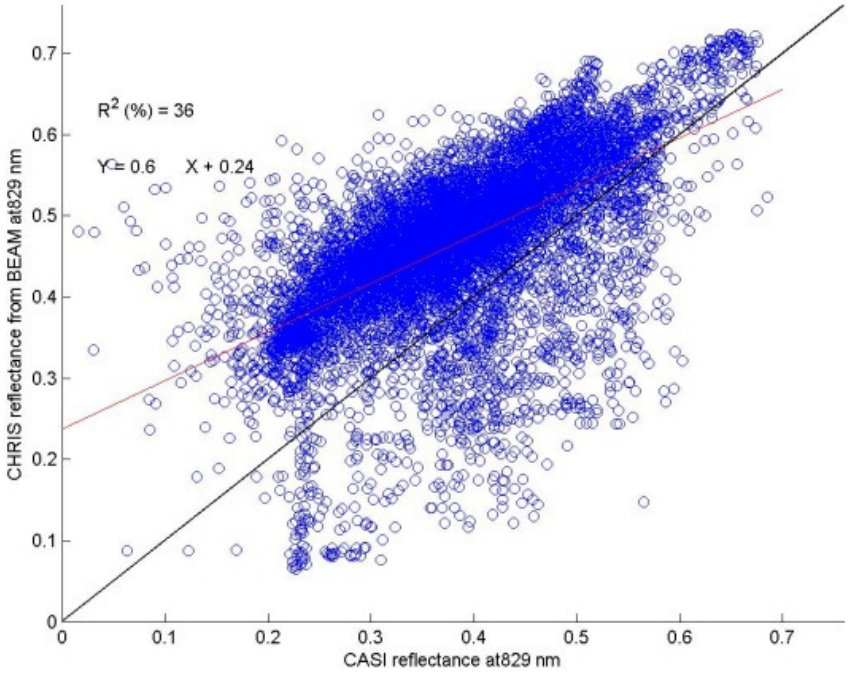
R2 (%) = 36
Y = 0.6 X + 0.24
CHRIS reflectance from BEAM at829 nm
CASI reflectance at829 nm
0
0.1
0.2
0.3
0.4
0.5
0.6
0.7

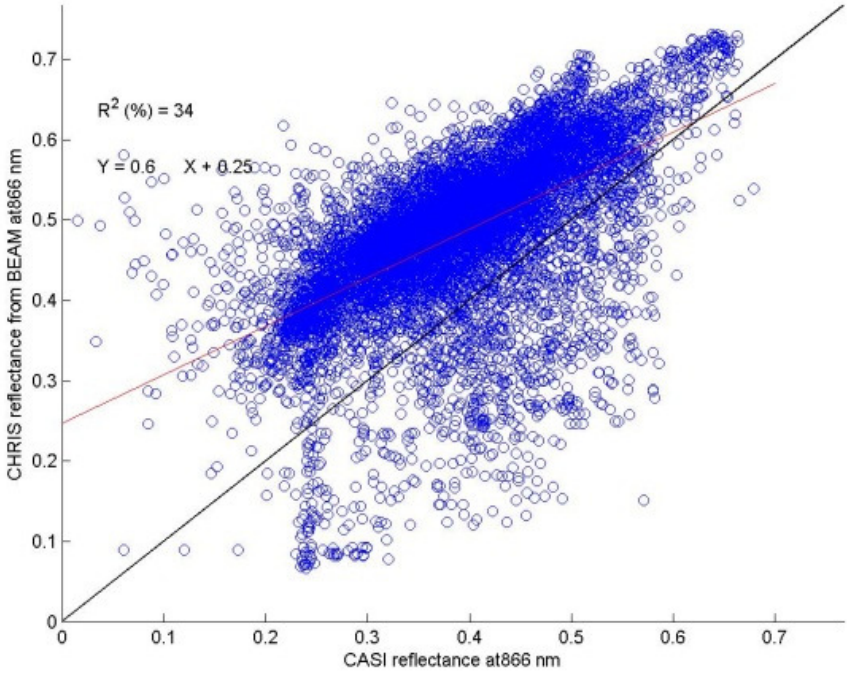
R2 (%) = 34
Y = 0.6 X + 0.25
CHRIS reflectance from BEAM at866 nm
CASI reflectance at866 nm
0
0.1
0.2
0.3
0.4
0.5
0.6
0.7

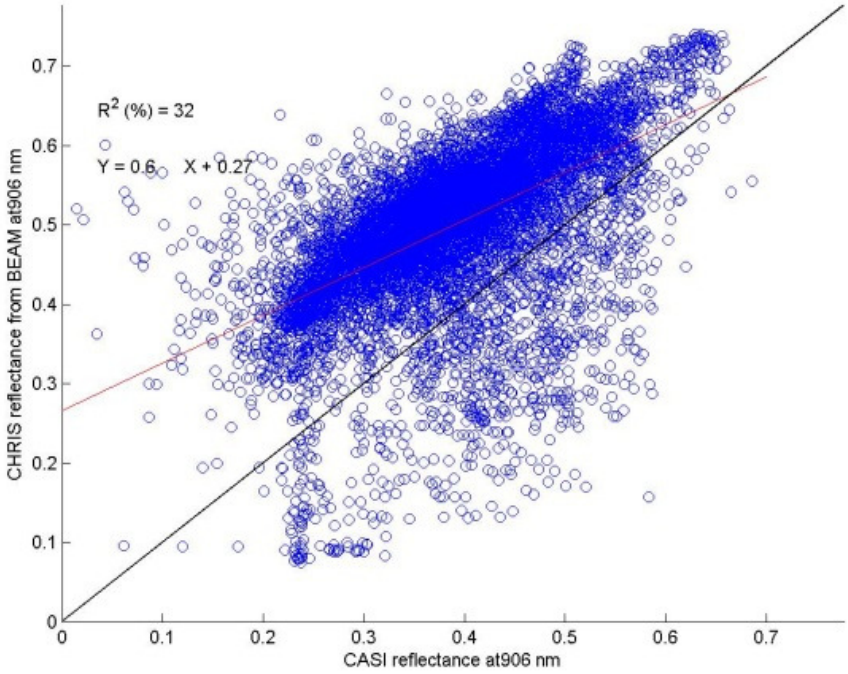
R2 (%) = 32
Y = 0.6 X + 0.27
CHRIS reflectance from BEAM at906 nm
CASI reflectance at906 nm
0
0.1
0.2
0.3
0.4
0.5
0.6
0.7

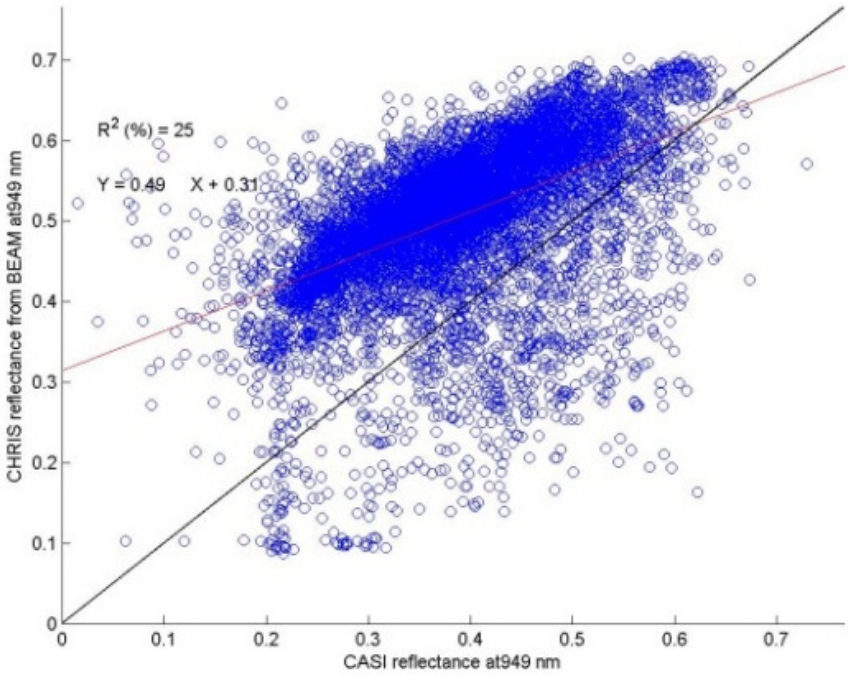
R2 (%) = 25
Y = 0.49 X + 0.31
CHRIS reflectance from BEAM at949 nm
CASI reflectance at949 nm
0
0.1
0.2
0.3
0.4
0.5
0.6
0.7

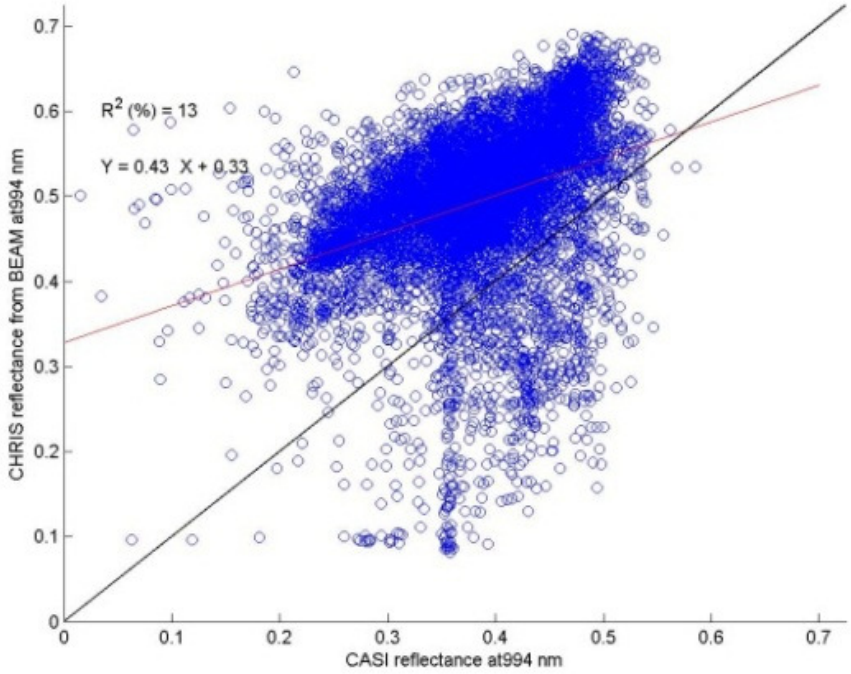
R2 (%) = 13
Y = 0.43 X + 0.33
CHRIS reflectance from BEAM at994 nm
CASI reflectance at994 nm
0
0.1
0.2
0.3
0.4
0.5
0.6
0.7

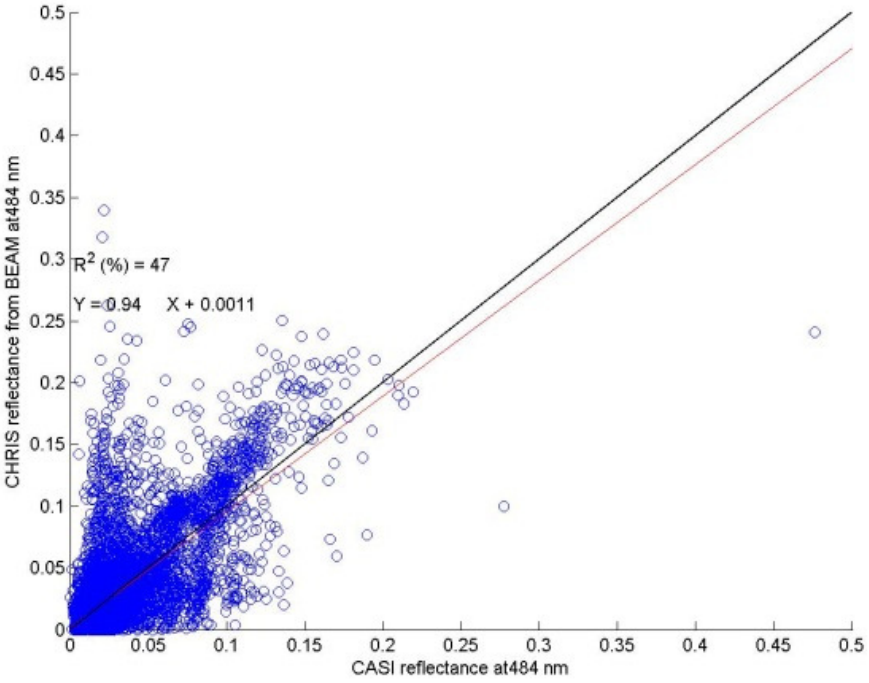
R2 (%) = 47
Y = 0.94 X + 0.0011
CHRIS reflectance from BEAM at484 nm
CASI reflectance at484 nm
0
0.05
0.1
0.15
0.2
0.25
0.3
0.35
0.4
0.45
0.5

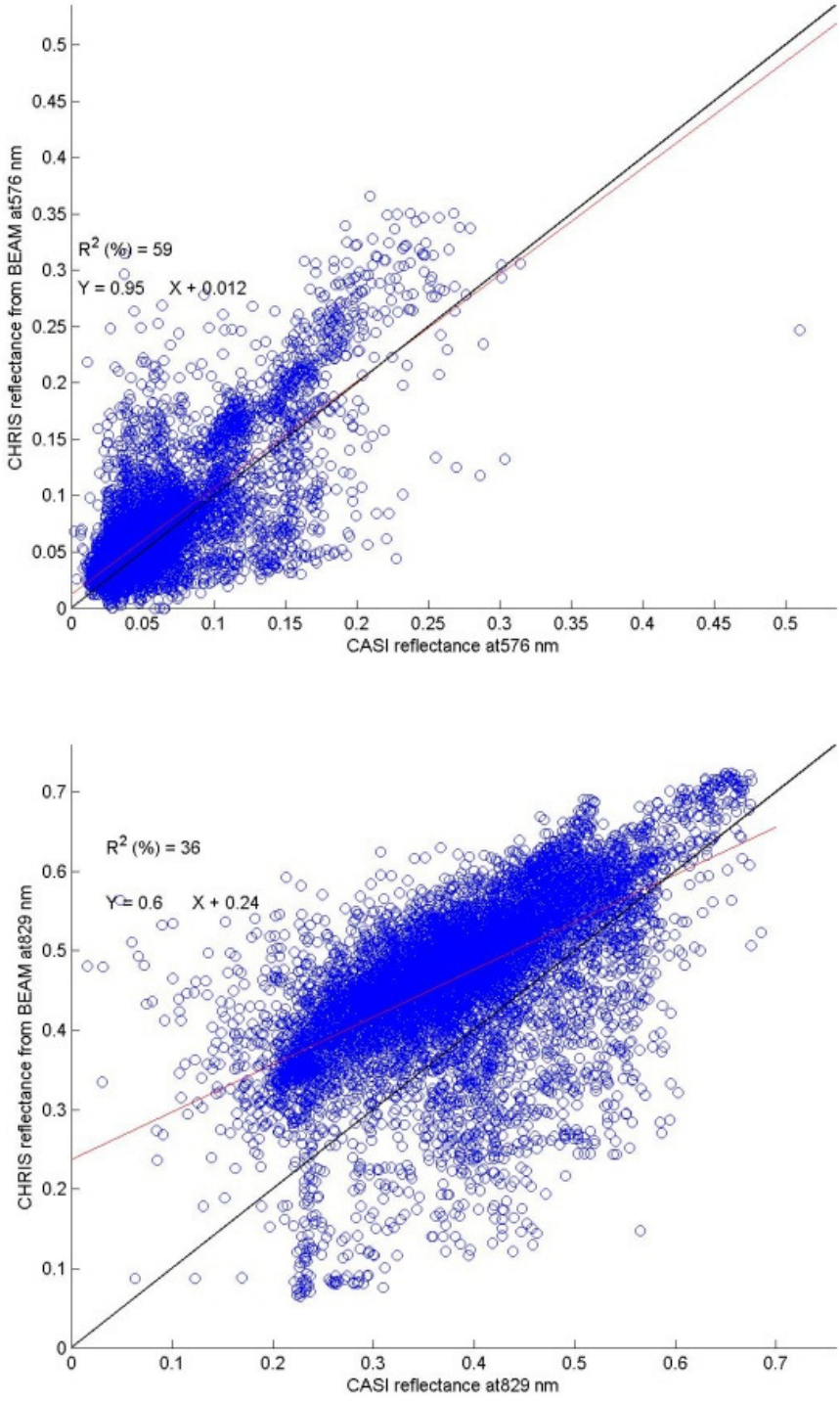

Figure A1- 7-4 Scatter plot of atmospherically corrected CHRIS/PROBA using BEAM software against EA-CASI reflectance.

A1.6 Results of the validation of CHRIS reflectance from ATCOR2

The CHRIS/PROBA data at nadir view were atmospherically corrected using ATCOR2 software. The CHRIS data were resampled to EA-CASI spectral bands while the EA-CASI data were upscaled to the CHRIS spatial resolution. The CHRIS surface reflectance was then validated against the reference EA-CASI data.

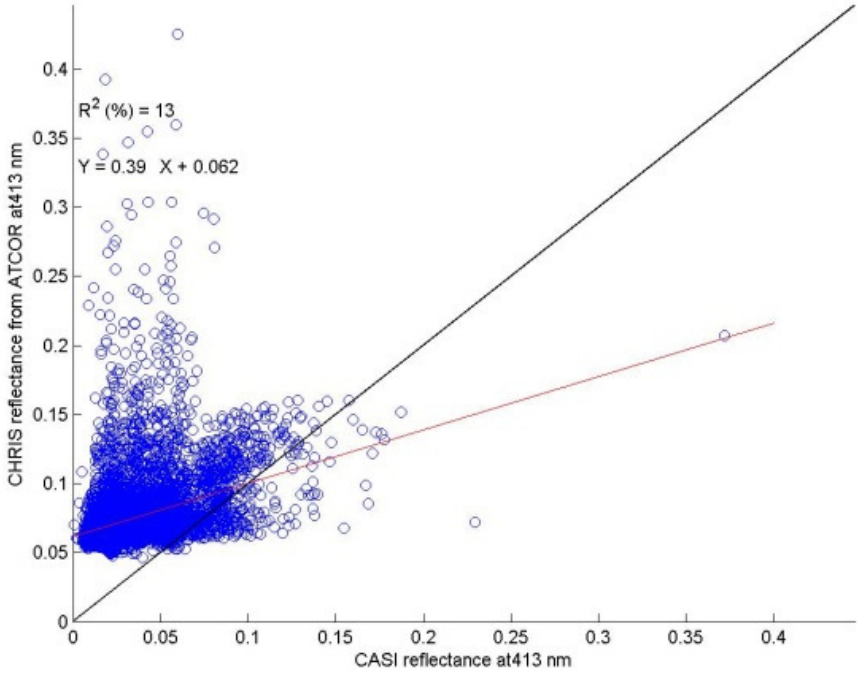
R² (%) = 13
Y = 0.39 X + 0.062
CHRIS reflectance from ATCOR at413 nm
CASI reflectance at413 nm
0
0.05
0.1
0.15
0.2
0.25
0.3
0.35
0.4

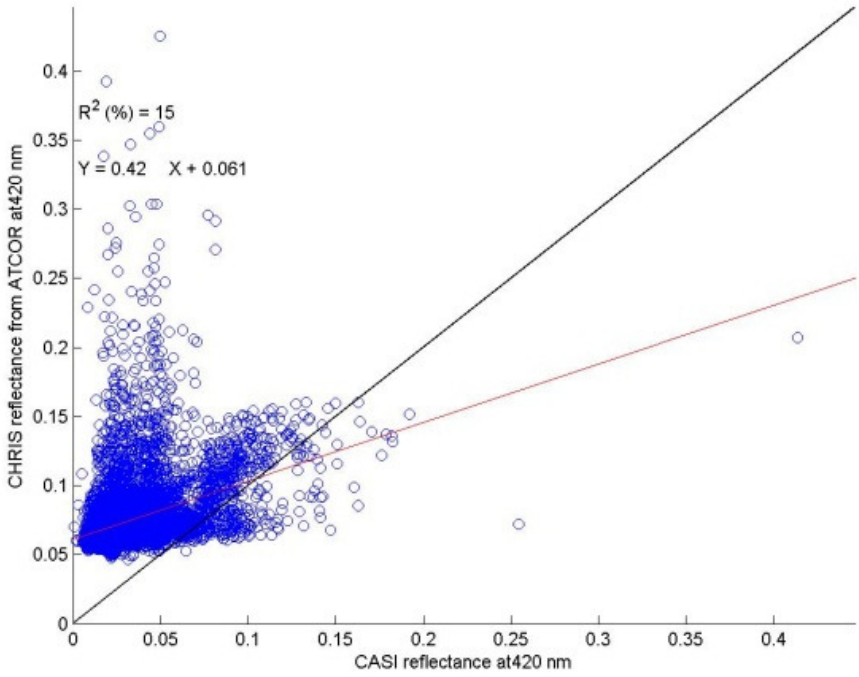
R² (%) = 15
Y = 0.42 X + 0.061
CHRIS reflectance from ATCOR at420 nm
CASI reflectance at420 nm
0
0.05
0.1
0.15
0.2
0.25
0.3
0.35
0.4

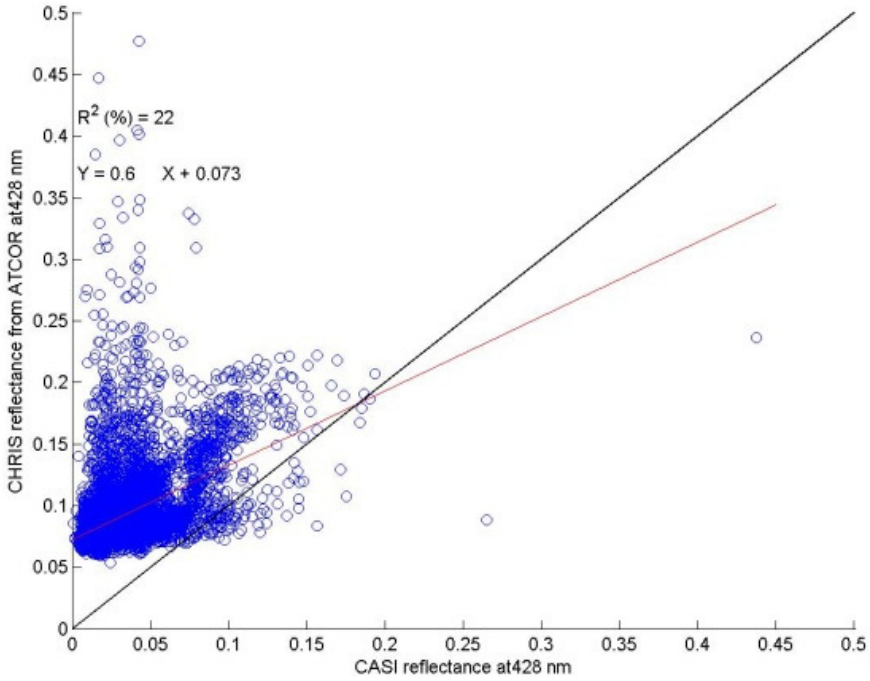
R2 (%) = 22
Y = 0.6 X + 0.073
CHRIS reflectance from ATCOR at428 nm
CASI reflectance at428 nm
0
0.05
0.1
0.15
0.2
0.25
0.3
0.35
0.4
0.45
0.5

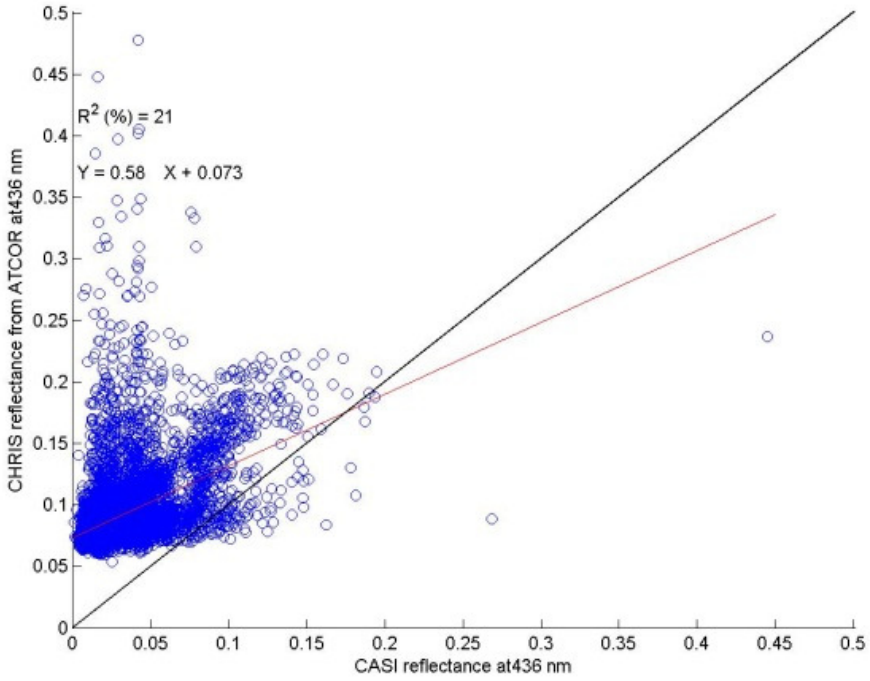
R2 (%) = 21
Y = 0.58 X + 0.073
CHRIS reflectance from ATCOR at436 nm
CASI reflectance at436 nm
0
0.05
0.1
0.15
0.2
0.25
0.3
0.35
0.4
0.45
0.5

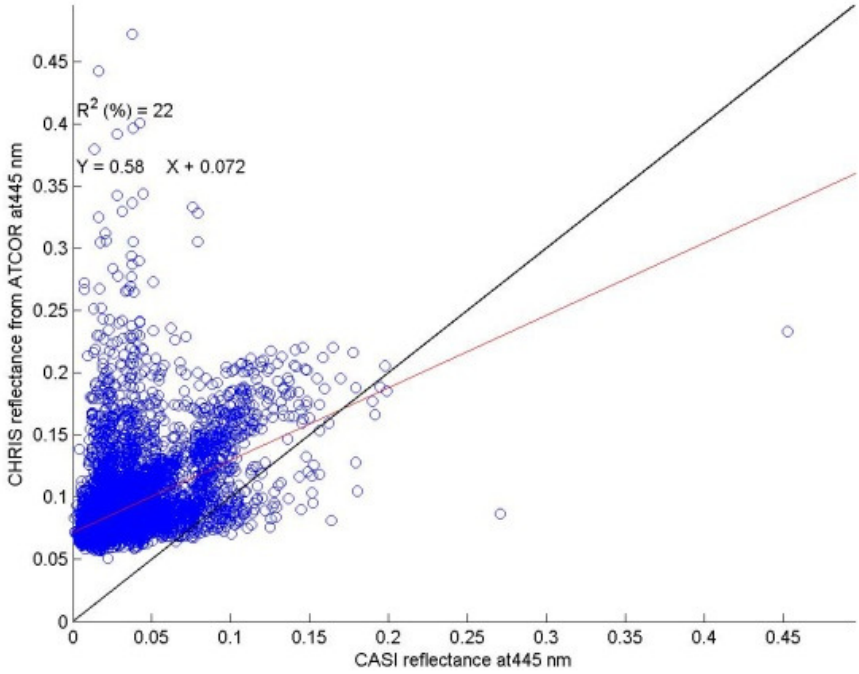
R2 (%) = 22
Y = 0.58 X + 0.072
CHRIS reflectance from ATCOR at445 nm
CASI reflectance at445 nm
0
0.05
0.1
0.15
0.2
0.25
0.3
0.35
0.4
0.45

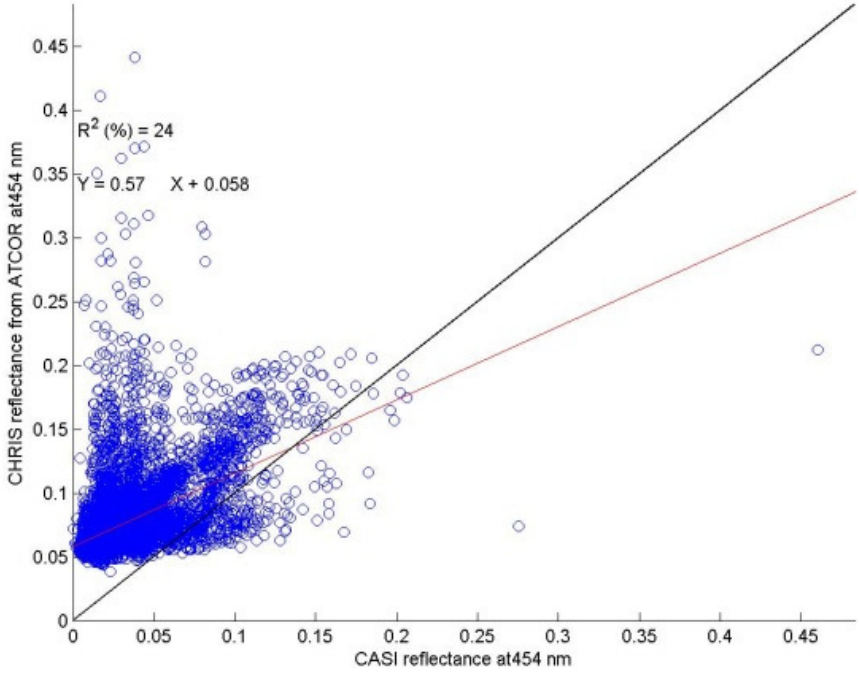
R2 (%) = 24
Y = 0.57 X + 0.058
CHRIS reflectance from ATCOR at454 nm
CASI reflectance at454 nm
0
0.05
0.1
0.15
0.2
0.25
0.3
0.35
0.4
0.45

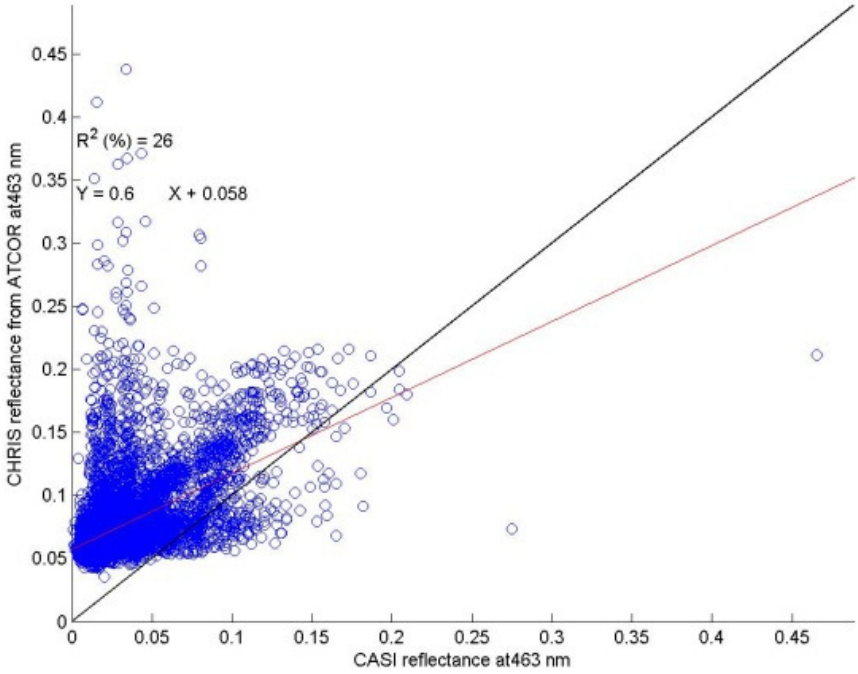
R2 (%) = 26
Y = 0.6 X + 0.058
CHRIS reflectance from ATCOR at463 nm
CASI reflectance at463 nm
0
0.05
0.1
0.15
0.2
0.25
0.3
0.35
0.4
0.45

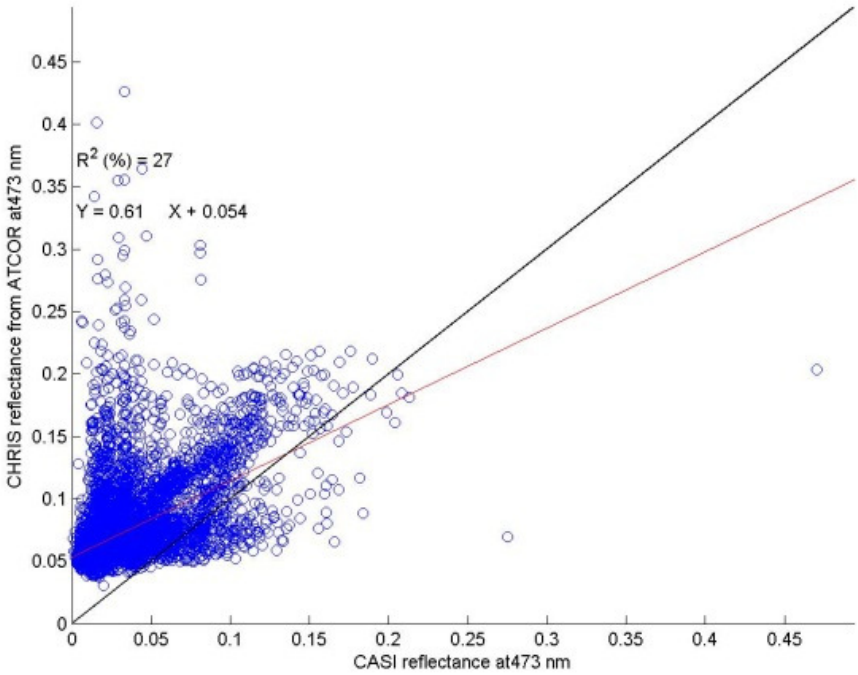
R2 (%) = 27
Y = 0.61 X + 0.054
CHRIS reflectance from ATCOR at473 nm
CASI reflectance at473 nm
0
0.05
0.1
0.15
0.2
0.25
0.3
0.35
0.4
0.45

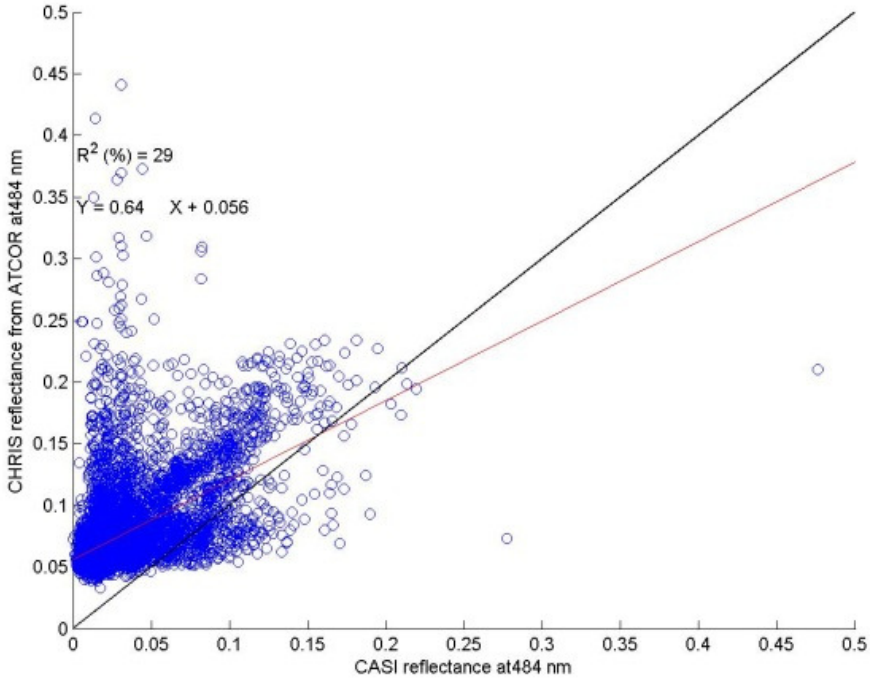
R2 (%) = 29
Y = 0.64 X + 0.056
CHRIS reflectance from ATCOR at484 nm
CASI reflectance at484 nm

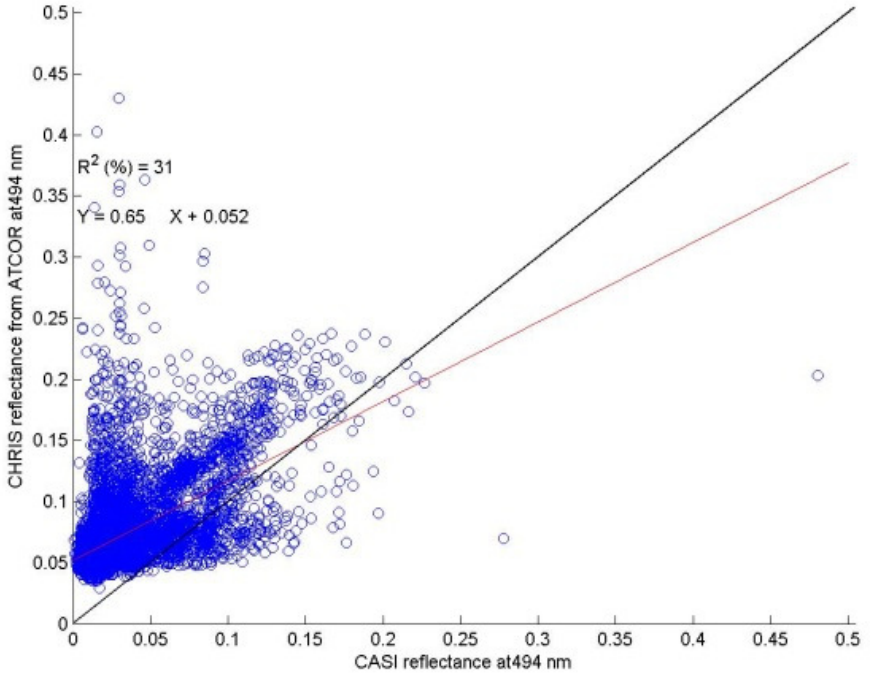
R2 (%) = 31
Y = 0.65 X + 0.052
CHRIS reflectance from ATCOR at494 nm
CASI reflectance at494 nm

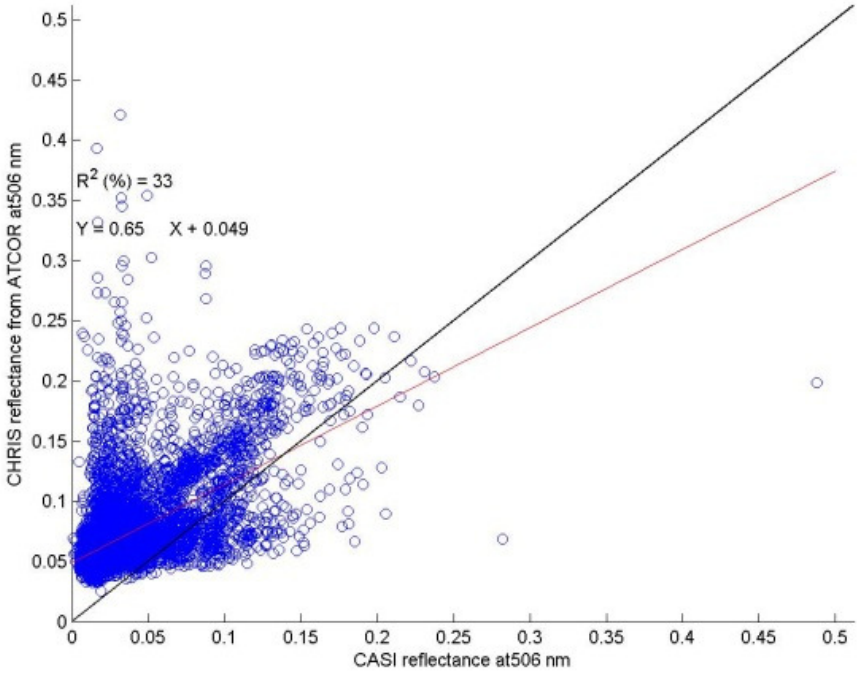
CHRIS reflectance from ATCOR at506 nm
CASI reflectance at506 nm
R2 (%) = 33
Y = 0.65 X + 0.049
0
0.05
0.1
0.15
0.2
0.25
0.3
0.35
0.4
0.45
0.5

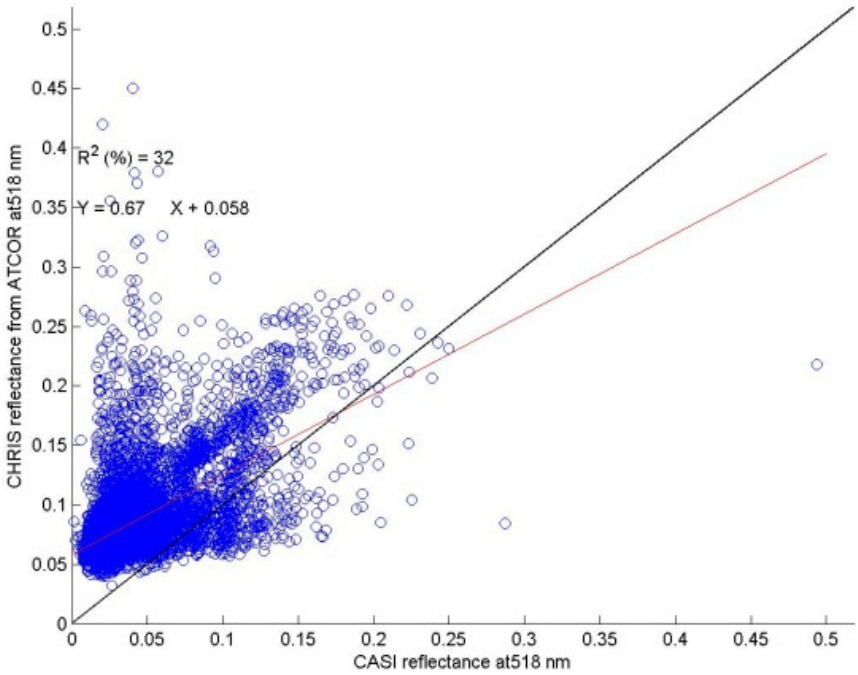
CHRIS reflectance from ATCOR at518 nm
CASI reflectance at518 nm
R2 (%) = 32
Y = 0.67 X + 0.058
0
0.05
0.1
0.15
0.2
0.25
0.3
0.35
0.4
0.45
0.5

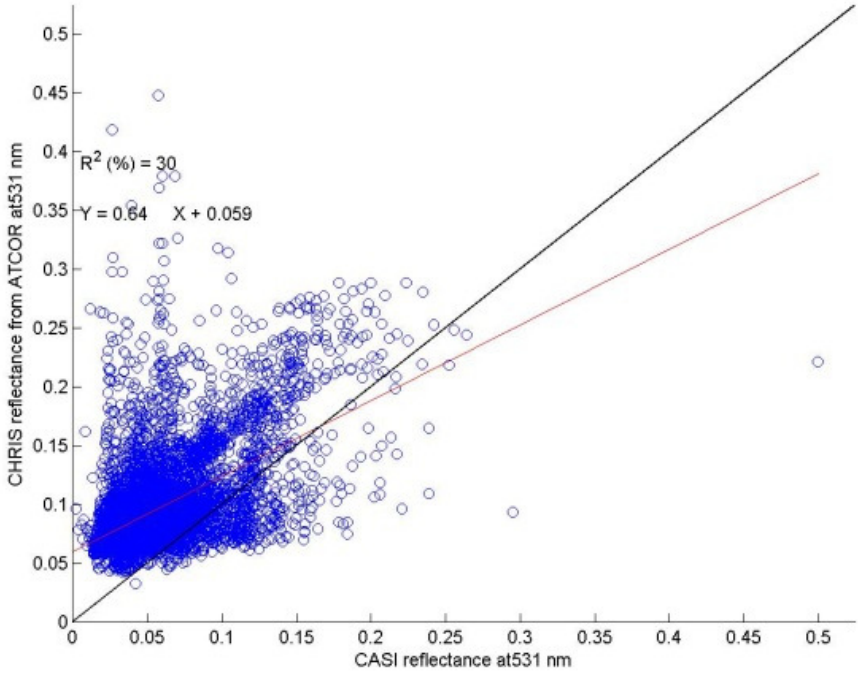
R2 (%) = 30
Y = 0.64 X + 0.059
CHRIS reflectance from ATCOR at531 nm
CASI reflectance at531 nm
0
0.05
0.1
0.15
0.2
0.25
0.3
0.35
0.4
0.45
0.5

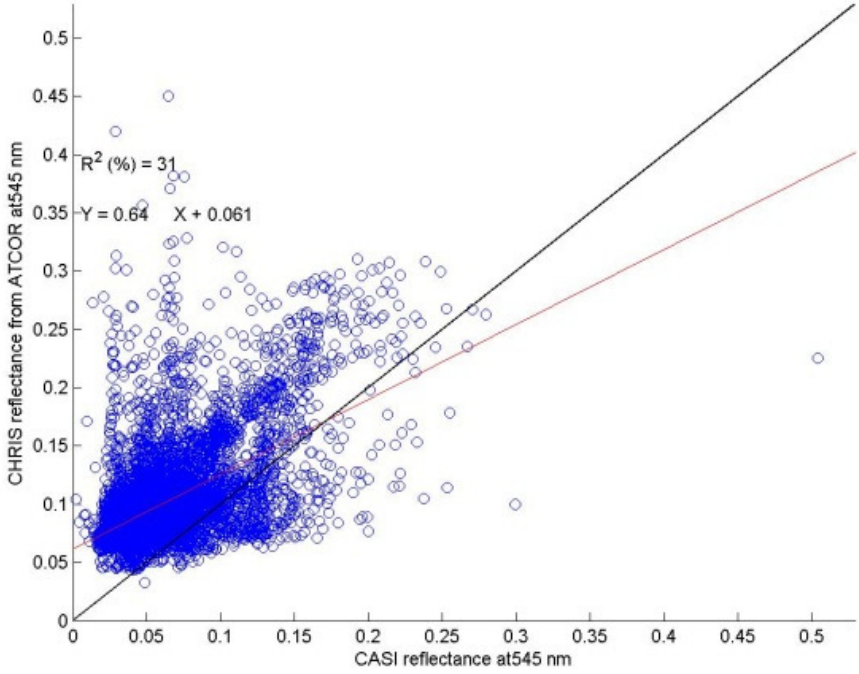
R2 (%) = 31
Y = 0.64 X + 0.061
CHRIS reflectance from ATCOR at545 nm
CASI reflectance at545 nm
0
0.05
0.1
0.15
0.2
0.25
0.3
0.35
0.4
0.45
0.5

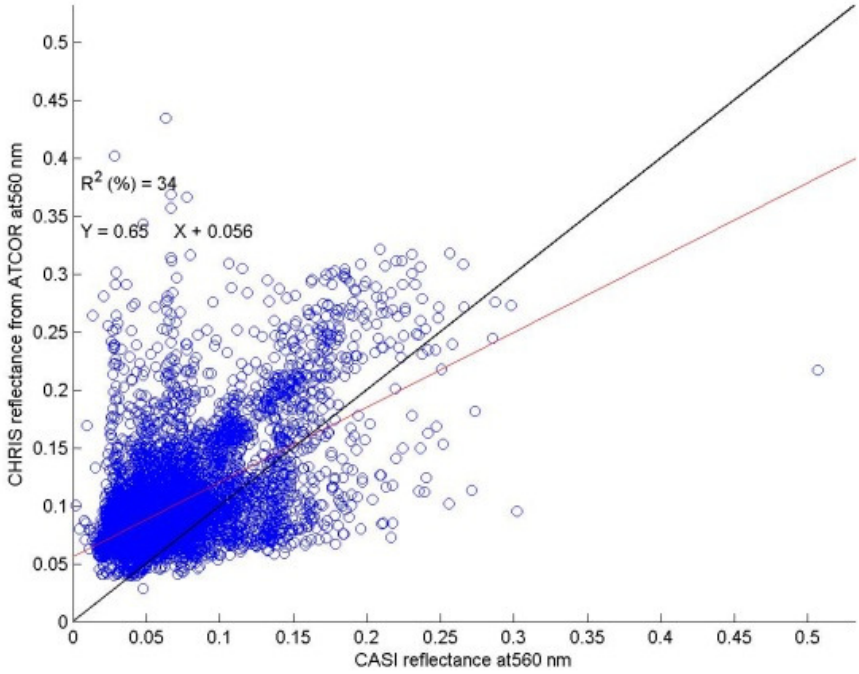
R2 (%) = 34
Y = 0.65 X + 0.056
CHRIS reflectance from ATCOR at560 nm
CASI reflectance at560 nm
0
0.05
0.1
0.15
0.2
0.25
0.3
0.35
0.4
0.45
0.5

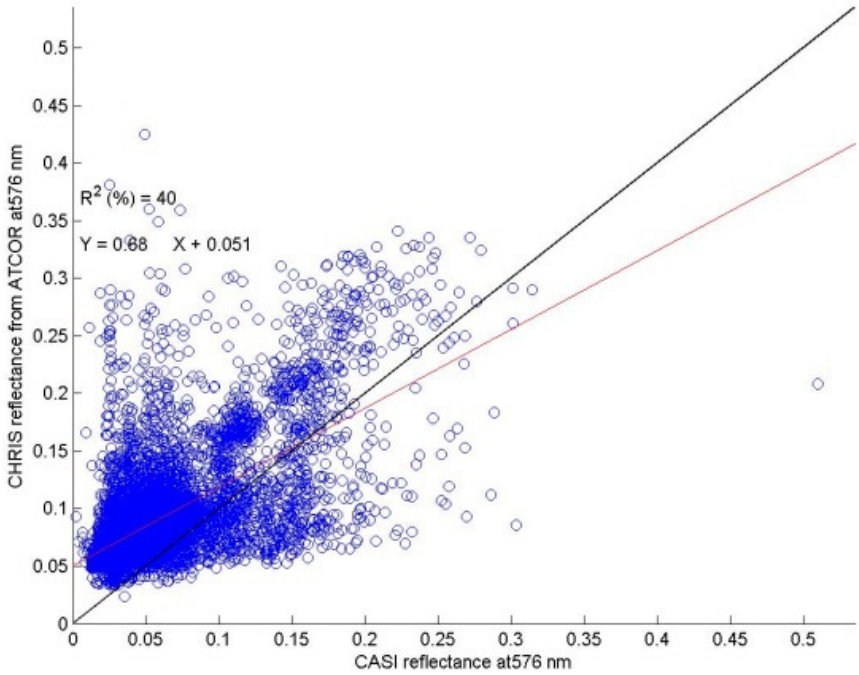
R2 (%) = 40
Y = 0.68 X + 0.051
CHRIS reflectance from ATCOR at576 nm
CASI reflectance at576 nm
0
0.05
0.1
0.15
0.2
0.25
0.3
0.35
0.4
0.45
0.5

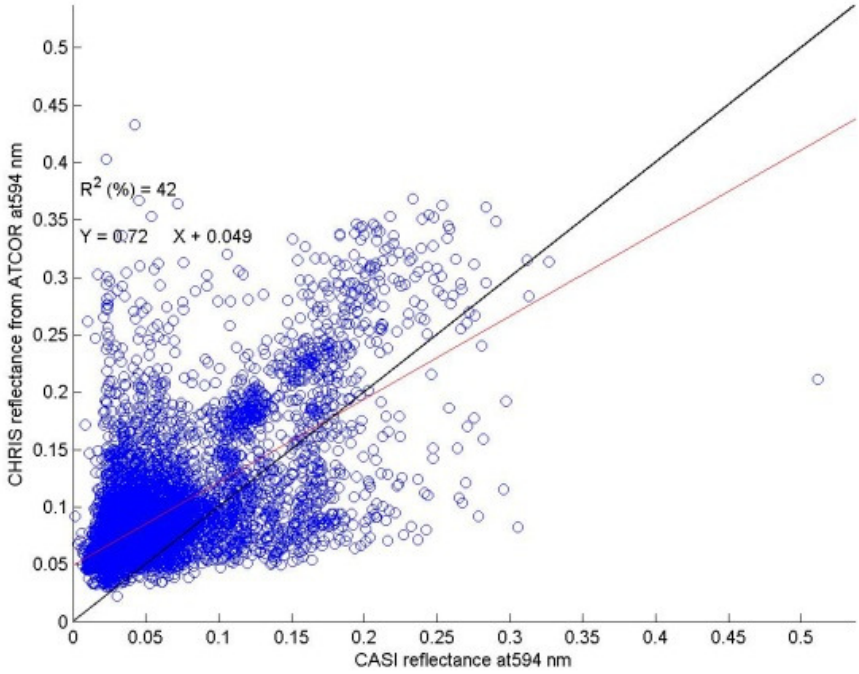
R2 (%) = 42
Y = 0.72 X + 0.049
CHRIS reflectance from ATCOR at594 nm
CASI reflectance at594 nm

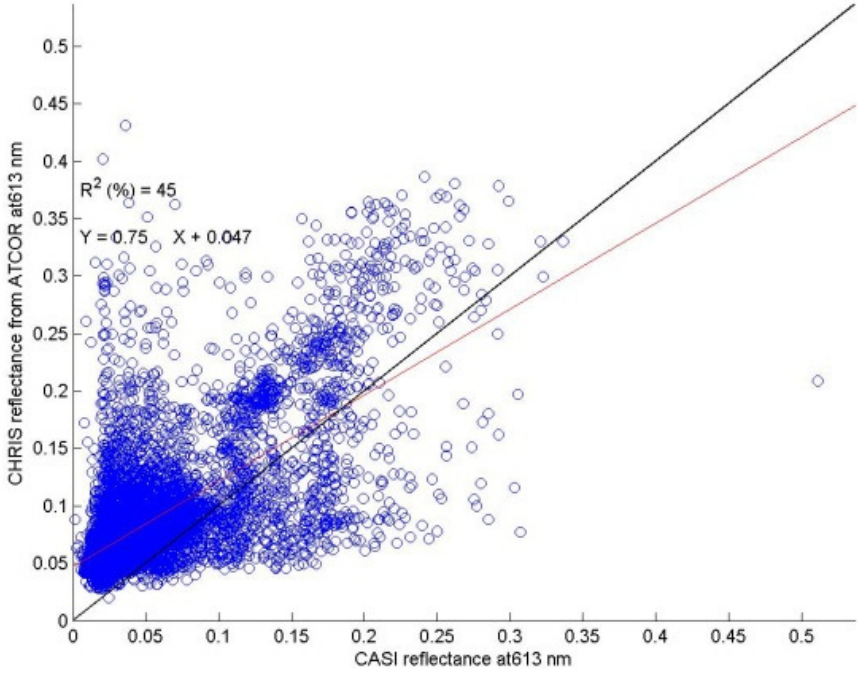
R2 (%) = 45
Y = 0.75 X + 0.047
CHRIS reflectance from ATCOR at613 nm
CASI reflectance at613 nm

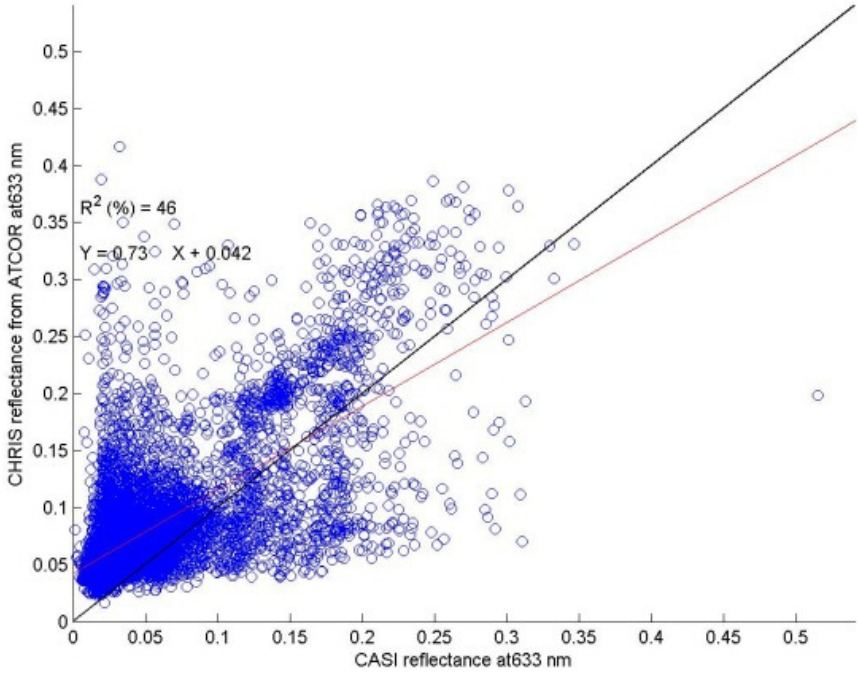
R² (%) = 46
Y = 0.73 X + 0.042
CHRIS reflectance from ATCOR at633 nm
CASI reflectance at633 nm
0
0.05
0.1
0.15
0.2
0.25
0.3
0.35
0.4
0.45
0.5

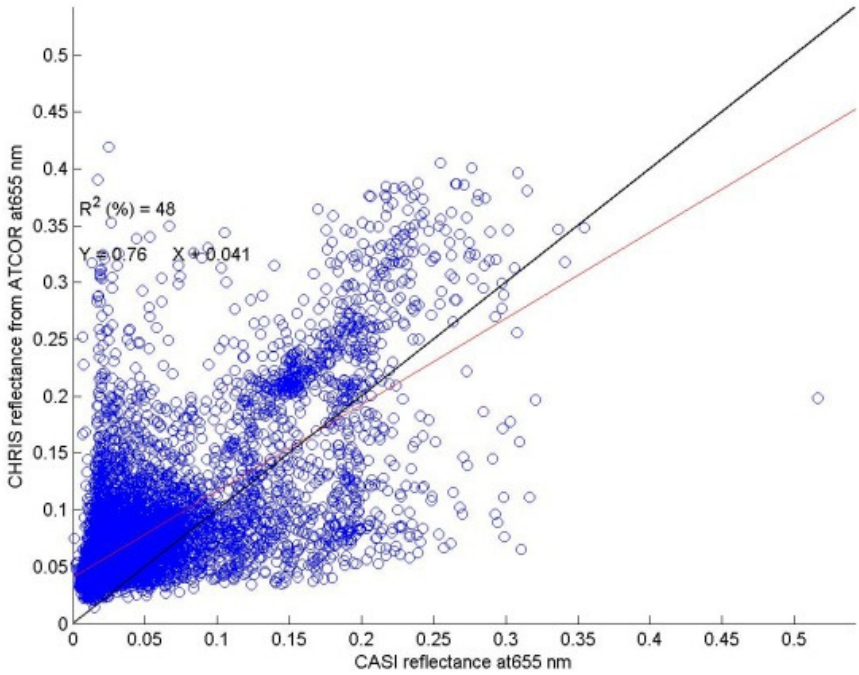
R² (%) = 48
Y = 0.76 X + 0.041
CHRIS reflectance from ATCOR at655 nm
CASI reflectance at655 nm
0
0.05
0.1
0.15
0.2
0.25
0.3
0.35
0.4
0.45
0.5

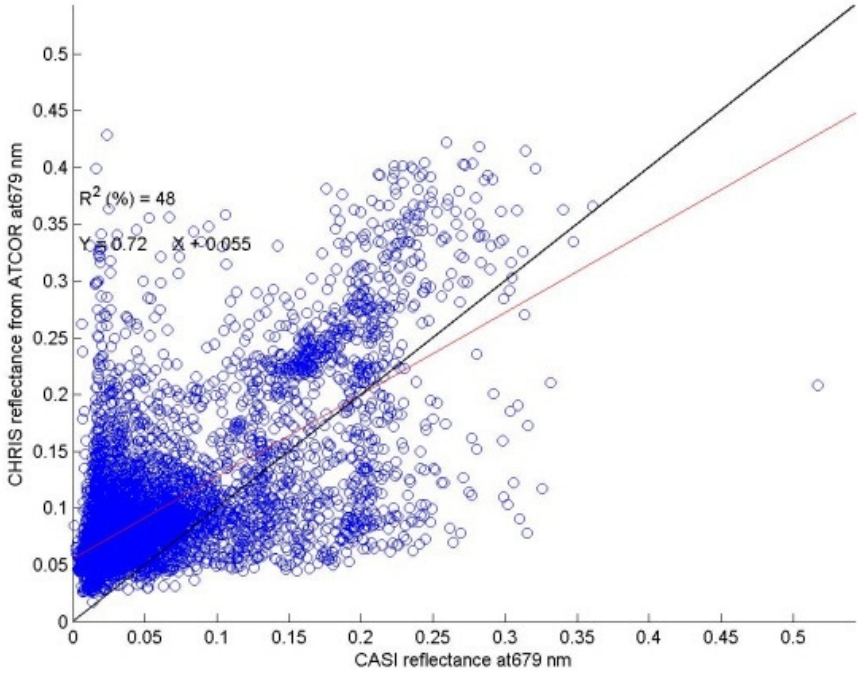
CHRIS reflectance from ATCOR at679 nm
CASI reflectance at679 nm
R2 (%) = 48
Y = 0.72 X + 0.055
0
0.05
0.1
0.15
0.2
0.25
0.3
0.35
0.4
0.45
0.5

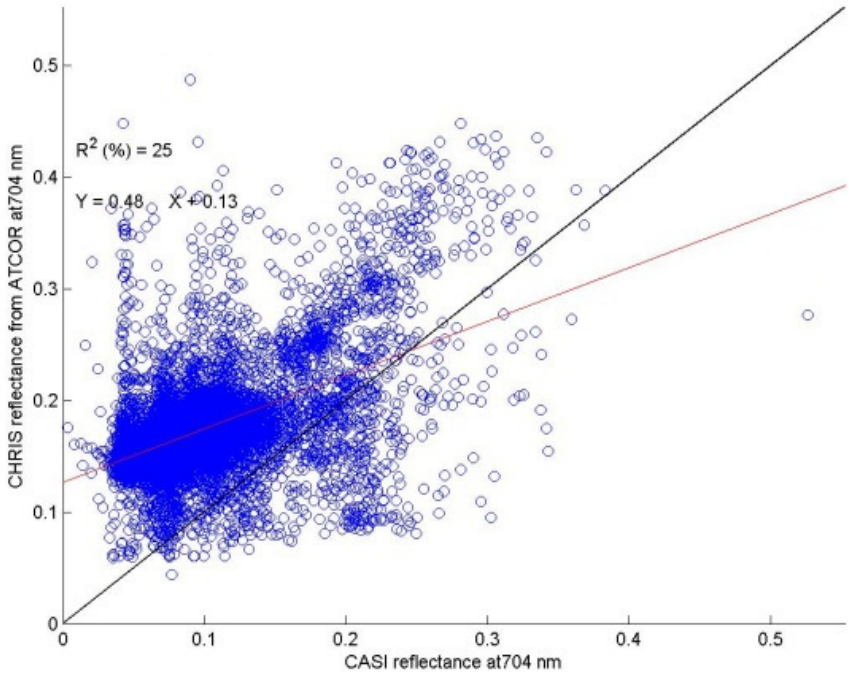
CHRIS reflectance from ATCOR at704 nm
CASI reflectance at704 nm
R2 (%) = 25
Y = 0.48 X + 0.13
0
0.1
0.2
0.3
0.4
0.5

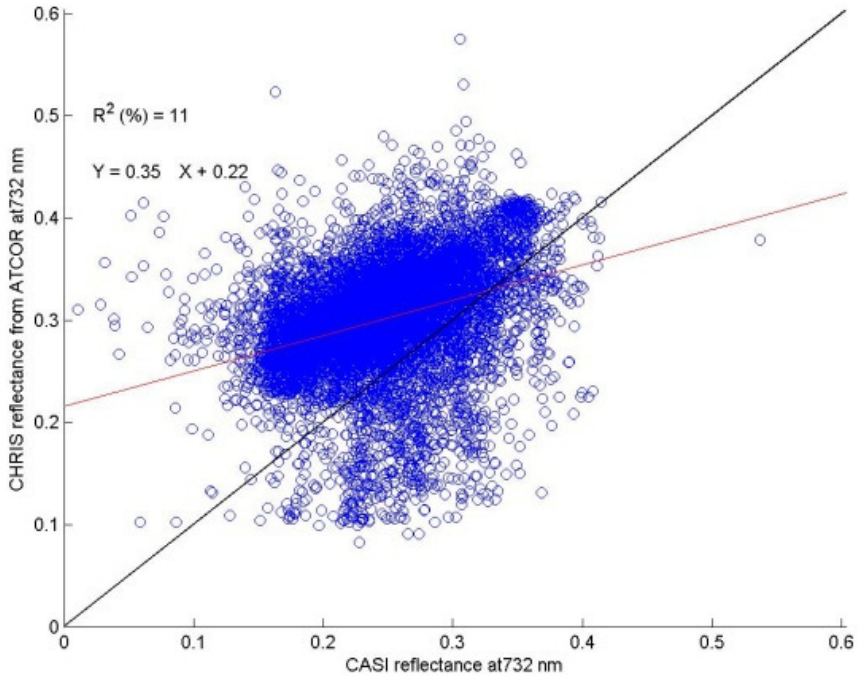
R2 (%) = 11
Y = 0.35 X + 0.22
CHRIS reflectance from ATCOR at732 nm
CASI reflectance at732 nm
0
0.1
0.2
0.3
0.4
0.5
0.6

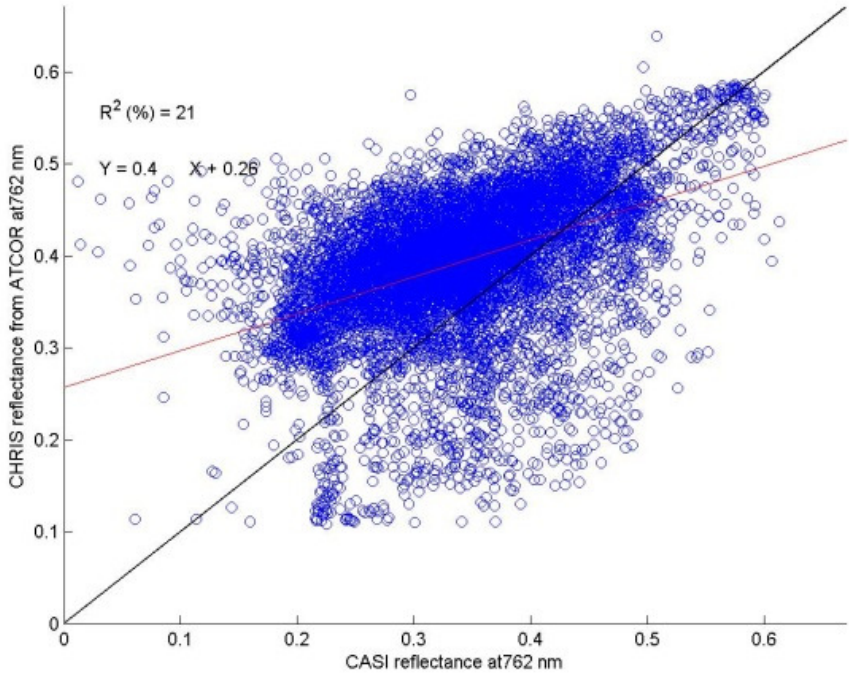
R2 (%) = 21
Y = 0.4 X + 0.26
CHRIS reflectance from ATCOR at762 nm
CASI reflectance at762 nm
0
0.1
0.2
0.3
0.4
0.5
0.6

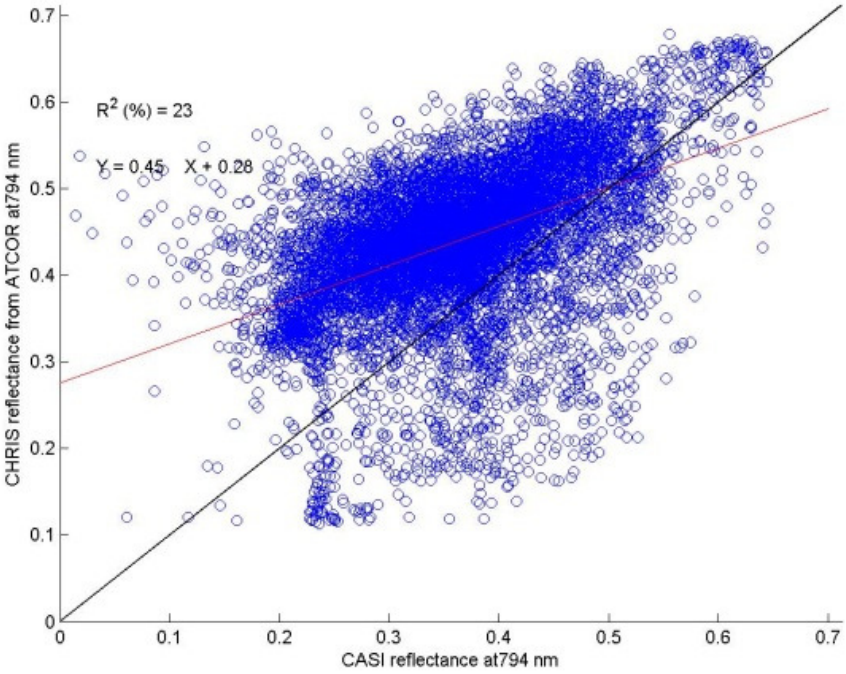
R2 (%) = 23
Y = 0.45 X + 0.28
CHRIS reflectance from ATCOR at794 nm
CASI reflectance at794 nm
0
0.1
0.2
0.3
0.4
0.5
0.6
0.7

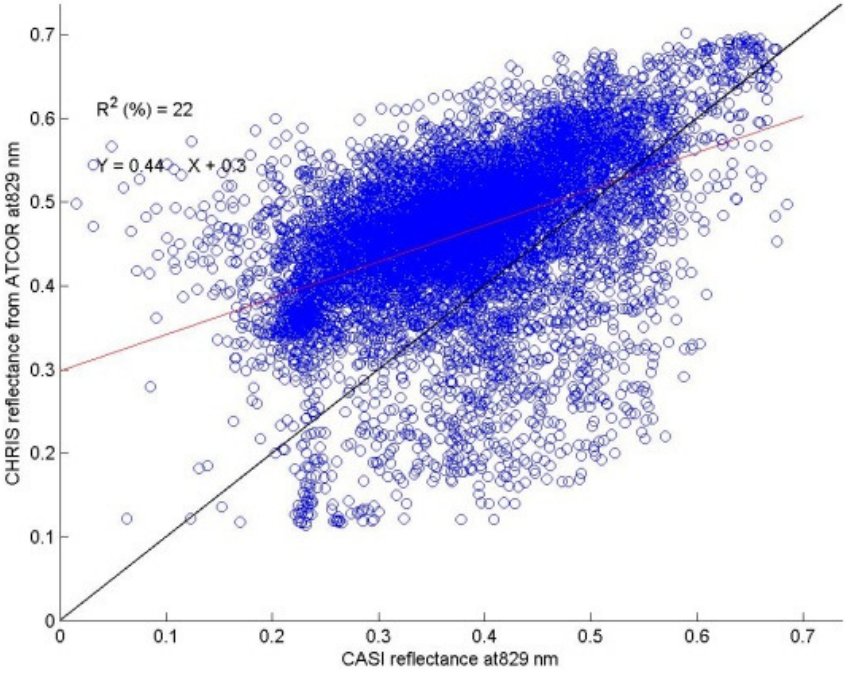
R2 (%) = 22
Y = 0.44 X + 0.3
CHRIS reflectance from ATCOR at829 nm
CASI reflectance at829 nm
0
0.1
0.2
0.3
0.4
0.5
0.6
0.7

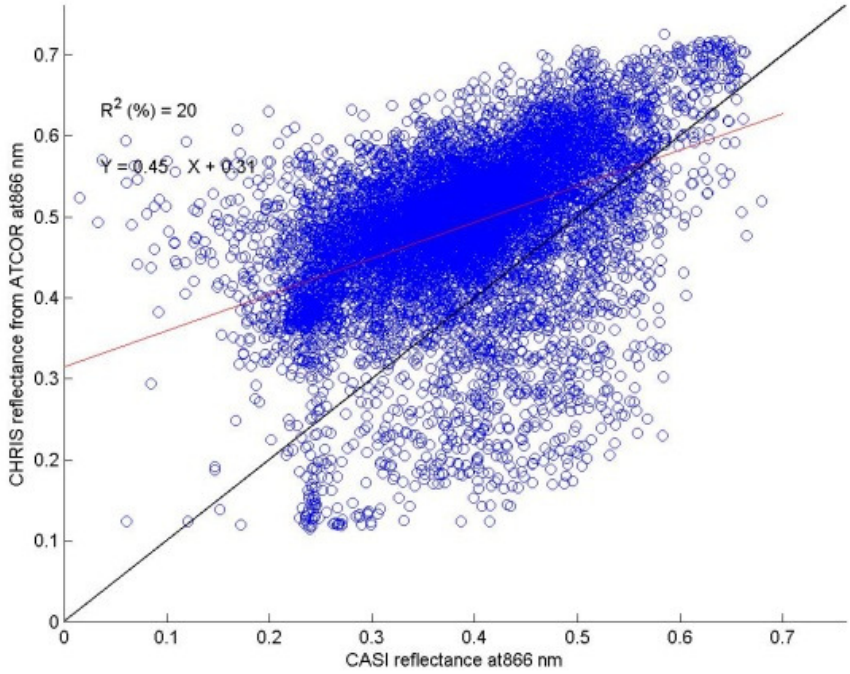
R2 (%) = 20
Y = 0.45 X + 0.31
CHRIS reflectance from ATCOR at866 nm
CASI reflectance at866 nm
0
0.1
0.2
0.3
0.4
0.5
0.6
0.7

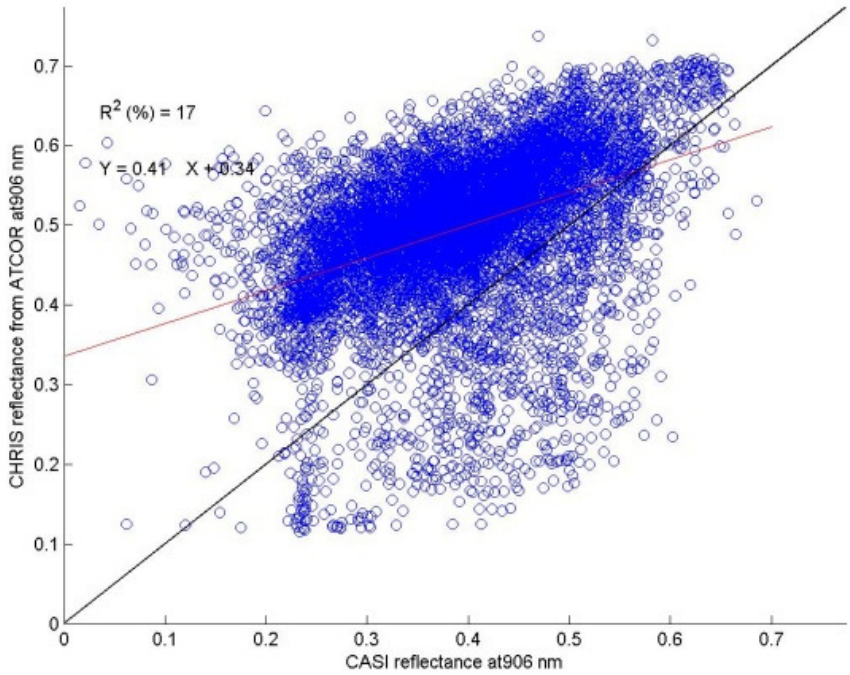
R2 (%) = 17
Y = 0.41 X + 0.34
CHRIS reflectance from ATCOR at906 nm
CASI reflectance at906 nm
0
0.1
0.2
0.3
0.4
0.5
0.6
0.7

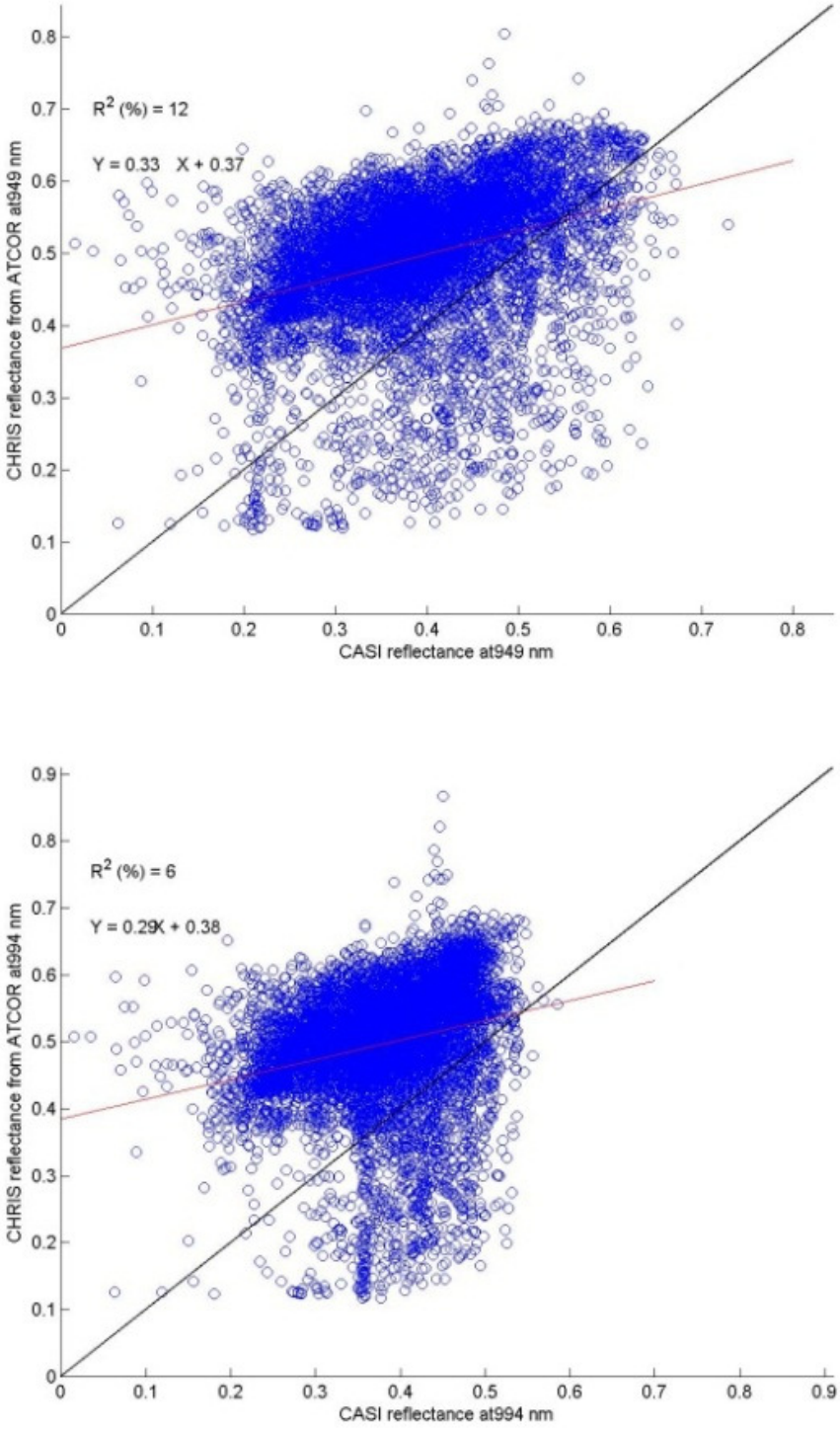

Figure A1- 7-5 Scatter plot of atmospherically corrected CHRIS/PROBA using ATCOR2 software against EA-CASI reflectance.

A1.7 Discussion

The results of the validation of the atmospheric correction showed a good overall correlation between CHRIS and EA-CASI surface reflectance. Correlation values resulting from the comparison of CHRIS data with EA-CASI data showed that BEAM performed a slightly better atmospheric correction than the ATCOR software. There was a positive shift (offset error) on the Y-Axis (CHRIS reflectance) relative to the origin 0,0 in the results of the atmospheric correction by ATCOR. The positive shift is seen in the visible bands and varies from 0.02-0.07 in different bands. In shorter wavelengths (blue band) it is higher and it is lower in the longer wavelengths (red band). Problems regarding atmospheric correction and radiometric calibration are assumed to be the reason for the shift.

BEAM seems to correct the miscalibration issues in the CHRIS data. The results of the atmospheric correction showed the disappearance of the positive shift relative to the origin 0,0 seen in the results from ATCOR. However, there were some negative reflectance values in the output surface reflectance. A problem in the BEAM software, as mentioned by the BEAM team in an email, is the reason for the occurrence of the negative values. It seems there is a bug in the code related to the aerosol optical thickness retrieval module making AOT too high for some scenes, which lead to negative values. This could not be fixed in the BEAM codes because it was found only once the project and funding had concluded.

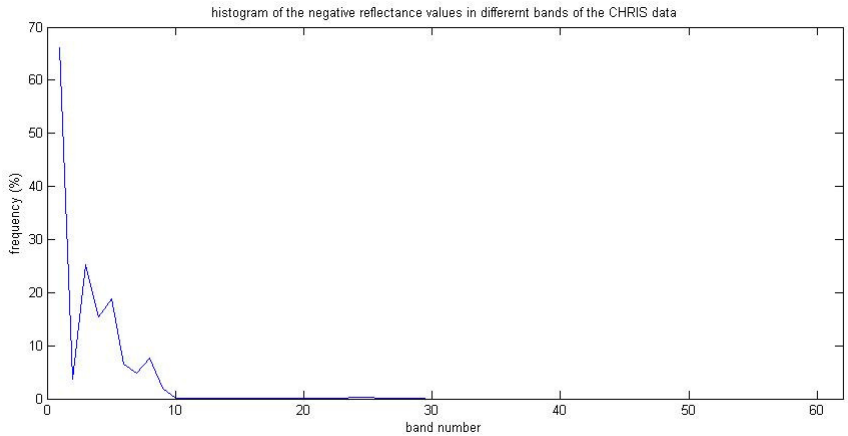

Figure A1- 7-6 Histogram of the negative reflectance values in the CHRIS data corrected by BEAM software

AOT values were then changed to ignore zero values. Three AOT values 0.05, 0.15, and 0.27 were used. The last value, 0.27, is from the ground measurements. Figure A1- 7-7 shows that as AOT value decreases, output surface reflectance from BEAM

increases. The errors in the water vapour estimation only affect the NIR bands (Figure A1- 7-8). As the amount of aerosol and water vapour may change as the view angle increases, there is uncertainty regarding the estimation of these atmospheric variables in high view zenith angles in the MODTRAN code which is used in both BEAM and ATCOR.

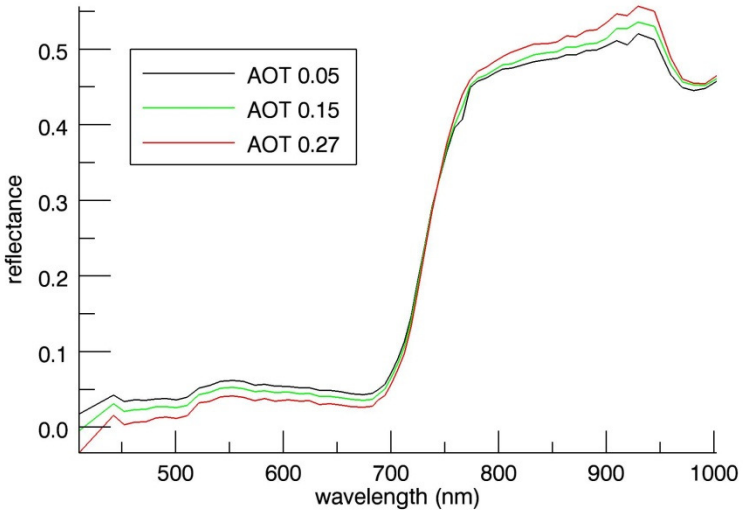

Figure A1- 7-7 Spectral variation of surface reflectance with three different AOT values 0.05, 0.15, and 0.27 as obtained from BEAM.

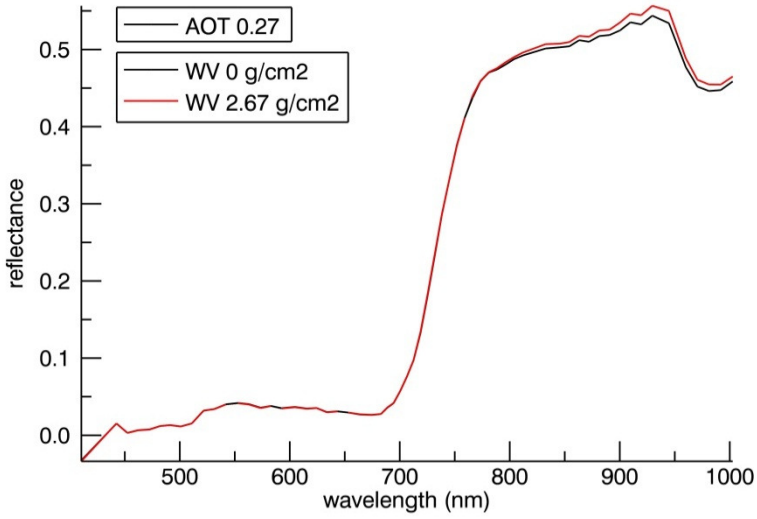

Figure A1- 7-8 Spectral variation of reflectance with two different water vapour values (g/cm²) 0.0 and 2.67 as obtained from BEAM.

Both ATCOR and BEAM use MODTRAN4 radiative transfer code, and the uncertainties in this atmospheric model can introduce some errors in the outputs. One of the problems with using MODTRAN is that it is a scalar code which assumes the at-sensor signal is not polarized whereas the signal is polarized when it hits the aerosols and the Earth's surface. Radiative transfer models (RTMs) such as MODTRAN use dark objects such as dense vegetation to estimate the path radiance, assuming that the radiance above a certain threshold is due to aerosol effect. The existence of clouds and shadows can lead to incorrect choice of dark objects, thus incorrect calculation of visibility and aerosol optical thickness which may subsequently result in over- or underestimation of surface reflectance. The atmospherically corrected data were not masked for clouds and shadows. Since there are lots of clouds and shadows in the data (Figure 5-1), this may have caused an incorrect estimation of visibility and resulting surface reflectance.

ATCOR-2 seems not to take into account BRDF effects and is more appropriate for nadir-view images. In relation to our data, even if it has a high accuracy for nadir-view data it may not have the same accuracy for off-nadir data (view zenith angle > 10°).

There are lots of clouds across the image which affect the atmospheric correction results. In ATCOR2 the cloudy pixels were not masked before atmospheric correction which may introduce larger errors than BEAM in the output surface reflectance. In BEAM software, pixels with brightness greater than 37% were identified as cloudy. This may affect the pixels with high brightness such as desert areas which was not the case in the case study. Using this condition, only thick clouds were masked but some cloudy pixels at the edge of thick clouds which were thinner and also cirrus clouds were not masked. Figure A1- 7-9 shows the effect of the presence of thick and thin clouds on the surface reflectance from vegetation. However, this only shows the variation in surface reflectance for one specific land cover (one pixel) and the errors in the surface reflectance in other land covers may be different. It was assumed that Figure A1- 7-9 is a typical example of the effect of clouds on surface reflectance in the area as modelled by BEAM. The errors are mostly seen in the NIR bands and the magnitude of the error is at most 1% of the absolute values. Therefore, the errors from unmasked clouds which are mostly thin clouds including cirrus clouds, can be ignored.

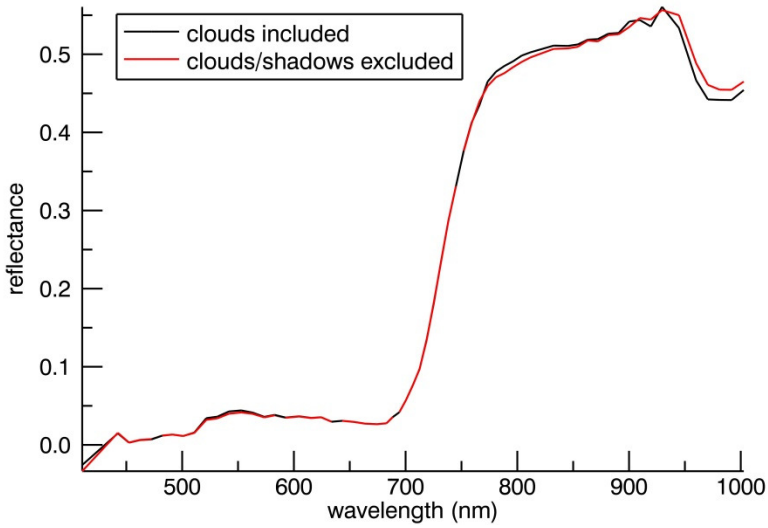

Figure A1- 7-9 The effect of clouds in BEAM's atmospheric correction .

Since the study area is relatively flat, only shadows of clouds affect the atmospheric correction. The surface reflectance from ATCOR2 was overestimated in all bands. This could be due to the incorrect estimation of aerosol optical thickness and visibility. In ATCOR visibility, which is used to estimate AOT, automatically increased to minimise the number of the dark vegetation pixels with negative reflectance in the red band (660 nm). The visibility was determined to be 50 km for the CHRIS data. There is a probability that the visibility is not accurate and is higher than the actual value. The high visibility value will result in a low optical thickness value. This will cause an undercorrection of atmospheric effect, mainly aerosol, which will result in higher reflectance values. ATCOR created a log file which summarises the values of the atmospheric correction variables as well as the quality of the process. According to this log file, the number of negative pixels in the CHRIS bands 3-25, 41 and 48 is greater than 1%. The probable reasons mentioned are excessively low visibility, incorrect aerosol type, cloud shadow regions and calibration problems.

In the BEAM software, pixels with brightness less than 8% were identified as shadow. This may affect pixels with low brightness such as water bodies which was not the case in the case study. Figure A1- 7-10 shows how shadow affects the results of atmospheric correction from BEAM. Although the existence of shadow may not have a significant effect on some pixels, it will probably have an effect in the increasing number of negative output values.

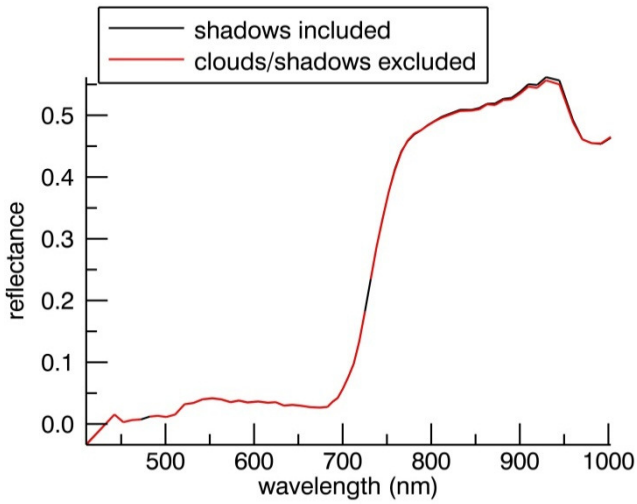

Figure A1- 7-10 The effect of shadows in BEAM's atmospheric correction.

A1.8 Conclusion

The results of the atmospheric correction performed by ATCOR 2 are not reliable. A positive shift on the surface reflectance from ATCOR2, most probably due to sensor calibration issues, was detected. Atmospheric correction was carried out without masking clouds and shadows which will introduce some errors in the output surface reflectance. Also, ATCOR2 is designed for the atmospheric correction of data with low to medium view zenith angle which is not the case for the CHRIS data with a ±55 flyby view zenith angle.

The results of the atmospheric correction undertaken by BEAM were accepted; however there are some uncertainties in the results. BEAM apparently corrected the miscalibration issue in the CHRIS data. However, some negative values were observed in the output from BEAM. This is due to an error in BEAM which overestimates AOT. The problem was dealt with by choosing a lower AOT of 0.15, which, however, introduced some errors in the outputs.

A2 Appendix 2

The following figures show the relationship between directional reflectance and albedo at the visible, NIR and broadband bands.

* There was a mislabelling of stubble land cover which was labelled as bare soil. Therefore, the figures relating to the results in bare soil belong to stubble land cover.

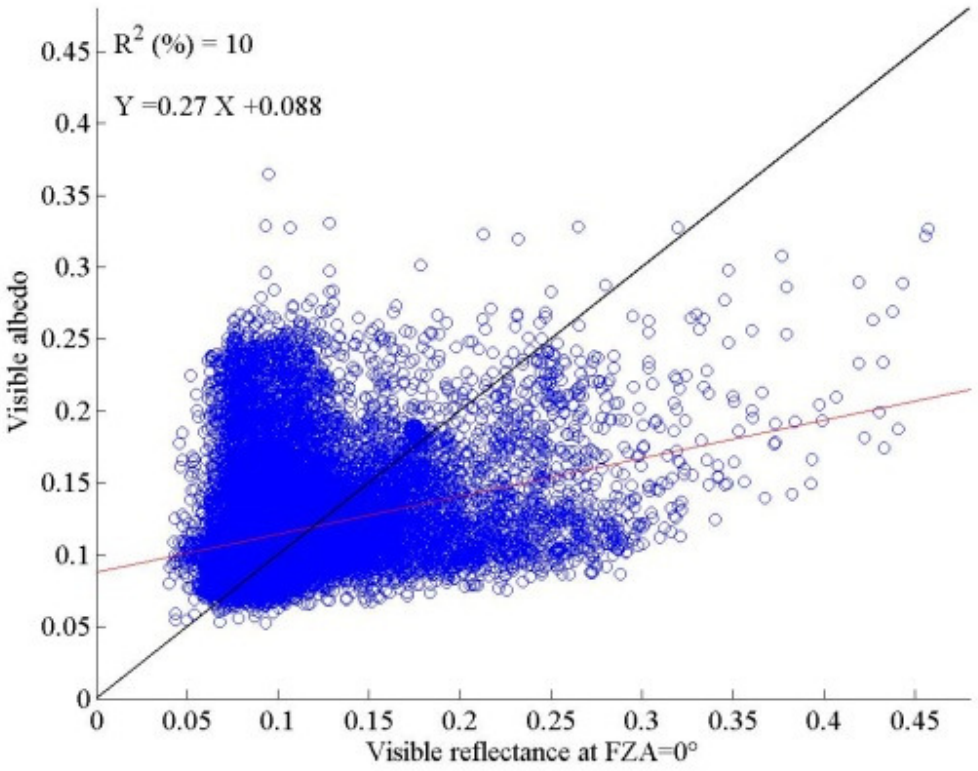
R2 (%) = 10
Y =0.27 X +0.088
Visible albedo
Visible reflectance at FZA=0°
0
0.05
0.1
0.15
0.2
0.25
0.3
0.35
0.4
0.45

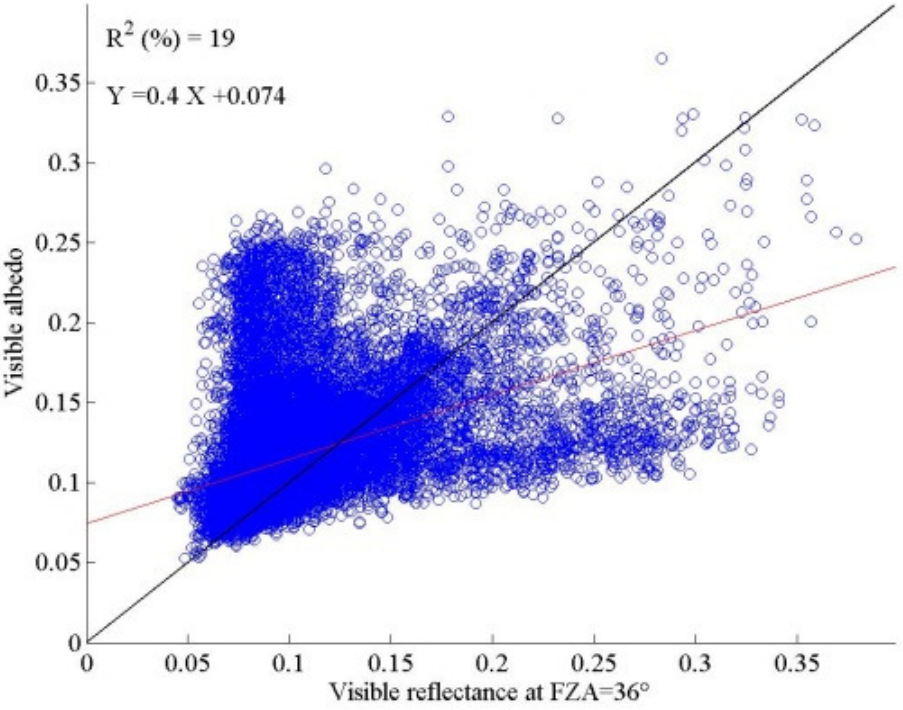
R2 (%) = 19
Y =0.4 X +0.074
Visible albedo
Visible reflectance at FZA=36°
0
0.05
0.1
0.15
0.2
0.25
0.3
0.35

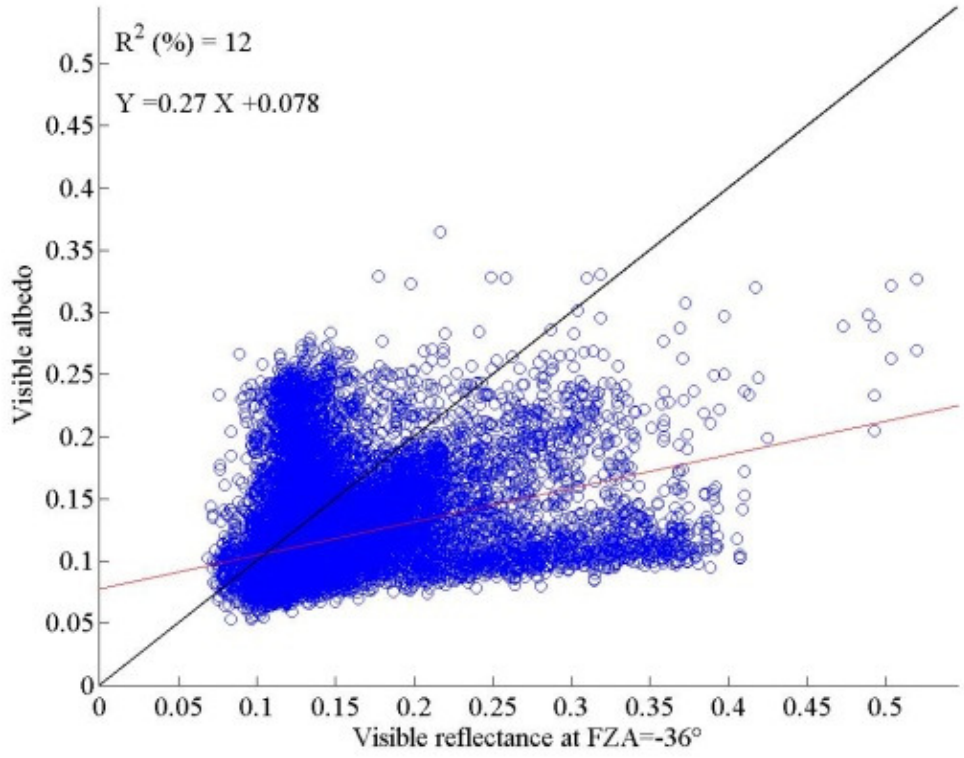
R2 (%) = 12
Y =0.27 X +0.078
Visible albedo
Visible reflectance at FZA=-36°
0
0.05
0.1
0.15
0.2
0.25
0.3
0.35
0.4
0.45
0.5

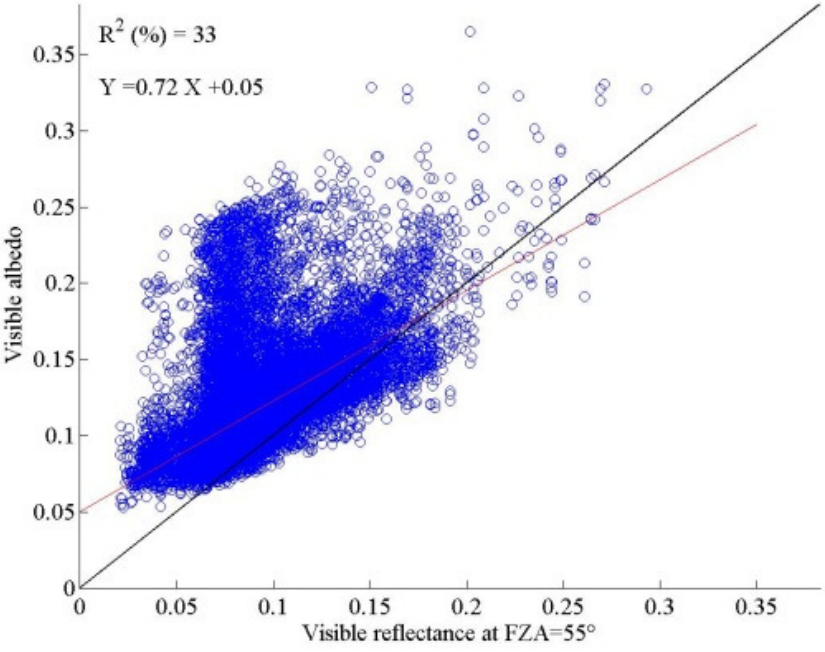
R2 (%) = 33
Y =0.72 X +0.05
Visible albedo
Visible reflectance at FZA=55°
0
0.05
0.1
0.15
0.2
0.25
0.3
0.35

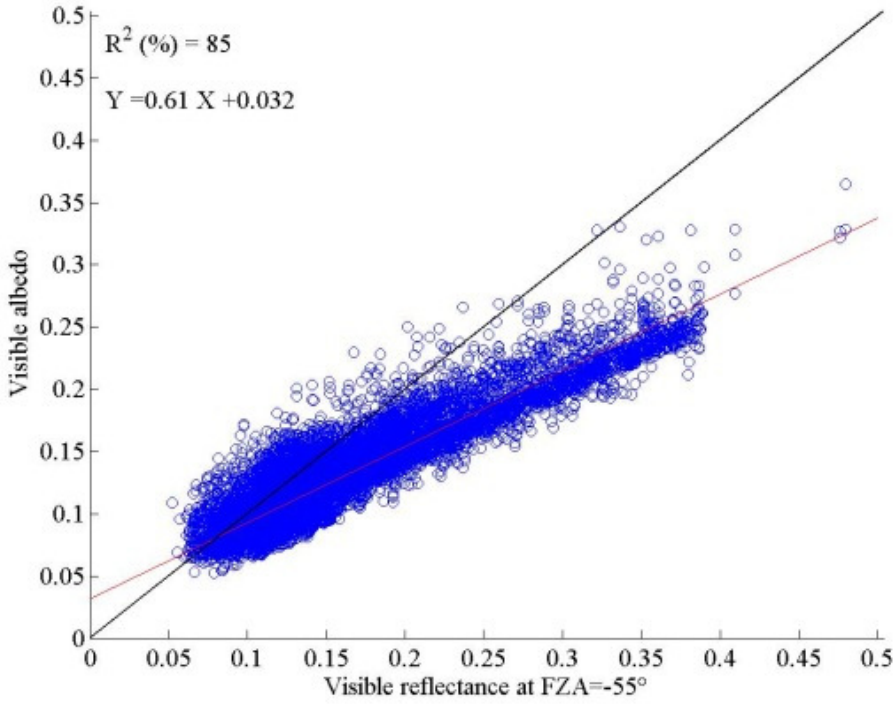

Figure A2- 1 Scatterplot of directional reflectance and albedo at the visible band

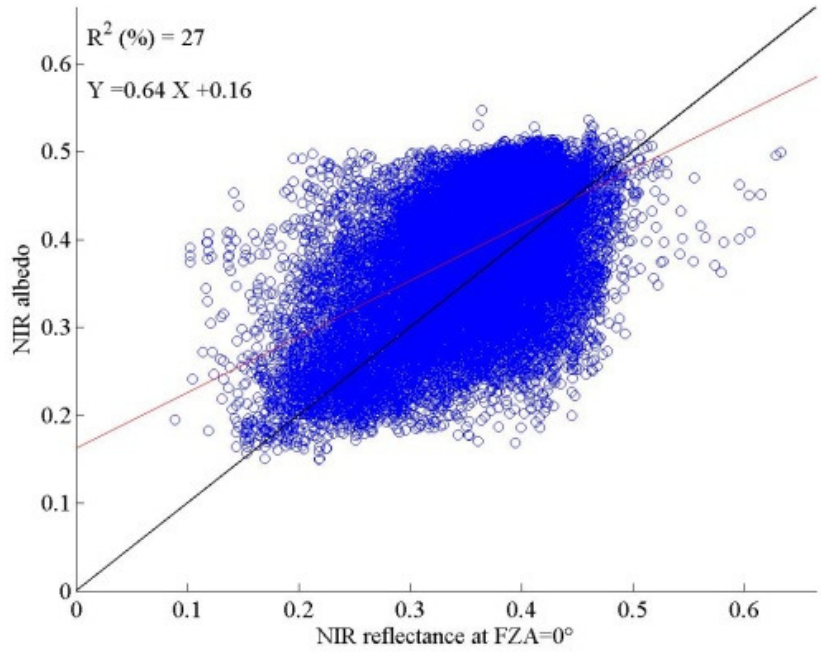
R2 (%) = 27
Y =0.64 X +0.16
NIR albedo
NIR reflectance at FZA=0°
0
0.1
0.2
0.3
0.4
0.5
0.6

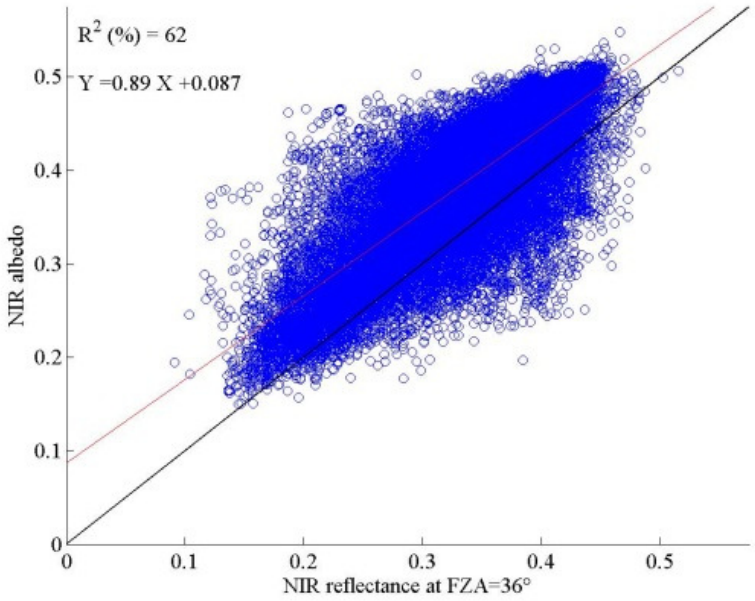
R2 (%) = 62
Y =0.89 X +0.087
NIR albedo
NIR reflectance at FZA=36°
0
0.1
0.2
0.3
0.4
0.5

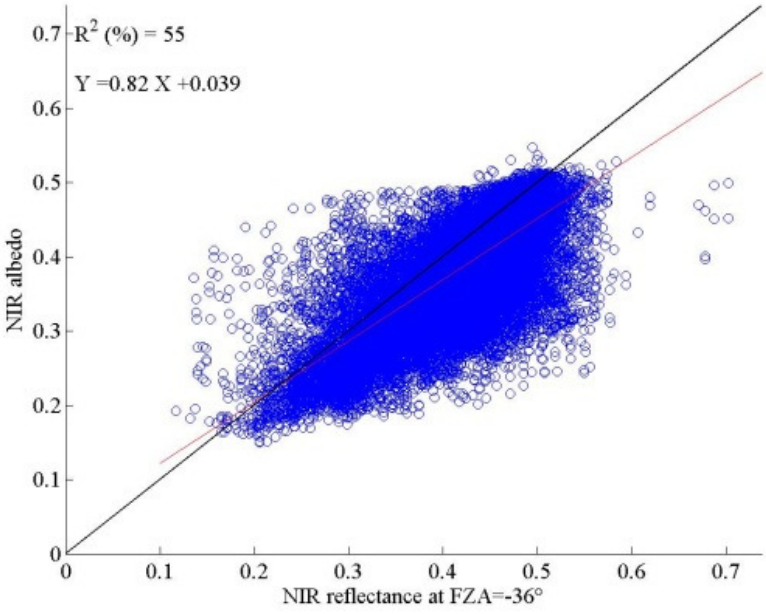
R2 (%) = 55
Y =0.82 X +0.039
NIR albedo
NIR reflectance at FZA=-36°
0
0.1
0.2
0.3
0.4
0.5
0.6
0.7

ERROR: stackunderflow
OFFENDING COMMAND: ~

STACK: